A SIMULATOR WITH NUMERICAL UPSCALING FOR THE ANALYSIS OF COUPLED MULTIPHASE FLOW AND GEOMECHANICS IN HETEROGENEOUS AND DEFORMABLE POROUS AND FRACTURED MEDIA

A Dissertation

by

DAEGIL YANG

Submitted to the Office of Graduate Studies of
Texas A&M University
in partial fulfillment of the requirements for the degree of

DOCTOR OF PHILOSOPHY

Chair of Committee,	Thomas A. Blasingame
Co-Chair of Committee,	George J. Moridis
Committee Members,	Eduardo Gildin
	Marcelo Sanchez
Head of Department,	A. Daniel Hill

August 2013

Major Subject: Petroleum Engineering

ABSTRACT

A growing demand for more detailed modeling of subsurface physics as ever more challenging reservoirs - often unconventional, with significant geomechanical particularities - become production targets has motivated research in coupled flow and geomechanics. Reservoir rock deforms to given stress conditions, so the simplified approach of using a scalar value of the rock compressibility factor in the fluid mass balance equation to describe the geomechanical system response cannot correctly estimate multi-dimensional rock deformation.

A coupled flow and geomechanics model considers flow physics and rock physics simultaneously by coupling different types of partial differential equations through primary variables. A number of coupled flow and geomechanics simulators have been developed and applied to describe fluid flow in deformable porous media but the majority of these coupled flow and geomechanics simulators have limited capabilities in modeling multiphase flow and geomechanical deformation in a heterogeneous and fractured reservoir. In addition, most simulators do not have the capability to simulate both coarse and fine scale multiphysics.

In this study I developed a new, fully implicit multiphysics simulator (TAM-CFGM: Texas A&M Coupled Flow and Geomechanics simulator) that can be applied to simulate a 2D or 3D multiphase flow and rock deformation in a heterogeneous and/or fractured reservoir system. I derived a mixed finite element formulation that satisfies local mass conservation and provides a more accurate estimation of the velocity solution in the fluid flow equations. I used a continuous Galerkin formulation to solve the geomechanics equation. These formulations allowed me to use unstructured meshes, a full-tensor permeability, and elastic stiffness. I proposed a numerical upscaling of the permeability and of the elastic stiffness tensors to generate a coarse-scale description of the fine-scale grid in the model, and I implemented the methodology in the simulator.

I applied the code I developed to the simulation of the problem of multiphase flow in a fractured tight gas system. As a result, I observed unique phenomena (not reported before) that could not have been determined without coupling. I demonstrated the importance and advantages of using unstructured meshes to effectively and realistically model a reservoir. In particular, high resolution discrete fracture models allowed me to obtain more detailed physics that could not be resolved with a structured grid. I performed numerical upscaling of a very heterogeneous geologic model and observed that the coarse-scale numerical solution matched the fine scale reference solution well. As a result, I believed I developed a method that can capture important physics of the fine-scale model with a reasonable computation cost.

DEDICATION

To my better half, Jiu Choe,
for being with me and sharing happiness, joy, and sadness.
Now, it is my turn to do my utmost to love you better.

To my beautiful son, Nathaniel Heejae Yang,
for giving me a big joy in my life.

To my parents and parents-in-laws,
for their unconditional support and love.

To my uncle Dennis,
for mentoring my professional life with warm advice and support.

ACKNOWLEDGEMENTS

I would like to express my gratitude to Dr. George Moridis, my academic co-advisor and committee co-chair, for academic guidance and financial support of my research. He introduced me a world of numerical simulation and trained me hard to become a simulation expert. He taught me how to understand complex physics and translate the physics into a mathematical model so I could solve an engineering problem. All the experience and knowledge that I obtained from him are very valuable and became a strong asset in my effort to succeed in my professional life.

I would like to thank Dr. Tom Blasingame, my academic co-advisor and committee co-chair, for providing financial support, warm advice, and strong encouragement, all of which really helped me to complete my Ph.D study. He motivated me to work on a unique and high quality Ph.D work and supported my research with a good guidance and patience.

Also, I would like to thank to Dr. Eduardo Gildin and Dr. Marcelo Sanchez, for serving on my dissertation committee. Dr. Gildin has been providing me this expertise in reservoir simulation and always open to my questions. I really enjoyed the discussions we had in his class. Dr. Sanchez's invaluable knowledge in geomechanics really helped to complete this work.

TABLE OF CONTENTS

LIST OF FIGURES

FIGURE Page

FIGURE Page

FIGURE Page

FIGURE Page

FIGURE Page

FIGURE Page

FIGURE Page

FIGURE Page

FIGURE Page

LIST OF TABLES

TABLE Page

CHAPTER I

INTRODUCTION

1.1 Statement of the Problem

A reservoir simulator is a sophisticated tool to describe flow physics in a reservoir and most oil and gas companies use reservoir simulators to design production and predict reservoir performance. Thus, reservoir simulation has become one of the important research areas in petroleum engineering. Over the years, there have been significant improvements in reservoir simulation, mostly focused on the aspects of flow physics in porous media. The geomechanical behavior of reservoirs had not received the same level of attention, and it is only recently that it has become an important issue as extension of production into reservoirs with significant geomechanical challenges (mainly unconventional) necessitated consideration and analysis of the matter. In reality, porous media are deformable, requiring consideration of the interrelation between fluid flow and rock deformation. In conventional reservoirs with consolidated/lithified media, low pore compressibility, stiff overburdens and mild pressure drops, full consideration of geomechanics may be unnecessary, and its effect can be adequately accounted for by adjusting the flow equation. This is not the case in unconventional reservoirs, unconsolidated media, large pressure drops and hydraulically-fractured systems, in which the interdependence of, and interaction between, flow and geomechanical properties is significant, affects production, and has to be explicitly described. To analyze such problems, coupled flow-geomechanical simulators are needed.

Even though reservoir simulation engineers want to incorporate more realistic physics while modeling and simulating reservoir performance, they also strive for efficient computation (in terms of memory requirement and execution speed) without sacrificing quality. If a full field reservoir model with aqueous and organic phases involved a grid with multi-million cells and a heterogeneous property distribution, its application to the analysis of reservoir performance would require large memory (less of a problem currently) and long execution times (a pervasive problem). Parallelization of the reservoir simulator can help significantly to achieve a faster computation, but the number of linearly independent equations and the memory requirements during the simulation do not change. Furthermore, because of high demand caused by the extensive use of numerical simulation in reservoir analyses, the number of computational nodes that companies make available for reservoir studies involving parallel simulations is limited.

From a reservoir simulation engineer's point of view, it would be very favorable to deal with a coarse-scale (CS) model that accounts for most of the important physics represented in a fine-scale (FS) model. Such a model is described as an *upscaled* model. This would result in a faster computation, allowing more

time for the analysis and evaluation of the model predictions and their sensitivity to key parameters and conditions.

Most reservoir systems are by nature heterogeneous. As such, they are characterized by spatial variations in the distribution of their flow properties such as the intrinsic permeability, which is coefficient of Darcy's equation that controls the flow velocity. In this case, obtaining a more accurate velocity solution is very important since flow path will be determined by the direction of the velocity. In addition, obtaining better descriptions of the saturation solution is always very favorable.

Heterogeneous media contain anisotropic properties that should be considered in the flow and geomechanics equations by using full tensors. For an accurate description of the reservoir system, upscaled (coarse-scale) multiphysics models need to have the capability of full-tensor description of permeability and elastic stiffness.

A reservoir model with complex geometry (*e.g.,* discrete fracture, complex shape of cracks, and fracture network) is difficult to model with structured grids (*i.e.*, rectangular Cartesian grid). In this case, unstructured grids provide the means to construct more realistic representations of the complex geometry of such systems.

In this study, I developed a multiphysics simulator (TAM-CFGM) that can model the interdepenedent processes of multiphase flow and rock deformation during production from a petroleum reservoir. I proposed a mixed finite element formulation of the flow equations that allows an accurate estimation of velocity and satisfies local mass conservation. TAM-CFGM has the capability to preprocess a fine-scale (FS) model to generate a coarse-scale (CS) multiphysics model and simulate its performance, which captures most of the performance of the FS model. In addition, TAM-CFGM incorporates unstructured grids and can describe permeability and elastic stiffness as full tensors.

1.2 Background

Fig. 1.1 shows highly heterogeneous porosity (**Fig. 1.1(a)**) and permeability (**Fig. 1.1(b)**) fields adapted from the reservoir model of the tenth SPE comparative project (SPE10 problem) to compare upscaling techniques (Christie and Blunt 2001). The figure indicates that the permeability field has a channelized barrier in the middle of the domain which would make fluid flow from the upper area to the lower area difficult, or vice versa. Since the permeability and porosity fields are highly heterogeneous it is likely that the mechanical properties (*e.g.*, Young's modulus) are very heterogeneous as well.

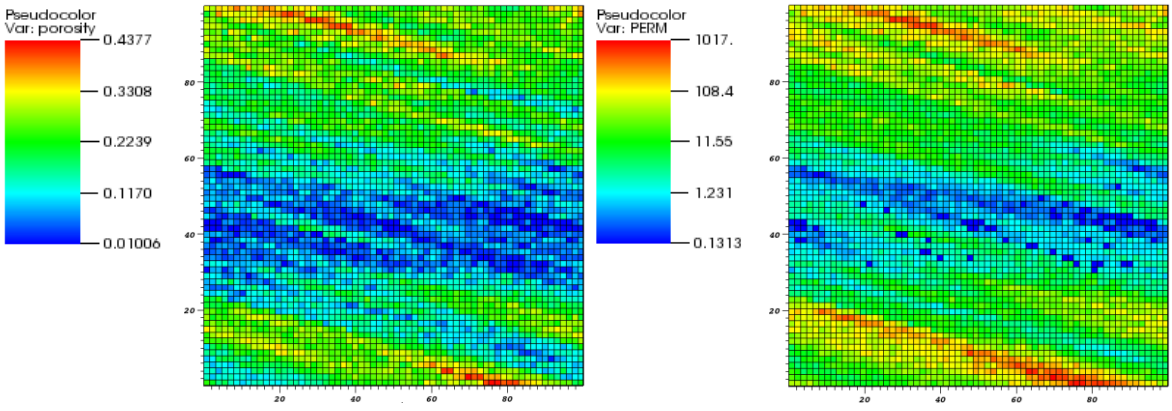

Fig. 1.1—(a) Porosity field and (b) x-direction permeability field. I assumed that y-direction permeability field is the same as x-direction permeability. The permeability values within this field differ by a factor of up to 10,000. Note that the permeability field follows a logarithmic distribution, and that the permeability unit is the millidarcy (md).

Reservoir rock is deformable, so the rock and fluid in the reservoir interact with each other. This physical phenomenon is described in a conventional reservoir simulator as a constant pore compressibility factor, but this assumption is not valid when the rock deformation is significant and/or dramatically affects fluid flow in the porous media. The reservoir system is in equilibrium initially; however, production and/or injection of oil and gas change the system, thus inducing a response. For example, mass production from the reservoir will lower the pore pressure, and the decrease in pore pressure will increase the effective stress in the reservoir. The effective stress is the real in-situ stress that deforms the porous medium according to the principles of poroelasticity (Terzaghi 1923; Biot 1941). The deformation of the porous medium caused by the change in effective stress is more significant when the reservoir system is unconsolidated. Such deformation would change (potentially considerably) the permeability field in the reservoir. In order to consider the flow and the geomechanics simultaneously, the flow problem and the geomechanics problem should

be coupled, which means that the reservoir simulator needs to have the capability to solve simultaneously the mass balance (flow) equations and the geomechanical equilibrium (geomechanics) equations.

A coupled flow and geomechanics simulator solves at least two sets of governing equations, namely, the mass balance equations (corresponding to each of the fluids/components in the system) and geomechanical equilibrium equations (describing stresses and displacements). The numerical solution of the geomechanical equilibrium equation is a displacement vector. When we use a finite element discretization to solve the geomechanical equilibrium equation corresponding to a 3-D reservoir model, the solution contains three displacement values at each node. When using a finite volume discretization, the numerical solution of the flow problem is a scalar solution at the center of each gridblock (cell or element). A mixed finite element discretization with the lowest order Raviart-Thomas space satisfies local mass conservation, and yields an additional velocity solution at each faces of the gridblock (Raviart and Thomas 1977). The geomechanical solution domain is usually larger than the flow domain because of the effects of the overburden and the underburden cannot be ignored, thus increasing the cost of computation. Solving this FS heterogeneous problem with a fully coupled flow and geomechanics simulator is computationally demanding.

To resolve these problems efficiently, we need to define different scales of the reservoir model (FS and CS) and to develop a method that effectively captures the FS effect on the CS grid without directly computing all the small features. The resulting upscaled model can represent the complex physics of the model using the coarse grid that contains the contribution of the fine scale physics.

Upscaling techniques reduce not only the size of the global matrix, but also the number of solutions and parameters to save, allowing an efficient computation to be achieved. The purpose of the numerical simulation is to obtain approximate solutions of the integro-differential and partial differential equations that describe physical phenomena at discrete points, namely, the mesh. The upscaling procedure can coarsen the mesh so that the number of discrete points is lower than that in the original problem. The most important task is to assign the most accurate equivalent properties to each discrete point after coarsening.

Conventional finite-difference or finite-volume based reservoir simulators calculate velocity after obtaining the pressure solution and this procedure often produces inaccurate approximation of fluid velocity because of rough coefficients such as a discontinuous permeability (Darlow et al. 1984). A combination of inaccurate fluid velocities and upstream weighting may result in numerical dispersion, and the solution may be further affected adversely by grid orientation effects (Ewing and Heinemann 1983). Therefore, it is important to obtain a more accurate velocity solution when dealing with a heterogeneous reservoir system. For multiphase simulation, it would be desirable to obtain a better estimate of the saturation solution than the saturation solution from a conventional simulator.

If permeability and elastic stiffness tensors are upscaled, they result in full tensors even though the FS properties are represented by isotropic tensors. It is physically more accurate to model highly heterogeneous reservoir systems with full tensors, and this is even more important when the reservoir system is fractured. It is obvious that the multiphysics simulator should have the capability to use full tensor permeability and elastic stiffness.

Fig. 1.2 shows a 2D discretization domain with a single (a) and two (b) discrete fractures. Representation of the discrete fractures using a rectangular Cartesian grid is very challenging because the control volumes representing fractures overestimate the fractured region. The grid must be locally refined to represent discrete fractures. In terms of the physical behavior of flow, the characteristics of the fracture and the matrix are quite different. Likewise, the geomechanical properties of the matrix and fracture are different.

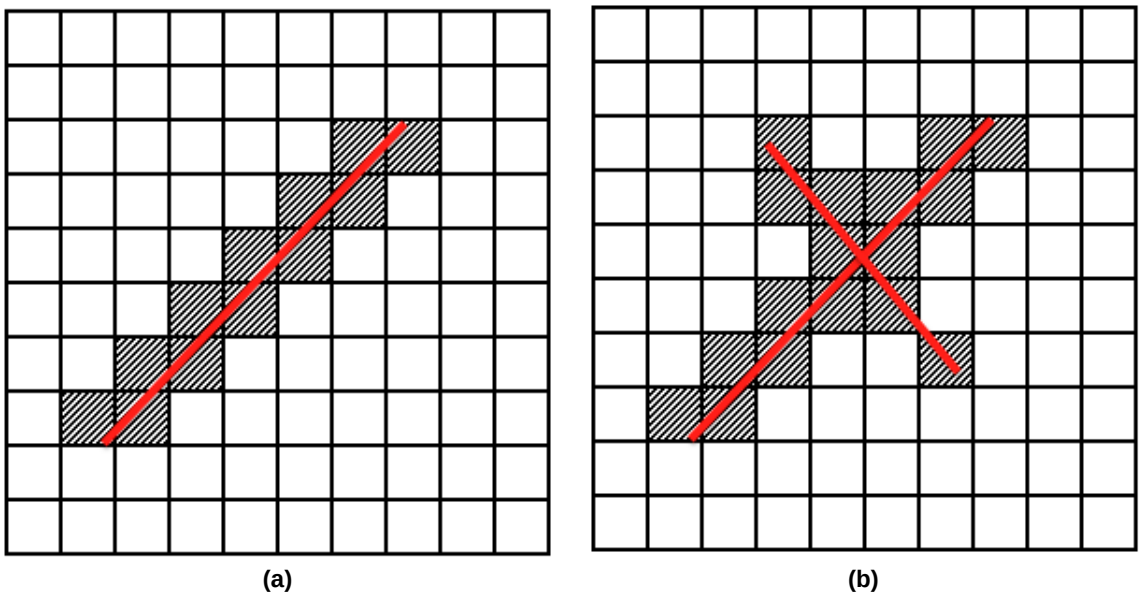

Fig. 1.2—Challenges in describing (a) a single discrete fracture and (b) multiple discrete fractures when using a discretization involving a 10×10 rectangular Cartesian grid. The red colored straight line is the actual geometry of the discrete fractures, and the shaded areas depict the representation of the discrete fractures with rectangular grids.

Fig. 1.3 shows the representation of a single discrete fracture using an unstructured mesh. It is obvious that a realistic representation of the fracture is possible with the unstructured mesh. If one uses a structured mesh, an enormous number of cells would have to be generated to accurately describe the system, thus making the computation much more difficult, if not nearly impossible. The use unstructured meshes in systems with complex features (such as individual fractures, faults, etc.) and formation geometries is a practical necessity in order to achieve a realistic system representation and efficient computation. For the

case of the discrete fracture model in **Fig. 1.3**, only 891 cells are used to generate the fine scale discrete fracture.

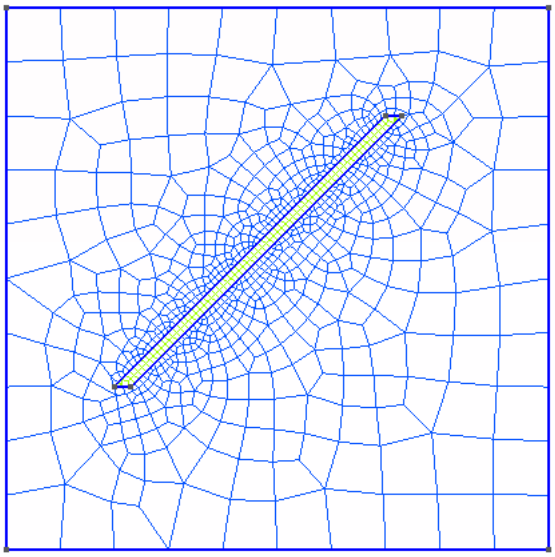

Fig. 1.3—Representation of a discrete fracture using unstructured grids. Only 891 cells are used to represent the fine scale discrete fracture.

Most of the conventional reservoir simulators use a finite volume discretization and the balance equations of mass (and/or heat) are expressed in the following integral form (Moridis et al. 2008)

$$\frac{d}{dt}\int_{\Omega} M^k d\Omega + \int_{\Gamma} \boldsymbol{F}^k \cdot \boldsymbol{n} d\Gamma = \int_{\Omega} q^k d\Omega \quad \text{(1-1)}$$

where the superscript k indicates component and the super subscript Ω and Γ indicate the domain and the boundary. M^k, $\boldsymbol{F}^k$, q^k, $\boldsymbol{n}$ are accumulation (kg/m^3), flux vector (kg/m^2s), source and sink of component k (kg/m^3s), and normal vector, respectively. The second term on the left hand side of Eq. 1-1 for a discretized element is approximated as

$$\int_{\Gamma} \boldsymbol{F}^k \cdot \boldsymbol{n} d\Gamma = \sum_{i=1}^{m} A_m F_m \quad \text{(1-2)}$$

where m is the number of interfaces. A_m and F_m are the area of the interface and the approximated flux through the interface. For Eq. 1-2 to be valid, the flux F_m must be normal to the interface. **Fig. 1.4** shows the approximation of the flux on an interface of two grid blocks (Moridis et al. 2008). Only conditions at, and the properties (fluid and rock) of the two grid blocks are required to compute the flux. This method is called the *two-point flux approximation* (TPFA).

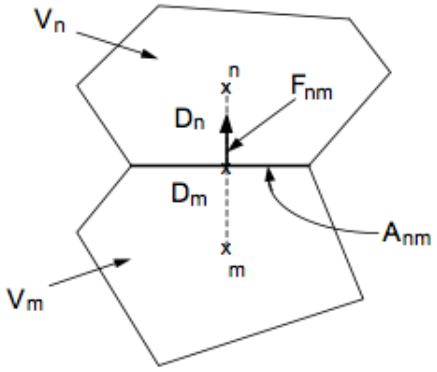

Fig. 1.4—Estimation of flux on the interface of the grid blocks. The flux on the interface is obtained by a suitable averaging (interpolation, harmonic mean, upstream weighting) of the two grid blocks (Moridis et al. 2008).

A conventional reservoir simulator uses the TPFA method to estimate the flux between two grid blocks by the difference in the corresponding pressures, taking into account gravitational effects. TPFA discretization of an elliptic operator can generate a positive definite M-matrix but this approximation is limited to K-orthogonality (Aavatsmark 2002; Potsepaev et al. 2009). K-orthogonality means that the grids are orthogonal to the permeability tensor (K) and this is the case of the rectangular Cartesian grid with a directional permeability tensor. When the K-orthogonality is lost (as is the case when a full tensor permeability field and/or an unstructured grid are involved), TPFA generates an error in estimating flux (Potsepaev et al. 2009). To alleviate this problem, the multi point flux approximation (MPFA) method was developed. This is capable of handling full tensors (e.g., of permeability and thermal conductivity) and/or distorted grids (Aavartsmark et al. 1996; Edwards and Rogers 1998; Lee at al. 1998; Aavatsmark 2002; Mlacnik and Durlofsky 2006; Martringe et al. 2008; Salama et al. 2013).

1.3 Objectives

The objectives of this work are to:

- Develop a state of the art multiphysics simulator that can handle unstructured grids and full tensor permeability and elastic stiffness.
- Investigate the physical behavior of flow and geomechanics in highly heterogeneous porous media.
- Apply the simulator to analyze the complex physics of fractured tight/shale gas systems.
- Propose a methodology to upscale permeability and elastic stiffness tensors to efficiently model heterogeneous and deformable porous media.
- Evaluate the efficiency of the computation and the correctness of the numerical solution of the simulator using the proposed upscaling methods.

1.4 Significance

In this study I introduce a fully implicit and coupled multiphase flow and geomechanics simulator (TAM-CFGM) that contains more advanced features than conventional coupled flow and geomechanics simulators. I developed a mixed finite element formulation to satisfy local mass conservation of the flow problem and to provide a more accurate velocity solution. For the geomechanics problem, I used a continuous Galerkin finite element formulation. With the proposed formations, TAM-CFGM can be applied to model a complex reservoir system such as a fractured tight gas reservoir with geologic heterogeneity and anisotropy of permeability and elastic stiffness tensors. TAM-CFGM is numerically stable because I used a fully implicit and fully coupled formation that guarantees the numerical stability of a coupled flow and geomechanics problem. The mixed finite element formation can alleviate oscillation of numerical solution that could be observed in modeling a consolidation problem with the standard finite element formation. TAM-CFGM can generate a coarse scale multiphysics model by upscaling a FS model. Furthermore, the code can describe very complex reservoir geometries and challenging features (such as fractures, faults, etc.) using unstructured grids and using with full tensors to represent permeability and elastic stiffness.

By comparing the corresponding numerical solutions, I show that the upscaled CS model accurately captures the most important physics of the FS model. This indicates that we can obtain a good approximation of complex physics of a FS model with a very reasonable computation cost.

Based on the results of the extensive literature review I conducted as part of this study, I believe this is the first attempt to use a fully implicit and coupled multiphase flow and geomechanics simulator to model a reservoir with complex fractures (such as discrete fractures, a complex crack, etc.) and would provide

more detailed physics of fluid flow in deformable and fractured reservoirs which may not observe with conventional reservoir simulators.

CHAPTER II

LITERATURE REVIEW

2.1 Coupled Flow and Geomechanics

In the reservoir simulation community, the importance of reservoir geomechanics in the correct description of reservoir behavior has been largely overlooked. Conventional reservoir simulators adopt simple scalar compressibility values to account for the effects of rock deformation on porosity, and the porosity-permeability interdependence is routinely overlooked. This simple approach is totally inadequate if the reservoir is poorly consolidated and/or heterogeneous, if the pressure drops are significant, if the mechanical strength of the reservoir rocks is low, and if the behavior of fractures (natural or induced) is to be described.

In the early 1940's, significant land subsidence was initiated in Long Beach, California because of oil and gas production (Allen 1972). The production of oil and gas lowered the pore pressure in the reservoir which resulted in the increase in effective stress. The increased effective stress resulted in compaction of the reservoir that caused the land subsidence. The magnitude of the subsidence continued to increase and the affected area reached 20 square miles in 1958, damaging many buildings and infrastructure in the region. The cost of resolving the associated problems totaled more than 100 million dollars (Allen 1972), which is equivalent to more than a billion dollars in today's money value. It is almost impossible to model a significant amount of subsidence with conventional reservoir simulators that limit the description of the geomechanical processes to a simple pore compressibility model because this approach cannot account for the effects of the varying local stresses during production (stresses that can have a significant impact on reservoir compaction and deformation). This is one of the main motivations for developing coupled flow and geomechanics simulators.

Coupling a geomechanics simulator to a reservoir simulator has been investigated by a number of researchers (Settari and Mourits 1994, 1998; Lewis and Schrefler 1998; Gutierrez et al. 2001; Settari and Walters 2001; Wan 2002; Mainguy and Longuemore 2002; Gai 2004; Tran et al. 2004; Dean et al. 2006; Jha and Juans 2007; Rutqvist and Moridis 2009; White 2010; Ferronato et al. 2010; Kim et al. 2012; Huang et al. 2013). Settari and Morits (1994; 1998) developed a modular approach to couple geomechanics code (stress code) with a commercial reservoir simulator. This is the so-called *iteratively coupled (IC)* approach in which each code solves its own governing equations and the two codes are coupled using a porosity correction term. The advantage of this method is that it does not require the development of a new multiphysics simulator (coupled flow and geomechanics), a very significant undertaking.

Instead, currently available codes can be used, and are coupled them with a relatively simple interface. Later, Settari and Walters (2001) showed the application of the iteratively coupled method for a full field reservoir model.

Gutierrez et al. (2001) showed the importance of coupling geomechanical deformation to multiphase flow in porous media. In their approach, the fully coupled multiphase flow and geomechanics equations are discretized with the finite element method. The resulting fully implicit linear system of equations, which use displacement and fluid pressures as the primary variables, is solved simultaneously. Gutierrez et al. (2001) mentioned that the iterative approach may not be sufficiently robust because there is no proof that the iterative algorithm guarantees a unique solution. One possible example is the case of shear dilation when the volume of the rock increases while the pore pressure decreases. This process would necessitate negative compressibility values in the reservoir simulation component of the coupled flow-geomechanics model, leading to numerical instability (Gutierrez et al. 2001; Huang et al. 2012).

Several fully and iteratively coupled methods have been proposed by several researchers (Wan 2002; Dean et al. 2006; Ferronato et al. 2010; Huang et al. 2013). Wan (2002) viewed the Jacobian matrix of the IC method as a modified Newton-Raphson approach to the fully coupled method, and noted that the number of iterations to reach convergence would be higher than in the fully coupled method because the Jacobian obtained from the iterative method is not exact. In addition, Wan (2002) indicated that a certain mapping of solutions might be required because the discretizations of two separate modules might be different. Dean et al. (2006) showed that the IC method would result in the same solution as the fully coupled method if it uses an adequately tight convergence criterion during the iteration process. They pointed out that the iterative method would provide a first-order convergence rate during the nonlinear iterations. This indicates that a large number of iterations would be needed to reach convergence in the simulation of difficult problems. In addition, Dean et al. (2006) indicated that the fully coupled approach (a) is the most stable one of the three approaches (explicitly coupled, iteratively coupled, and fully coupled) that they investigated, and (b) it guarantees second-order convergence, but (c) it requires more effort to develop the code and (d) it may be computationally more expensive than the iterative method.

Wheeler and Gai (2007) suggested that the convergence of the IC method is independent of permeability if the fluid is sufficiently compressible, and showed through numerical examples that the number of iterations depend on the values of permeability (more iterations for low permeability) only for lower fluid compressibility. Huang et al. (2013) developed a fully coupled, fully implicit flow and geomechanics simulator to model injection into heavy oil reservoirs. Their simulator was reported to solve nonlinear geomechanics equations and multicomponent flow equations. Huang et al. (2013) indicated that the IC method would be almost certain to face convergence challenges if it involves nonlinear flow and

geomechanics problems because this scheme was shown to be equivalent to solving the equations without a consistent tangent matrix.

In petroleum engineering, finite-volume or cell-centered finite difference discretization is commonly used for simulating fluid flow in undeformable porous media because it can conserve mass locally (Aziz and Settari 1979). For modeling solid deformation, the finite element is known to a better choice and is practiced by a number of researchers (Settari and Mourits 1994, 1998; Settari and Walters 2001; Bagheri and Settari 2008a). Therefore, many of the IC flow and geomechanics simulators used in reservoir simulation adopt a finite-volume or cell-centered finite difference formulation for the flow equations and a finite element formulation for the solid mechanics equation (Settari and Mourits 1994, 1998; Settari and Walters 2001).

The mixed finite element method is known to satisfy local mass conservation and to provide a more accurate and continuous description of the velocity solution by solving the coupled mass balance and Darcy's equations simultaneously (Chavent and Roberts 1991; Durlofsky 1994; Hoteit and Firoozabadi 2006a, 2006b). The fundamental difference of this method is that the formation treats the velocity as a primary variable rather than obtaining from the pressure solution. In addition, this method can deal with discontinuous full tensor permeability and unstructured meshes (Durlofsky and Chien 1993; Wheeler and Peszynska 2002; Younes et al. 2004; Klausen and Winther 2006; Wheeler et al. 2012).

Gai (2004) used a mixed finite element formulation to model multiphase flow equations that are coupled with the geomechanical equilibrium equation. The formulation of the multiphase flow equations ended up using a cell-centered finite difference scheme that is only applicable to a directional permeability field and a structured hexahedral mesh. Thus, as with conventional cell-centered finite difference reservoir simulators, the multi point flux approximation (Aavartsmark et al. 1996; Edwards and Rogers 1998; Lee at al. 1998; Aavatsmark 2002; Mlacnik and Durlofsky 2006; Wheeler and Yotov 2006; Martringe et al. 2008; Wheeler et al. 2012) must be used to handle full tensor permeability.

Jha and Rubens (2007) used a mixed finite element discretization to model coupled flow and geomechanics, and showed its applicability to deformable reservoir systems. Their work is limited to a single-phase flow equation that is a linear function of pressure, velocity, and displacement. They used analytical derivatives to obtain the Jacobian matrix because the coupled system of equations is linear and the simulator converges in a single Newton-Raphson iteration. However, if more complex problems are modeled (such as nonlinear multiphase flow with porosity and permeability changes), the process of obtaining the Jacobian matrix is more complicated. In addition, their work did not discuss the impact of strong heterogeneity of the rock.

Ferronato et al. (2010) used the mixed finite element method to model a 3D coupled flow and geomechanics problem. They used a mixed finite element formulation to solve the single-phase mass balance equation involving Darcy's equation, and a continuous Galerkin formulation to solve the geomechanical equilibrium equation. Ferronato et al. (2010) observed that the mixed finite element formulation satisfies local mass conservation (element-wise mass conservative) and is numerically more stable than the standard finite element (continuous Galerkin) formulation because it does not suffer from the significant oscillations of the pressure that afflict the standard finite element formulation. This issue was also investigated by Wan (2002) and White (2010) and they suggested the stabilized finite element formulation to alleviate the instability. Ferronato et al. (2010) stated that the mixed finite element formulation can model complex coupled problems, such as a sudden pressure buildup caused by an instant mechanical loading in a low permeability system.

2.2 Upscaling of Coupled Flow and Geomechanics

Computation of coupled flow and geomechanics problems are more demanding than of uncoupled problems. A way to mitigate this difficulty is to make the simulation grid coarser, thus decreasing the number of equations to solve. This process is called upscaling, and it assigns equivalent properties to the CS cells that are determined by solving FS boundary value problems.

Flow-based numerical upscaling has been widely used because it can capture the complex flow physics by solving only the pressure equation (Warren and Price 1961; Begg and Carter 1989; Durlofsky et al. 1991; King et al. 1995; King and Mansfield 1999; Chen et al. 2003; Wen et al. 2006). I will use the term *pressure solver* to describe a process involving the solution of the governing equation of single-phase flow of an incompressible fluid through an incompressible medium. Darcy's equation is either implicitly included in the governing equation or explicitly solved for by using a mixed framework (such as a mixed finite element formation). By solving a local boundary value problem (such as core flood boundary condition, linear pressure boundary condition, periodic boundary condition, etc.) of a FS model the upscaled permeability or transmissibility can be determined using Darcy's equation. The upscaled permeability or transmissibility obtained from the pressure solver is dependent on the choice of the boundary conditions.

The *core-flood boundary condition* (also known as the constant-pressure, no-flow boundary condition) is widely used to solve the local flow equation. The constant inlet and outlet pressures are defined on the local grids that are to be upscaled, and the no-flow condition (describing a zero normal component of velocity) is assigned to the boundary of the gridblocks parallel to the flow. This is a completely local problem since each coarse grid is considered to be an independent subsystem, and all the flow will be confined to the coarse grid.

The *linear pressure boundary condition* tries to overcome the limitations of the core flood boundary condition by imposing a linear pressure field on the boundary parallel to the flow direction (King and Mansfield 1999). The linear pressure boundary condition is a good candidate when there is a barrier (impermeable zone) in the reservoir model. This is because the flow will change direction when it encounters a barrier because the different pressures assigned to the boundary provide additional pressure gradient, so the flow can bypass the barrier. If a no-flow condition is assigned to the boundary, the flow will stop at the barrier and this would result in inaccurate approximation of the upscaled permeability.

By assuming spatial periodicity, a *periodic boundary condition* has also been widely used for solving local boundary value problems (Durlofsky 1991; Boe 1994; Pickup et al. 1994; Wen et al. 2003). A useful feature of this type of boundary condition is that it guarantees a symmetric and positive definite permeability tensor, thus negating a post-processing procedure to yield a symmetric positive definite permeability tensor. A limitation of this approach is that the spatial periodicity assumption may not provide a good approximation for a highly heterogeneous system.

Incorporation of neighboring grid blocks will provide more realistic results because this method, called *extended local upscaling*, considers the contribution of adjacent cells (Gomez-Hernandez and Journel 1994; Wu et al. 2002; Wen et al. 2003). Wen et al. (2003) showed that the incorporation of finely discretized cells in the vicinity of the boundary improves the accuracy of the solutions of global flow rate, oil rate, and saturation distribution in the boundary value problem.

In order to overcome the limitations of the local upscaling method, Chen et al. (2003) proposed the *local-global upscaling* method. Rather than solving expensive global problems, this method first solves the CS global problem, and then uses the CS solution as the boundary values of the local problem. An iterative procedure between the local problem and the global CS problem is required for accurate results. Chen et al. (2003) showed that this upscaling method provides considerably more accurate results than other local upscaling methods.

For the multiphase flow problem, a number of researchers in the reservoir simulation community have been working to capture fine scale heterogeneity in CS, two-phase flow problems (Kyte and Berry 1975; Stone 1991; Barker and Fayers 1994; Christie et al. 1995; Saad et al. 1995; Christie 1996; Darman et al. 2002; Lohne et al. 2006; Chen and Durlofsky 2006, 2008; Zhang et al. 2008; Suzuki 2011). Unfortunately, all this work has not yielded methods that are as robust and practical as the ones for upscaling of single-phase fluids.

The determination of upscaled absolute permeability is very important because it is necessary for critically important computations in both single- and multi-phase simulations. It is sometimes acceptable to use as

phase effective permeability the absolute permeability adjusted by a FS relative permeability that is estimated as a function of the averaged CS saturation. This is called *primitive coarse scale modeling*. However, if the sub-grid scale heterogeneity becomes strong (as is the case in high-permeability streaks or a thin high permeability channel) this approach would not correctly represent the movement of the saturation front because of the strong sub-grid scale heterogeneity (Durlosfky et al. 1994; Barker and Thibeau 1997).

In order to accurately capture sub-grid scale heterogeneity, *pseudo-function* (or sometimes called *dynamic pseudo-function*) methods have been proposed. Pseudo-functions of coarse cells are obtained by solving FS local transient problems. However, all the pseudo-functions that have been developed up to now have their own drawbacks, among which practicality is a serious concern (Christie 1996; Barker and Thibeau 1997; Christie 2001; Zhang et al. 2008; Suzuki 2011). Christie (1996) mentioned that the parameterization of each coarse pseudo-function requires excessive memory; an upscaled reservoir model with 20,000 coarse cells needed 120,000 pseudo-function curves, which occupied an inordinate amount of memory and lowered the efficiency of the computations because the process involved reading a very large number of parameterized values in order to determine the pseudo-mobility or fractional flow in each coarse cell. Because of this, the grouping of each pseudo-function into a manageable number of functions (*i.e.*, a rock type) was necessary.

Saad et al. (1995) presented grouping of effective relative permeability based on different water end points. In their work they investigated coarse scale effective relative permeability curves and made several relative permeability groups. The water end points in the effective relative permeability curves were the criterion to group. Christie (1996) suggested a three-point grouping that uses the Buckley-Leverett shock height (Buckley and Leverett 1942), the slope of the fractional-flow curve at that point, and the minimum on the total mobility curve. This method reduces many of the pseudo-function curves to a manageable number.

For the solid mechanics problem, a *mechanics solver* has been proposed to obtain the upscaled mechanical properties of the solid materials (Guedes and Kikuchi 1990; Huet 1990; Ghosh et al. 1995; Smit et al. 1998; Kouznetsova et al. 2001; Miehe and Koch 2002; Zysset 2003, Wang 2006; Pahr and Zysset 2008). The term *mechanics solver* is taken to indicate the solution of the geomechanical equlibrium equation. Hooke's law is used to define the stress-strain relation and the elastic stiffness tensor in the intrinsic material property to be upscaled. The upscaled elastic stiffness tensor is also dependent on the imposed boundary conditions of the mechanics solver.

Even though upscaling of the permeability and the elastic stiffness tensors is common in reservoir simulation and solid mechanics studies, the application of both methods to the solution of coupled flow and geomechanics problems has been limited. Chalon et al. (2004) proposed a method of upscaling the elastic

stiffness tensor that can be used for large-scale coupled flow and geomechanical simulations. Their purpose was to determine the equivalent elastic stiffness tensors that include the FS contribution in their effort to coarsen the geomechanical mesh, as the size of the geomechanical domain is larger than the flow domain. The resulting coarse scale elastic stiffness tensors were orthotropic. They tested the upscaled elastic stiffness tensors by conducting numerical simulations with different loading conditions. They observed good agreement of the displacement solutions from the FS and CS geomechanical models, but they did not discuss the application of upscaled elastic stiffness tensors to reservoir simulations.

Larsson et al. (2010) applied computational homogenization to model a 2D uncoupled consolidation of an asphalt-concrete pavement system. They used a classical first-order homogenization to upscale the micro-scale heterogeneity of the porous medium on a representative volume element and devised an iterative finite element algorithm to deal with nonlinearity, but computed only the pore pressure solution. Their group later extended their work to model a 2D fully-coupled consolidation problem (Su et al. 2011), and they obtained a more accurate numerical solution than in the uncoupled approach. The computational homogenization approach of Larsson et al. (2010) and Su et al. (2011) assumed that the material is heterogeneous on the micro-scale but homogeneous on the macro-scale, and used the periodic boundary condition to upscale the micro-scale heterogeneity and the large deformation theory to model consolidation. This approach is applicable to the simulation of a limited-size domain, but it is computationally challenging for the simulation of a large reservoir system with macro-scale heterogeneity.

Zhang and Fu (2010) modeled a consolidation problem in a highly heterogeneous porous media that involved fully-coupled single-phase flow and geomechanics. They used (a) a continuous Galerkin discretization to solve both the flow and the geomechanics problems, (b) the flow-based upscaling approach developed by Wen et al. (2003), and (c) the mechanics upscaling proposed by Huet (1990). In their study, they did not consider heterogeneity in the porosity, and assumed that the permeability was constant, i.e., independent of pressure and displacement. Comparison of the numerical solution to the solution of their previous work (the so-called coupling multiscale finite element method, Zhang et al. 2009) indicated that the upscaling method provides a more accurate solution than the coupling multiscale finite element method.

Khajeh et al. (2012) applied a numerical local upscaling approach to the estimation of the elastic stiffness tensors. They obtained upscaled elastic stiffness tensors by solving boundary value problems for a coarse cell, and they used a commercial geomechanics simulator to compare the numerical solution of the analytically upscaled coarse model to that of the numerically upscaled coarse model. They showed that the numerically upscaled model provides a more accurate displacement solution than the analytically upscaled model. Similar to Chalon et al. (2004), they did not consider upscaling of the flow part and, consequently, they did not discuss coupled flow and geomechanics in a coarse multiphysics model.

Recently, Settari et al. (2013) presented a methodology to determine a dynamic equivalent stiffness tensor that can be applied to a heterogeneous compacting reservoir. The analytical upscaling method, based on uniaxial deformation, was used to determine the equivalent stiffness tensor. They formulated the equivalent Young's modulus as a function of the pressure depletion, the Young's modulus ratio of shale and sand layers, and the net to gross (NTG) ratio. Thus, the upscaled elastic stiffness tensor changes over the simulation time. The upscaling method is based on a simple analytical approach and is easy to implement in a coupled flow and geomechanics simulator.

2.3 Modeling Fluid Flow in Deformable and Fractured Media

The interaction between the geomechanical regime and the fluid flow in deformable and fractured media is a very complex problem because of the challenge of modeling the complex geometry of fractures and the complex mathematical problem of solving the coupled equations (Pao and Lewis 2002). Modeling of coupled flow and geomechanics in fractured media has been studied by modifying Biot's single porosity poroelastic theory (Biot 1941) to take into account dual porosity models (Warren and Root 1963).

Valliappan and Khalili-Naghadeh (1990) derived a set of coupled differential equations governing the behavior of a fractured reservoir. Their mathematical formulation involves various coefficients that have been explicitly defined in terms of measurable physical parameters. They used a standard Galerkin method and compared their proposed non-linear coefficient formulation to the constant coefficient formulation (Wilson and Aifantis 1982; Khaled et al. 1984). They determined that if the reservoir formation is very deformable, then the linearity assumption results in a significant level of error in the numerical solution. Later, they developed an implicit coupled double-porosity model to study the same problem (Khalili-Naghadeh and Valliappan 1991). The underlying mathematical model has only one governing equation that solves for pressure in the matrix and the fracture. Instead of solving for a displacement vector, they derived several constitutive relations to consider the effect of geomechanical deformation on pressure. Their results from the single-equation approach were the same with those from the two-equation approach in their earlier study (Valliappan and Khalili-Naghadeh 1990).

Bai et al. (1993a; 1993b) proposed a multi-porosity/multi-permeability formulation to model fluid flow and rock deformation in naturally fractured reservoirs. The proposed single-phase flow and geomechanics model was based on discretization by the standard continuous Galerkin finite element method. Their study showed that the permeability is a critical factor in understanding reservoir behavior and concluded that their approach identified the strong coupling between fluid flow and solid deformation.

Using the double porosity concept, Lewis and Ghafouri (1997) developed a formulation for multi-phase flow in deformable and fractured reservoirs. However, the formulation ignored fracture deformation. Lat-

er, a new formulation for three-phase flow in a deformable fractured reservoir was developed (Pao and Lewis 2002; Lewis and Pao 2002). Their formulation was based on the geomechanical equilibrium equations and multiphase mass conservation equations and used a standard Galerkin finite element formulation to discretize the governing equations. They used a dual porosity model to describe a fractured reservoir. Their formulation involved cross coupling terms that describe the internal deformation of the solid skeleton as a function of the pressure differential between the matrix and fractures. These had been ignored in the formulation developed by Bai et al (1998) and Lewis and Ghafouri (1997).

Bagheri and Settari (2006; 2008a) proposed the *joint-mechanics theory* to develop a general and rigorous coupling between the fluid-flow equation and the deformation of fractured media that considers both porosity and permeability coupling. The fractures in the reservoir are assumed to be parallel to the coordinate axes, which results in a diagonal permeability tensor. They also used the dual porosity approach to model the matrix and the fracture. The coupled equations were solved sequentially by two separate modules, namely, a dual-porosity reservoir module and a geomechanics module. The relationship between the two modules is described by a porosity correction. The geomechanics module treated the fractured grid blocks as a single continuum, while the reservoir flow module treated them as dual porosity media. They then determined an *average continuum pore pressure*, which is quantity that considers the effects of the fracture pressure and of the matrix pressure. The average continuum pore pressure was used to obtain the effective stress. They suggested implementing a full-tensor permeability because this was likely to develop in the fractured region (depending on the distribution of fractures).

In more recent studies, Bagheri and Settari (2008b) extended their previous work by considering naturally fractured media characterized by sets of fractures of arbitrary orientation and spatial distribution. They used the multi point flux approximation (MPFA) in their flow model, considering full tensor permeability. The results of their numerical simulation showed remarkable differences in saturation and pressure profiles between the solution with and without full tensor representation of the permeability field. They concluded that the incorporation of full tensor permeability might be necessary to mode deformable and fractured reservoirs because it is possible that a directional permeability could be changed into full tensor permeability as a result of deformation of the porous media.

Du and Wong (2009) developed a coupled geomechanics-multiphase flow-heat transfer simulator. They stated that most of the commercial simulators that can simulate coupled flow (fluid and heat) and geomechanics do not incorporate the full tensor permeability, which they considered necessary because the contribution of micro-fractures can significantly affect the permeability of the fractured rock. They also indicated that the shear dilation in a thermal recovery process would result in permeability anisotropy. Their simulator used a finite element formulation that could easily deal with full tensor permeability. Their simulator solved the pressure, heat, and equilibrium equations simultaneously, and used the pressure, tem-

perature, and displacement solutions to solve the saturation equation sequentially. They applied their simulator to the study of a steam assisted gravity drainage (SAGD) project.

Not many researchers in the reservoir simulation community investigated the modeling of coupled fluid flow and geomechanics in discrete fracture media. The problem was addressed in two recent studies (Monteagudo et al. 2011; Moinfar et al. 2013). Monteagudo et al. (2011) first attempted to model the geomechanical impact on discrete fractures. They used the control volume discrete fracture simulator they had developed earlier (Monteagudo and Firoozabadi 2004) to solve the flow problem, and used a continuous Galerkin finite element formulation to solve the geomechanics problem. Thus, two separate simulators were iteratively coupled. They used separate meshes for each simulator, and applied the solution of the flow problem as the boundary condition at the fracture walls. They observed the difference in water saturation and cumulative oil and water production between the coupled and uncoupled simulations with fractures. However, they applied a single value of Young's modulus and Poisson's ratio to the entire domain. Because they excluded the discrete fracture from the computation domain of the geomechanics problem, there was no displacement solution in the fracture and the fracture walls could not touch (the fracture could not close) as the fracture wall were the boundaries of the geomechanics problem. In addition, the formulation they used was valid only for slightly compressible flow (*i.e.*, water and oil system).

Moinfar et al. (2013) used their embedded discrete fracture model (EDFM) to simulate fluid flow in a discrete fracture. They tried to model the geomechanical impact on the fracture by adding the deformation of fracture to the EDFM model. They used an empirical model called the "non-linear Barton-Bandis joint model" to relate the effective normal stress to the normal closure of the fracture (Bandis et al. 1983). Because they did not use a coupled geomechanics simulator in their study, presenting a more accurate description of geomechanical deformation and its impact on the fluid flow is difficult. For example, the model could only account for normal deformation and would not be correct if the reservoir underwent a significant shear deformation.

2.4 Unique Contributions of This Study

According to my literature review, most of the fully implicit and coupled flow and geomechanic simulators used standard finite element formulations to solve for fully coupled multiphase flow and geomechanics equations. Few simulators have used a mixed finite element formulation for flow equations, but they have some limited capabilities (single phase or limitation of incorporating full tensor permeability). In addition, application of numerical upscaling for the analysis of coupled single phase and/or multiphase flow and geomechanics problems has not done.

The unique contributions of this study include:

- Development a new coupled flow and geomechanics simulator with advanced features that can be used to find new simulation results that could be difficult to get with conventional simulators.
- Analysis of complex physics of a challenging reservoir such as a discrete fracture system by utilizing the simulator.
- Presentation of numerical upscaling for coupled flow and geomechanics problems and its successful application.

CHAPTER III

MATHEMATICAL MODELS

3.1 Coupled Single Phase Flow and Geomechanics

A form of the governing equation that describes single phase flow in porous media is expressed as

$$\frac{\partial}{\partial t}(\phi\rho_f) + \nabla \cdot (\phi\rho_f \tilde{\mathbf{v}}) = \rho_f f \quad \text{(3-1)}$$

where ϕ is the porosity, ρ_f is the fluid density, $\tilde{\mathbf{v}}$ is the interstitial fluid velocity and f is the source and sink. The interstitial fluid velocity can be expressed as a combination of the solid phase velocity and the relative interstitial velocity of the fluid with respect to the solid as

$$\tilde{\mathbf{v}} = \mathbf{v}_s + \tilde{\mathbf{v}}_{fs} \quad \text{(3-2)}$$

where $\mathbf{v_s}$ and $\tilde{\mathbf{v}}_{\boldsymbol{fs}}$ are, respectively, the solid phase velocity and the relative interstitial velocity of the fluid with respect to the solid phase. The Darcy velocity can be expressed in terms of the relative interstitial fluid velocity as

$$\mathbf{v} = \phi\tilde{\mathbf{v}}_{fs} = \frac{\boldsymbol{k}}{\mu} \cdot \left[-\nabla p + \rho_f \boldsymbol{g}\right] \quad \text{(3-3)}$$

where $\boldsymbol{k}$ is the second order permeability tensor, μ is the fluid viscosity, ρ_f is the fluid density, p is the fluid pressure, and $\boldsymbol{g}$ is the gravity vector. Substituting Eq. 3-2 into Eq. 3-1 results in

$$\frac{\partial}{\partial t}(\phi\rho_f) + \nabla \cdot \left(\phi\rho_f(\mathbf{v}_s + \tilde{\mathbf{v}}_{fs})\right) = \rho_f f \quad \text{(3-4)}$$

Eq. 3-4 is expanded as

$$\frac{\partial}{\partial t}(\phi\rho_f) + \nabla \cdot (\phi\rho_f \mathbf{v}_s) + \nabla \cdot (\phi\rho_f \tilde{\mathbf{v}}_{fs}) = \rho_f f \quad \text{(3-5)}$$

$$\frac{\partial}{\partial t}(\phi\rho_f) + \mathbf{v}_s \cdot \nabla(\phi\rho_f) + \phi\rho_f \nabla \cdot \mathbf{v}_s + \nabla \cdot (\phi\rho_f \tilde{\mathbf{v}}_{fs}) = \rho_f f \quad \text{(3-6)}$$

The material derivative is defined as

$$\frac{d}{dt}(\phi\rho_f) = \frac{\partial}{\partial t}(\phi\rho_f) + \mathbf{v}_s \cdot \nabla(\phi\rho_f) \quad \text{(3-7)}$$

Using Eq. 3-7, Eq. 3-6 becomes

$$\frac{d}{dt}(\phi\rho_f) + \phi\rho_f \nabla \cdot \mathbf{v}_s + \nabla \cdot (\phi\rho_f \tilde{\mathbf{v}}_{fs}) = \rho_f f \quad \text{(3-8)}$$

The third term on the left hand side of Eq. 3-8 can be expressed in terms of Darcy's velocity (Eq. 3-3) as

$$\frac{d}{dt}(\phi\rho_f) + \phi\rho_f \nabla \cdot \mathbf{v}_s + \nabla \cdot (\rho_f \mathbf{v}) = \rho_f f \quad \text{(3-9)}$$

Applying the small deformation theory (infinitesimal transformation), $\frac{\partial}{\partial t}(\phi\rho_f) \gg \mathbf{v_s} \cdot \nabla(\phi\rho_f)$, I make the assumption that

$$\frac{d(\phi\rho_f)}{dt} = \frac{\partial(\phi\rho_f)}{\partial t} + \mathbf{v_s} \cdot \nabla(\phi\rho_f) \approx \frac{\partial(\phi\rho_f)}{\partial t} \quad \text{(3-10)}$$

Substituting Eq. 3-10 into Eq. 3-9 yields

$$\frac{\partial(\phi\rho_f)}{\partial t} + \phi\rho_f \nabla \cdot \mathbf{v}_s + \nabla \cdot (\rho_f \mathbf{v}) = \rho_f f \quad \text{(3-11)}$$

Note that the compressibility of the fluid is defined as

$$c_f = \left(\frac{1}{\rho_f}\right)\frac{\partial \rho_f}{\partial p_f} \quad \text{(3-12)}$$

Using Eq. 3-12, Eq. 3-11 becomes

$$\rho_f \frac{\partial \phi}{\partial t} + \phi c_f \rho_f \frac{\partial p}{\partial t} + \phi\rho_f \nabla \cdot \frac{\partial \boldsymbol{u}}{\partial t} + \nabla \cdot (\rho_f \mathbf{v}) = \rho_f f \quad \text{(3-13)}$$

where $\boldsymbol{u}$ is the displacement vector. From the work of Geertsma (1957), the time derivative of porosity in Eq. 3-13 can be expressed as

$$\frac{\partial \phi}{\partial t} = \frac{b-\phi}{K_s}\frac{\partial p}{\partial t} + (b-\phi)\frac{\partial \varepsilon_v}{\partial t} \quad \text{(3-14)}$$

where ε_v is the volumetric strain ($\varepsilon_v = \nabla \cdot \boldsymbol{u}$) and b and K_s are Biot's coefficient and the solid grain stiffness, respectively. Using Eq. 3-14, I derive the mass balance equation as

$$\rho_f \left(\frac{b-\phi}{K_s}\frac{\partial p}{\partial t} + (b-\phi)\frac{\partial \varepsilon_v}{\partial t}\right) + \phi c_f \rho_f \frac{\partial p}{\partial t} + \phi\rho_f \frac{\partial \varepsilon_v}{\partial t} + \nabla \cdot (\rho_f \mathbf{v}) = \rho_f f \quad \text{(3-15)}$$

By arranging Eq. 3-15, I obtain

$$\rho_f \left(\frac{b-\phi}{K_s} + \phi c_f\right)\frac{\partial p}{\partial t} + \rho_f b \frac{\partial \varepsilon_v}{\partial t} + \nabla \cdot (\rho_f \mathbf{v}) = \rho_f f \quad \text{(3-16)}$$

Eq. 3-16 is the mass balance equation for single-phase, slightly compressible fluid flow. In the case of highly compressible flow, such as gas flow, we need to account for the significant compressibility. Then, the mass balance equation for a gas is derived from Eq. 3-11 as

$$\rho_g \frac{\partial \phi}{\partial t} + \phi \frac{\partial \rho_g}{\partial t} + \phi \rho_g \nabla \cdot \mathbf{v}_s + \nabla \cdot \left(\rho_g \mathbf{v}\right) = \rho_g f \quad \text{(3-17)}$$

where ρ_g is the gas density, which is estimated from the real gas law as

$$\rho_g = \frac{p_g M_g}{Z_g RT} \quad \text{(3-18)}$$

where p_g is the gas pressure, M_g (g/mol or kg/kmol) is the molar mass of the gas, Z_g is the compressibility of the gas, R (J/mol-Kelvin or J/kmol-Kelvin) is the gas constant and T is the absolute temperature (Kelvin). Z_g is determined from an appropriate equation of state, the most common of which are cubic equations of state, such as the Peng-Robinson (Peng and Robinson 1976) or the Soave modification of Redlich–Kwong (Soave 1972) model. Z_g is a nonlinear function of pressure and temperature. When a gas is assumed to behave as an ideal gas, Z_g.= 1. The time derivative of the gas density (for isothermal conditions) can be expressed as

$$\frac{\partial \rho_g}{\partial t} = \frac{\partial}{\partial t}\left(\frac{p_g M_g}{Z_g RT}\right) = \frac{M_g}{RT}\frac{\partial}{\partial t}\left(\frac{p_g}{Z_g}\right) \quad \text{(3-19)}$$

Using the chain rule Eq. 3-19 can also be expressed as

$$\frac{\partial \rho_g}{\partial t} = \left.\frac{\partial \rho_g}{\partial p_g}\right|_T \frac{\partial p_g}{\partial t} \quad \text{(3-20)}$$

Note that $\frac{\partial}{\partial t}\left(\frac{p_g}{Z_g}\right)$ can be expressed as

$$\frac{\partial}{\partial t}\left(\frac{p_g}{Z_g}\right) = \frac{1}{Z_g}\frac{p_g}{\rho_g}\left.\frac{d\rho_g}{dp_g}\right|_T \frac{\partial p_g}{\partial t} = \frac{p_g c}{Z_g}\frac{\partial p_g}{\partial t} \quad \text{(3-21)}$$

The variable c in Eq. 3-21 is defined as

$$c = \frac{1}{\rho_g}\left.\frac{d\rho_g}{dp_g}\right|_T = \frac{1}{\rho_g}\left.\frac{d\rho_g(p_g, Z_g(p_g))}{dp_g}\right|_T = \frac{Z_g RT}{p_g M_g}\frac{M_g}{Z_g RT} - \frac{Z_g RT}{p_g M_g}\frac{p_g M_g}{Z_g^2 RT}\frac{\partial Z_g}{\partial p_g} = \frac{1}{p_g} - \frac{1}{Z_g}\frac{\partial Z_g}{\partial p_g} \quad \text{(3-22)}$$

Introducing the variable $\zeta\left(p_g, Z_g(p_g)\right) = \frac{p_g}{Z_g}$, Eq. 3-21 becomes

$$\frac{\partial}{\partial t}\left(\frac{p_g}{Z_g}\right) = \frac{\partial \zeta\left(p_g, Z_g(p_g)\right)}{\partial t} = \frac{\partial \zeta}{\partial p_g}\frac{\partial p_g}{\partial t} = \left(\frac{\partial}{\partial p_g}\left(\frac{p_g}{Z_g}\right) + \frac{\partial \zeta}{\partial Z}\frac{\partial Z_g}{\partial p_g}\right)\frac{\partial p_g}{\partial t} = \left(\frac{1}{Z_g} - \frac{p}{Z_g^2}\frac{\partial Z_g}{\partial p_g}\right)\frac{\partial p_g}{\partial t} \quad \text{(3-23)}$$

I introduce the variable $\chi\left(p_g, Z_g(p_g)\right) = \frac{1}{Z_g} - \frac{p}{Z_g^2}\frac{\partial Z_g}{\partial p_g}$. Then Eq. 3-19 becomes

$$\frac{\partial \rho_g}{\partial t} = \frac{\partial}{\partial t}\left(\frac{p_g M_g}{ZRT}\right) = \frac{M_g}{RT}\frac{\partial}{\partial t}\left(\frac{p_g}{Z}\right) = \frac{M_g}{RT}\chi\frac{\partial p_g}{\partial t} \quad \text{(3-24)}$$

By substituting Eq. 3-24 and Eq. 3-14 into Eq. 3-17, I obtain

$$\rho_g\left(\frac{b-\phi}{K_s}\frac{\partial p_g}{\partial t} + (b-\phi)\frac{\partial \varepsilon_v}{\partial t}\right) + \phi\frac{M_g}{RT}\chi\frac{\partial p_g}{\partial t} + \phi\rho_g\nabla\cdot\mathbf{v}_s + \nabla\cdot\left(\rho_g\mathbf{v}\right) = \rho_g f \quad \text{(3-25)}$$

Rearranging terms in Eq. 3-25, I obtain

$$\rho_g\left(\frac{b-\phi}{K_s} + \phi\frac{M_g}{\rho_g RT}\chi\right)\frac{\partial p}{\partial t} + \rho_g b\frac{\partial \varepsilon_v}{\partial t} + \nabla\cdot\left(\rho_g\mathbf{v}\right) = \rho_g f \quad \text{(3-26)}$$

where $p = p_g$ for a single-phase flow equation. Then, the derived mass balance equations for slightly compressible, single-phase flow is

$$\rho_f\left(\frac{b-\phi}{K_s} + \phi c_f\right)\frac{\partial p}{\partial t} + \rho_f b\frac{\partial \varepsilon_v}{\partial t} + \nabla\cdot\left(\rho_f\mathbf{v}\right) = \rho_f f \quad \text{(3-16)}$$

and the mass balance equation for gas (highly compressible, single-phase) flow is

$$\rho_g\left(\frac{b-\phi}{K_s} + \phi\frac{M_g}{\rho_g RT}\chi\right)\frac{\partial p}{\partial t} + \rho_g b\frac{\partial \varepsilon_v}{\partial t} + \nabla\cdot\left(\rho_g\mathbf{v}\right) = \rho_g f \quad \text{(3-26)}$$

Note that only the compressibility term changes for gas flow. Instead of the constant compressibility factor of the slightly compressible flow, the nonlinear compressibility factor Z_g is included in the gas flow equation.

The governing equation describing the deformation of solid material is called the geomechanical equilibrium equation. This is defined as

$$\nabla \cdot \boldsymbol{\sigma} + \rho_b \boldsymbol{g} = \mathbf{0} \quad \text{(3-27)}$$

where $\boldsymbol{\sigma}$ is the Cauchy total-stress tensor. Using Biot's theory of consolidation (Biot 1941), the effective stress can be expressed as

$$\boldsymbol{\sigma} - \boldsymbol{\sigma_0} = \boldsymbol{\sigma}' - b(p - p_0)\boldsymbol{I} \quad \text{(3-28)}$$

where $\boldsymbol{\sigma}'$, $\boldsymbol{\sigma_0}, p_0, p,$ and $\boldsymbol{I}$ are the effective stress tensor (Pa), the initial total stress tensor (Pa), the initial total pore pressure (Pa), the current total pore pressure, and the second order identity tensor, respectively.

In Eq. 3-28, $\boldsymbol{g}$ is the gravity vector, and ρ_b is the bulk density that is defined as

$$\rho_b = \phi\rho_f + (1 - \phi)\rho_s \quad \text{(3-29)}$$

Assuming an isotropic material, the total Cauchy stress can be expressed as

$$\boldsymbol{\sigma} = \boldsymbol{\sigma_0} + \lambda\nabla \cdot \boldsymbol{u}\boldsymbol{I} + 2\mu\boldsymbol{\varepsilon}(\boldsymbol{u}) - b(p - p_0)\boldsymbol{I} \quad \text{(3-30)}$$

where λ is the first Lamé's constant and μ is the second Lamé's constant (shear modulus). Note that $\lambda\nabla \cdot \boldsymbol{u}\boldsymbol{I} + 2\mu\boldsymbol{\varepsilon}(\boldsymbol{u})$ is the effective stress and the convention for compression is negative. Using Eq. 3-28, Eq. 3-30 can be written as

$$\nabla \cdot (\boldsymbol{\sigma_0} + \lambda\nabla \cdot \boldsymbol{u}\boldsymbol{I} + 2\mu\boldsymbol{\varepsilon}(\boldsymbol{u}) - b(p - p_0)\boldsymbol{I}) + \rho_b \boldsymbol{g} = 0 \quad \text{(3-31)}$$

I can summarize the governing equations that describe coupled fluid flow and geomechanical deformation as

$$\mathbf{v} = \frac{\boldsymbol{k}}{\mu} \cdot \left[-\nabla p + \rho_f \boldsymbol{g}\right] \quad \text{(3-3)}$$

$$\rho_f \left(\frac{b-\phi}{K_s} + \phi c_f\right)\frac{\partial p}{\partial t} + \rho_f b \frac{\partial \varepsilon_v}{\partial t} + \nabla \cdot \left(\rho_f \mathbf{v}\right) = \rho_f f \quad \text{(3-16)}$$

$$\rho_g \left(\frac{b-\phi}{K_s} + \phi \frac{M_g}{\rho_g RT}\chi\right)\frac{\partial p}{\partial t} + \rho_f b \frac{\partial \varepsilon_v}{\partial t} + \nabla \cdot \left(\rho_g \mathbf{v}\right) = \rho_g f \quad \text{(3-26)}$$

$$\nabla \cdot (\boldsymbol{\sigma_0} + \lambda\nabla \cdot \boldsymbol{u}\boldsymbol{I} + 2\mu\boldsymbol{\varepsilon}(\boldsymbol{u}) - b(p - p_0)\boldsymbol{I}) + \rho_b \boldsymbol{g} = 0 \quad \text{(3-31)}$$

Note that the mass balance equations (Eq. 3-16 or Eq. 3-26) and the geomechanical equilibrium equation (Eq. 3-31) are coupled through the displacement and the pressure. Darcy's equation (Eq. 3-3) is only cou-

pled with the mass balance equation. If I formulate the permeability as a function of porosity or stress, then Darcy's equation can be coupled with the mass balance equation and the equilibrium equation through pressure and displacement. An appropriate porosity-permeability relationship is given by

$$\boldsymbol{k} = \boldsymbol{k}_{ref} exp\left(\gamma\left(\frac{\phi}{\phi_{ref}} - 1\right)\right) \quad (3\text{-}32)$$

where $\boldsymbol{k}_{ref}$ and ϕ_{ref} are the reference permeability and porosity, respectively, and ϕ and γ are the current porosity and an experimentally determined constant (Rutqvist and Tsang 2002). Eq. 3-14 states that porosity is a function of pressure and volumetric strain. Therefore, permeability became a function of pressure and volumetric strain as well.

The initial condition of the mass balance equation is

$$p = p_0 \quad (3\text{-}33)$$

Usually the initial condition is obtained after a gravity equilibration. If the system is a 2D layer (areal cross section) then gravity equilibration is not needed. The boundary condition for the case of a no-flow (Neumann) boundary is

$$\mathbf{v} \cdot \boldsymbol{n} = 0 \quad (3\text{-}34)$$

The boundary condition for the geomechanical equilibrium equation is

$$\boldsymbol{u} \cdot \boldsymbol{n} = 0 \text{ on } \Gamma_1 \quad (3\text{-}35)$$

$$\boldsymbol{\sigma} \cdot \boldsymbol{n} = \boldsymbol{t} \text{ on } \Gamma_2 \quad (3\text{-}36)$$

where $\Gamma_1 \bigcap \Gamma_2 = \phi$. Eq. 3-35 and Eq. 3-36 indicate the prescribed zero normal displacement and traction boundary conditions, respectively.

These governing equations and their initial and boundary conditions construct a mathematical model of coupled single-phase flow and geomechanics.

3.2 Coupled Multiphase Flow and Geomechanics

The governing equations that describe multiphase flow in a water and gas system in porous media are

$$\frac{\partial}{\partial t}\left(\phi S_g \rho_g\right) + \nabla \cdot \left(\phi S_g \rho_g \tilde{\mathbf{v}}_{\boldsymbol{g}}\right) = (\rho f)_g \quad (3\text{-}37)$$

$$\frac{\partial}{\partial t}(\phi S_w \rho_w) + \nabla \cdot (\phi S_w \rho_w \tilde{\mathbf{v}}_{\boldsymbol{w}}) = (\rho f)_w \quad (3\text{-}38)$$

where S_g and S_w are the gas and water saturations, respectively, $\tilde{\mathbf{v}}_{\boldsymbol{g}}$and $\tilde{\mathbf{v}}_{\boldsymbol{w}}$ are the interstitial velocities of the gas phase flow and the water phase flow, ρ_g and ρ_w are the gas phase and water phase densities, f_g and f_w are the source and sink (rate of injection and production) of the gas phase flow and water phase flow. The subscript w denotes water or the aqueous phase, and the subscript g the gas phase. I assume that the water and gas are immiscible. I then treat the water component as an aqueous phase and the gas component as a gaseous phase. The interstitial velocity of the gas and the water phase are defined as

$$\tilde{\mathbf{v}}_g = \mathbf{v}_s + \tilde{\mathbf{v}}_{gs} \quad (3\text{-}39)$$

$$\tilde{\mathbf{v}}_w = \mathbf{v}_s + \tilde{\mathbf{v}}_{ws} \quad (3\text{-}40)$$

where $\mathbf{v}_s$, $\tilde{\mathbf{v}}_{gs}$, and $\tilde{\mathbf{v}}_{ws}$ are the solid phase velocity, the relative interstitial velocity of gas phase with respect to the solid phase, and the interstitial velocity of water phase with respect to the solid phase. In addition, Darcy velocity can be expressed as a function of the relative interstitial velocities of the gas and water phases as

$$\mathbf{v}_g = \phi S_g \tilde{\mathbf{v}}_{gs} = \frac{\boldsymbol{k} k_{rg}}{\mu_g} \cdot \left[-\nabla p_g + \rho_g g\right] \quad (3\text{-}41)$$

$$\mathbf{v}_w = \phi S_w \tilde{\mathbf{v}}_{ws} = \frac{\boldsymbol{k} k_{rw}}{\mu_w} \cdot [-\nabla p_w + \rho_w g] \quad (3\text{-}42)$$

Substituting Eq. 3-39 and Eq. 3-40 into Eq. 3-37 and Eq. 3-38 results in

$$\frac{\partial}{\partial t}\left(\phi S_g \rho_g\right) + \nabla \cdot \left(\phi S_g \rho_g \left(\mathbf{v}_s + \tilde{\mathbf{v}}_{gs}\right)\right) = (\rho f)_g \quad (3\text{-}43)$$

$$\frac{\partial}{\partial t}(\phi S_w \rho_w) + \nabla \cdot \left(\phi S_w \rho_w (\mathbf{v}_s + \tilde{\mathbf{v}}_{ws})\right) = (\rho f)_w \quad (3\text{-}44)$$

Eq. 3-43 and Eq. 3-44 can be expanded to yield

$$\frac{\partial}{\partial t}\left(\phi S_g \rho_g\right) + \nabla \cdot \left(\phi S_g \rho_g \mathbf{v_s}\right) + \nabla \cdot \left(\phi S_g \rho_g \tilde{\mathbf{v}}_{\boldsymbol{gs}}\right) = (\rho f)_g \quad (3\text{-}45)$$

$$\frac{\partial}{\partial t}(\phi S_w \rho_w) + \nabla \cdot (\phi S_w \rho_w \mathbf{v_s}) + \nabla \cdot (\phi S_w \rho_w \tilde{\mathbf{v}}_{\boldsymbol{ws}}) = (\rho f)_w \quad (3\text{-}46)$$

I further expand the second divergence term of Eq. 3-45 and Eq. 3-46 as

$$\frac{\partial}{\partial t}\left(\phi S_g \rho_g\right) + \mathbf{v_s} \cdot \nabla\left(\phi S_g \rho_g\right) + \phi S_g \rho_g \nabla \cdot \mathbf{v_s} + \nabla \cdot \left(\phi S_g \rho_g \tilde{\mathbf{v}}_{\boldsymbol{gs}}\right) = (\rho f)_g \quad (3\text{-}47)$$

$$\frac{\partial}{\partial t}(\phi S_w \rho_w) + \mathbf{v_s} \cdot \nabla(\phi S_w \rho_w) + \phi S_w \rho_w \nabla \cdot \mathbf{v_s} + \nabla \cdot (\phi S_w \rho_w \tilde{\mathbf{v}}_{\boldsymbol{ws}}) = (\rho f)_w \quad (3\text{-}48)$$

I then rewrite Eq. 3-47 and Eq. 3-48 using material derivatives and the definition of Darcy velocity as

$$\frac{d}{dt}\left(\phi S_g \rho_g\right) + \phi S_g \rho_g \nabla \cdot \mathbf{v_s} + \nabla \cdot \left(\rho_g \mathbf{v_g}\right) = (\rho f)_g \quad (3\text{-}49)$$

$$\frac{d}{dt}(\phi S_w \rho_w) + \phi S_w \rho_w \nabla \cdot \mathbf{v_s} + \nabla \cdot (\rho_w \mathbf{v_w}) = (\rho f)_w \quad (3\text{-}50)$$

The assumption made for Eq. 3-10 is applied to Eq. 3-49 and 3-50, resulting in

$$\frac{\partial(\phi S_g \rho_g)}{\partial t} + \phi S_g \rho_g \nabla \cdot \mathbf{v_s} + \nabla \cdot \left(\rho_g \mathbf{v_g}\right) = (\rho f)_g \quad (3\text{-}51)$$

$$\frac{\partial(\phi S_w \rho_w)}{\partial t} + \phi S_w \rho_w \nabla \cdot \mathbf{v_s} + \nabla \cdot (\rho_w \mathbf{v_w}) = (\rho f)_w \quad (3\text{-}52)$$

Note that the compressibility of the water phase is defined as

$$c_w = \left(\frac{1}{\rho_w}\right)\frac{\partial \rho_w}{\partial p_w} \quad (3\text{-}53)$$

Using Eq. 3-53, Eq. 3-52 becomes

$$S_w \rho_w \frac{\partial \phi}{\partial t} + \rho_w \phi \frac{\partial S_w}{\partial t} + \phi S_w c_w \rho_w \frac{\partial p_w}{\partial t} + \phi S_w \rho_w \nabla \cdot \frac{\partial \boldsymbol{u}}{\partial t} + \nabla \cdot (\rho_w \mathbf{v_w}) = (\rho f)_w \quad (3\text{-}54)$$

Eq. 3-51 can be expanded to

$$S_g \rho_g \frac{\partial \phi}{\partial t} + \rho_g \phi \frac{\partial S_g}{\partial t} + \phi S_g \frac{\partial \rho_g}{\partial t} + \phi S_g \rho_g \nabla \cdot \frac{\partial \boldsymbol{u}}{\partial t} + \nabla \cdot \left(\rho_g \mathbf{v_g}\right) = (\rho f)_g \quad (3\text{-}55)$$

I express the time derivative of porosity as

$$\frac{\partial \phi}{\partial t} = \frac{b-\phi}{K_s}\frac{\partial p_t}{\partial t} + (b-\phi)\frac{\partial \varepsilon_v}{\partial t} \quad \text{(3-56)}$$

where p_t is the total pressure defined as

$$p_t = S_g p_g + S_w p_w \quad \text{(3-57)}$$

Using Eq. 3-56, I then derive the multiphase mass balance equations as

$$S_w \rho_w \left(\frac{b-\phi}{K_s}\frac{\partial p_t}{\partial t} + (b-\phi)\frac{\partial \varepsilon_v}{\partial t}\right) + \rho_w \phi \frac{\partial S_w}{\partial t} + \phi S_w c_w \rho_w \frac{\partial p_w}{\partial t} + \phi S_w \rho_w \frac{\partial \varepsilon_v}{\partial t} + \nabla \cdot (\rho_w \mathbf{v}_w) = (\rho f)_w \quad \text{(3-58)}$$

$$S_g \rho_g \left(\frac{b-\phi}{K_s}\frac{\partial p_t}{\partial t} + (b-\phi)\frac{\partial \varepsilon_v}{\partial t}\right) + \rho_g \phi \frac{\partial S_g}{\partial t} + \phi S_g \frac{\partial \rho_g}{\partial t} + \phi S_g \rho_g \nabla \cdot \frac{\partial \boldsymbol{u}}{\partial t} + \nabla \cdot \left(\rho_g \mathbf{v}_g\right) = (\rho f)_g \quad \text{(3-59)}$$

where $\delta p_t = S_g \delta p_g + S_w \delta p_w$ and $p_{cg} = p_g - p_w$. By rearranging Eq. 3-58 and Eq. 3-59, I obtain

$$\rho_w \left(S_w \frac{b-\phi}{K_s} S_g + S_w \frac{b-\phi}{K_s} S_w + \phi S_w c_w\right)\frac{\partial p_g}{\partial t} - \rho_w \left(S_w \frac{b-\phi}{K_s} S_w \frac{\partial p_{cg}}{\partial S_w} - \phi + \phi S_w c_w \frac{\partial p_{cg}}{\partial S_w}\right)\frac{\partial S_w}{\partial t} + \rho_w S_w b \frac{\partial \varepsilon_v}{\partial t} + \nabla \cdot (\rho_w \mathbf{v}_w) = (\rho f)_w \quad \text{(3-60)}$$

$$\rho_g \left(S_g \frac{b-\phi}{K_s} S_g + S_g \frac{b-\phi}{K_s} S_w\right)\frac{\partial p_g}{\partial t} + \phi S_g \frac{\partial \rho_g}{\partial t} + \rho_g \left(-S_g \frac{b-\phi}{K_s} S_w \frac{\partial p_{cg}}{\partial S_w} - \phi\right)\frac{\partial S_w}{\partial t} + \rho_g S_g b \frac{\partial \varepsilon_v}{\partial t} + \nabla \cdot \left(\rho_g \mathbf{v}_g\right) = (\rho f)_g \quad \text{(3-61)}$$

The gas density is obtained from the real gas law through a process already discussed previously. Using the gas density, I rewrite the two-phase mass balance equations as

$$\rho_w \left(S_w \frac{b-\phi}{K_s} S_g + S_w \frac{b-\phi}{K_s} S_w + \phi S_w c_w\right)\frac{\partial p_g}{\partial t} - \rho_w \left(S_w \frac{b-\phi}{K_s} S_w \frac{\partial p_{cg}}{\partial S_w} - \phi + \phi S_w c_w \frac{\partial p_{cg}}{\partial S_w}\right)\frac{\partial S_w}{\partial t} + \rho_w S_w b \frac{\partial \varepsilon_v}{\partial t} + \nabla \cdot (\rho_w \mathbf{v}_w) = (\rho f)_w \quad \text{(3-62)}$$

$$\rho_g \left(S_g \frac{b-\phi}{K_s} S_g + S_g \frac{b-\phi}{K_s} S_w + \phi S_g \frac{M_g}{\rho_g RT}\chi\right)\frac{\partial p_g}{\partial t} + \rho_g \left(-S_g \frac{b-\phi}{K_s} S_w \frac{\partial p_{cg}}{\partial S_w} - \phi\right)\frac{\partial S_w}{\partial t} + \rho_g S_g b \frac{\partial \varepsilon_v}{\partial t} + \nabla \cdot \left(\rho_g \mathbf{v}_g\right) = (\rho f)_g \quad \text{(3-63)}$$

where $S_g + S_w = 1$ and $\chi\left(p_g, Z_g(p_g)\right) = \frac{1}{Z_g} - \frac{p}{Z_g^2}\frac{\partial Z_g}{\partial p_g}$.

I then rewrite Eq. 3-62 and Eq. 3-63 as

$$\rho_w S_w \left(\frac{b-\phi}{K_s} + \phi c_w\right)\frac{\partial p_g}{\partial t} - \rho_w \left(S_w \frac{b-\phi}{K_s} S_w \frac{\partial p_{cg}}{\partial S_w} - \phi + \phi S_w c_w \frac{\partial p_{cg}}{\partial S_w}\right)\frac{\partial S_w}{\partial t} + \rho_w S_w b \frac{\partial \varepsilon_v}{\partial t} + \nabla \cdot (\rho_w \mathbf{v}_w) = (\rho f)_w \quad (3\text{-}64)$$

$$\rho_g S_g \left(\frac{b-\phi}{K_s} + \phi \frac{M_g}{\rho_g RT}\chi\right)\frac{\partial p_g}{\partial t} + \rho_g \left(-S_g \frac{b-\phi}{K_s} S_w \frac{\partial p_{cg}}{\partial S_w} - \phi\right)\frac{\partial S_w}{\partial t} + \rho_g S_g b \frac{\partial \varepsilon_v}{\partial t} + \nabla \cdot \left(\rho_g \mathbf{v}_g\right) = (\rho f)_g \quad (3\text{-}65)$$

Dividing Eq. 3-64 and Eq. 3-65 by the gas (ρ_g) and water (ρ_w) densities, respectively, and assuming the spatial gradient of the density is negligible, results in

$$S_g \left(\frac{b-\phi}{K_s} + \phi \frac{M_g}{\rho_g RT}\chi\right)\frac{\partial p_g}{\partial t} + \left(-S_g \frac{b-\phi}{K_s} S_w \frac{\partial p_{cg}}{\partial S_w} - \phi\right)\frac{\partial S_w}{\partial t} + S_g b \frac{\partial \varepsilon_v}{\partial t} + \nabla \cdot \mathbf{v}_g = f_g \quad (3\text{-}66)$$

$$S_w \left(\frac{b-\phi}{K_s} + \phi c_w\right)\frac{\partial p_g}{\partial t} - \left(S_w \frac{b-\phi}{K_s} S_w \frac{\partial p_{cg}}{\partial S_w} - \phi + \phi S_w c_w \frac{\partial p_{cg}}{\partial S_w}\right)\frac{\partial S_w}{\partial t} + S_w b \frac{\partial \varepsilon_v}{\partial t} + \nabla \cdot \mathbf{v}_w = f_w \quad (3\text{-}67)$$

Adding Eq. 3-66 and Eq. 3-67, I obtain

$$S_g \left(\frac{b-\phi}{K_s} + \phi \frac{M_g}{\rho_g RT}\chi\right)\frac{\partial p_g}{\partial t} + S_w \left(\frac{b-\phi}{K_s} + \phi c_w\right)\frac{\partial p_g}{\partial t} + \left(-S_g \frac{b-\phi}{K_s} S_w \frac{\partial p_{cg}}{\partial S_w} - \phi\right)\frac{\partial S_w}{\partial t} - \left(S_w \frac{b-\phi}{K_s} S_w \frac{\partial p_{cg}}{\partial S_w} - \phi + \phi S_w c_w \frac{\partial p_{cg}}{\partial S_w}\right)\frac{\partial S_w}{\partial t} + S_g b \frac{\partial \varepsilon_v}{\partial t} + S_w b \frac{\partial \varepsilon_v}{\partial t} + \nabla \cdot \mathbf{v}_g + \nabla \cdot \mathbf{v}_w = f_g + f_w \quad (3\text{-}68)$$

Eq. 3-68 can be reduced to

$$\left(\frac{b-\phi}{K_s} + S_g \phi \frac{M_g}{\rho_g RT}\chi + S_w \phi c_w\right)\frac{\partial p_g}{\partial t} - \left(\frac{b-\phi}{K_s} S_w \frac{\partial p_{cg}}{\partial S_w} + \phi S_w c_w \frac{\partial p_{cg}}{\partial S_w}\right)\frac{\partial S_w}{\partial t} + b \frac{\partial \varepsilon_v}{\partial t} + \nabla \cdot \mathbf{v}_t = f_g + f_w \quad (3\text{-}69)$$

Recall Darcy's equation for each phase

$$\mathbf{v_g} = \phi S_g \tilde{\mathbf{v}}_{\boldsymbol{gs}} = \frac{\boldsymbol{k} k_{rg}}{\mu_g} \cdot \left[-\nabla p_g + \rho_g g\right] \quad (3\text{-}41)$$

$$\mathbf{v_w} = \phi S_w \tilde{\mathbf{v}}_{\boldsymbol{ws}} = \frac{\boldsymbol{k} k_{rw}}{\mu_w} \cdot \left[-\nabla p_w + \rho_w g\right] \quad (3\text{-}42)$$

By adding Eq. 3-41 and Eq. 3-42, I obtain the total velocity as

$$\mathbf{v}_t = \frac{\boldsymbol{k} k_{rw}}{\mu_w} \cdot \left[-\nabla p_w + \rho_w \boldsymbol{g}\right] + \frac{\boldsymbol{k} k_{rg}}{\mu_g} \cdot \left[-\nabla p_g + \rho_g \boldsymbol{g}\right] \quad (3\text{-}70)$$

Now, I use the mobility relation to rewrite Eq. 3-70 as

$$\mathbf{v}_t = (\lambda_g + \lambda_w)\boldsymbol{k} \cdot [-\nabla p_g + \rho_g \boldsymbol{g}] + \lambda_w \boldsymbol{k} \cdot [\nabla p_{cg} + (\rho_w - \rho_g)\boldsymbol{g}] \quad (3\text{-}71)$$

where $\lambda_w = \frac{k_{rw}}{\mu_w}$ and $\lambda_g = \frac{k_{rg}}{\mu_g}$. Eq. 3-71 is referred to as the velocity or the total velocity equation. I use the definition of fractional flow to express the water phase velocity as

$$\mathbf{v_w} = F_w[\mathbf{v_t} + \lambda_g \boldsymbol{k} \cdot (\nabla p_{cg} + (\rho_w - \rho_g)\boldsymbol{g})] \quad (3\text{-}72)$$

where $F_w = \frac{\lambda_w}{\lambda_g + \lambda_w}$ is called the fractional flow of water. By substituting Eq. 3-72 into Eq. 3-67, I obtain

$$S_w \left(\frac{b-\phi}{K_s} + \phi c_w\right)\frac{\partial p_g}{\partial t} - \left(S_w \frac{b-\phi}{K_s} S_w \frac{\partial p_{cg}}{\partial S_w} - \phi + \phi S_w c_w \frac{\partial p_{cg}}{\partial S_w}\right)\frac{\partial S_w}{\partial t} + S_w b \frac{\partial \varepsilon_v}{\partial t} + \nabla \cdot \{F_w[\mathbf{v}_t + \lambda_g \boldsymbol{k} \cdot (\nabla p_{cg} + (\rho_w - \rho_g)\boldsymbol{g})]\} = f_w \quad (3\text{-}73)$$

This can be expanded as follows:

$$S_w \left(\frac{b-\phi}{K_s} + \phi c_w\right)\frac{\partial p_g}{\partial t} - \left(S_w \frac{b-\phi}{K_s} S_w \frac{\partial p_{cg}}{\partial S_w} - \phi + \phi S_w c_w \frac{\partial p_{cg}}{\partial S_w}\right)\frac{\partial S_w}{\partial t} + S_w b \frac{\partial \varepsilon_v}{\partial t} + F_w \nabla \cdot \mathbf{v}_t + \mathbf{v}_t \cdot \nabla F_w + \nabla \cdot [F_w \lambda_g \boldsymbol{k} \cdot (\nabla p_{cg} + (\rho_w - \rho_g)\boldsymbol{g})] = f_w \quad (3\text{-}74)$$

Expanding the divergence term in Eq. 3-74 and using the chain rule of the capillary pressure relation yields

$$S_w \left(\frac{b-\phi}{K_s} + \phi c_w\right)\frac{\partial p_g}{\partial t} - \left(S_w \frac{b-\phi}{K_s} S_w \frac{\partial p_{cg}}{\partial S_w} - \phi + \phi S_w c_w \frac{\partial p_{cg}}{\partial S_w}\right)\frac{\partial S_w}{\partial t} + S_w b \frac{\partial \varepsilon_v}{\partial t} + \nabla \cdot (\mathbf{v}_t F_w) + \nabla \cdot \left(\boldsymbol{k} \cdot \left(F_w \lambda_g \frac{\partial p_{cg}}{\partial S_w} \nabla S_w\right)\right) + \frac{\partial (F_w \lambda_g)}{\partial S_w} \nabla S_w \cdot (\boldsymbol{k} \cdot (\rho_w - \rho_g)\boldsymbol{g}) = f_w \quad (3\text{-}75)$$

Eq. 3-75 is termed the saturation equation.

The deformation of rock can be modeled using the equilibrium equation, which was already shown in Eq. 3-27 as

$$\nabla \cdot \boldsymbol{\sigma} + \rho_b \boldsymbol{g} = \mathbf{0} \quad (3\text{-}27)$$

where the bulk density ρ_b is as defined in Eq. 3-29

$$\rho_b = \phi \rho_f + (1 - \phi)\rho_s \quad (3\text{-}29)$$

I define a composite fluid density as

$$\rho_f = S_g\rho_g + S_w\rho_w \quad (3\text{-}76)$$

Assuming an isotropic material the total stress can be expressed as

$$\boldsymbol{\sigma} = \boldsymbol{\sigma_0} + \lambda\nabla\cdot\boldsymbol{u}\boldsymbol{I} + 2\mu\boldsymbol{\varepsilon}(\boldsymbol{u}) - b\left(p_t - p_{t,0}\right)\boldsymbol{I} \quad (3\text{-}77)$$

Note that the pressure term in Eq. 3-31 is replaced by the total pressure term for the case of multiphase flow. The geomechanical equilibrium equation for the case of the multiphase flow system can be expressed as

$$\nabla\cdot\left(\boldsymbol{\sigma_0} + \lambda\nabla\cdot\boldsymbol{u}\boldsymbol{I} + 2\mu\boldsymbol{\varepsilon}(\boldsymbol{u}) - b\left(p_t - p_{t,0}\right)\boldsymbol{I}\right) + \rho_b\boldsymbol{g} = 0 \quad (3\text{-}78)$$

I now summarize the governing equations that describe coupled multiphase flow and geomechanics as

$$\left(\frac{b-\phi}{K_s} + S_g\phi\frac{M_g}{\rho_g RT}\chi + S_w\phi c_w\right)\frac{\partial p_g}{\partial t} - \left(\frac{b-\phi}{K_s}S_w\frac{\partial p_{cg}}{\partial S_w} + \phi S_w c_w\frac{\partial p_{cg}}{\partial S_w}\right)\frac{\partial S_w}{\partial t} + b\frac{\partial \varepsilon_v}{\partial t} + \nabla\cdot\mathbf{v}_t = f_g + f_w \quad (3\text{-}69)$$

$$S_w\left(\frac{b-\phi}{K_s} + \phi c_w\right)\frac{\partial p_g}{\partial t} - \left(S_w\frac{b-\phi}{K_s}S_w\frac{\partial p_{cg}}{\partial S_w} - \phi + \phi S_w c_w\frac{\partial p_{cg}}{\partial S_w}\right)\frac{\partial S_w}{\partial t} + S_w b\frac{\partial \varepsilon_v}{\partial t} + \nabla\cdot(\mathbf{v}_t F_w) + \nabla\cdot$$
$$\left(\boldsymbol{k}\cdot\left(F_w\lambda_g\frac{\partial p_{cg}}{\partial S_w}\nabla S_w\right)\right) + \frac{\partial(F_w\lambda_g)}{\partial S_w}\nabla S_w\cdot\left(\boldsymbol{k}\cdot\left(\rho_w - \rho_g\right)\boldsymbol{g}\right) = f_w \quad (3\text{-}75)$$

$$\mathbf{v}_t = \left(\lambda_g + \lambda_w\right)\boldsymbol{k}\cdot\left[-\nabla p_g + \rho_g\boldsymbol{g}\right] + \lambda_w\boldsymbol{k}\cdot\left[\nabla p_{cg} + \left(\rho_w - \rho_g\right)\boldsymbol{g}\right] \quad (3\text{-}71)$$

$$\nabla\cdot\left(\boldsymbol{\sigma_0} + \lambda\nabla\cdot\boldsymbol{u}\boldsymbol{I} + 2\mu\boldsymbol{\varepsilon}(\boldsymbol{u}) - b\left(p_t - p_{t,0}\right)\boldsymbol{I}\right) + \rho_b\boldsymbol{g} = 0 \quad (3\text{-}78)$$

Eq. 3-69, Eq. 3-75, Eq. 3-71, and Eq. 3-78 are called the pressure, saturation, velocity, and geomechanical equilibrium equations, respectively. Note that if I use a porosity-dependent permeability in Eq. 3-32, the permeability becomes a function of pressure, saturation, and displacement considering capillarity, and a function of pressure and displacement without capillarity.

The initial conditions of the pressure and saturation equations are

$$p_g = p_{g,0} \quad (3\text{-}79)$$

$$S_w = S_{w,0} \quad (3\text{-}80)$$

The boundary condition for the case of a no-flow (Neumann) boundary is

$$\mathbf{v_t}\cdot\boldsymbol{n} = 0 \quad (3\text{-}81)$$

I can impose a constant pressure and/or a constant saturation boundary condition by prescribing the pressure and/or saturation on the boundary. The boundary condition for the geomechanical equilibrium equation is

$$\boldsymbol{u} \cdot \boldsymbol{n} = 0 \text{ on } \Gamma_1 \quad (3\text{-}82)$$

$$\boldsymbol{\sigma} \cdot \boldsymbol{n} = \boldsymbol{t} \text{ on } \Gamma_2 \quad (3\text{-}83)$$

where $\Gamma_1 \cap \Gamma_2 = \phi$. Eq. 3-82 and Eq. 3-83 indicate the zero normal displacement and prescribed traction boundary conditions, respectively. The described governing equations together with the initial and boundary conditions make a mathematical model of coupled multiphase flow and geomechanics.

If this is the case of oil and water system, Eq. 3-69 becomes

$$\left(\frac{b-\phi}{K_s} + S_o \phi c_o + S_w \phi c_w\right)\frac{\partial p_o}{\partial t} - \left(\frac{b-\phi}{K_s} S_w \frac{\partial p_{co}}{\partial S_w} + \phi S_w c_w \frac{\partial p_{co}}{\partial S_w}\right)\frac{\partial S_w}{\partial t} + b\frac{\partial \varepsilon_v}{\partial t} + \nabla \cdot \mathbf{v}_t = f_o + f_w \quad (3\text{-}84)$$

where c_o is the compressibility of oil and p_{co} is the capillary pressure between oil and water. Note that I replaced the nonlinear term $\left(\frac{M_g}{\rho_g RT}\chi\right)$ in Eq. 3-69 with the oil compressibility (c_o). The saturation equation (Eq. 3-75) and velocity equation (Eq. 3-71) become

$$S_w\left(\frac{b-\phi}{K_s} + \phi c_w\right)\frac{\partial p_o}{\partial t} - \left(S_w \frac{b-\phi}{K_s} S_w \frac{\partial p_{co}}{\partial S_w} - \phi + \phi S_w c_w \frac{\partial p_{co}}{\partial S_w}\right)\frac{\partial S_w}{\partial t} + S_w b\frac{\partial \varepsilon_v}{\partial t} + \nabla \cdot (\mathbf{v}_t F_w) + \nabla \cdot \left(\boldsymbol{k} \cdot \left(F_w \lambda_o \frac{\partial p_{co}}{\partial S_w}\nabla S_w\right)\right) + \frac{\partial (F_w \lambda_o)}{\partial S_w}\nabla S_w \cdot (\boldsymbol{k} \cdot (\rho_w - \rho_o)\boldsymbol{g}) = f_w \quad (3\text{-}85)$$

$$\mathbf{v}_t = (\lambda_o + \lambda_w)\boldsymbol{k} \cdot [-\nabla p_o + \rho_o \boldsymbol{g}] + \lambda_w \boldsymbol{k} \cdot [\nabla p_{co} + (\rho_w - \rho_o)\boldsymbol{g}] \quad (3\text{-}86)$$

Note I simply changed the terms with gas phase in Eq. 3-75 and Eq. 3-71 with the terms $(p_o, p_{co}, \lambda_o, \rho_o)$ oil phase. The geomechanical equilibrium equation is

$$\nabla \cdot \left(\boldsymbol{\sigma_0} + \lambda \nabla \cdot \boldsymbol{u}\boldsymbol{I} + 2\mu\boldsymbol{\varepsilon}(\boldsymbol{u}) - b\left(p_t - p_{t,0}\right)\boldsymbol{I}\right) + \rho_b \boldsymbol{g} = 0 \quad (3\text{-}87)$$

where the total pressure is

$$p_t = S_o p_o + S_w p_w \quad (3\text{-}88)$$

CHAPTER IV

FINITE ELEMENT FORMULATION

In this chapter, I present the finite element formulations of the mathematical models presented in Chapter III. I used the DEAL.II C++ Finite Element Library (Bangerth et al. 2007) that contains state of the art C++ algorithms and some of the algorithms (such as error estimator for adaptive grid refinement and interface for parallel packages, etc.) can be used for the future expansion of TAM-CFGM.

4.1 Finite Element Formulation of Single Phase Flow and Geomechanics

I present a finite element formulation to solve the coupled single-phase flow and geomechanics problem. I used a mixed finite element discretization to satisfy the local mass conservation equation, and a standard Galerkin finite element discretization to solve the geomechanical equilibrium equation. The three fully coupled equations (pressure, velocity, and displacement) were solved using the Newton-Raphson method.

Focusing on single phase flow, the governing equations that I derived in CHAPTER III are Eq. 3-3, Eq. 3-16, Eq. 3-26 and Eq. 3-31.

Eq. 3-16 and Eq. 3-26 are the mass balance equations for slightly compressible flow and highly compressible (gas) flow, respectively. The initial condition is described by Eq. 3-33, and the boundary conditions are described by equations 3-34 to 3-36. By assuming the spatial gradient of the density is negligible, I divided Eq. 3-16 and Eq. 3-26 by the density of slightly compressible flow and highly compressible flow, respectively.

In order to obtain a finite element formulation, I need to define the spaces of solutions ($p_h, \mathbf{v_h}, \boldsymbol{u_h}$) and test functions ($\psi, \boldsymbol{\omega}, \boldsymbol{v}$) as

$$\boldsymbol{H}(div,\Omega) \equiv \left\{\boldsymbol{\omega} \in \left(L^2(\Omega)\right)^d : \nabla \cdot \boldsymbol{\omega} \in L^2(\Omega)\right\} \quad (4\text{-}1)$$

$$\boldsymbol{V} \equiv \boldsymbol{H}(div,\Omega) \cap \{\boldsymbol{\omega}: \boldsymbol{\omega} \cdot \boldsymbol{n} = 0 \text{ on } \Gamma\} \quad (4\text{-}2)$$

$$W \subset L^2(\Omega) \quad (4\text{-}3)$$

$$U \subset (H^1)^d(\Omega) \quad (4\text{-}4)$$

I now multiply the test functions by the governing equations and integrate the resulting functions over the domain, and obtain the following weak forms

$$\left(\psi, \left(\frac{b-\phi}{K_s} + \phi c_f\right)\frac{p^{n+1}-p^n}{\Delta t}\right)_\Omega + \left(\psi, b\frac{\varepsilon_v^{n+1}-\varepsilon_v^n}{\Delta t}\right)_\Omega + (\psi, \nabla\cdot\mathbf{v}^{n+1})_\Omega = (\psi, f)_\Omega \quad \text{(4-5)}$$

$$\left(\psi, \left(\frac{b-\phi}{K_s} + \phi\frac{M_g}{\rho_g RT}\chi\right)\frac{p^{n+1}-p^n}{\Delta t}\right)_\Omega + \left(\psi, b\frac{\varepsilon_v^{n+1}-\varepsilon_v^n}{\Delta t}\right)_\Omega + (\psi, \nabla\cdot\mathbf{v}^{n+1})_\Omega = (\psi, f)_\Omega \quad \text{(4-6)}$$

$$(\boldsymbol{w}, \boldsymbol{k}^{-1}\mu\mathbf{v}^{n+1})_\Omega = -\left(\boldsymbol{w}, \rho_f \boldsymbol{g}\right)_\Omega + (\nabla\cdot\boldsymbol{w}, p^{n+1})_\Omega - (\boldsymbol{w}\cdot\boldsymbol{n}, p^{n+1})_\Gamma \quad \text{(4-7)}$$

$$(-\boldsymbol{\varepsilon}(\boldsymbol{v}),\ \boldsymbol{\sigma_0})_\Omega - 2\left(\boldsymbol{\varepsilon}(\boldsymbol{v}), \mu\boldsymbol{\varepsilon}(\boldsymbol{u}^{n+1})\right)_\Omega - \left(\lambda(\nabla\cdot\boldsymbol{v}), (\nabla\cdot\boldsymbol{u}^{n+1})\right)_\Omega + (\nabla\cdot\boldsymbol{v}, bp^{n+1})_\Omega - (\nabla\cdot\boldsymbol{v}, bp_0)_\Omega + (\boldsymbol{v}, \rho_b\boldsymbol{g})_\Omega + (\boldsymbol{v}, \boldsymbol{t})_\Gamma = 0 \quad \text{(4-8)}$$

where $(a,b)_\Omega = \int_\Omega ab$ and $(a,b)_\Gamma = \int_\Gamma ab$. Note the original governing equations that I derived are called strong formations and Eq. 4-5 to Eq. 4-8 are the weak formations.

The aim of the finite element formulation (weak formulation) is to find $p_h \in W$, $\mathbf{v}_h \in \boldsymbol{V}$, and $\boldsymbol{u}_h \in U$, such that

$$R^p = \left(\psi_i, \left(\frac{b-\phi}{K_s} + \phi c_f\right)\frac{p_h^{n+1}-p_h^n}{\Delta t}\right)_\Omega + \left(\psi_i, b\frac{\nabla\cdot\boldsymbol{u}_h^{n+1}-\nabla\cdot\boldsymbol{u}_h^n}{\Delta t}\right)_\Omega + (\psi_i, \nabla\cdot\mathbf{v}_h^{n+1})_\Omega - (\psi_i, f)_\Omega, \forall\psi \in W. \quad \text{(4-9)}$$

$$R^{\mathbf{v}} = -(\boldsymbol{\omega}_i, \boldsymbol{k}^{-1}\mu\mathbf{v}_h^{n+1})_\Omega + \left(\boldsymbol{\omega}_i, \rho_f\boldsymbol{g}\right)_\Omega + (\nabla\cdot\boldsymbol{\omega}_i, p_h^{n+1})_\Omega - (\boldsymbol{\omega}_i\cdot\boldsymbol{n}, p_h^{n+1})_\Gamma, \forall\boldsymbol{\omega} \in \boldsymbol{V} \quad \text{(4-10)}$$

$$R^{\boldsymbol{u}} = (-\boldsymbol{\varepsilon}(\boldsymbol{v_i}),\ \boldsymbol{\sigma_0})_\Omega - 2\left(\boldsymbol{\varepsilon}(\boldsymbol{v_i}), \mu\boldsymbol{\varepsilon}(\boldsymbol{u}_h^{n+1})\right)_\Omega - \left(\lambda(\nabla\cdot\boldsymbol{v}_i), (\nabla\cdot\boldsymbol{u}_h^{n+1})\right)_\Omega + (\nabla\cdot\boldsymbol{v_i}, bp_h^{n+1})_\Omega - (\nabla\cdot\boldsymbol{v}_i, bp_0)_\Omega + (\boldsymbol{v}_i, \rho_b\boldsymbol{g})_\Omega + (\boldsymbol{v}_i, \boldsymbol{t})_\Gamma, \forall\boldsymbol{v} \in U \quad \text{(4-11)}$$

where the subscript *i* indicates the degree of freedom. Compute this finite element formulation involves looping over all the degrees of freedom and computing the given governing equations. The residual formulation has only a single index *i* because the residual equations become the right hand side (vector) of the linearized equations. The solutions are approximated as

$$p_h^{n+1}(\boldsymbol{x}) = \sum_{i=1}^{n_p}\psi_i(\boldsymbol{x})P_i^{n+1} \quad \text{(4-12)}$$

$$\mathbf{v}_h^{\boldsymbol{n+1}}(\boldsymbol{x}) = \sum_{e=1}^{n_e}\boldsymbol{\omega}_e(\boldsymbol{x})\mathrm{v}_e^{n+1} \quad \text{(4-13)}$$

$$\boldsymbol{u}_h^{\boldsymbol{n+1}}(\boldsymbol{x}) = \sum_{a=1}^{n_u} v_a(\boldsymbol{x})u_a^{n+1} \quad \text{(4-14)}$$

where $P_i^{n+1}, \mathrm{v}_e^{n+1}, u_a^{n+1}$ are the unknown expansion coefficients that I need to determine (the degrees of freedom of this problem), and $\psi_i(\boldsymbol{x}), \boldsymbol{\omega}_e(\boldsymbol{x}), v_a(\boldsymbol{x})$ are the finite element shape functions that I will use. In

addition, e, a, and i indicate an edge, a node and the center of an element, respectively. Note that the solution of the velocity is a scalar value, and the basis of the velocity is a vector. The degree of freedom of the displacement solution n_u is defined as the number of node times the number of the dimension $(a \times dim)$.

Fig. 4.1 and **Fig. 4-2** show the location of the different unknowns (degree of freedom) and the three different basis functions for the three different solution variables. The pressure solution is located at the center of the element. The velocity solution is a vector solution located on each edge of the element and is normal to each edge. The displacement solution is a nodal solution that is defined as a vector on each node. In a mixed finite element formulation, the velocity is defined as a primary variable rather than a derived (secondary) variable estimated from the pressure (difference of potential) using the TPFA or MPFA approach, which is the standard method in the cell-centered finite difference or the finite volume discretizations. The mixed finite element formulation guarantees flux normal to the edge regardless of the shape of the mesh.

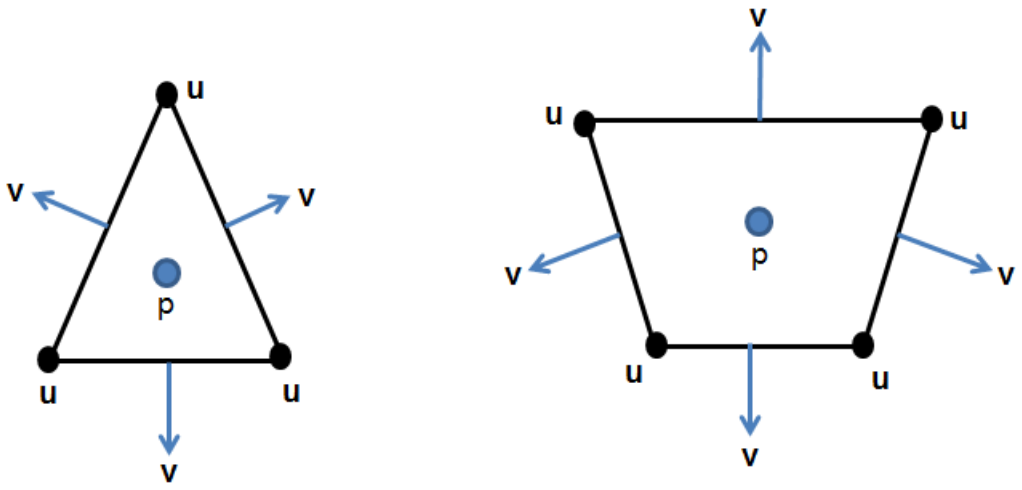

Fig. 4.1—Locations of the solution variables (degree of freedom) on a 2D triangle (left) and a quadrilateral (right). The displacement solution is located on a node of the element. The velocity solution is located on the edge of the element. The pressure solution is located at the center of the element. Note that the displacement solution at each node is a vector. The velocity vector has scalar component with a vector basis function (see Fig. 4.2).

The element basis functions in **Fig. 4.2** show that the displacement basis function is a nodal function and the node contains n-dimensional degrees of freedom. For example, each node contains two displacement solutions for a 2D problem. The velocity basis function is a vector function normal to each edge of the element. Thus, the scalar velocity solution, which is obtained from this computation, determines the magnitude of the velocity vector. The pressure basis function is a piecewise-constant basis function that has a value of one at the cell center and zero elsewhere.

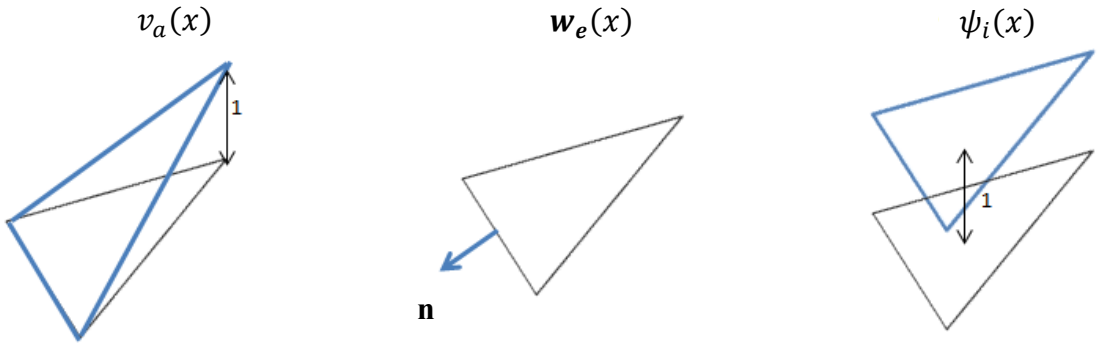

Fig. 4.2—Element basis function for the displacement, velocity, and pressure respectively on 2D triangle. Note that the element basis function for the velocity is a normal vector function.

For the porosity update, I used the discretized form of Eq. 3-14 as

$$\phi^{n+1,k} = \phi^n + \frac{b-\phi^n}{K_s}(p^{n+1,k} - p^n) + (b-\phi^n)\left(\varepsilon_v^{n+1,k} - \varepsilon_v^n\right) \quad \text{(4-15)}$$

where the superscript n indicates the number of time step and k indicates the number of the Newton-Raphson iteration. Eq. 4-15 states that the porosity is a function of pressure and volumetric strain. Eq. 4-9, Eq. 4-10, and Eq. 4-11 are the residual forms of the pressure, velocity and displacement equations. The derivatives of the residual equations are

$$\frac{\partial R^p}{\partial p} = \left(\psi_i, \left(\partial\left(\left(\frac{b-\phi}{K_s} + \phi c_f\right)\frac{p_h^{n+1}-p_h^n}{\Delta t}\right)/\partial p\right)\psi_j\right)_\Omega \quad \text{(4-16)}$$

$$\frac{\partial R^p}{\partial \mathrm{v}} = \left(\psi_i, \nabla\cdot\boldsymbol{\omega}_j\right)_\Omega \quad \text{(4-17)}$$

$$\frac{\partial R^p}{\partial \mathrm{u}} = \left(\psi_i, \left(\left(\frac{-1}{K_s}\frac{\partial\phi}{\partial\varepsilon_v} + \frac{\partial\phi}{\partial\varepsilon_v}c_f\right)\frac{p_h^{n+1}-p_h^n}{\Delta t}\right)\nabla\cdot\boldsymbol{v_j}\right)_\Omega + \left(\psi_i, b\nabla\cdot\boldsymbol{v_j}\frac{1}{\Delta t}\right)_\Omega \quad \text{(4-18)}$$

where $\frac{\partial\phi^{n+1,k}}{\partial\varepsilon_v^{n+1,k}} = (b-\phi^n)$.

The term

$$\frac{\partial R^{\mathrm{v}}}{\partial p} = -\left(\boldsymbol{\omega_i}, \left(\partial\left(\frac{1}{\boldsymbol{k}}\right)/\partial p\right)\mu\mathbf{v}_h^{n+1}\psi_j\right)_\Omega + \left(\boldsymbol{\omega}, \left(\partial\rho_f/\partial p\right)\boldsymbol{g}\psi_j\right)_\Omega + \left(\nabla\cdot\boldsymbol{\omega_i}, \psi_j\right)_\Omega \quad \text{(4-19)}$$

where $\boldsymbol{k}\left(\phi(p,\boldsymbol{u})\right)$ is the permeability as a function of porosity. Additionally,

$$\frac{\partial R^{\mathrm{v}}}{\partial \mathrm{v}} = -\left(\boldsymbol{\omega_i}, \frac{\mu}{\boldsymbol{k}}\boldsymbol{\omega_j}\right)_{\Omega} \quad (4\text{-}20)$$

$$\frac{\partial R^{\mathrm{v}}}{\partial u} = -\left(\boldsymbol{\omega_i}, \left(\partial\left(\frac{1}{\boldsymbol{k}}\right)/\partial\varepsilon_v\right)\mu\mathbf{v}_h^{n+1}\nabla\cdot\boldsymbol{v_j}\right)_{\Omega} \quad (4\text{-}21)$$

$$\frac{\partial R^{\mathrm{u}}}{\partial p} = \left(\nabla\cdot\boldsymbol{v_i}, b\psi_j\right)_{\Omega} + \left(\boldsymbol{v_i}, (\partial\rho_b/\partial p)\boldsymbol{g}\psi_j\right)_{\Omega} \quad (4\text{-}22)$$

$$\frac{\partial R^{\mathrm{u}}}{\partial u} = -2\left(\boldsymbol{\varepsilon}(\boldsymbol{v_i}), \mu\boldsymbol{\varepsilon}(\boldsymbol{v_j})\right)_{\Omega} - \left(\lambda(\nabla\cdot\boldsymbol{v_i}), (\nabla\cdot\boldsymbol{v_j})\right)_{\Omega} + \left(\boldsymbol{v_i}, (\partial\rho_b/\partial\varepsilon_v)\boldsymbol{g}\nabla\cdot\boldsymbol{v_j}\right)_{\Omega} \quad (4\text{-}23)$$

Note that I used a combination of analytical and numerical derivatives. When an equation is a linear function of a primary variable it is straightforward to obtain the analytical derivative. However, if the equation is a nonlinear function, it is difficult to get analytical derivatives and I use numerical derivatives. For example, for Eq. 4-16 the derivative of the function is a nonlinear function of pressure because the porosity is a function of pressure, consequently the derivative is estimated numerically. The subscripts *i* and *j* indicate the degree of freedom. To compute the Jacobian matrix in an element (local element), I need to loop over $n \times n$ degrees of freedoms, where n is the total number of degrees of freedom in the element (local element). I then assemble the contributions of each element to construct the global matrix.

The linear system of equations is written in a matrix form as

$$\begin{bmatrix} \frac{\partial R^{\mathrm{v}}}{\partial \mathrm{v}} & \frac{\partial R^{\mathrm{v}}}{\partial p} & \frac{\partial R^{\mathrm{v}}}{\partial u} \\ \frac{\partial R^{p}}{\partial \mathrm{v}} & \frac{\partial R^{p}}{\partial p} & \frac{\partial R^{p}}{\partial u} \\ 0 & \frac{\partial R^{u}}{\partial p} & \frac{\partial R^{u}}{\partial u} \end{bmatrix}^{n+1,k} \begin{bmatrix} \delta\mathrm{v}_h^{n+1} \\ \delta p_h^{n+1} \\ \delta u_h^{n+1} \end{bmatrix}^{k} = -\begin{bmatrix} R^{\mathrm{v},n+1} \\ R^{p,n+1} \\ R^{u,n+1} \end{bmatrix}^{k} \quad (4\text{-}24)$$

The primary variables are improved at each iteration as

$$\mathrm{v}_h^{n+1,k+1} = \mathrm{v}_h^{n+1,k} + \delta\mathrm{v}_h^{n+1,k} \quad (4\text{-}25)$$

$$p_h^{n+1,k+1} = p_h^{n+1,k} + \delta p_h^{n+1,k} \quad (4\text{-}26)$$

$$u_h^{n+1,k+1} = u_h^{n+1,k} + \delta u_h^{n+1,k} \quad (4\text{-}27)$$

For the case of gas flow, the only difference is the compressibility factor (Z_g-factor). In this case, I first express Eq. 4-6 as

$$\left(\psi, \left(\frac{b-\phi}{K_s} + \phi \frac{Z_g}{p_h^{n+1}} \chi(p_h^{n+1})\right) \frac{p_h^{n+1} - p_h^n}{\Delta t}\right)_\Omega + \left(\psi, b \frac{\varepsilon_v^{n+1} - \varepsilon_v^n}{\Delta t}\right)_\Omega + (\psi, \nabla \cdot \mathbf{v}^{n+1})_\Omega = (\psi, f)_\Omega \quad \text{(4-28)}$$

The derivatives that need to be replaced in Eq. 4-24 are

$$\frac{\partial R^p}{\partial p} = \left(\psi_i, \left(\partial \left(\left(\frac{b-\phi}{K_s} + \phi \frac{Z_g}{p_h^{n+1}} \chi(p_h^{n+1})\right) \frac{p_h^{n+1} - p_h^n}{\Delta t}\right) / \partial p\right) \psi_j\right)_\Omega \quad \text{(4-29)}$$

$$\frac{\partial R^p}{\partial u} = \left(\psi_i, \left(\left(\frac{-1}{K_s} \frac{\partial \phi}{\partial \varepsilon_v} + \frac{\partial \phi}{\partial \varepsilon_v} \frac{Z_g}{p_h^{n+1}} \chi(p_h^{n+1})\right) \frac{p_h^{n+1} - p_h^n}{\Delta t}\right) \nabla \cdot \boldsymbol{v_j}\right)_\Omega + \left(\psi_i, b \nabla \cdot \boldsymbol{v_j} \frac{1}{\Delta t}\right)_\Omega \quad \text{(4-30)}$$

4.2 Finite Element Formulation of Multiphase Flow and Geomechanics

In this section, I present a finite element formulation for a coupled multiphase flow and geomechanics simulator. I used a mixed finite element formulation to solve the pressure and the total velocity equations, and a stabilized finite element formulation to solve the saturation equation. I also used a standard Galerkin finite element discretization to solve the displacement equation. The four governing equations are fully coupled and solved using the Newton-Raphson method.

The governing equations for the coupled multiphase flow and geomechanics model are Eq. 3-69, Eq. 3-75, Eq. 3-71 and Eq. 3-78. The corresponding initial and boundary conditions are described by equations 3-79 to 3-83.

In order to perform a finite element discretization, I need to define spaces of solutions and test functions $p_h, \mathbf{v}_h, S_{w,h}, \boldsymbol{u}_h, \psi, \boldsymbol{\omega}, \varphi,$ and $\boldsymbol{v}$ as

$$\boldsymbol{H}(div, \Omega) \equiv \left\{\boldsymbol{\omega} \in \left(L^2(\Omega)\right)^d : \nabla \cdot \boldsymbol{\omega} \in L^2(\Omega)\right\} \quad \text{(4-31)}$$

$$\boldsymbol{V} \equiv \boldsymbol{H}(div, \Omega) \cap \{\boldsymbol{\omega} : \boldsymbol{\omega} \cdot \boldsymbol{n} = 0 \text{ on } \Gamma\} \quad \text{(4-32)}$$

$$W \subset L^2(\Omega) \quad \text{(4-33)}$$

$$U \subset (H^1)^d(\Omega) \quad \text{(4-34)}$$

$$Q \subset H^1(\Omega) \quad \text{(4-35)}$$

where H^1 is the function space that contains first order differentiation and $(H^1)^d$ is the H^1 space that has a vector solution. Then the goal of the finite element formulation (weak formulation) is to find $p_{g,h} \in W$, $S_{w,h} \in Q$, $\mathbf{v}_{t,h}, \in \boldsymbol{V}$, and $\boldsymbol{u}_h, \in U$ such that

$$R^p = \left(\psi_i, \left(\frac{b-\phi}{K_s} + \left(1 - S_{w,h}^{n+1}\right)\phi \frac{Z_g}{p_{g,h}^{n+1}} \chi(p_g^{n+1}) + S_{w,h}^{n+1} \phi c_w\right) \frac{p_{g,h}^{n+1} - p_{g,h}^n}{\Delta t}\right)_\Omega - \left(\psi_i, \left(\frac{b-\phi}{K_s} S_{w,h}^{n+1} \frac{\partial p_{cg}}{\partial S_w} + \phi S_{w,h}^{n+1} c_w \frac{\partial p_{cg}}{\partial S_w}\right) \frac{S_{w,h}^{n+1} - S_{w,h}^n}{\Delta t}\right)_\Omega + \left(\psi_i, b \frac{\nabla \cdot \boldsymbol{u_h^{n+1}} - \nabla \cdot \boldsymbol{u_h^n}}{\Delta t}\right)_\Omega + \left(\psi_i, \nabla \cdot \mathbf{v}_{\boldsymbol{t,h}}^{\boldsymbol{n+1}}\right)_\Omega - \left(\psi_i, f_g + f_w\right)_\Omega, \forall \psi \in W \quad (4\text{-}36)$$

$$R^S = \left(\varphi_i, S_{w,h}^{n+1}\left(\frac{b-\phi}{K_s} + \phi c_w\right) \frac{p_{g,h}^{n+1} - p_{g,h}^n}{\Delta t}\right)_\Omega - \left(\varphi_i, \left(S_{w,h}^{n+1} \frac{b-\phi}{K_s} S_{w,h}^{n+1} \frac{\partial p_{cg}}{\partial S_w} - \phi + \phi S_{w,h}^{n+1} c_w \frac{\partial p_{cg}}{\partial S_w}\right) \frac{S_{w,h}^{n+1} - S_{w,h}^n}{\Delta t}\right)_\Omega + \left(\varphi_i, S_{w,h}^{n+1} b \frac{\nabla \cdot \boldsymbol{u_h^{n+1}} - \nabla \cdot \boldsymbol{u_h^n}}{\Delta t}\right)_\Omega - \left(\nabla \varphi_i, F_w \mathbf{v}_{\boldsymbol{t,h}}^{\boldsymbol{n+1}}\right)_\Omega + \left(\varphi_i, \boldsymbol{n} \cdot F_w \mathbf{v}_t\right)_\Gamma - \left(\nabla \varphi_i, \boldsymbol{k} \cdot \left(F_w \lambda_g \frac{\partial p_{cg}}{\partial S_w} \nabla S_{w,h}^{n+1}\right)\right)_\Omega + \left(\varphi_i, \boldsymbol{n} \cdot \left(\boldsymbol{k} \cdot \left(F_w \lambda_g \frac{\partial p_{cg}}{\partial S_w} \nabla S_w\right)\right)\right)_\Gamma + \left(\varphi_i, \frac{\partial (F_w \lambda_g)}{\partial S_w} \nabla S_w \cdot \left(\boldsymbol{k} \cdot \left(\rho_w - \rho_g\right)\boldsymbol{g}\right)\right)_\Omega - \left(\varphi_i, f_w\right)_\Omega + \left(\nu \nabla \varphi_i, \nabla S_{w,h}^{n+1}\right)_\Omega, \forall \varphi \in Q \quad (4\text{-}37)$$

$$R^{\mathrm{v}_t} = -\left(\boldsymbol{\omega_i}, \frac{1}{\boldsymbol{k}(\lambda_g + \lambda_w)} \mathbf{v}_{\boldsymbol{t,h}}^{\boldsymbol{n+1}}\right)_\Omega + \left(\nabla \cdot \boldsymbol{\omega_i}, p_{g,h}^{n+1}\right)_\Omega - \left(\boldsymbol{\omega} \cdot \boldsymbol{n}, p_{g,h}^{n+1}\right)_\Gamma + \left(\boldsymbol{\omega_i}, \rho_g \boldsymbol{g}\right)_\Omega + \left(\boldsymbol{\omega_i}, F_w \left[\frac{\partial p_{cg}}{\partial S_w} \nabla S_{w,h}^{n+1} + \left(\rho_w - \rho_g\right)\boldsymbol{g}\right]\right)_\Omega, \forall \boldsymbol{\omega} \in \boldsymbol{V} \quad (4\text{-}38)$$

where $\phi = \phi\left(p_t^{n+1}\left(p_g^{n+1}, S_{w,h}^{n+1}\right), \boldsymbol{u_h^{n+1}}\right)$ and $\boldsymbol{k} = \boldsymbol{k}\left(\phi\left(p_t^{n+1}\left(p_g^{n+1}, S_{w,h}^{n+1}\right), \boldsymbol{u_h^{n+1}}\right)\right)$.

$$R^{\boldsymbol{u}} = \left(-\boldsymbol{\varepsilon}(\boldsymbol{v}), \boldsymbol{\sigma_0}\right)_\Omega - 2\left(\boldsymbol{\varepsilon}(\boldsymbol{v_i}), \mu \boldsymbol{\varepsilon}\left(\boldsymbol{u_h^{n+1}}\right)\right)_\Omega - \left(\lambda(\nabla \cdot \boldsymbol{v_i}), \left(\nabla \cdot \boldsymbol{u_h^{n+1}}\right)\right)_\Omega + \left(\nabla \cdot \boldsymbol{v_i}, b\left(p_{g,h}^{n+1} - S_{w,h}^{n+1} p_{cg}^{n+1}\right)\right)_\Omega - \left(\nabla \cdot \boldsymbol{v}, b p_{t,0}\right)_\Omega + \left(\boldsymbol{v_i}, \rho_b^{n+1} \boldsymbol{g}\right)_\Omega + \left(\boldsymbol{v}, \boldsymbol{t}\right)_\Gamma, \forall \boldsymbol{v} \in U \quad (4\text{-}39)$$

where $\nabla p_c = \frac{\partial p_{co}}{\partial S_w} \nabla S_w$. The solutions are approximated as

$$p_{g,h}^{n+1}(\boldsymbol{x}) = \sum_{i=1}^{n_p} \psi_i(\boldsymbol{x}) P_{g,i}^{n+1} \quad (4\text{-}40)$$

$$\mathbf{v}_{\boldsymbol{t,h}}^{\boldsymbol{n+1}}(\boldsymbol{x}) = \sum_{e=1}^{n_e} \boldsymbol{\omega_e}(\boldsymbol{x}) \mathrm{v}_e^{n+1} \quad (4\text{-}41)$$

$$S_{w,h}^{n+1}(\boldsymbol{x}) = \sum_{a=1}^{n_{sw}} \varphi_a(\boldsymbol{x}) S_{w,a}^{n+1} \quad (4\text{-}42)$$

$$\boldsymbol{u_h^{n+1}}(\boldsymbol{x}) = \sum_{a=1}^{n_u} v_a(\boldsymbol{x}) u_a^{n+1} \quad (4\text{-}43)$$

where $P_{g,i}^{n+1}, \mathrm{v}_{t,e}^{n+1}, S_{w,a}^{n+1}, u_a^{n+1}$ are the unknown expansion coefficients I need to determine and $\psi_i(\boldsymbol{x}), \boldsymbol{\omega_e}(\boldsymbol{x}), \varphi_a(\boldsymbol{x}), v_a(\boldsymbol{x})$ are the finite element shape functions I will use.

The location of the unknowns (degrees of freedom) and the basis functions are already shown in **Fig. 4.1** and **Fig. 4.2**. The only difference is that the multiphase formulation also includes the saturation solution. The saturation solution and its basis function are located at the same location as the displacement solution and the displacement basis function, respectively. Unlike the displacement solution, the number of saturation solutions in a domain is equal to the number of nodes.

Note that the solution space of the saturation is $S_h \in Q$, which means a standard Galerkin finite element formulation is used to discretize the saturation equation. A finite volume discretization is typically used to solve a transport equation such as the saturation equation. The saturation equation is usually a hyperbolic partial differential equation, which introduces a "directional dependency" of the fluid. In order to deal with this issue, the finite volume formulation uses an upstream weighting scheme. A similar form for a finite element formulation is called the *discontinuous Galerkin (DG) method*, which uses discontinuous basis functions in each element and an upstream weighting scheme. However, using the DG method generates several terms for integration in the saturation equation, especially when the formulation contains a capillary pressure term. In addition, the numerical flux used in the discontinuous Galerkin method generates additional numerical diffusion (Chueh et al. 2010). In order to avoid this problem, I used a continuous Galerkin (standard Galerkin) discretization (Q) with a stabilization term. This approach allowed me to easily deal with the saturation equation while accounting for the capillary pressure because the saturation gradient can be obtained using the continuous basis function (Q). In addition, this formulation provides a higher resolution of the saturation solution.

Eq. 4-37 contains the stabilization term that uses an artificial viscosity ν, defined as

$$\nu(\mathbf{v}, S_w)|_K = \beta \|\mathbf{v}\|_{L^\infty(K)} \times min\left\{h_k, h_k^\alpha \frac{\|R^S\|_{L^\infty(K)}}{c(\mathbf{v}, S_w)}\right\} \quad (4\text{-}44)$$

where $\|\mathbf{v}\|_{L^\infty(K)}$ is the infinity norm of the cell, h_k is the cell diameter, α is a stabilization exponent and β is a dimensionless, user-defined, stabilization constant. Guermond and Pasquetti (2008) proposed the velocity and saturation global normalization constant $c(\mathbf{v}, S_w)$, which is defined as

$$c(\mathbf{v}, S_w) = c_R \|\mathbf{v}\|_{L^\infty(\Omega)} var(S)^\alpha |diam(\Omega)|^{\alpha-2} \quad (4\text{-}45)$$

where c_R is a dimensionless user defined constant, $diam(\Omega)$ is the diameter of the domain and $var(S) = max_\Omega S_w - min_\Omega S_w$ is the range of saturation values in the entire domain. $\|R^S\|_{L^\infty(K)}$ is the infinity norm of the saturation residual equation without the artificial viscosity. To compute this, I need to find the max-

imum norm of the saturation residual equation in the cell. The residual of the saturation equation can be obtained from Eq. 3-75 as

$$R^S = S_w\left(\frac{b-\phi}{K_s}+\phi c_w\right)\frac{\partial p_g}{\partial t}-\left(S_w\frac{b-\phi}{K_s}S_w\frac{\partial p_{cg}}{\partial S_w}-\phi+\phi S_w c_w\frac{\partial p_{cg}}{\partial S_w}\right)\frac{\partial S_w}{\partial t}+S_w b\frac{\partial \varepsilon_v}{\partial t}+\nabla\cdot(\mathbf{v}_t F_w)+\nabla\cdot\left(\boldsymbol{k}\cdot\left(F_w\lambda_g\frac{\partial p_{cg}}{\partial S_w}\nabla S_w\right)\right)+\frac{\partial(F_w\lambda_g)}{\partial S_w}\nabla S_w\cdot\left(\boldsymbol{k}\cdot(\rho_w-\rho_g)\boldsymbol{g}\right)-f_w \quad (4\text{-}46)$$

Eq. 4-46 can be simplified by ignoring the capillary pressure term as

$$R^S = S_w\left(\frac{b-\phi}{K_s}+\phi c_w\right)\frac{\partial p_g}{\partial t}+\phi\frac{\partial S_w}{\partial t}+S_w b\frac{\partial \varepsilon_v}{\partial t}+F_w\nabla\cdot\mathbf{v}_t+\mathbf{v}_t\cdot\nabla F_w+\frac{\partial(F_w\lambda_g)}{\partial S_w}\nabla S_w\cdot\left[(\rho_w-\rho_g)\boldsymbol{k}\cdot\boldsymbol{g}\right]-f_w \quad (4\text{-}47)$$

Without the gravity term, Eq. 4-47 becomes

$$R^S = \left(\frac{b-\phi}{K_s}+\phi c_w\right)\frac{\partial p_o}{\partial t}+\phi\frac{\partial S_w}{\partial t}+S_w b\frac{\partial \varepsilon_v}{\partial t}+F_w\nabla\cdot\mathbf{v}_t+\mathbf{v}_t\cdot\nabla F_w-f_w \quad (4\text{-}48)$$

where $\nabla F_w = \frac{dF_w}{dS_w}\nabla S_w$.

Note that the artificial viscosity is a nonlinear function of pressure, saturation, velocity, and displacement. Adding the artificial viscosity into the formulation would increase the computation time because of the increased degree of nonlinearity and the additional computations to estimate the artificial viscosity. The purpose of adding the artificial viscosity is to stabilize the "directional dependency" of the hyperbolic type saturation equation. Velocity is the most important factor in the process to stabilize the saturation equation.

The upstream weighting scheme in a finite volume formulation uses the direction of the flux. In order to improve the computational efficiency, I use a lagging method, in which I compute Eq. 4-46 with the primary variables obtained from the previous time step, thus avoiding the nonlinearity. Alternatively, I can simply use the infinity norm of the velocity expressed as

$$\nu|_K = \beta\|\mathbf{v}\|_{L^\infty(K)}\times h_k \quad (4\text{-}49)$$

In this case, I do not have to make a separate routine to compute the artificial viscosity, and adding this equation will not increase the degree of nonlinearity.

I update the porosity as

$$\phi^{n+1,k} = \phi^n+\frac{b-\phi^n}{K_s}\left(p_t^{n+1,k}-p_t^n\right)+(b-\phi^n)\left(\varepsilon_v^{n+1,k}-\varepsilon_v^n\right) \quad (4\text{-}50)$$

The only difference between E. 4-50 and 4-15 is that the pressure term in latter is replaced with the total pressure (Eq. 3-57) in Eq. 4-50. The derivatives of each residual equation with respect to the primary variables are computed as

$$\frac{\partial R^{\mathrm{p}}}{\partial \mathrm{p}_g} = \left(\psi_i, \left(\partial \left(\left(\frac{b-\phi}{K_s} + \left(1 - S_{w,h}^{n+1}\right)\phi \frac{Z_g}{p_{g,h}^{n+1}} \chi(p_g^{n+1}) + S_{w,h}^{n+1}\phi c_w \right) \frac{p_{g,h}^{n+1} - p_{g,h}^{n}}{\Delta t} \right) / \partial p_g \right) \psi_j \right)_{\Omega} -$$

$$\left(\psi_i, \left[\partial \left(\left(\frac{b-\phi}{K_s} S_{w,h}^{n+1} \frac{\partial p_{cg}}{\partial S_w} + \phi S_{w,h}^{n+1} c_w \frac{\partial p_{cg}}{\partial S_w} \right) \frac{S_{w,h}^{n+1} - S_{w,h}^{n}}{\Delta t} \right) / \partial p_g \right] \psi_j \right)_{\Omega} \quad (4\text{-}51)$$

$$\frac{\partial R^{\mathrm{p}}}{\partial \mathrm{S}_w} = \left(\psi_i, \left(\partial \left(\left(\frac{b-\phi}{K_s} + \left(1 - S_{w,h}^{n+1}\right)\phi \frac{Z_g}{p_{g,h}^{n+1}} \chi(p_g^{n+1}) + S_{w,h}^{n+1}\phi c_w \right) \frac{p_{g,h}^{n+1} - p_{g,h}^{n}}{\Delta t} \right) / \partial S_w \right) \varphi_j \right)_{\Omega} -$$

$$\left(\psi_i, \left(\partial \left(\left(\frac{b-\phi}{K_s} S_{w,h}^{n+1} \frac{\partial p_{cg}}{\partial S_w} + \phi S_{w,h}^{n+1} c_w \frac{\partial p_{cg}}{\partial S_w} \right) \frac{S_{w,h}^{n+1} - S_{w,h}^{n}}{\Delta t} \right) / \partial S_w \right) \varphi_j \right)_{\Omega} \quad (4\text{-}52)$$

$$\frac{\partial R^{\mathrm{p}}}{\partial \mathrm{v}_t} = \left(\psi_i, \nabla \cdot \boldsymbol{\omega_j} \right)_{\Omega} \quad (4\text{-}53)$$

$$\frac{\partial R^{\mathrm{p}}}{\partial \mathrm{u}} = \left(\psi_i, \left(\left(\frac{-1}{K_s} \frac{\partial \phi}{\partial \varepsilon_v} + \left(1 - S_{w,h}^{n+1}\right) \frac{\partial \phi}{\partial \varepsilon_v} \frac{Z_g}{p_{g,h}^{n+1}} \chi(p_g^{n+1}) + S_{w,h}^{n+1} \frac{\partial \phi}{\partial \varepsilon_v} c_w \right) \frac{p_{g,h}^{n+1} - p_{g,h}^{n}}{\Delta t} \right) \nabla \cdot \boldsymbol{v_j} \right)_{\Omega} -$$

$$\left(\psi_i, \left(\left(\frac{-1}{K_s} \frac{\partial \phi}{\partial \varepsilon_v} S_{w,h}^{n+1} \frac{\partial p_{cg}}{\partial S_w} + \frac{\partial \phi}{\partial \varepsilon_v} S_{w,h}^{n+1} c_w \frac{\partial p_{cg}}{\partial S_w} \right) \frac{S_{w,h}^{n+1} - S_{w,h}^{n}}{\Delta t} \right) \nabla \cdot \boldsymbol{v_j} \right)_{\Omega} + \left(\psi_i, b \nabla \cdot \boldsymbol{v_j} \frac{1}{\Delta t} \right)_{\Omega} \quad (4\text{-}54)$$

$$\frac{\partial R^{\mathrm{v}t}}{\partial \mathrm{v}_t} = -\left(\boldsymbol{\omega_i}, \frac{1}{\boldsymbol{k}} \frac{\mathbf{1}}{\lambda_t} \boldsymbol{\omega_j} \right)_{\Omega} \quad (4\text{-}55)$$

where $\lambda_t = \lambda_g + \lambda_w$.

$$\frac{\partial R^{\mathrm{v}t}}{\partial \mathrm{S}_w} = -\left(\boldsymbol{\omega_i}, \frac{\partial \left(\frac{1}{\lambda_t} \frac{1}{\boldsymbol{k}} \right)}{\partial \mathrm{S}_w} \mathbf{v}_t^{n+1} \varphi_j \right)_{\Omega} + \left(\boldsymbol{\omega_i}, \nabla S_{w,h}^{n+1} \left(\partial \left(F_w \frac{\partial p_{cg}}{\partial S_w} \right) / \partial S_w \right) \varphi_j \right)_{\Omega} + \left(\boldsymbol{\omega_i}, F_w \frac{\partial p_{cg}}{\partial S_w} \nabla \varphi_j \right)_{\Omega} +$$

$$\left(\boldsymbol{\omega_i}, \left(\partial \left(F_w \left(\rho_w - \rho_g \right) \boldsymbol{g} \right) / \partial S_w \right) \varphi_j \right)_{\Omega} \quad (4\text{-}56)$$

$$\frac{\partial R^{\mathrm{v}t}}{\partial \mathrm{p}_g} = -\left(\boldsymbol{\omega_i}, \left(\frac{\partial \left(\frac{1}{k \lambda_t} \right)}{\partial p_g} \right) \mathbf{v}_{\boldsymbol{t,h}}^{\boldsymbol{n+1}} \psi_j \right)_{\Omega} + \left(\nabla \cdot \boldsymbol{\omega_i}, \psi_j \right)_{\Omega} + \left(\boldsymbol{\omega_i}, \boldsymbol{g} \frac{\partial \rho_g}{\partial p_g} \psi_j \right)_{\Omega} + \left(\boldsymbol{\omega_i}, -F_w \boldsymbol{g} \frac{\partial \rho_g}{\partial p_g} \psi_j \right)_{\Omega} \quad (4\text{-}57)$$

$$\frac{\partial R^{\mathrm{v}t}}{\partial \mathrm{u}} = -\left(\boldsymbol{\omega_i}, \left(\partial \left(\frac{1}{\boldsymbol{k}} \right) / \partial \varepsilon_v \right) \frac{\mathbf{1}}{\lambda_t} \mathbf{v}_{\boldsymbol{t,h}}^{\boldsymbol{n+1}} \nabla \cdot \boldsymbol{v_j} \right)_{\Omega} \quad (4\text{-}58)$$

$$\frac{\partial R^S}{\partial \mathrm{p}_g} = \left(\varphi_i, \partial \left(S_{w,h}^{n+1} \left(\frac{b-\phi}{K_s} + \phi c_w \right) \frac{p_{g,h}^{n+1} - p_{g,h}^{n}}{\Delta t} \right) / \partial p_g \right)_\Omega - \left(\varphi_i, \left(\partial \left(\left(S_{w,h}^{n+1} \frac{b-\phi}{K_s} S_{w,h}^{n+1} \frac{\partial p_{cg}}{\partial S_w} - \phi + \right. \right. \right.$$

$$\left. \left. \left. \phi S_{w,h}^{n+1} c_w \frac{\partial p_{cg}}{\partial S_w} \right) \frac{S_{w,h}^{n+1} - S_{w,h}^{n}}{\Delta t} \right) / \partial p_g \right) \psi_j \right)_\Omega - \left(\nabla \varphi_i, \left(\frac{\partial \left(\boldsymbol{k} \cdot \left(F_w \lambda_g \frac{\partial p_{cg}}{\partial S_w} \nabla S_{w,h}^{n+1} \right) \right)}{\partial p_g} \right) \psi_j \right)_\Omega +$$

$$\left(\varphi_i, \left(\partial \left(\frac{\partial (F_w \lambda_g)}{\partial S_w} \nabla S_w \cdot \left(\boldsymbol{k} \cdot (\rho_w - \rho_g) \boldsymbol{g} \right) \right) / \partial p_g \right) \psi_j \right)_\Omega \quad \text{(4-59)}$$

$$\frac{\partial R^{\mathrm{S}}}{\partial \mathrm{S}_w} =$$

$$\left(\varphi_i, \left(\frac{\partial \left(S_{w,h}^{n+1} \left(\frac{b-\phi}{K_s} + \phi c_w \right) \frac{p_{g,h}^{n+1} - p_{g,h}^{n}}{\Delta t} \right)}{\partial S_w} \right) \varphi_j \right)_\Omega -$$

$$\left(\varphi_i, \left(\frac{\partial \left(\left(S_{w,h}^{n+1} \frac{b-\phi}{K_s} S_{w,h}^{n+1} \frac{\partial p_{cg}}{\partial S_w} - \phi + \phi S_{w,h}^{n+1} c_w \frac{\partial p_{cg}}{\partial S_w} \right) \frac{S_{w,h}^{n+1} - S_{w,h}^{n}}{\Delta t} \right)}{\partial S_w} \right) \varphi_j \right)_\Omega + \left(\varphi_i, b \frac{\nabla \cdot \boldsymbol{u_h^{n+1}} - \nabla \cdot \boldsymbol{u_h^n}}{\Delta t} \varphi_j \right)_\Omega -$$

$$\left(\nabla \varphi_i, \frac{\partial F_w}{\partial \mathrm{S}_w} \mathbf{v}_t^{n+1} \varphi_j \right)_\Omega - \left(\nabla \varphi_i, \nabla S_{w,h}^{n+1} \left[\frac{\partial \left(\boldsymbol{k} \cdot \left(F_w \lambda_g \frac{\partial p_{cg}}{\partial S_w} \right) \right)}{\partial S_w} \right] \varphi_j \right) - \left(\nabla \varphi_i, \boldsymbol{k} \cdot \left(F_w \lambda_g \frac{\partial p_{cg}}{\partial S_w} \right) \nabla \varphi_j \right)_\Omega +$$

$$\left(\varphi_i, \nabla S_w \cdot \left[\partial \left(\frac{\partial (F_w \lambda_g)}{\partial S_w} \left(\boldsymbol{k} \cdot (\rho_w - \rho_g) \boldsymbol{g} \right) \right) / \partial S_w \right] \varphi_j \right)_\Omega + \left(\varphi_i, \frac{\partial (F_w \lambda_g)}{\partial S_w} \left(\boldsymbol{k} \cdot (\rho_w - \rho_g) \boldsymbol{g} \right) \nabla \varphi_j \right)_\Omega +$$

$$\left(\nu \nabla \varphi_i, \nabla \varphi_j \right)_\Omega \quad \text{(4-60)}$$

$$\frac{\partial R^{\mathrm{S}}}{\partial \mathrm{v}_t} = -\left(F_w \nabla \varphi_i, \boldsymbol{\omega_j} \right)_\Omega \quad \text{(4-61)}$$

$$\frac{\partial R^{S}}{\partial u} =$$

$$\left(\varphi_i, \left(\frac{\partial\left(S_{w,h}^{n+1}\left(\frac{b-\phi}{K_s}+\phi c_w\right)\frac{p_{g,h}^{n+1}-p_{g,h}^{n}}{\Delta t}\right)}{\partial \varepsilon_v}\right)\nabla\cdot\boldsymbol{v_j}\right)_{\Omega} -$$

$$\left(\varphi_i, \left(\frac{\partial\left(\left(S_{w,h}^{n+1}\frac{b-\phi}{K_s}S_{w,h}^{n+1}\frac{\partial p_{cg}}{\partial S_w}-\phi+\phi S_{w,h}^{n+1}c_w\frac{\partial p_{cg}}{\partial S_w}\right)\frac{S_{w,h}^{n+1}-S_{w,h}^{n}}{\Delta t}\right)}{\partial \varepsilon_v}\right)\nabla\cdot\boldsymbol{v_j}\right)_{\Omega} +$$

$$\left(\varphi_i, S_{w,h}^{n+1} b\nabla\cdot\boldsymbol{v_j}\frac{1}{\Delta t}\right)_{\Omega} - \left(\nabla\varphi_i, \frac{\partial\left(\boldsymbol{k}\cdot\left(F_w\lambda_g\frac{\partial p_{cg}}{\partial S_w}\nabla S_{w,h}^{n+1}\right)\right)}{\partial \varepsilon_v}\nabla\cdot\boldsymbol{v_j}\right)_{\Omega} + \left(\varphi_i, \frac{\partial\left(\frac{\partial(F_w\lambda_g)}{\partial S_w}\nabla S_w\cdot(\boldsymbol{k}\cdot(\rho_w-\rho_g)\boldsymbol{g})\right)}{\partial \varepsilon_v}\nabla\cdot\boldsymbol{v_j}\right)_{\Omega}$$

..... (4-62)

$$\frac{\partial R^{u}}{\partial p_g} = \left(\nabla\cdot\boldsymbol{v_i}, b\psi_j\right)_{\Omega} + \left(\boldsymbol{v_i}, \frac{\partial \rho_b^{n+1}}{\partial p_g}\boldsymbol{g}\psi_j\right)_{\Omega} \quad \text{..... (4-63)}$$

$$\frac{\partial R^{\mathrm{u}}}{\partial \mathrm{S}_w} = -\left(\nabla\cdot\boldsymbol{v_i}, b\left(\frac{\partial\left(S_{w,h}^{n+1}p_{cg}(S_{w,h}^{n+1})\right)}{\partial S_w}\right)\varphi_j\right)_{\Omega} + \left(\boldsymbol{v_i}, \frac{\partial \rho_b^{n+1}}{\partial S_w}\boldsymbol{g}\varphi_j\right)_{\Omega} \quad \text{..... (4-64)}$$

where the capillary pressure is also a function of water saturation ($p_{cg}\left(S_{w,h}^{n+1}\right)$).

$$\frac{\partial R^{u}}{\partial u} = -\left(\lambda(\nabla\cdot\boldsymbol{v_i}), (\nabla\cdot\boldsymbol{v_j})\right)_{\Omega} - 2\left(\boldsymbol{\varepsilon}(\boldsymbol{v_i}), \mu\boldsymbol{\varepsilon}(\boldsymbol{v_j})\right)_{\Omega} + \left(\boldsymbol{v_i}, \frac{\partial \rho_b^{n+1}}{\partial \varepsilon_v}\boldsymbol{g}\nabla\cdot\boldsymbol{v_j}\right)_{\boldsymbol{\Omega}} \quad \text{..... (4-65)}$$

When the residual form of the displacement equation is nonlinear – the elastic stiffness tensor is a function of damage (porosity) - with respect to displacement, I formulate the displacement equation as follows

$$R^{\boldsymbol{u}} = (-\boldsymbol{\varepsilon}(\boldsymbol{v}),\ \boldsymbol{\sigma_0})_{\Omega} - 2\left(\boldsymbol{\varepsilon}(\boldsymbol{v_i}), \mu\phi\boldsymbol{\varepsilon}\left(\boldsymbol{u_h^{n+1}}\right)\right)_{\Omega} - \left(\lambda\phi(\nabla\cdot\boldsymbol{v_i}), \left(\nabla\cdot\boldsymbol{u_h^{n+1}}\right)\right)_{\Omega} +$$

$$\left(\nabla\cdot\boldsymbol{v_i}, b\left(p_g^{n+1} - S_{w,h}^{n+1}p_{cg}^{n+1}\right)\right)_{\Omega} - \left(\nabla\cdot\boldsymbol{v}, bp_{t,0}\right)_{\Omega} + (\boldsymbol{v_i}, \rho_b^{n+1}\boldsymbol{g})_{\Omega} + (\boldsymbol{v}, \boldsymbol{t})_{\Gamma}, \forall\boldsymbol{v}\in U \quad \text{..... (4-66)}$$

where ϕ is the porosity or the damage variable in continuum damage mechanics defined by the 2nd law of thermodynamics.

The matrix-vector form of the linear equations is

$$\begin{bmatrix} \frac{\partial R^{\mathrm{v}t}}{\partial \mathrm{v}_t} & \frac{\partial R^{\mathrm{v}t}}{\partial p_g} & \frac{\partial R^{\mathrm{v}t}}{\partial S_w} & \frac{\partial R^{\mathrm{v}t}}{\partial u} \\ \frac{\partial R^{p}}{\partial \mathrm{v}_t} & \frac{\partial R^{\mathrm{p}}}{\partial p_g} & \frac{\partial R^{\mathrm{p}}}{\partial S_w} & \frac{\partial R^{p}}{\partial u} \\ \frac{\partial R^{S}}{\partial \mathrm{v}_t} & \frac{\partial R^{S}}{\partial p_g} & \frac{\partial R^{S}}{\partial S_w} & \frac{\partial R^{S}}{\partial u} \\ 0 & \frac{\partial R^{u}}{\partial p_g} & \frac{\partial R^{u}}{\partial S_w} & \frac{\partial R^{u}}{\partial u} \end{bmatrix}^{n+1,k} \begin{bmatrix} \delta \mathrm{v}_t^{n+1} \\ \delta p_g^{n+1} \\ \delta S_w^{n+1} \\ \delta u^{n+1} \end{bmatrix}^{k} = - \begin{bmatrix} R^{\mathrm{v}t,n+1} \\ R^{p,n+1} \\ R^{w,n+1} \\ R^{\boldsymbol{u},n+1} \end{bmatrix}^{k} \quad \text{..... (4-67)}$$

where n and k indicate the time step and iteration indices. The numerical solutions for the next iteration are improved as

$$\mathrm{v}_{t,h}^{n+1,k+1} = \mathrm{v}_{t,h}^{n+1,k} + \delta \mathrm{v}_t^{n+1,k} \quad \text{..... (4-68)}$$

$$p_{g,h}^{n+1,k+1} = p_{g,h}^{n+1,k} + \delta p_g^{n+1,k} \quad \text{..... (4-69)}$$

$$S_{w,h}^{n+1,k+1} = S_{w,h}^{n+1,k} + \delta S_{w,h}^{n+1,k} \quad \text{..... (4-70)}$$

$$u_h^{n+1,k+1} = u_h^{n+1,k} + \delta u_h^{n+1,k} \quad \text{..... (4-71)}$$

For the case of a slightly compressible system (oil and water) I can simply modify the compressibility term of pressure equation as

$$R^p = \left(\psi_i, \left(\frac{b-\phi}{K_s} + \left(1 - S_{w,h}^{n+1}\right)\phi c_o + S_{w,h}^{n+1}\phi c_w\right)\frac{p_{o,h}^{n+1} - p_{o,h}^{n}}{\Delta t}\right)_{\Omega} -$$
$$\left(\psi_i, \left(\frac{b-\phi}{K_s} S_{w,h}^{n+1}\frac{\partial p_{co}}{\partial S_w} + \phi S_{w,h}^{n+1} c_w \frac{\partial p_{co}}{\partial S_w}\right)\frac{S_{w,h}^{n+1} - S_{w,h}^{n}}{\Delta t}\right)_{\Omega} + \left(\psi_i, b\frac{\nabla \cdot \boldsymbol{u_h^{n+1}} - \nabla \cdot \boldsymbol{u_h^{n}}}{\Delta t}\right)_{\Omega} + \left(\psi_i, \nabla \cdot \mathbf{v}_{\boldsymbol{t,h}}^{\boldsymbol{n+1}}\right)_{\Omega} -$$
$$(\psi_i, f_o + f_w)_{\Omega}, \forall \psi \in W \quad \text{..... (4-72)}$$

The derivatives that need to be replaced in Eq. 4-67 are

$$\frac{\partial R^{\mathrm{p}}}{\partial \mathrm{p}_o} = \left(\psi_i, \left(\partial\left(\left(\frac{b-\phi}{K_s} + \left(1 - S_{w,h}^{n+1}\right)\phi c_o + S_{w,h}^{n+1}\phi c_w\right)\frac{p_{o,h}^{n+1} - p_{o,h}^{n}}{\Delta t}\right)/\partial p_o\right)\psi_j\right)_{\Omega} -$$
$$\left(\psi_i, \left[\partial\left(\left(\frac{b-\phi}{K_s} S_{w,h}^{n+1}\frac{\partial p_{co}}{\partial S_w} + \phi S_{w,h}^{n+1} c_w \frac{\partial p_{co}}{\partial S_w}\right)\frac{S_{w,h}^{n+1} - S_{w,h}^{n}}{\Delta t}\right)/\partial p_o\right]\psi_j\right)_{\Omega} \quad \text{..... (4-73)}$$

$$\frac{\partial R^{\mathrm{p}}}{\partial \mathrm{S}_w} = \left(\psi_i, \left(\partial\left(\left(\frac{b-\phi}{K_s} + \left(1 - S_{w,h}^{n+1}\right)\phi c_o + S_{w,h}^{n+1}\phi c_w\right)\frac{p_{o,h}^{n+1} - p_{o,h}^{n}}{\Delta t}\right)/\partial S_w\right)\varphi_j\right)_{\Omega} -$$
$$\left(\psi_i, \left(\partial\left(\left(\frac{b-\phi}{K_s} S_{w,h}^{n+1}\frac{\partial p_{co}}{\partial S_w} + \phi S_{w,h}^{n+1} c_w \frac{\partial p_{co}}{\partial S_w}\right)\frac{S_{w,h}^{n+1} - S_{w,h}^{n}}{\Delta t}\right)/\partial S_w\right)\varphi_j\right)_{\Omega} \quad \text{..... (4-74)}$$

$$\frac{\partial R^{\mathrm{p}}}{\partial \mathrm{u}} = \left(\psi_i, \left(\left(\frac{-1}{K_s} \frac{\partial \phi}{\partial \varepsilon_v} + \left(1 - S_{w,h}^{n+1}\right) \frac{\partial \phi}{\partial \varepsilon_v} c_o \right) + S_{w,h}^{n+1} \frac{\partial \phi}{\partial \varepsilon_v} c_w \right) \frac{p_{o,h}^{n+1} - p_{o,h}^{n}}{\Delta t} \right) \nabla \cdot \boldsymbol{v_j} \right)_{\Omega} -$$

$$\left(\psi_i, \left(\left(\frac{-1}{K_s} \frac{\partial \phi}{\partial \varepsilon_v} S_{w,h}^{n+1} \frac{\partial p_{co}}{\partial S_w} + \frac{\partial \phi}{\partial \varepsilon_v} S_{w,h}^{n+1} c_w \frac{\partial p_{co}}{\partial S_w} \right) \frac{S_{w,h}^{n+1} - S_{w,h}^{n}}{\Delta t} \right) \nabla \cdot \boldsymbol{v_j} \right)_{\Omega} + \left(\psi_i, b \nabla \cdot \boldsymbol{v_j} \frac{1}{\Delta t} \right)_{\Omega} \quad \text{..... (4-75)}$$

4.3 Numerical Experiments

4.3.1 Verification Problem

I tested the code by comparing its numerical solution to the analytical solution of Terzaghi's 1-D consolidation problem. The detailed procedure for obtaining the analytical solution is well described by Verruijt (1995). A mechanical load (5 MPa) is applied suddenly (t=0) to the top of the 1D domain, the top and bottom boundaries of which have drainage (constant-pressure) boundary conditions (**Fig. 4.3**). Initially the pore pressure on the domain is zero but pore pressure instantaneously jumps to the maximum value because of the loading. Immediately after the mechanical loading, the fluid in the domain begins to drain through the drainage boundaries (top and bottom).

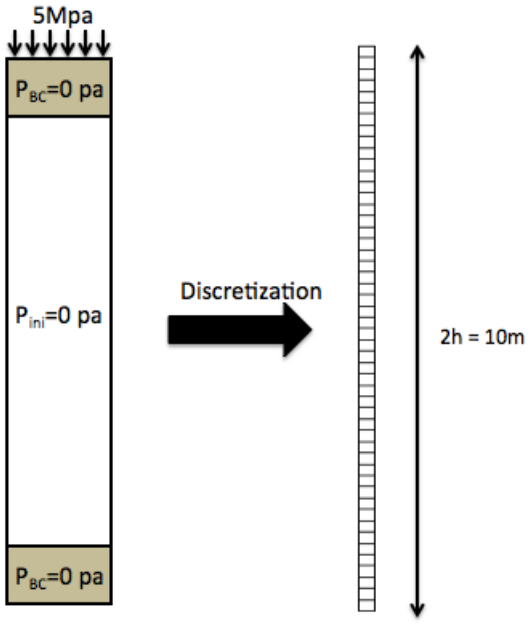

Fig. 4.3—Terzaghi's 1-D consolidation problem. The top and bottom boundaries have drainage (constant-pressure) boundary condition.

For the numerical solution, I discretized the domain into 50 square cells with dimensions of $0.2m \times 0.2m$. The mixed finite element discretization I used stipulates that each element had its pressure estimated at its

centroid (or center of gravity), and its displacement solution at each node. The permeability, porosity, and rock compressibility are 100 *md*, 0.3, and $5.0 \times 10^{-10}\ pa^{-1}$ respectively. The viscosity and fluid compressibility are 1 *cp* and $1.0 \times 10^{-10}\ pa^{-1}$. **Fig. 4.4** shows the comparison between the analytical and numerical solution at different dimensionless times. The comparison indicates that the numerical solution matches the analytical solution very well.

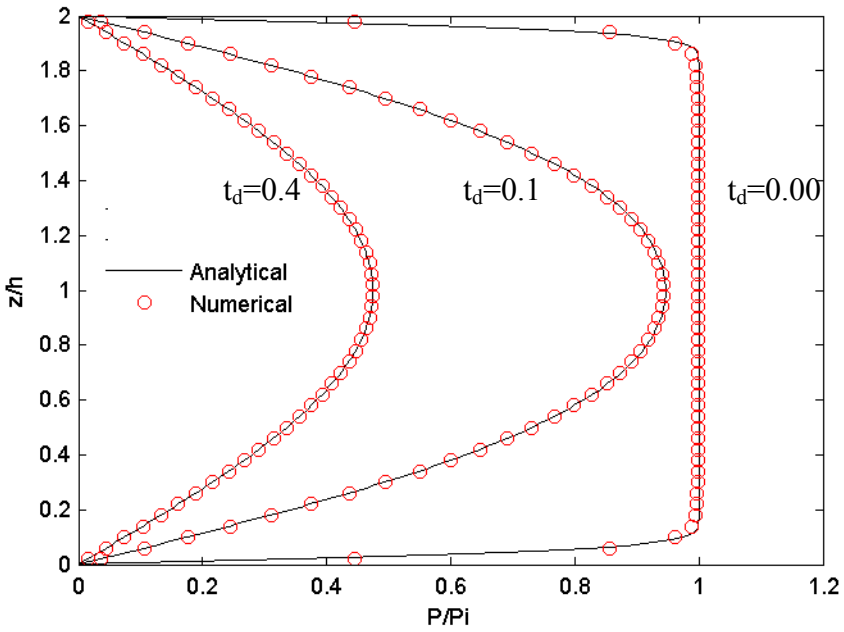

Fig. 4.4—Comparison of the numerical and analytical solutions of the 1D consolidation problem at different dimensionless time. The numerical solutions practically coincide with the analytical solutions (t_d is the dimensionless time defined as $t_d = \frac{c_v t}{h^2}$ where $c_v = \frac{k}{(c_r + \phi c_f)\mu}$).

4.3.2 Comparison between Coupled and Uncoupled Simulations

I compare the difference between the coupled and uncoupled simulations to emphasize the importance of coupled flow and geomechanics in a porous medium exhibiting a strong geomechanical behavior. The uncoupled simulation does not consider the contribution of rock deformation to the pressure and/or saturation because the geomechanical equilibrium equation is not coupled with the mass balance equation.

Fig. 4.5 shows a homogeneous 2D reservoir domain (2D areal cross section) and describes its boundary conditions. The size of the reservoir domain is 100 m by 100 m. The permeability and porosity are 100 md and 0.3 respectively, and they are constant over time. The fluid viscosity and compressibility are 5 *cp* and $1.0 \times 10^{-9}\ pa^{-1}$, respectively. For the mechanical problem, Lamé's first constant and shear modulus are

$5.56 \times 10^8\ pa$ and $8.33 \times 10^8\ pa$, respectively. The observation well, which monitors pore pressure, is located at the center of the domain. A no flow boundary condition is imposed around the perimeter of the whole domain and the geomechanical equilibrium equation has a roller and prescribed traction boundary conditions. The roller boundary condition constrains the deformation of the boundary in the normal direction. The prescribed traction means I specify the surface traction vector, which is the representation of the force acting on the unit area at a point of the surface. TAM-CFGM automatically initializes a reservoir system subject to a given set of flow and mechanical boundary conditions. The reservoir pore pressure will be determined from the interaction between the fluid compressibility and the rock deformation caused by the imposed traction. After initialization, TAM-CFGM uses the primary variables determined from the initialization to conduct the production simulation. The sink is located at the lower left corner of the domain with a rate of $2 \times 10^{-6} s^{-1}$. Note that the rate of production is per second (s^{-1}) the flow equations (*i.e.* mass balance equations) that I derived have unit of per second (s^{-1}).

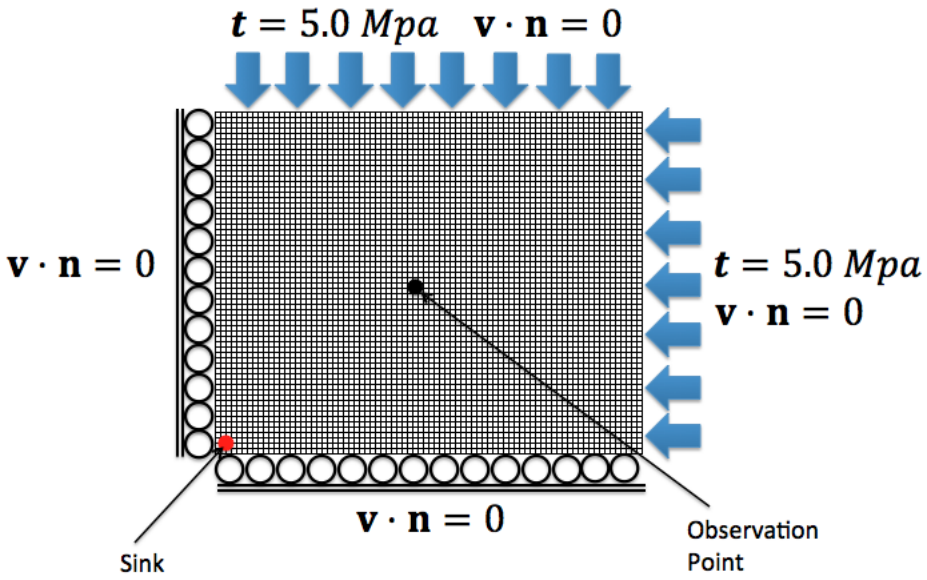

Fig. 4.5—2D reservoir domain for the coupled and uncoupled simulations.

Fig. 4.6 shows the pressure solution of the coupled and the uncoupled simulations after 12 days of production. The coupled simulation results show a higher pore pressure because of the mechanical loading (traction boundary condition). On the other hand, uncoupled simulation does not have any pressure support from the boundary because the mechanical response is not incorporated into the simulation. The numerical solutions for both cases converge in a single Newton-Raphson iteration because the governing equations are linear functions of the primary variables.

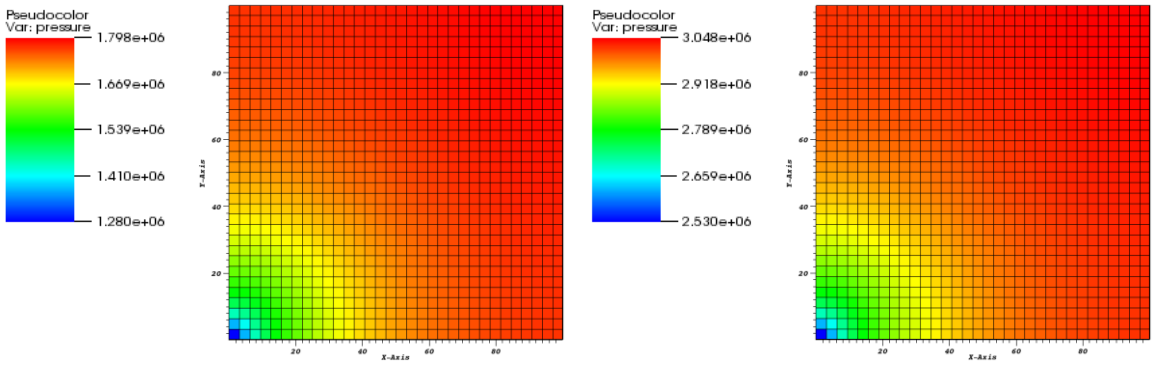

(a) **(b)**

Fig. 4.6—Pressure solutions from the (a) uncoupled and (b) the coupled simulations after 12 days of production indicate that the coupled simulation yields a higher reservoir pressure because of the imposed traction boundary condition (pressure in Pa).

Fig. 4.7 compares the time-dependent pressure solutions at the observation point between the coupled and uncoupled simulations. **Fig. 4.7 (a)** indicates that the coupled simulation yields a substantially higher pore pressure than the uncoupled simulation, and the magnitude of the difference between the two solutions increases with time. **Fig. 4.7 (b)** shows pore pressure at the beginning of production. The pore pressure for the coupled simulation rose above the initial pore pressure, but then decreased with time. This behavior indicates the Mandel-Cryer effect (Cryer 1963). The results of this study indicate the need to consider the geomechanical impact on flow/production in a porous medium system, especially when the rock is deformable such as in an unconsolidated formation; otherwise it may not be possible to obtain a realistic estimate of the reservoir performance.

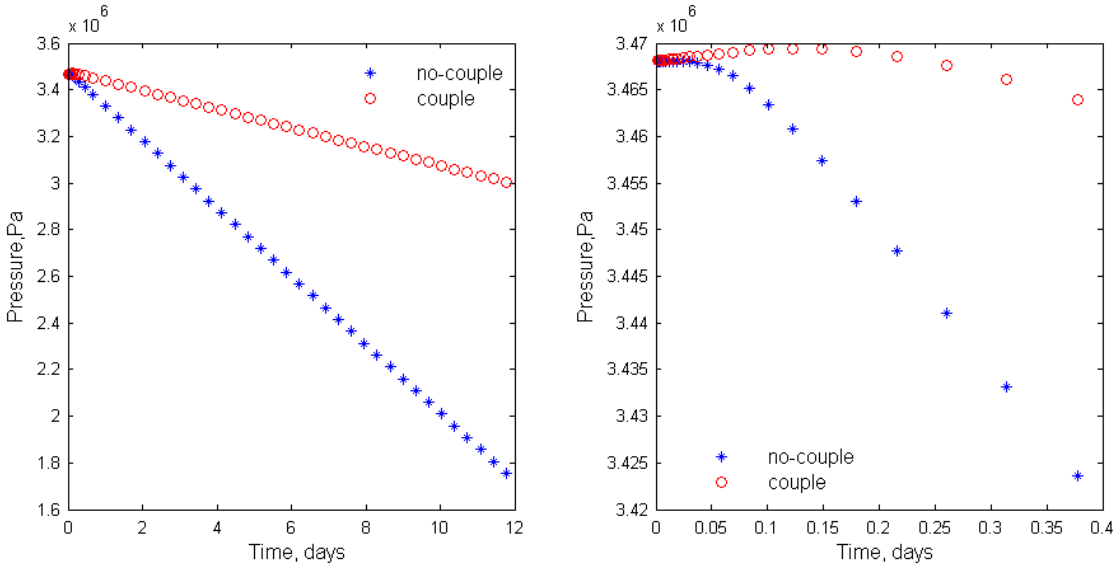

(a) **(b)**

Fig. 4.7—(a) Reservoir pore pressure after 12 days of production shows that the coupled simulation predicted a higher pore pressure because of the imposed traction boundary condition, and a pressure difference that increased with time. (b) At the early stage of the production, the pore pressure from the coupled simulation rose above the initial pore pressure. This is consistent with the Mandel-Cryer effect (Cryer 1963).

Fig. 4.8 shows the spatial distribution of porosity at t =12 days (**Fig 4.8 (a)**), and the evolution of porosity at the production location over time (**Fig 4.8 (b)**). Unlike the previous experiment, the numerical solutions converged in two or three Newton-Raphson iterations because the governing equations are nonlinear functions of pressure and displacement. The porosity distribution (**Fig 4.8 (a)**) follows a pattern that is very similar to that of the pressure distribution in **Fig. 4.6**. This is because the porosity change is strongly affected by changes in pressure and displacement. The pressure and displacement solutions are interrelated because the mass balance and the equilibrium equations are coupled. If the production rate increases or a constant bottom hole pressure boundary is imposed, the porosity change increases accordingly. Note that a lower Young's modulus would change the porosity substantially.

In addition to the study depicted in **Fig. 4.8**, I also ran another coupled flow and geomechanics simulation in which the porosity and permeability were a function of two primary variables (pressure and displacement). The porosity change was not significant in this case because of the imposition of a constant mass production rate.

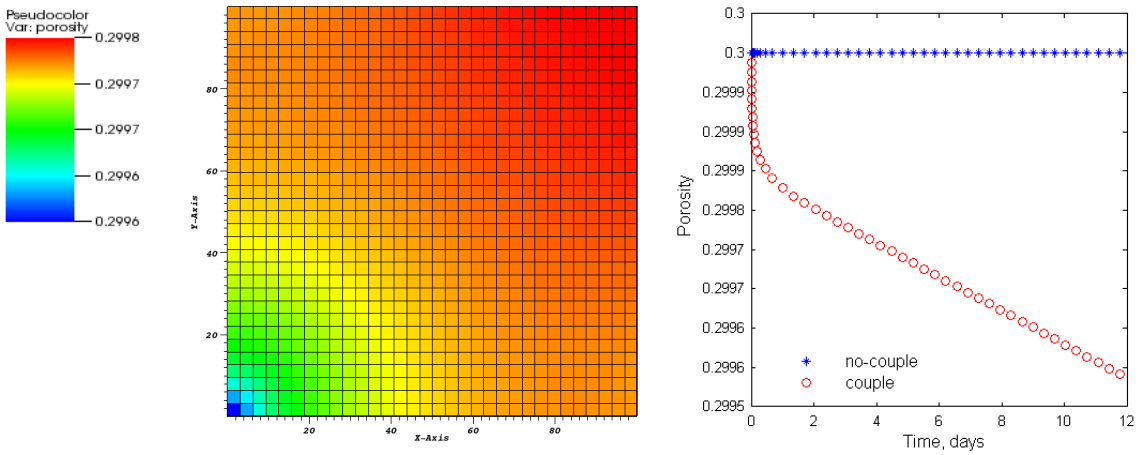

Fig. 4.8—(a) Reservoir porosity distribution after 12 days of production period and (b) the change in porosity at the production area. Porosity rapidly decreased in the very early time due to the production. Uncoupled simulation set the porosity as constant.

4.3.3 Waterflooding Simulation for a Homogeneous Reservoir

Fig. 4.9 shows a homogeneous 2D reservoir domain (a 2D areal cross section) and describes the boundary conditions. The 2D domain was discretized into 32 x 32 uniform-sized elements. The size of the reservoir domain was 10 m by 10 m. The permeability and porosity were 1000 md and 0.3 respectively. The fluid viscosity and compressibility were 1 cp for water and 2 cp for oil and $1.0 \times 10^{-9}\ pa^{-1}$ for water and $2.0 \times 10^{-9}\ pa^{-1}$ for oil respectively. For the geomechanical problem, Lamé's first constant and shear modulus were $1.0 \times 10^{8}\ pa$ and $3.0 \times 10^{8}\ pa$. A no flow boundary condition is imposed around the perimeter of the whole domain, and the equilibrium equation had a zero displacement along the entire boundary. Initially, the reservoir domain was saturated with 100% oil. Water was injected at the lower left corner of the domain at a rate of $3.51 \times 10^{-6} s^{-1}$and oil was produced at the upper right corner of the domain at rate of $3.50 \times 10^{-6} s^{-1}$. The simulation input data is summarized in **Table 4.1**.

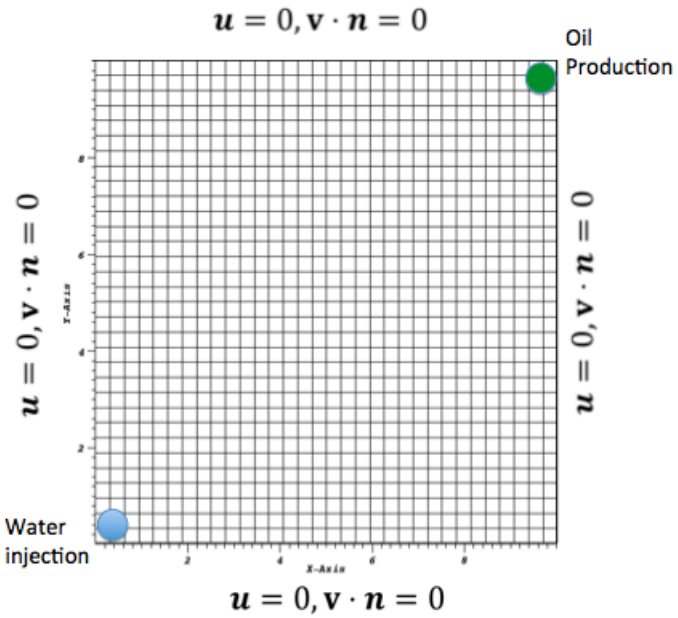

Fig. 4.9—The homogeneous 2D reservoir domain (2D areal cross section) in the waterflooding problem.

Table 4.1—Input data for the waterflooding simulation	
Water viscosity (cp)	1.0
Water compressibility (Pa^{-1})	1.00E-09
Oil viscosity (cp)	2.0
Oil compressibility (Pa^{-1})	2.00E-09
Initial water saturation	0
Biot's coefficient	1.0
Permeability function	Porosity dependent
Relative perm. curve	Quadratic
Initial reservoir pressure (MPa)	3.0

Fig. 4.10 shows (a) the saturation and velocity solutions and (b) the pressure and velocity solutions after 20 days of simulation. The spatial distribution of saturation (**Fig 4.10 (a)**) shows a uniform propagation of the injected water front, with the same saturation values at the same radial distance from the well. This is because the reservoir has homogeneous properties and no flow boundary conditions. The pressure distribution in **Fig. 4.8(b)** shows a pressure gradient between the injector and the producer, with the highest veloc-

ities occurring near the injector and the producer. The saturation, pressure, and velocity solutions indicate that the simulator estimates the correct physics of multiphase flow in porous media.

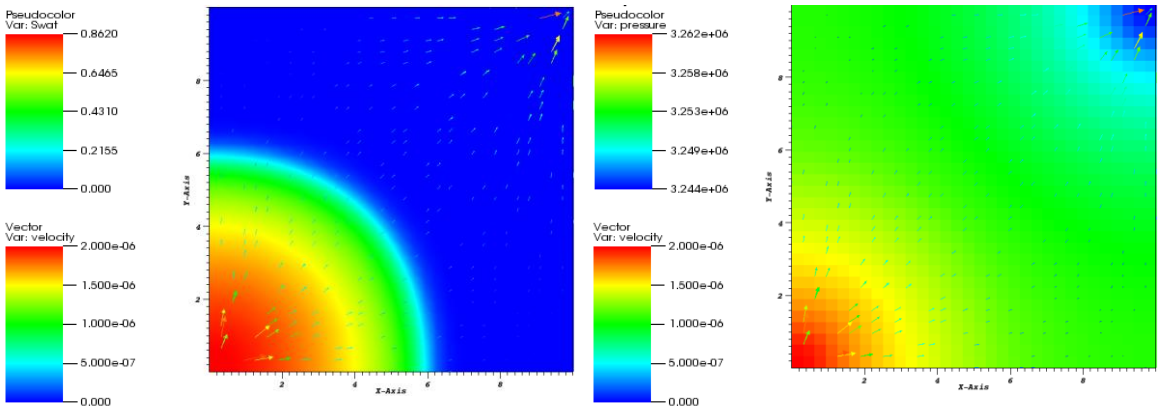

(a) **(b)**

Fig. 4.10—(a)Saturation and velocity solutions and (b) pressure and velocity solution after 20 days of water flooding (velocity in m/s; pressure in Pa)

I magnified the velocity solution (**Fig. 4.11**) to investigate the direction of the flow. The mixed finite element formulation directly solves Darcy's equation as a governing equation, an approach that provides a more accurate velocity solution. The velocity vectors clearly show that the injected water flows to the producer, and it implies that the shortest travel time to reach the producer occurs along the diagonal of the domain as this involves the shortest path.

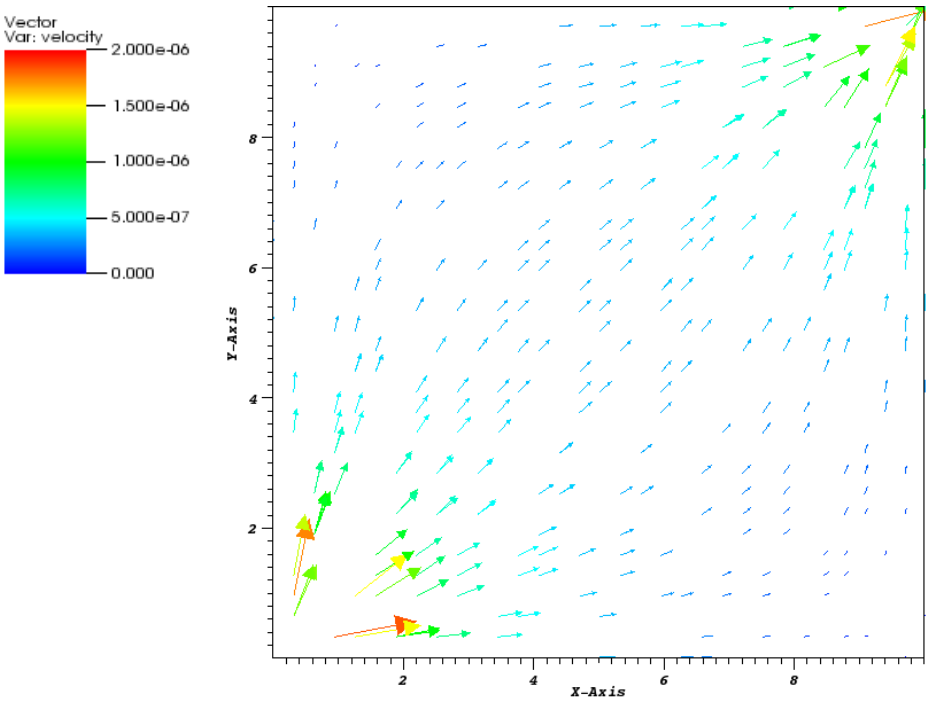

Fig. 4.11—Waterflooding problem: the velocity (m/s) distribution after 20 days of simulation.

Fig. 4.12 shows the x-direction and y-direction displacement solutions at t = 20 days. Because of an isotropic elastic stiffness tensor that is applied to the entire system, the displacement solutions are very smooth and dependent on the pressure gradient because of the poroelastic model used for this study. As expected, the displacement solution shows diagonal symmetry ($(x, y) = (y, x)$). **Fig. 4.13** lists the values of the x and y direction displacement solutions, which shows the diagonal symmetry of the displacement vectors ($\boldsymbol{u_1} = 9.98162 \times 10^{-7}, 1.14977 \times 10^{-6}, \boldsymbol{u_2} = 1.14977 \times 10^{-6}, 9.98162 \times 10^{-7}$). This result indicates that the simulator correctly estimates the physics.

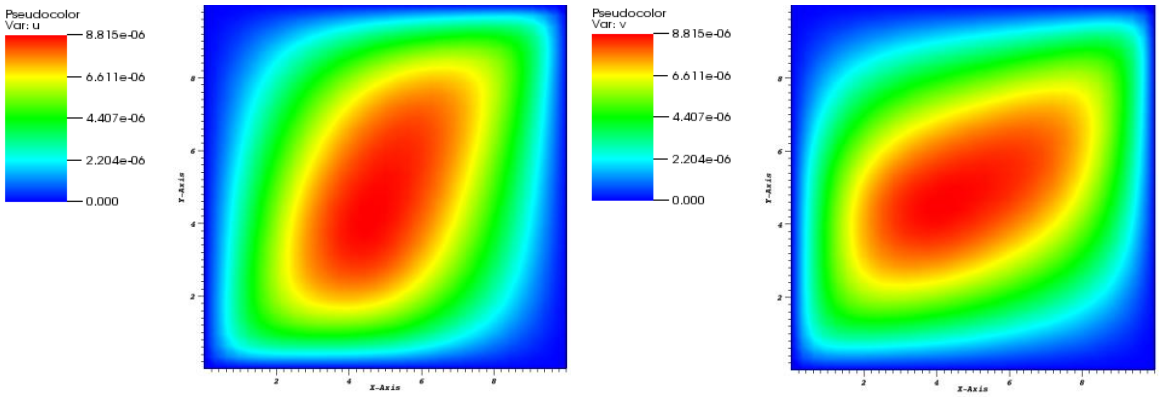

(a) (b)

Fig. 4.12—(a) X-direction displacement and (b) y-direction displacement solutions after 20 days of water flooding. The unit of the displacement solution is meter (m).

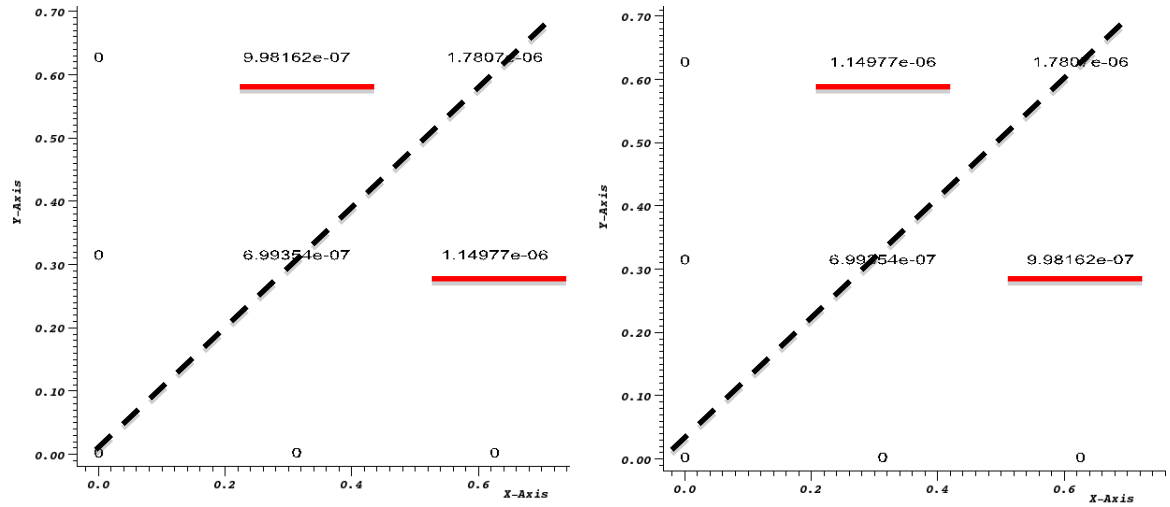

(a) (b)

Fig. 4.13—Values of the (a) x-direction displacement and (b) y-direction displacement solutions after 20 days of water flooding at the area of 0.6mx0.6m. The two displacement vectors show diagonal symmetry (displacement in m).

To test the performance of TAM-CFGM in a 3D problem of coupled flow and geomechanics, I repeated the waterflooding study using a 3D (instead of the 2D) domain. I used the same areal discretization used in the 2D waterflooding problem, and discretized the reservoir thickness into 5 uniform-sized layers along the z-direction. The vertical length of the 3D domain was 5/32 of the x- or y-direction length. The flow and rock properties were identical to those in the 2D problem.

Fig. 4.14 shows the discretized 3D model, which had the same boundary conditions with the 2D problem (no flow and zero displacement boundary conditions). Thus, no flow and zero displacement conditions were assigned to the outer surfaces of the 3D model. For complete analogy with the 2D problem, the 3D study ignored gravitational effects. Water was injected at the corner column of the domain (indicated with a blue line) with a constant rate of $3.51 \times 10^{-6} s^{-1}$ and oil was produced at the opposite column of the domain (indicated with a green line) at a constant rate of $3.50 \times 10^{-6} s^{-1}$.

Fig. 4.15 shows the saturation and pressure solutions after 20 days of waterflooding, which agree very well with the 2D solutions. **Fig. 4.16** shows the velocity solution and the saturation (visualized as a 3d volume) with velocity in the 3D model. The velocity distribution shows a flow pattern that is very similar to that obtained from the 2D model.

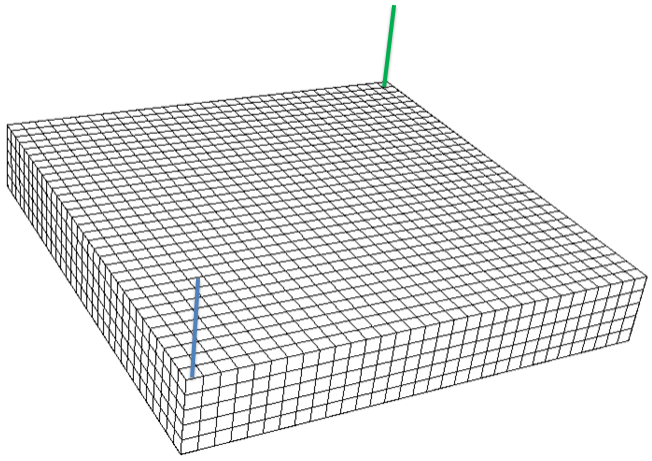

Fig. 4.14—The 3D reservoir domain (with discretization) used for the 3D simulation of the waterfooding problem.

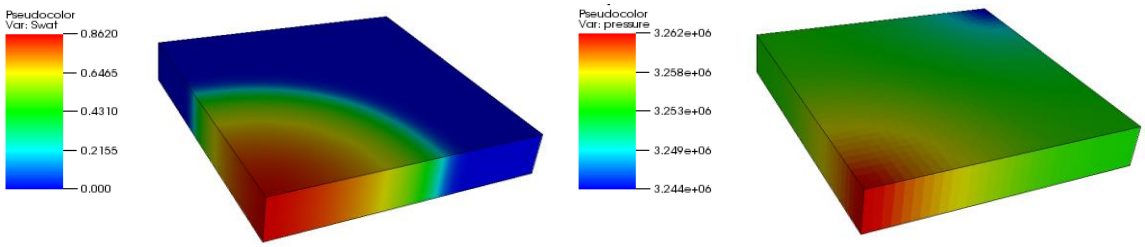

(a) (b)

Fig. 4.15— (a) Saturation and (b) pressure solutions after 20 days of water flooding (pressure in Pa).

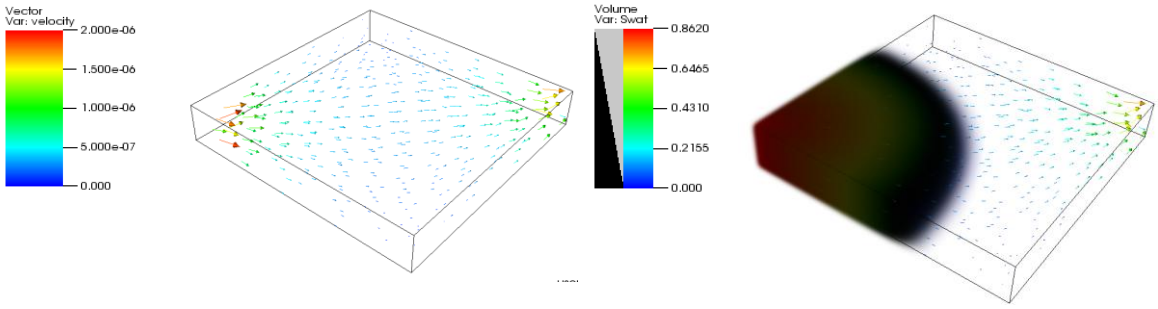

(a) (b)

Fig. 4.16—(a) Velocity solution and (b) saturation (visualized as a 3d volume) with velocity after 20 days of water flooding. The unit of the velocity magnitude is meter per second (m/s).

Fig. 4.17 shows the x- and y-direction displacement solutions on the middle layer of the 3D model. The displacements are substantially smaller than those estimated in the 2D simulation. This is because the 2D geomechanics problem with a plane strain condition assumed an infinite geomechanical domain along the z-direction, which basically indicates no gradient of displacement along that direction. As a result, only the mechanical loadings along the x- and y-direction change the formation, but no changes occur in the z-direction. In the 3D problem, the geomechanical model does not assume a plane strain condition because the z-directional layer is finite and limited. As a result, the displacement solutions are not only affected by the zero displacement boundary condition along the x- and y-direction, but also by the same boundary condition in the z-direction. The z-direction boundary condition imposed on the short reservoir thickness (shorter than the x- and y-direction length) resulted in substantially smaller displacements than in the 2D problem.

The results of the 3D simulation indicate that the simulator is capable of modeling a 3D coupled flow and geomechanics problem with a correct numerical solution.

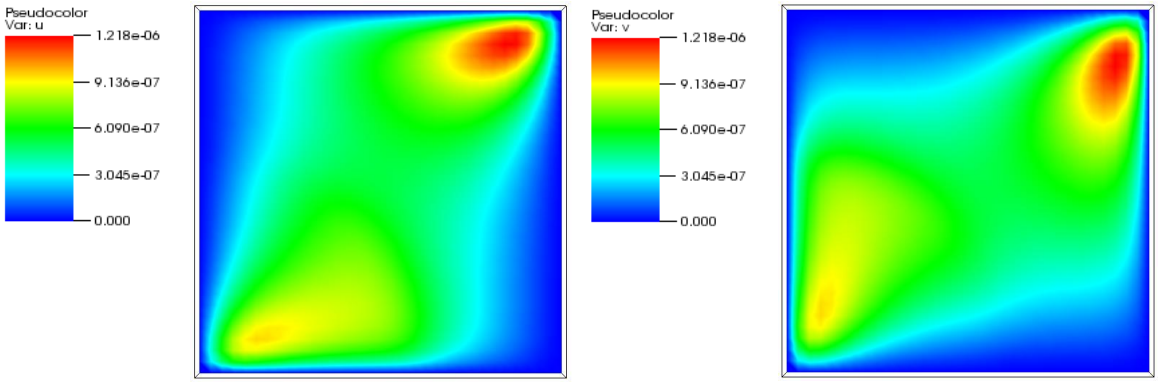

Fig. 4.17—(a) X-direction displacement and (b) y-direction displacement solutions from the 3D problem after 20 days of water flooding (displacement in m).

4.3.4 Comparison of the Saturation Solution with Discontinuous Galerkin (DG) Formulation

I compared the saturation solution obtained from my TAM-CFGM to that using the DG formulation. TAM-CFGM uses piecewise linear nodal basis functions for the saturation equation, and the saturation solutions are located at each node. The zero-order DG formulation uses an upstream weighting scheme and piecewise-constant basis functions, and the saturation solutions are located at the center of each element. The domain for this comparison study was the one used in the previous waterflooding problem, but I used different flow boundary conditions. Rather than imposing source and sink constraints (injection and production rates), I imposed an x-direction core-flood boundary condition by specifying constant inlet (along the left edge) and outlet (along the right edge) pressure and saturation. A no flow boundary condition was imposed on the sides parallel to the flow direction. The inlet pressure and water saturation were 3 MPa and 1.0, respectively. The outlet pressure and water saturation were 1.0 MPa and 0, respectively. The directional permeability tensor is used for the comparison and is defined as

$$\boldsymbol{K}(\boldsymbol{x}) = \alpha k(\boldsymbol{x})\boldsymbol{I} \quad \text{(4-76)}$$

where $\boldsymbol{I}$ is the second order identity tensor, α is a multiplication factor that determines the magnitude of the permeability, $k(\boldsymbol{x})$ is a spatial permeability function, and $\boldsymbol{x}$ is a vector indicating the location of the current element. For $k(\boldsymbol{x})$, I used a single crack permeability model (Bangerth 2006) defined as

$$k(\boldsymbol{x}) = max\left\{exp\left(-\left(\frac{y/y_{max}-0.5-0.1\sin(10x/x_{max})}{0.1}\right)^2\right), 0.01\right\} \quad \text{(4-77)}$$

where x and y indicate the coordinates of the element and x_{max} and y_{max} are the maximum x and y lengths.

Fig. 4.18 shows the saturation and velocity solutions with the DG method and my method (TAM-CFGM). My method provides a higher resolution of the saturation solution. This is more noticeable in an additional study I conducted, which involved a random permeability model (Bangerth 2006) defined as

$$k(\boldsymbol{x}) = min\{max\{\sum_{i-1}^{N} \boldsymbol{\Lambda_i}(\boldsymbol{x}), 0.01\}, 4\} \quad \text{(4-78)}$$

where $\boldsymbol{\Lambda_i}(\boldsymbol{x})$ is defined as

$$\boldsymbol{\Lambda_i}(\boldsymbol{x}) = exp\left(-\left(\frac{|\boldsymbol{x}-\boldsymbol{x_i}|}{0.05}\right)^2\right) \quad \text{(4-79)}$$

where $\boldsymbol{x_i}$ is the center of the randomly chosen locations (40 locations in this case).

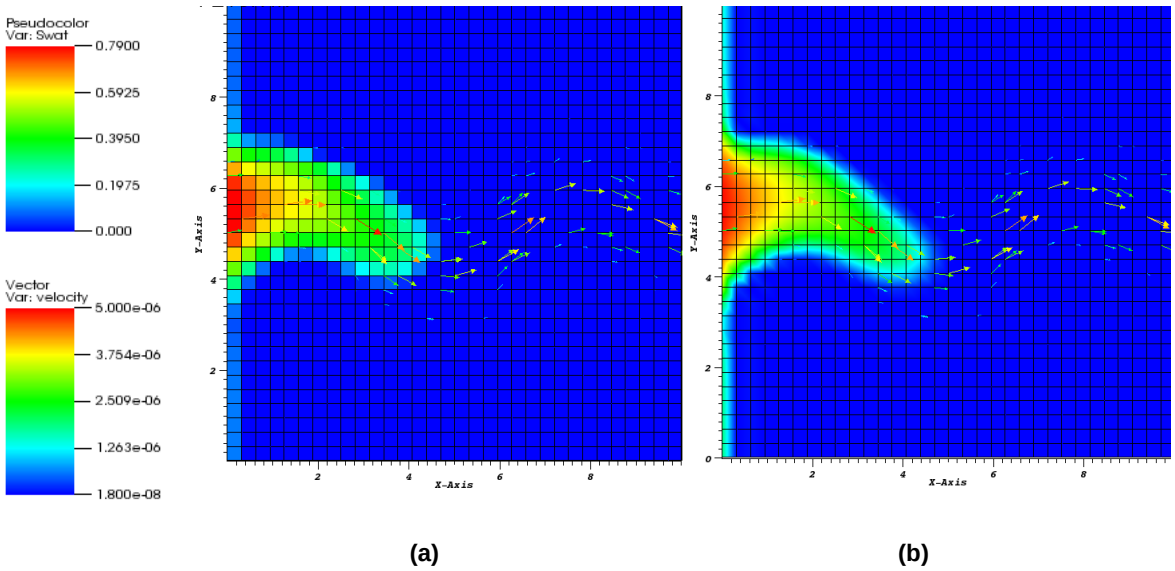

(a) **(b)**

Fig. 4.18—Comparison of the (a) saturation and velocity (m/s) solutions with the DG method and (b) my method indicates the better resolution of saturation obtained from my method (velocity in m/s).

Fig. 4.19 compares the saturation and velocity solutions with the DG method and my method in the random permeability problem. The difference in saturation solution is more noticeable than the previous single crack permeability problem. The saturation distributions indicate that my method provides a better resolution of the saturation solution. The DG method did not capture the sharp gradients in the profile of the saturation distribution with the random permeability model.

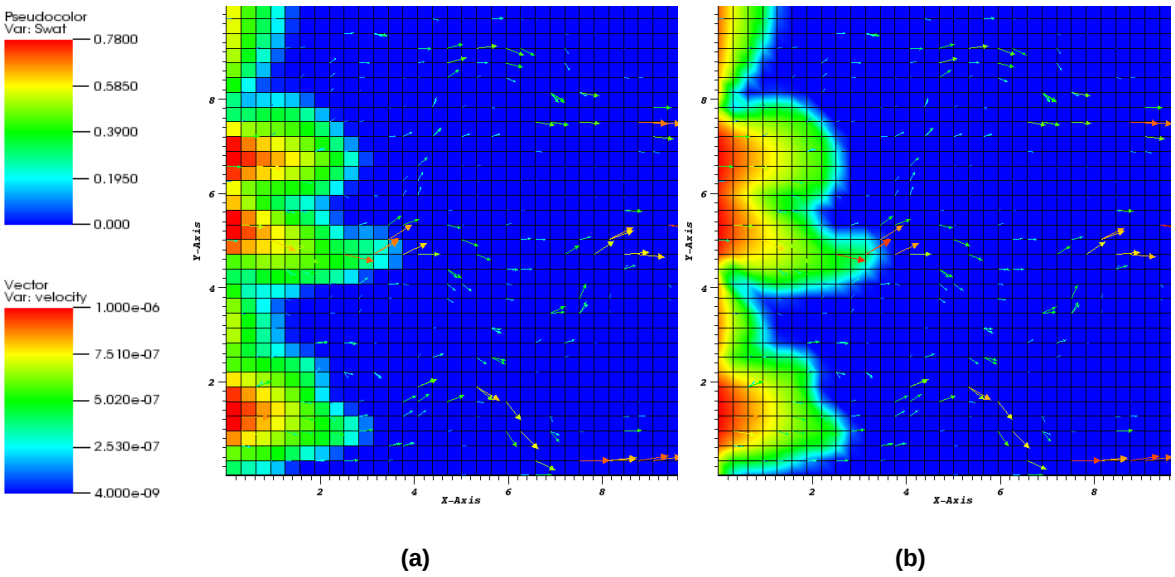

Fig. 4.19—Comparison of the saturation and velocity (m/s) solutions using (a) the DG method and (b) my method in the random permeability problem (velocity in m/s).

Fig. 4.20 compares the saturation and velocity solutions from my method to those from the DG method obtained with a very fine discretization of the domain (four times finer mesh than the one in my solution). Even though my method produced solutions using mesh that was four times coarser than that in the DG study, the saturation solutions are in good agreement. This indicates that my method provides a higher resolution of the saturation with less computation cost and proves that the higher resolution of the saturation is not just the result of interpolation algorithm/method in my plotting software but the saturation solution with my method is more accurate than the DG method when using same discretization.

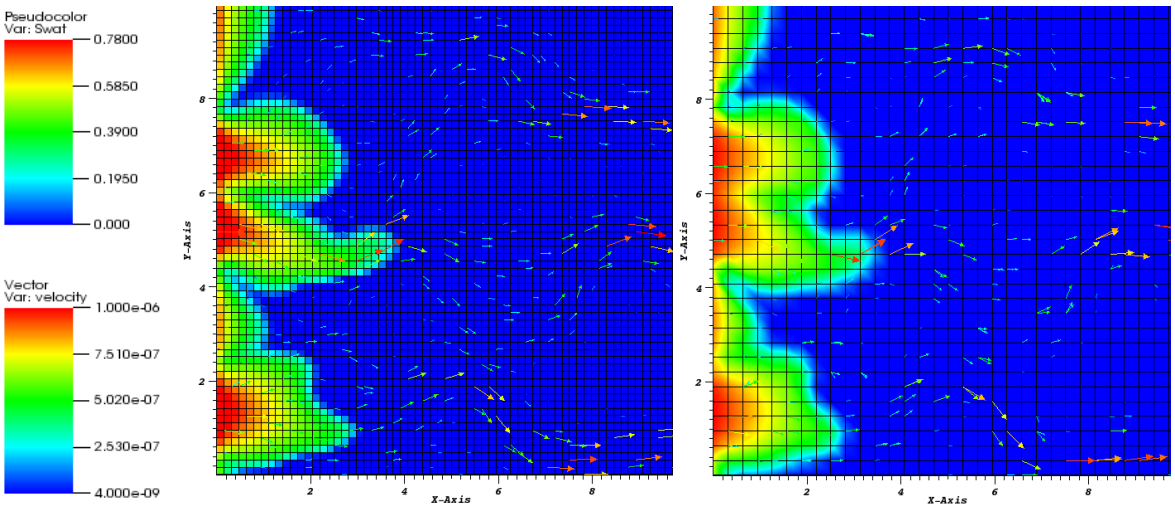

Fig. 4.20—Comparison of the saturation and velocity (m/s) solutions of (a) the DG method with very fine discretization and (b) my method with coarse discretization in the random permeability problem.

4.3.5 The Effect of Full Tensor Permeability and Elastic Stiffness

As mentioned previously, TAM-CFGM can handle full tensor permeability and elastic stiffness. Here I discuss the effects of using full tensors in multiphysics simulations. I applied a single permeability tensor and a single elastic stiffness tensor to the entire domain. The simulation conditions were those used in the previous waterflooding problem, and the study included the following directional permeability and orthotropic elastic stiffness tensors:

$$\boldsymbol{K} = \begin{bmatrix} 200 & 0 \\ 0 & 50 \end{bmatrix} \quad \text{(4-80)}$$

$$\boldsymbol{E} = \begin{bmatrix} 607.4 & 188.2 & 0 \\ 188.2 & 606.9 & 0 \\ 0 & 0 & 149.4 \end{bmatrix} \quad \text{(4-81)}$$

The units of the permeability and elastic stiffness are *md* and *MPa*, respectively.

In order to make the permeability and the elastic stiffness full tensors, I applied a 30 degree (counter clock wise) orthogonal rotation of the permeability and elastic stiffness tensors. The orthogonal rotation matrix is defined as

$$\boldsymbol{R} = \begin{bmatrix} cos\theta & sin\theta \\ -sin\theta & cos\theta \end{bmatrix} \quad (4\text{-}82)$$

where the direction of the angle θ is counter clock-wise. Then, the rotated permeability tensor is obtained by

$$\bar{\boldsymbol{K}} = \boldsymbol{R^{-1}KR} \quad (4\text{-}83)$$

where $\boldsymbol{K}$ is the original permeability tensor, and $\bar{\boldsymbol{K}}$ is the rotated permeability tensor. The components of the rotated permeability tensor are estimated from the following equations

$$k_{xx} = k_x cos^2\theta + k_y sin^2\theta \quad (4\text{-}84)$$

$$k_{yy} = k_y cos^2\theta + k_x sin^2\theta \quad (4\text{-}85)$$

$$k_{xy} = k_{yx} = (k_x - k_y) sin\theta cos\theta \quad (4\text{-}86)$$

The rotation of the fourth-order elastic stiffness tensor in index notation is described by

$$\bar{E}_{ijkl} = R_{ip}R_{jq}E_{pqrs}R_{kr}R_{ls} \quad (4\text{-}87)$$

where E_{pqrs} is the elasticity tensor in a reference coordinate system, and $\bar{E}_{ijkl}$ is the rotated elasticity tensor. $R_{kr}R_{ls}$ is the transpose of $R_{ip}R_{jq}$ and $R_{ip}R_{jq}$ is defined as an orthogonal transformation matrix

$$\boldsymbol{T} = \begin{bmatrix} c^2 & s^2 & 2cs \\ s^2 & c^2 & -2cs \\ -cs & cs & c^2 - s^2 \end{bmatrix} \quad (4\text{-}88)$$

where $s = sin\theta$ and $c = cos\theta$, respectively. Then the rotated elastic stiffness tensor can be computed as

$$\bar{\boldsymbol{E}} = \boldsymbol{TET^T} \quad (4\text{-}89)$$

After the computation, I obtained the following full tensor permeability and elastic stiffness as

$$\boldsymbol{K} = \begin{bmatrix} 162.5 & 64.95 \\ 64.95 & 87.5 \end{bmatrix} \quad \text{(4-90)}$$

$$\boldsymbol{E} = \begin{bmatrix} 562.3 & 233.3 & -26.13 \\ 233.3 & 562.0 & 25.89 \\ -26.13 & 25.89 & 194.4 \end{bmatrix} \quad \text{(4-91)}$$

Fig. 4.21 compares the saturation and velocity solutions from the study using directional permeability and orthotropic elastic stiffness tensor (**Fig. 4.21 (a)**), and from the study using full tensor permeability and elastic stiffness (**Fig. 4.21 (b)**) at t = 23 days. The saturation and velocity distributions from the two models show significant differences. The x-direction permeability in Eq. 4-80 has four times higher value than the y-direction permeability, which results in a higher velocity along the x-direction. Consequently, the saturation is no longer the same at the same distance from the injection point, and has an elliptical shape instead of the circular shape in (**Fig. 4.21 (a)**). The full tensor permeability resulting from the 30-degree rotation of the directional permeability generated off diagonal terms in the permeability tensor, which induced a diagonally strong flow pattern. Therefore, the saturation distribution showed elongation along the diagonal connecting the injector and the producer, indicating enhanced migration of the injected water toward the producer. This indicates that the full tensor permeability model will have a faster breakthrough time.

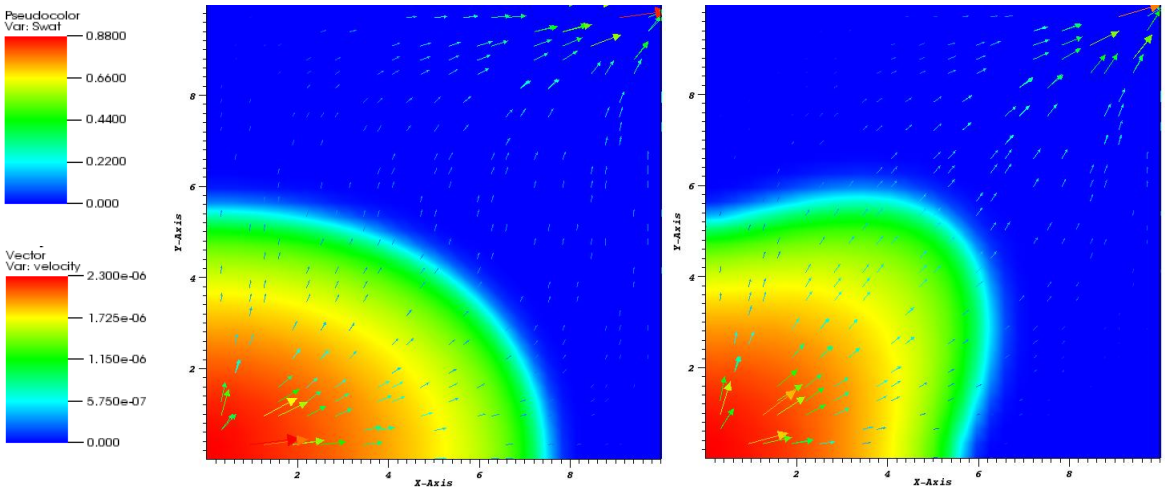

(a) **(b)**

Fig. 4.21—Saturation and velocity (m/s) solutions of (a) the directional permeability and orthotropic elastic stiffness model and (b) the full tensor permeability and elastic stiffness model at t = 23 days of simulation.

Fig. 4.22 shows a comparison of the pressure distributions obtained from the two models. Even though the injection and production rates of the two models are the same, their pressure gradients are different because their respective permeability tensors are different. The full-tensor permeability model results in a more diagonally-dominant flow pattern. With such a permeability tensor model, a lower pressure gradient (than that in the case of the directional permeability model) is needed to maintain the same production and injection rate.

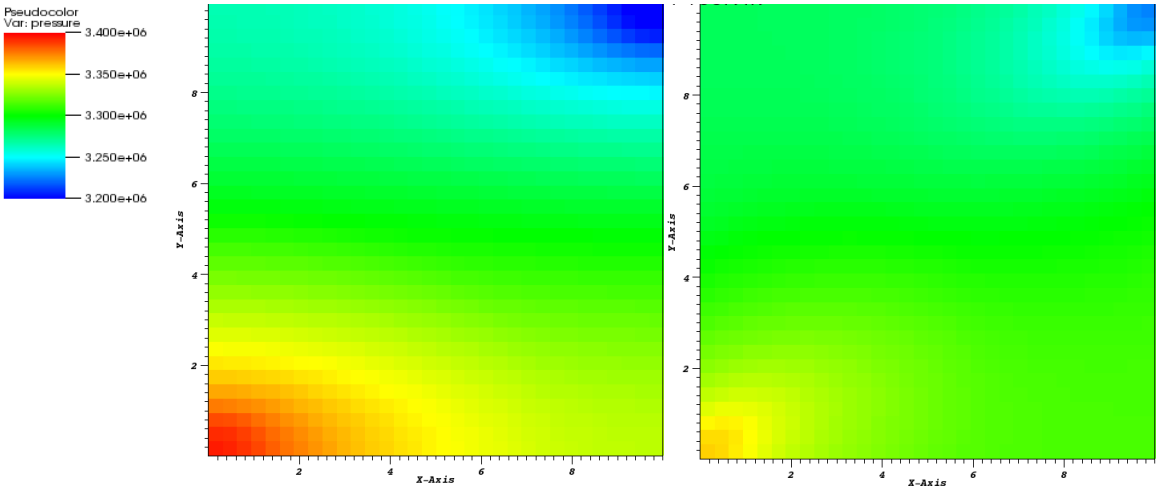

(a) **(b)**

Fig. 4.22—Pressure (Pa) distributions from (a) the directional permeability and orthotropic elastic stiffness model and (b) the full tensor permeability and elastic stiffness model at t = 23 days.

Because of the zero-displacement boundary condition in the geomechanics problem, deformation is only affected by the pressure gradient caused by poroelasticity. The directional permeability and orthotropic elastic stiffness model is associated with higher pressure differentials than the full-tensor model (**Fig. 4.22**). Consequently, larger x-direction (**Fig. 4.23**) and y-direction (**Fig. 4.24**) deformations are observed in the case of the directional permeability and orthotropic elastic stiffness model.

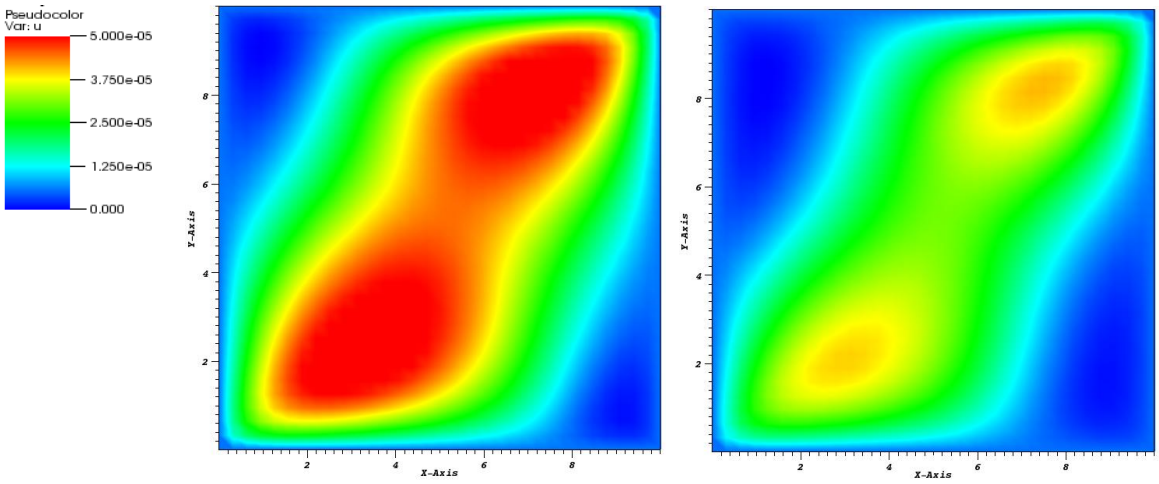

(a) **(b).**

Fig. 4.23—X-direction displacement solutions from (a) the directional permeability and orthotropic elastic stiffness model and (b) the full tensor permeability and elastic stiffness model at t = 23 days (displacement in m).

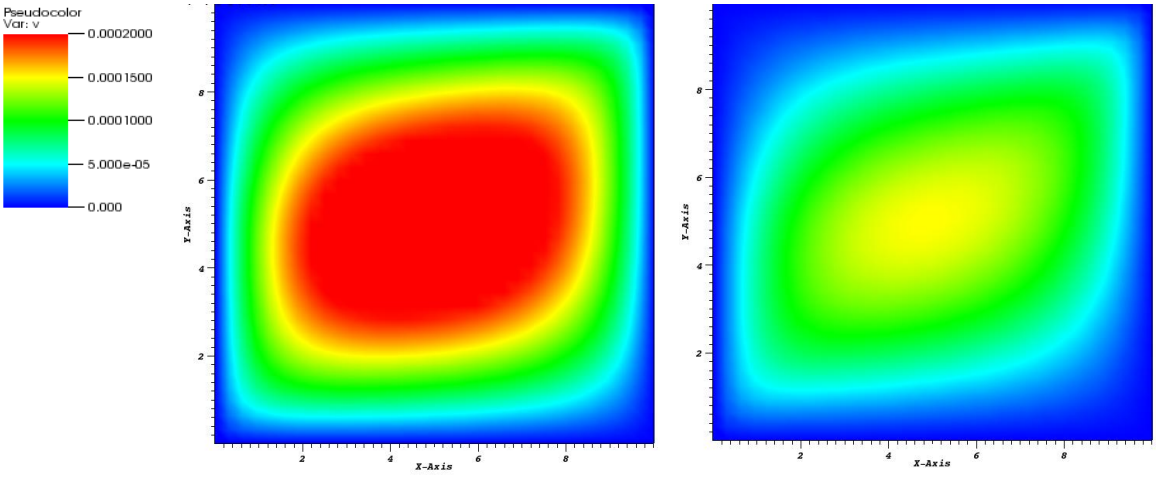

(a). **(b).**

Fig. 4.24—Y-direction displacement solutions from (a) the directional permeability and orthotropic elastic stiffness model and (b) the full tensor permeability and elastic stiffness model at t = 23 days (displacement in m).

4.3.6 Simulation of a Tight Gas System with a High-Permeability (High-k) Subdomain

I used the coupled multiphase flow (water and gas) and geomechanics simulator to model a tight gas reservoir system with a high-permeability (high-k) subdomain. The geomechanical impact on a fractured tight gas system is important because stress changes can significantly change the pore space of this high-k subdomain, thus affecting its permeability. **Fig. 4.25** shows a 2D simulation model with the high-k subdomain. The subdomain began at the middle point of the left edge, had a sinusoidal shape, and its tip reached to about half of the system width. A constant bottom hole pressure (B.H.P) constraint was assigned to the left end of the fracture with a value of 2.0 MPa, and a no flow boundary condition was assigned to the other boundaries. The traction vector imposed at the top boundary will tend to compress and consolidate the system as the reservoir depressurizes. A roller boundary condition was assigned to the sides and bottom boundaries, thus allowing only y-directional deformation (vertical deformation). I ignored gravitational and the capillarity effects. The initial reservoir pressure is 20.0 MPa (the same as the traction vector) and the initial water saturation is 0.2. The 2D model was discretized into 64 by 64 elements. **Table 4.2** shows the simulation input data.

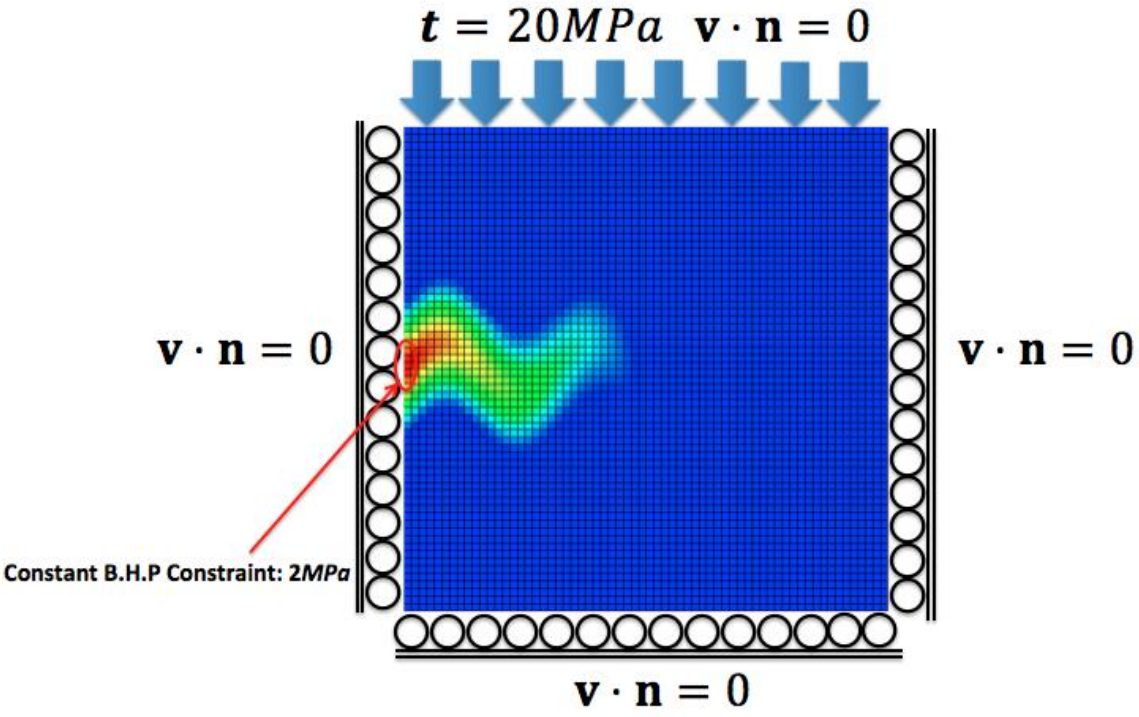

Fig. 4.25—The 2D domain used in the simulation of the problem of a tight gas system with a high-permeability subdomain.

Table 4.2—Simulation input data for tight gas system with a high permeabiilty subdomain	
Water Viscosity (cp)	1.0
Water Compressibility (Pa^{-1})	1.00E-09
Methane Viscosity (cp)	0.011
Initial Water Saturation	0.2
Biot's coefficient	1.0
Permeability function	Porosity dependent
Relative Perm. Curve	Quadratic
Poisson's Ratio	0.2
Reservoir Temperature (^oC)	30
Initial Reservoir Pressure (MPa)	20
Bottom Hole Pressure (MPa)	2

Fig. 4-26 shows the porosity and permeability fields of this problem. The values of porosity ranged from 0.1 to 0.7, and the permeability values ranged from 1 microdary (μd) to 90 microdarcy (μd). I used the directional permeability tensor (involving only the diagonal components of the permeability tensor) and assumed that the x-direction permeability is equal to the y-direction permeability ($k_x = k_y$). I used a simplified version of the micro-mechanics concept to model the mechanical behavior of the high-k subdomain. Using this approach (Grechka and Kachanov 2006a; 2006b; 2006c), I calculated the effective elasticity of the high-k subdomain as a function of porosity that can be expressed as

$$\boldsymbol{E} = \overline{\boldsymbol{E}} \left(\frac{1-\phi_{ini}}{\phi_{ini}}\right)^n \quad \text{(4-92)}$$

where $\boldsymbol{E}$ is the elastic stiffness tensor for the computation that is a function of porosity, $\overline{\boldsymbol{E}}$ is the reference elastic stiffness tensor, ϕ_{ini} is the initial porosity and n is a constant. I used a reference Young's modulus of 4.0 MPa and the constant n = 1.5. Thus, the highest Young's modulus is about 100 times higher than its lowest value (ranged from 11 MPa to 1.1 GPa).

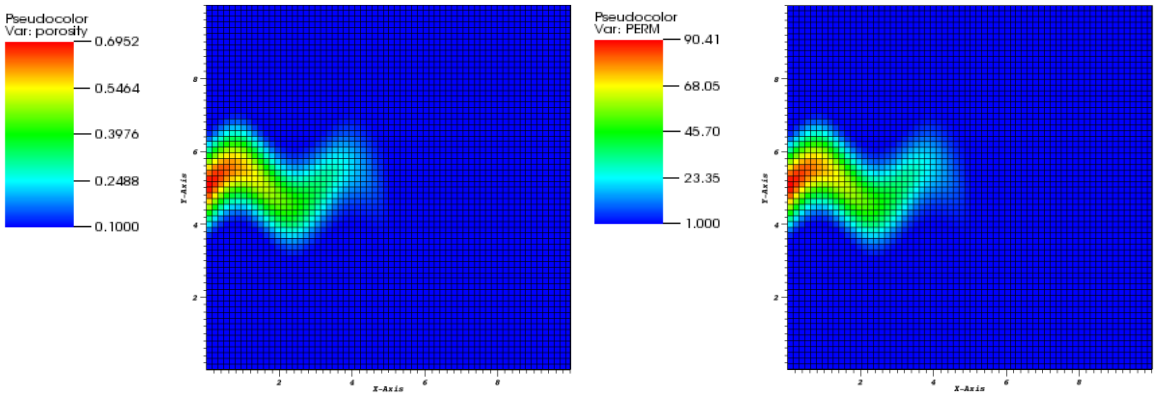

(a) (b)

Fig. 4.26— (a) Porosity field and (b) x-direction permeability field in the problem of Fig. 4.25. The y-direction permeability field is the same as that in the x-direction (permeability in μd).

Fig. 4.27 shows the pressure and saturation distributions after 4.6 hours of production. Initially, the maximum pressure of the system rose locally (mainly in the matrix) above the initial pressure (20 MPa) because of reservoir compaction caused by the pressure drawdown at the left end of the high-k subdomain (2 MPa). The water saturation near the left end of the subdomain became larger than in the rest of it because of compaction. Gas is significantly more compressible than water, so the volume of the gas decreased because of compaction but the volume of water did not decrease significantly as it is very slightly compressible. In addition, gas has a higher mobility than water, so the gas phase inside the high-k subdomain moved to the production point faster than the water. This also contributed to the water saturation increases in the subdomain.

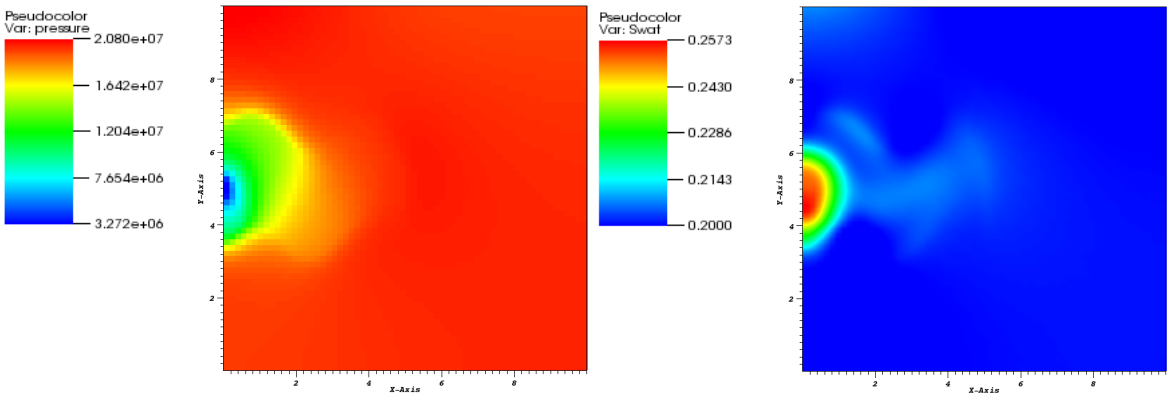

(a) (b)

Fig. 4.27—(a) Pressure and (b) saturation distributions after 4.6 hours of production in the problem of Fig. 4.25. The reservoir pressure rose locally above than the initial pressure (20 MPa).

Fig. 4.28 shows the x- and y-direction displacement solutions after 4.6 hours of production. Significant x- and y-direction compaction occurred near the left end of the high-k subdomain. The sudden pressure drawdown made a considerable contribution to the x-direction (negative) displacement. Along the y-direction, negative and positive displacements were observed. This is because the decrease in the pore pressure inside the subdomain increased the effective stress, which compressed the rock and decreased the loading in the area below the subdomain (unloading), which dilated the rock.

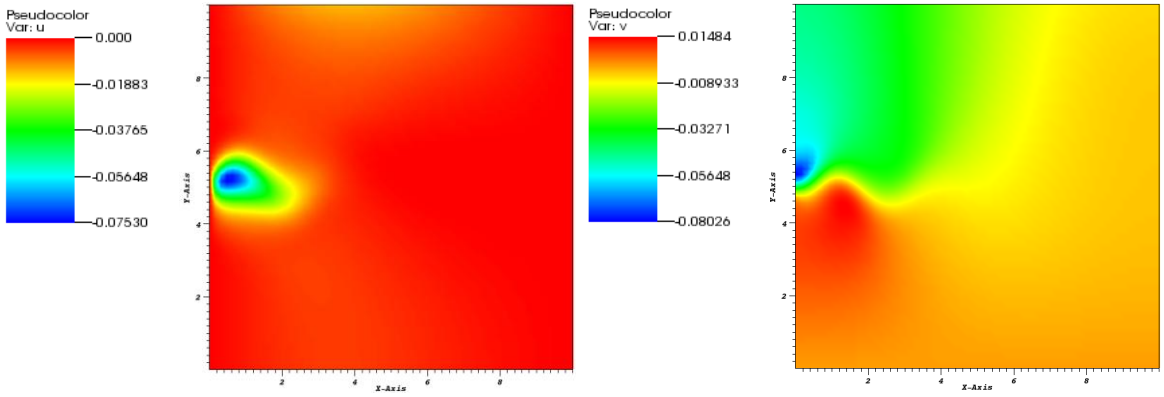

(a) (b)

Fig. 4.28—(a) X-direction displacement and (b) y-direction displacement solutions after 4.6 hours of production in the problem of Fig. 4.25. Both distributions indicate compaction inside the high-k subdomain because of the pressure drawdown (displacement in m).

After 12 days of production, the low pressure at the left end of the subdomain had propagated more than 2/3rds of the domain (**Fig. 4.29**). The shape of the pressure distribution was similar to the shape of the subdomain (sinusoidal). Due to the higher mobility of gas, its saturation decreased inside and near the subdomain. Conversely, the water saturation increased because gas is much more compressible than water. An interesting observation is the increase in water saturation near the upper left corner of the domain. This was the region where the vertical deformation was the highest. This caused the pore space in this area to decrease, which compressed both the gas and water. Because of the higher compressibility of the gas and its higher mobility (leading to increased gas migration from this area) the upper left area of the system exhibited higher water saturation.

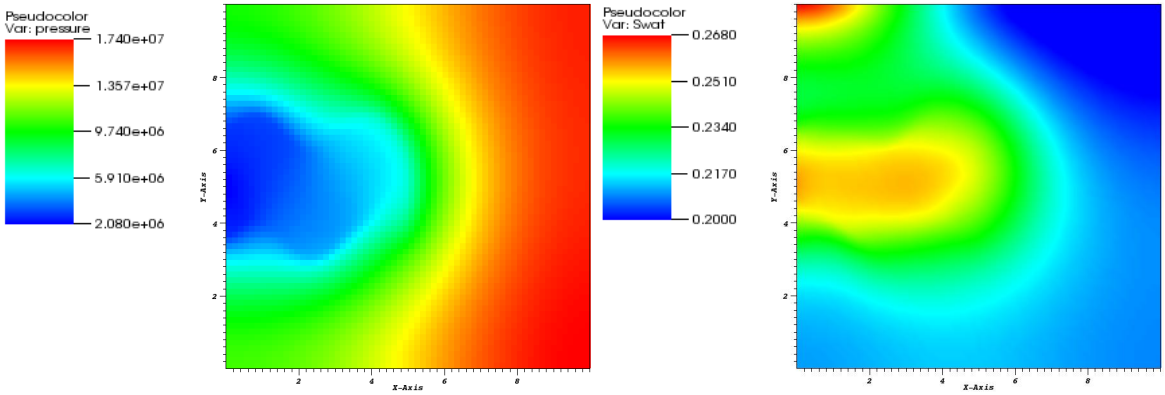

(a) **(b)**

Fig. 4.29—(a) Pressure and (b) water saturation distributions after 12 days of production in the problem of Fig. 4.25 (pressure in Pa).

Fig. 4.30 shows x- and y-direction displacements after 12 days of simulation. Because only vertical deformation (a roller boundary condition) had been allowed, the magnitude of the y-direction displacement was about 4 times higher than that in the x-direction. The nature of the roller boundary condition is such that the x-displacement on the sides of the domain was zero (maintaining the x-direction length constant). The x-direction displacement at the center of the top region is the highest because of the overburden stress and pressure gradient, which indicates compaction caused by pressure depletion and the overburden stress. The y-direction displacement describes the magnitude of the vertical deformation (**Fig. 4.30(b)**). Compression is seen to occur above the high-k subdomain, while dilation is observed below the subdomain. The highest compression occurred on the upper left part of the domain because of overburden stress and pressure depletion.

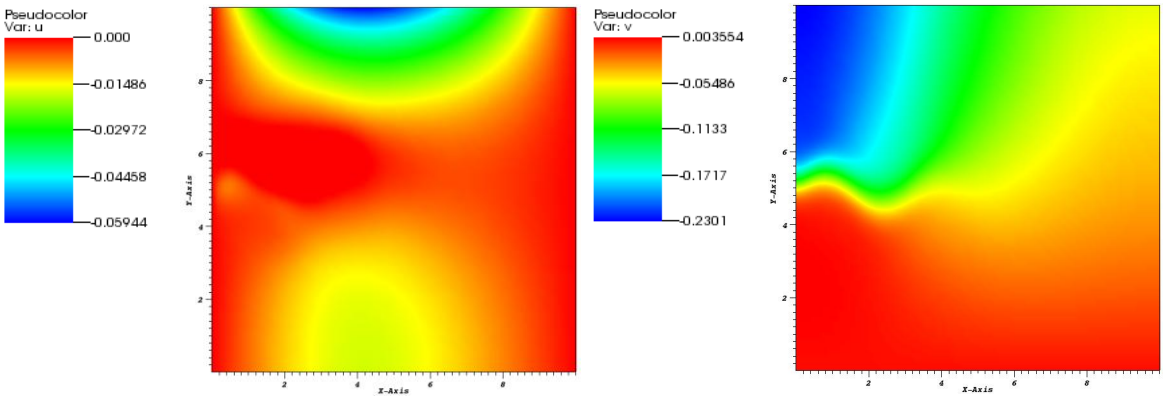

(a) (b)

Fig. 4.30—(a) X-direction displacement and (b) y-direction displacement solutions after 12 days of production in the problem of Fig. 4.25 (displacement in m).

Fig. 4.31 shows porosity reduction in the high-k subdomain with time. Initially (**Fig. 4.31(b)**), the region near the left end of the high-k subdomain experienced a significant porosity reduction (contour color changed from red to green). This was because the sudden pressure drop in that region caused a rapid decrease of the pore space, which was induced both by vertical compression caused by overburden stress also by x-direction compression, caused by the corresponding pressure gradient. These processes are evident in **Fig. 4.28**, which shows that the maximum absolute value (negative originally) of the x-direction displacement is very similar to the y-direction displacement. When the magnitude of the pressure gradient inside the high-k subdomain decreased (**Fig. 4.31(d)**), porosity at the left end of the subdomain recovered but remained substantially lower than its initial value. Remember the earlier observation from **Fig. 4.30** that the magnitude of the vertical displacement was about 4 times higher than the x-direction displacement. In general, porosity in the high-k subdomain declined due to the pressure depletion there. This was a very conservative approach, as mechanical deformation inside the subdomain could be substantially larger, leading to correspondingly larger porosity reduction and a potentially considerable effect on fluid flow regime.

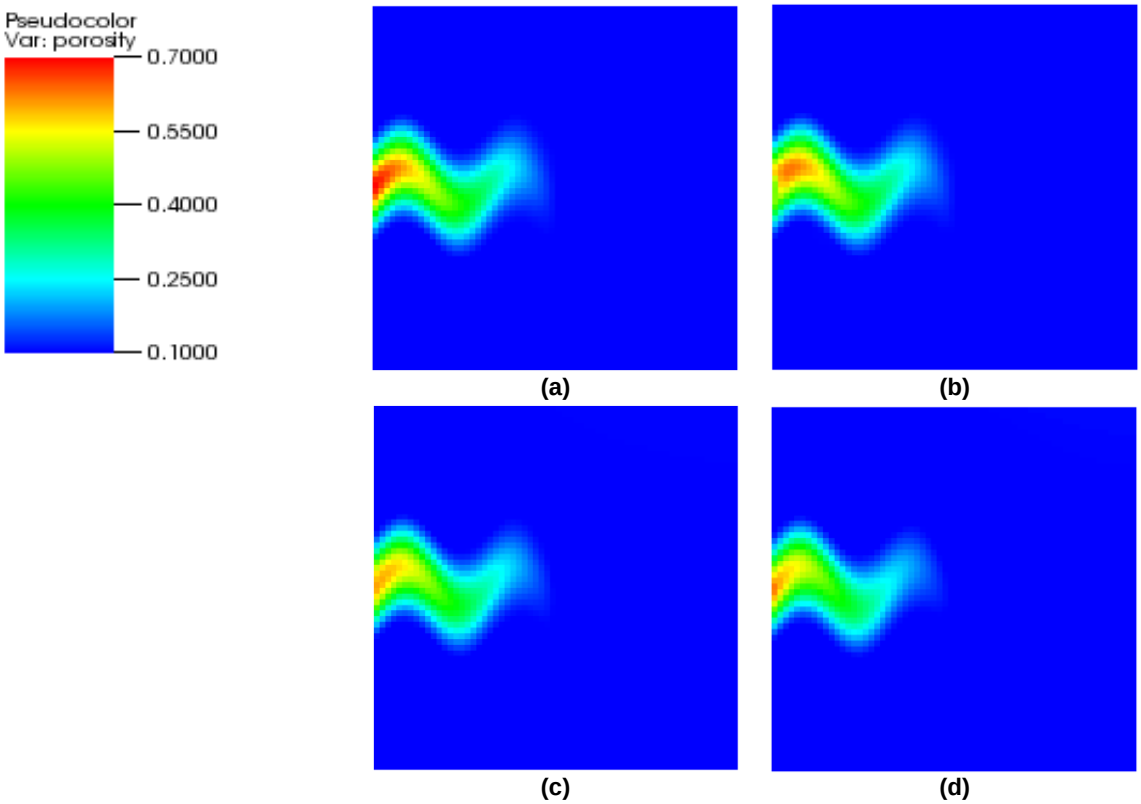

Fig. 4.31—Change in porosity at (a) 1 second, (b) 1.12 hours, (c) 1.5 day, and (d) 12 day shows that the values of porosity in the high-k subdomain decreased during production.

CHAPTER V

MODELING COUPLED MULTIPHASE FLOW AND GEOMECHANICS WITH UNSTRUCTURED GRID

5.1 Mapping (Transformation)

One of the most important benefits of using a finite element discretization is the ability to model a complex geometry with unstructured meshes. If we are to model a reservoir with a complex geometry, the simple (if not simplistic) shoe-box model is patently inadequate as it is very difficult for its geometry to conform to the limitations of a rectangular Cartesian grid. In a finite element discretization, each element can be mapped to a different shape and size, so that the grid can be either locally refined or coarsened. In 2D modeling, either triangular or quadrilateral elements are routinely used. In 3D modeling, tetrahedral or hexahedral elements are routinely used. **Fig. 5.1** shows an example that maps a reference triangle to an actual triangle with an arbitrary shape and vice versa.

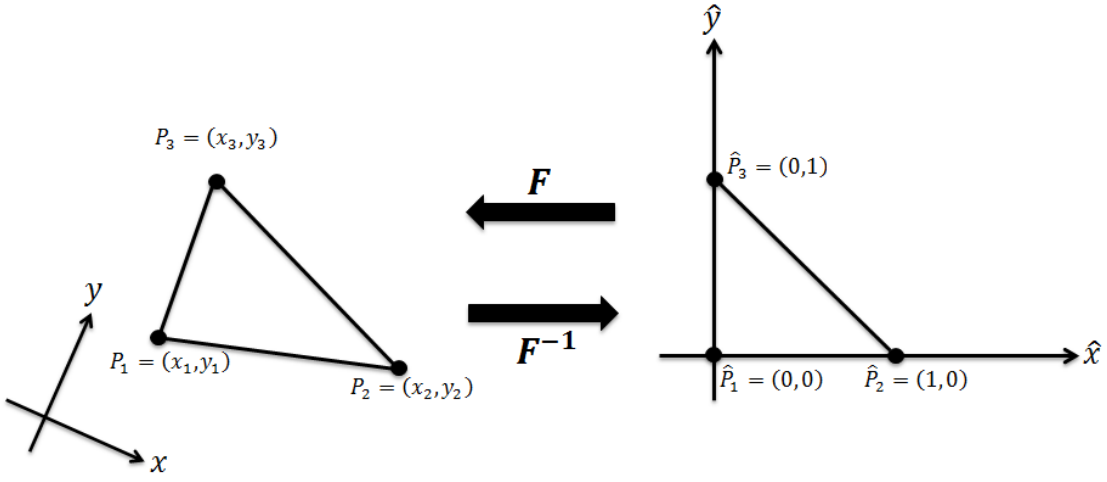

Fig. 5.1—Mapping of a triangular element. The reference triangle can be transformed to an actual triangle with an arbitrary shape and vice versa.

The following transformation can be defined from the actual triangle shown on the left of **Fig. 5.1**

$$\begin{cases} a_1 = y_2 - y_3 \\ a_2 = y_3 - y_1 \\ a_3 = y_1 - y_2 \\ b_1 = x_3 - x_2 \\ b_2 = x_1 - x_3 \\ b_3 = x_2 - x_1 \end{cases} \quad (5\text{-}1)$$

where $a_1 + a_2 + a_3 = 0$ and $b_1 + b_2 + b_3 = 0$.

Then the transformation of any arbitrary point in the reference triangle to the actual triangle is defined as

$$\boldsymbol{F}: \begin{bmatrix} x \\ y \end{bmatrix} = \begin{bmatrix} x_1 \\ y_1 \end{bmatrix} + \begin{bmatrix} x_2 - x_1 & x_3 - x_1 \\ y_2 - y_1 & y_3 - y_1 \end{bmatrix} \begin{bmatrix} \hat{x} \\ \hat{y} \end{bmatrix} \quad (5\text{-}2)$$

Eq. 5-2 can be also rewritten as

$$\begin{bmatrix} x \\ y \end{bmatrix} = \begin{bmatrix} x_1 \\ y_1 \end{bmatrix} + J \begin{bmatrix} \hat{x} \\ \hat{y} \end{bmatrix} \quad (5\text{-}3)$$

where $J = \begin{bmatrix} b_3 & -b_2 \\ -a_3 & a_2 \end{bmatrix}$.

In general form, the mapping of a 2D finite element is

$$x = \sum_i N_i(\hat{x}, \hat{y}) x_i \quad (5\text{-}4)$$

$$y = \sum_i N_i(\hat{x}, \hat{y}) y_i \quad (5\text{-}5)$$

where N_i for a triangular element is

$$N_1 = 1 - \hat{x} - \hat{y} \quad (5\text{-}6)$$

$$N_2 = \hat{x} \quad (5\text{-}7)$$

$$N_3 = \hat{y} \quad (5\text{-}8)$$

and for a quadrilateral element is

$$N_1 = \frac{1}{4}(1 - \hat{x})(1 - \hat{y}) \quad (5\text{-}9)$$

$$N_2 = \frac{1}{4}(1 + \hat{x})(1 - \hat{y}) \quad (5\text{-}10)$$

$$N_3 = \frac{1}{4}(1 + \hat{x})(1 + \hat{y}) \quad (5\text{-}11)$$

$$N_4 = \frac{1}{4}(1 - \hat{x})(1 + \hat{y}) \quad \text{(5-12)}$$

Applying the rules a change of variables in multiple integrals, I obtain

$$\int_{\tau} u(x,y)d\tau = \int_{\hat{\tau}} |det(J)| \hat{u}(\hat{x},\hat{y})d\hat{\tau} \quad \text{(5-13)}$$

where $|det(J)|$ is the determinant of matrix *J*, termed the Jacobian. Eq. 5-13 states that an integration of a function in an actual element can be obtained from a reference element using the Jacobian. Therefore, any shape functions that are integrated over the domain in a finite element formulation can use the reference element and map it into the actual element. A simple example is the stiffness matrix in Laplace's equation written as

$$\int_{\tau} \nabla\varphi_i \cdot \nabla\varphi_j d\tau = |det(J)| \int_{\hat{\tau}} (J^{-T}\nabla\hat{\varphi}_i) \cdot \left(J^{-T}\nabla\hat{\varphi}_j\right) d\hat{\tau} \quad \text{(5-14)}$$

where φ_i is the element shape function on the actual element and $\hat{\varphi}_i$ is the element shape function on the reference element.

Fig. 5.2 shows 2D meshes discretized using triangular and quadrilateral elements, respectively. Using elements of different shapes, a reservoir with irregular geometry can be effectively discretized. Additionally, areas where higher resolutions are needed, e.g., in the vicinity of wells, can be easily discretized into locally finer grids.

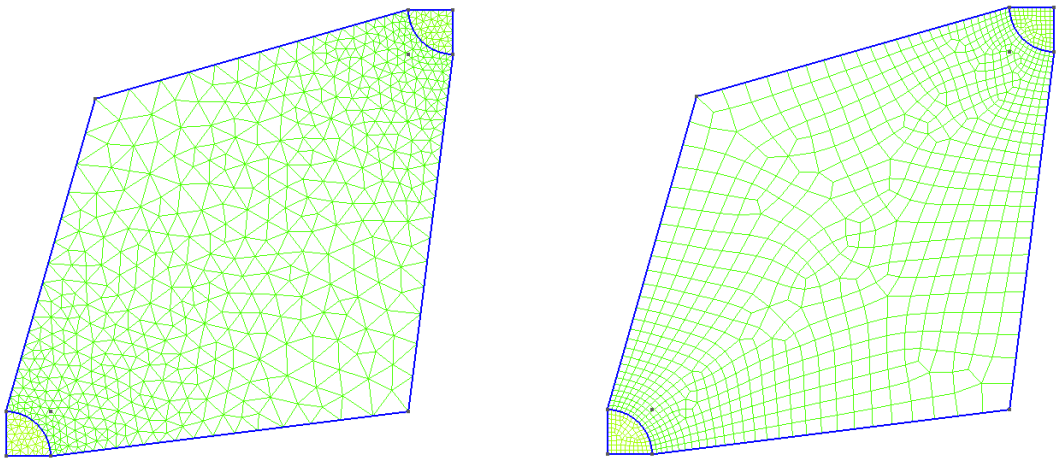

(a) **(b)**

Fig. 5.2—2D reservoir domains discretized using (a) triangular elements and (b) a quadrilateral element, with local grid refinement in the vicinity of the wells.

5.2 Waterflooding Simulation

I repeated the earlier waterflooding simulation, using an unstructured mesh this time. I used the Gmsh package (Geuzaine and Remacle, 2009) to generate an unstructured quadrilateral mesh. A detailed procedure to generate unstructured meshes with Gmsh is discussed in **Appendix B**.

Fig. 5.3 shows the 2D domain discretized using unstructured elements. The injection and production areas are locally refined. I compared the simulation results from this unstructured mesh (672 elements) to those from using a structured mesh discretized into 32×32 elements. The location of the quadrature points for an unstructured mesh is different from that in the structured mesh. In order to match the injection and production rates of both the unstructured and structured meshes, I made the areas of injection and production wells in the unstructured mesh the same as in the structured mesh. I used a well element size of $0.625m \times 0.625m$ because each grid block size in the structured mesh is $0.3125m \times 0.3125m$. This size is about 40% of the previous waterflooding experiment ($1m \times 1m$) in Section 4.3.3. Computation time (CPU time) for one month of simulation is 124.13 seconds with the unstructured mesh and 190.98 second with the structured mesh. The fewer cells of the unstructured grid lead to a reduction of the execution time to only 65% of that for the structured grid.

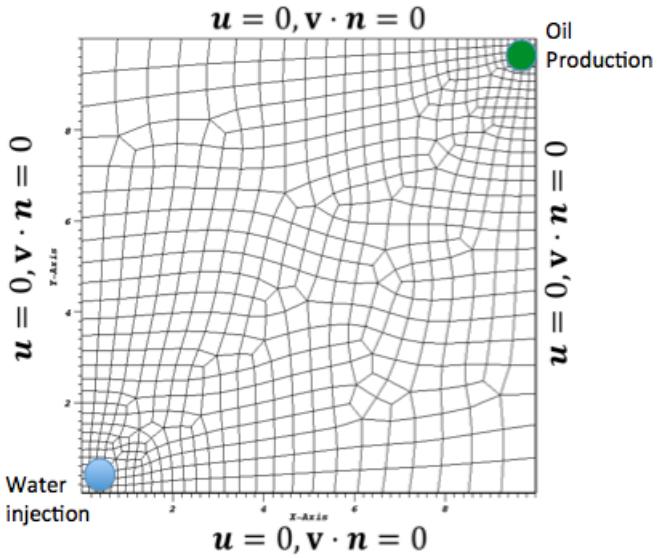

Fig. 5.3—A 2D waterfloording grid with 672 unstructured elements. The injection and the production areas are locally refined.

Fig. 5.4 compares the saturation and velocity solutions obtained from the simulation using the unstructured mesh (**Fig. 5.4 (a)**) and the one with the structured mesh (**Fig. 5.4 (b)**). The solutions of the two models are in very good agreement. The locally refined unstructured mesh shows a higher resolution of the velocity vectors near the wells. Such a local refinement improves the accuracy of a numerical solution because the gradients of the primary variables are usually large near a well.

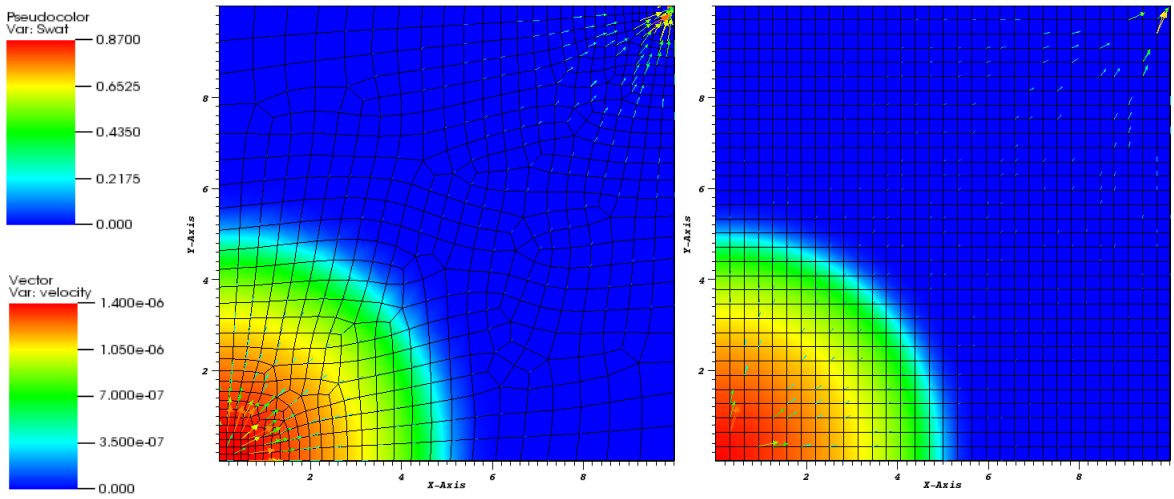

Fig. 5.4—Comparison of the saturation and velocity (m/s) solutions from (a) the unstructured and (b) the structured meshes. Note the higher resolution of velocity vectors near the wells, a result of the local refinement of the grid.

A comparison of the pressure (**Fig. 5.5**) and displacement (**Fig. 5.6** and **Fig. 5.7**) solutions indicated that the solutions of the two models matched very well. The obvious conclusion is that using an unstructured mesh allows a more efficient computation than using a structured grid because the same definition/accuracy can be attained using a significantly smaller number of cells. In addition, unstructured grids allow the easy local refinement of areas that need a higher accuracy of the numerical solution (*e.g.*, near wells or fractures). Note that in this example I used a domain that could be easily discretized using both a structured and an unstructured grid. The advantages of unstructured grids are far more evident in cases of complex system geometry that defy the capabilities of structured grids unless a practically impossibly large number of cells are used.

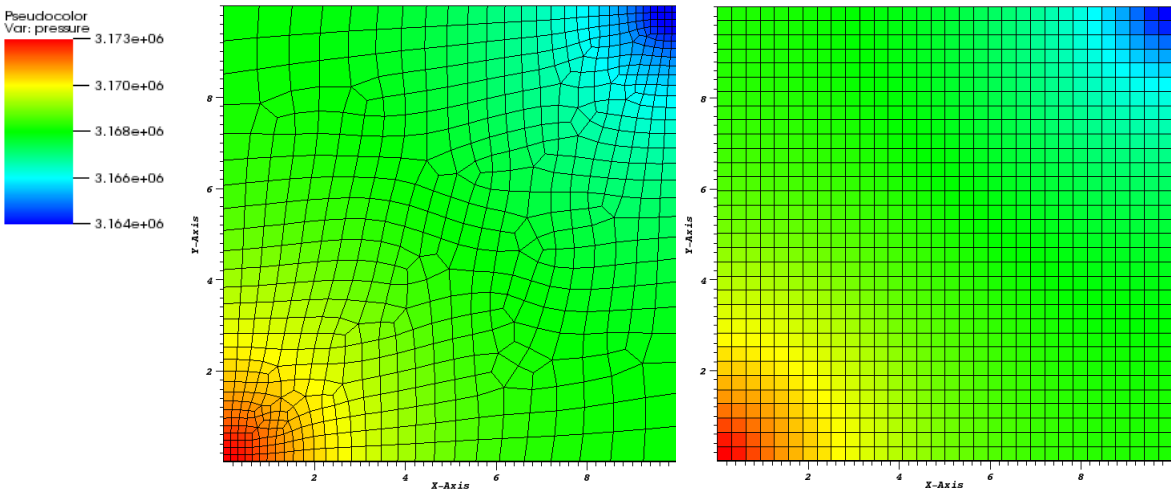

Fig. 5.5—Pressure solutions using (a) the unstructured and (b) the structured mesh are in very good agreement (pressure in Pa).

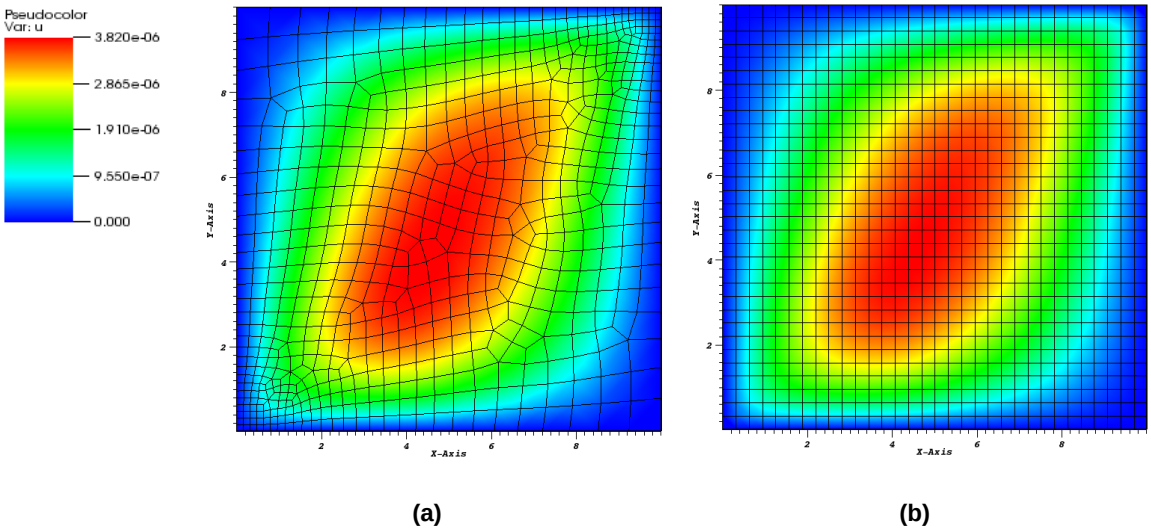

Fig. 5.6—X-direction displacement solutions using (a) the unstructured and (b) the structured mesh are in very good agreement (displacement in m).

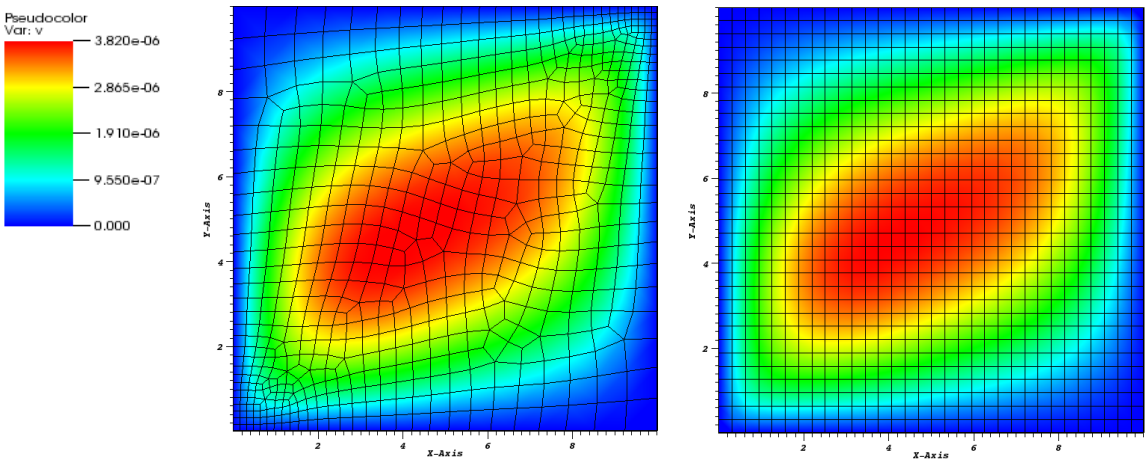

(a) (b)

Fig. 5.7—Y-direction displacement solution using (a) the unstructured and (b) the structured mesh are in very good agreement (displacement in m).

5.3 High-Permeability Subdomain Model in a Tight Gas System

I reproduced the previous simulations involving a high-k subdomain (see Section 4.3.6) using an unstructured mesh. **Fig. 5.8(a)** and **5.8(b)** show the corresponding porosity distributions obtained from the simulations using the unstructured and the structured mesh, respectively. In the unstructured mesh, I locally refined the areas inside and near the high-k subdomain to obtain a high resolution of the numerical solution in that area. I used only 2042 elements to generate the unstructured mesh, which is about half the number for the structured mesh (4096). The computation time (CPU time) to simulate a production period of 12 days was only 484.45 seconds for the unstructured mesh, as compared to 861.75 seconds for the structured mesh. Thus, as the subsequent results show, practically the same results are obtained from an unstructured grid with only half the elements. The fewer cells lead to a reduction of the execution time to only 56% of that for the structured grid.

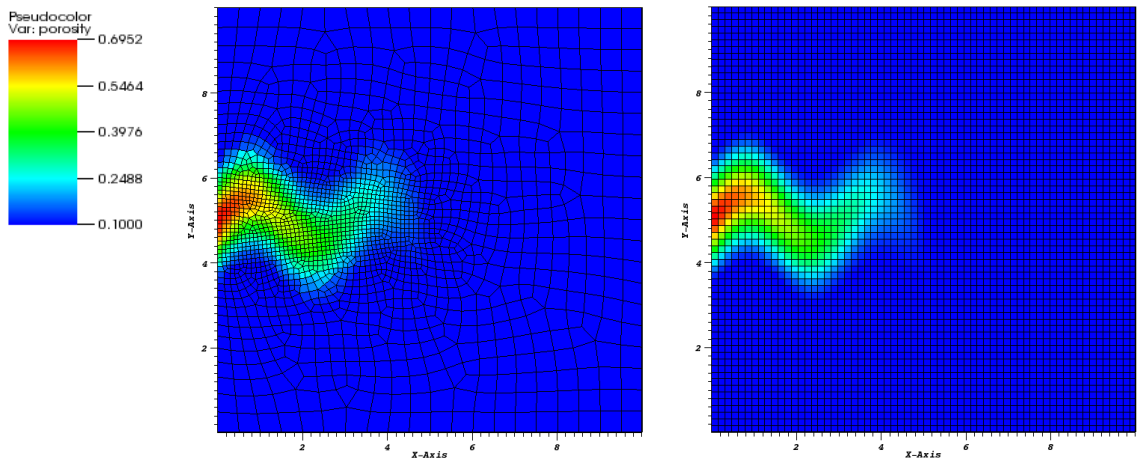

Fig. 5.8—Comparison of the porosity distributions in the high-k subdomain problem obtained using (a) the unstructured and (b) the structured mesh.

Fig. 5.9(a) and **Fig. 5.9(b)** show a comparison of the pressure solutions at t = 4.6 hrs obtained with the unstructured and the structured mesh, respectively. The two solutions are in very good agreement. Similarly, the saturation solutions (**Fig. 5.10**) match well. The unstructured mesh provides solutions of higher resolution (because of locally finer discretization) near the production area (B.H.P constraint area) than the structured mesh.

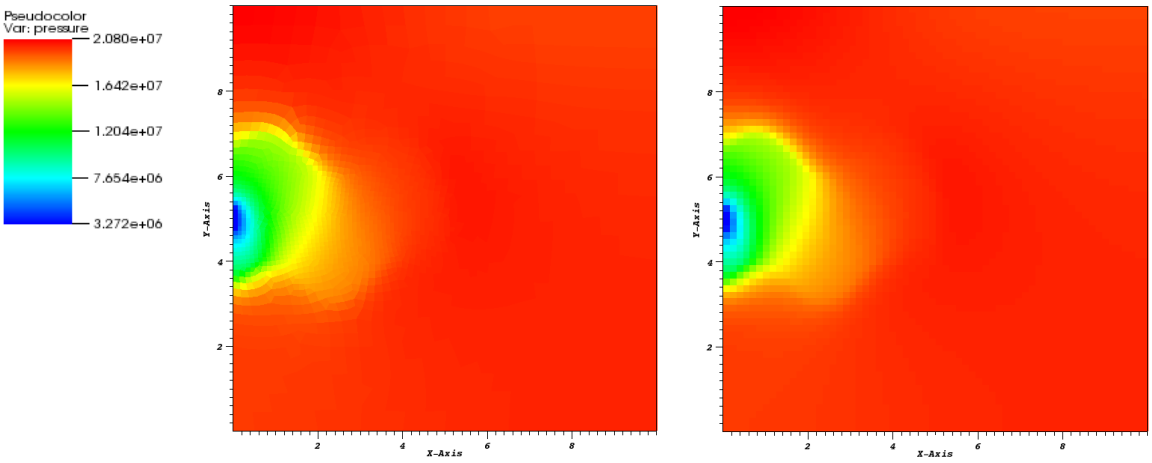

(a) **(b)**

Fig. 5.9—The pressure solutions obtained with (a) the unstructured and (b) the structured meshes match well (t = 4.6 hours of simulation; pressure in Pa).

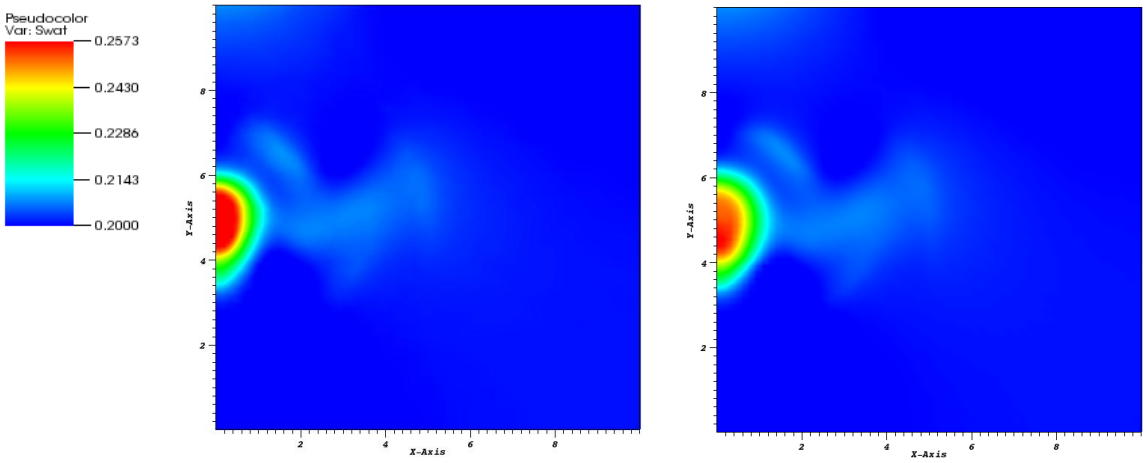

(a) **(b)**

Fig. 5.10—The saturation solutions obtained with (a) the unstructured and (b) the structured meshes match well.

Fig. 5.11 compares the y-direction displacement solutions at the same time. The solutions using the unstructured and the structured mesh are in good agreement.

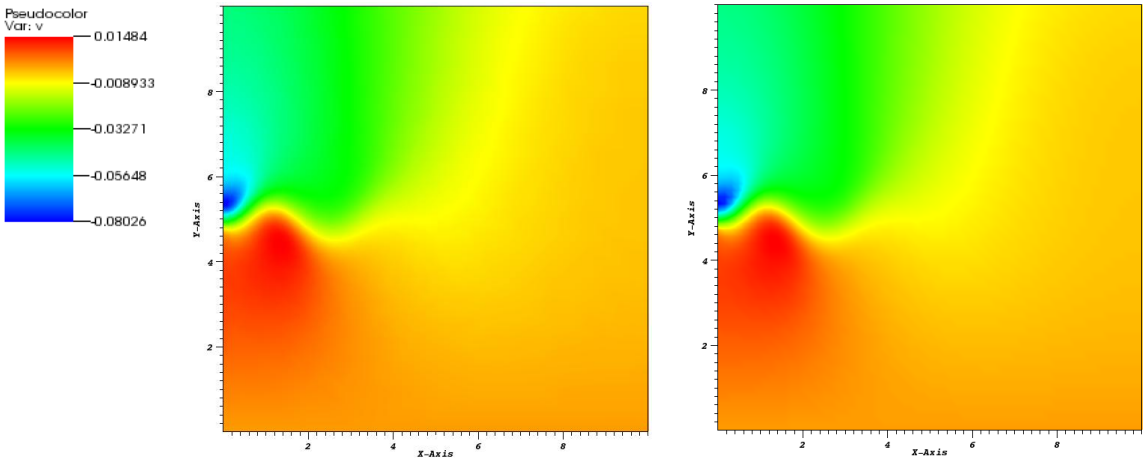

Fig. 5.11—The Y-direction displacement solutions obtained with (a) the unstructured and (b) the structured meshes are in very good agreement.

As discussed earlier, in this problem the pressure front advances to almost 2/3 of the domain (**Fig. 5.12**) at t = 12 days. Being in agreement, both meshes captured the pressure propagation in the domain well. Likewise, the saturation solutions (**Fig. 5.13**) and the y-direction displacement solutions (**Fig. 5.14**) of the two models are in good agreement. This comparison indicates the advantages of using unstructured meshes when modeling complex geometric features and/or subdomains with very different properties (e.g., fractures). By using unstructured meshes, one can obtain a good estimate of coupled multiphase flow and geomechanical behavior in such features with a reasonable computational cost.

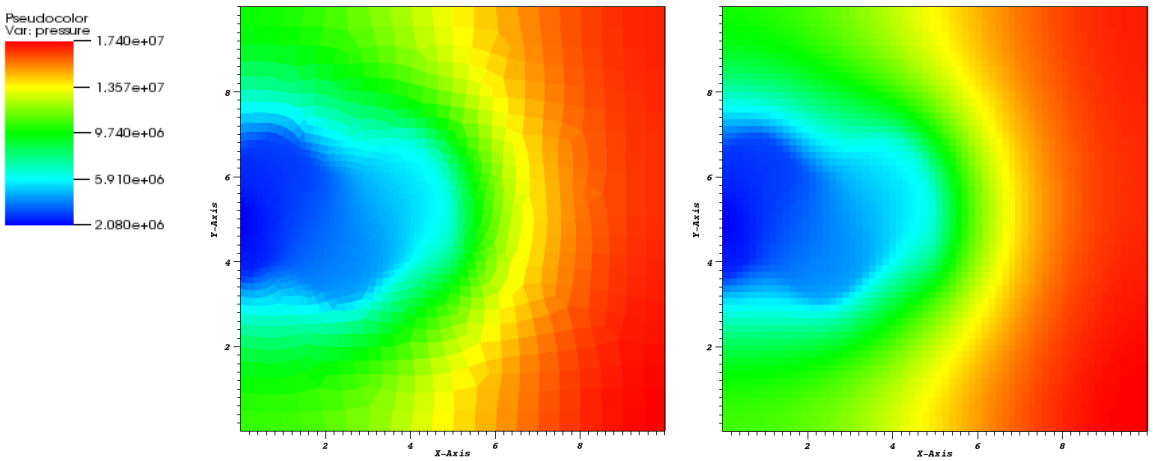

(a) (b)

Fig. 5.12—The pressure solutions from (a) the unstructured and (b) the structured meshes are in good agreement (t = 12 days; pressure in Pa).

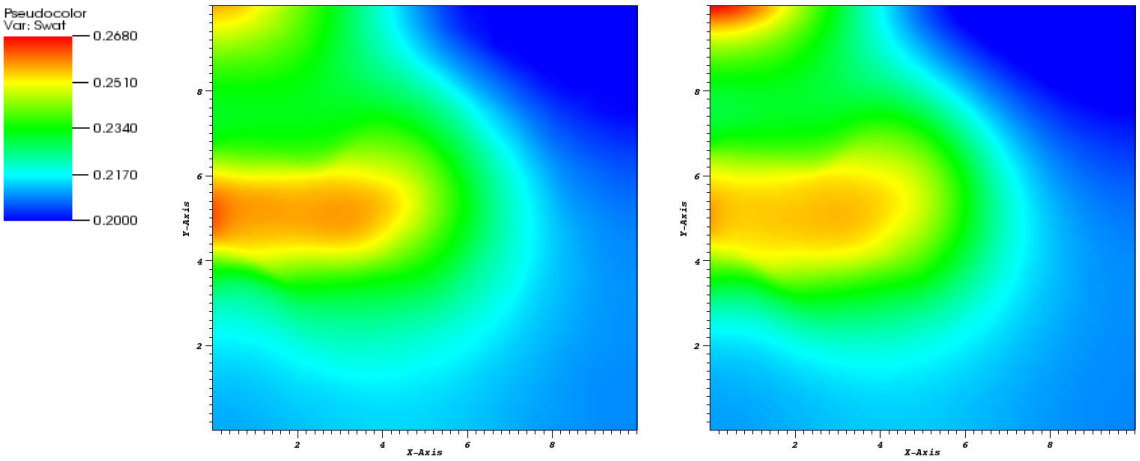

(a) (b)

Fig. 5.13—The saturation solutions from (a) the unstructured and (b) the structured meshes match well.

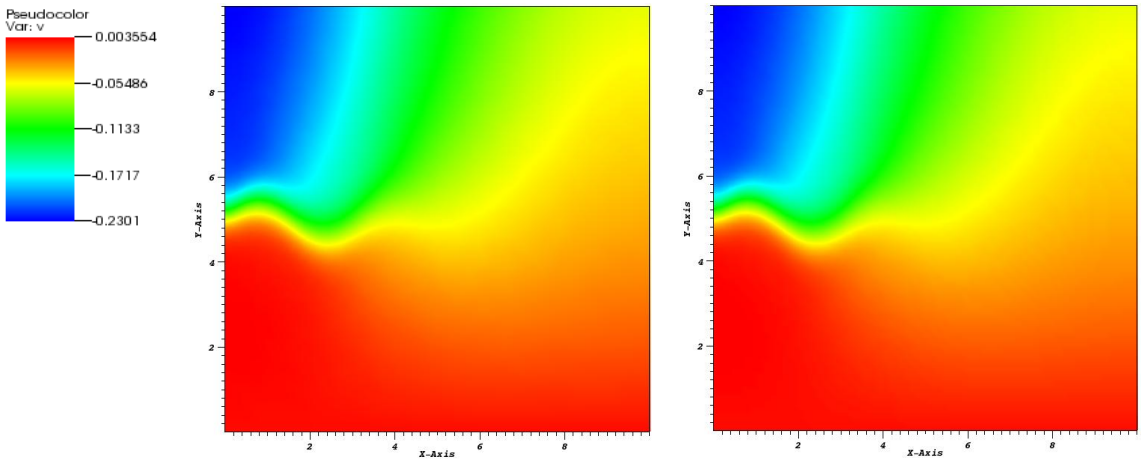

Fig. 5.14—Y-direction displacement solutions from (a) the unstructured and (b) the structured meshes are in very good agreement (t = 12 days; displacement in m).

5.4 Single Discrete Fracture Model

I modeled a single discrete fracture system with an unstructured mesh. Generating a discrete fracture model with a rectangular Cartesian grid system is very challenging because a very fine discretization is required inside and near the discrete fracture, especially when the fracture is at an angle to the sides of the domain. Unstructured meshes are essential when modeling such a discrete fracture system.

Fig. 5.15 shows the discretized 2D domain with a single discrete fracture that I studied in this problem. The unstructured mesh allowed easy local refinement within and near the fracture. A constant B.H.P constraint was assigned to the area located in the middle of the left boundary, at which pressure was kept constant at 2 MPa, and a no flow boundary was assigned to the rest of the boundaries of the domain. A traction vector was assigned to the top boundary with a constant value $\boldsymbol{t}$ = 20 MPa. The roller boundary condition allows vertical deformation of the system, and can be expected to lead to consolidation along the vertical direction as the system depressurizes in response to production. In this simulation I ignored gravitational and capillarity effects, and I used the initial conditions (pressure and water saturation) and gas and water properties listed in **Table 4.2**.

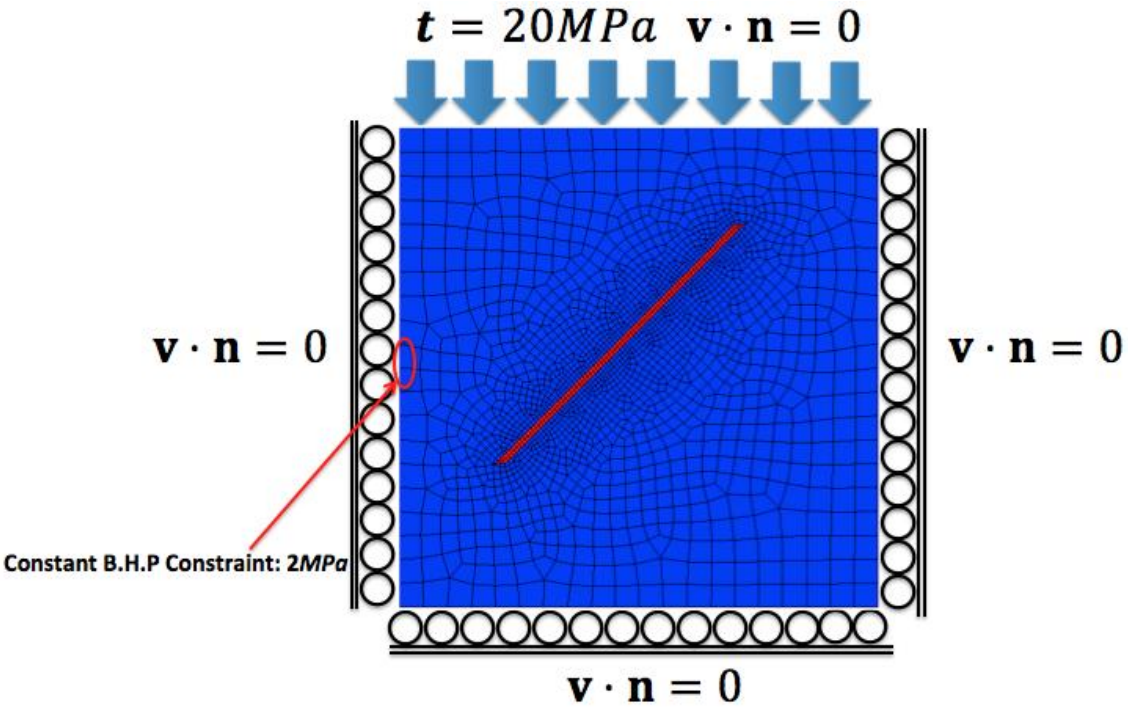

Fig. 5.15—The discretized 2D domain with a single discrete fracture used in the study of flow in a domain with a single discrete fracture at an angle to the domain sides. The unstructured grid allows easy local grid refinement within and near the fracture, and conforms to the challenging geometry without difficulty.

To investigate the effect of geomechanical properties of the rock on the system response during production, I ran simulations of discrete fracture model using two sets of mechanical properties, namely, hard and soft fracture properties. The soft fracture has substantially lower values of Young's moduli than the hard fracture. I used Eq. 4-92 to generate the Young's moduli for both the hard fracture and the soft fracture systems. The reference values for the Young's moduli were 40 MPa and 10 MPa for the hard and the soft fracture systems, respectively. I monitored the porosity change at three locations on the fracture (top tip, middle, and bottom tip).

5.3.1 The Hard Fracture System

The porosity and permeability of the intact rock were 0.1 and 1 microdarcy (μd), respectively; in the fracture, they were 0.5 and 100 μd. The value of the exponent in Eq. 4-92 was 1.5. The Young's moduli of the intact rock and of the fracture were 1.08 GPa and 40 MPa, respectively. **Fig. 5.16** shows the pressure and fluid velocity solutions at t = 29 days (**Fig. 5.16 (a)**) and t = 70 days (**Fig. 5.16 (b)**). The velocity is very high along the discrete fracture because the permeability in the fracture was drastically higher than in the intact rock. Once the flow reached the bottom tip of the fracture, it changed its direction and moved to-

ward the constant bottom hole pressure (B.H.P) boundary. The velocities are higher in **Fig. 5.16 (a)** because of a steeper pressure gradient from the fracture to the production point.

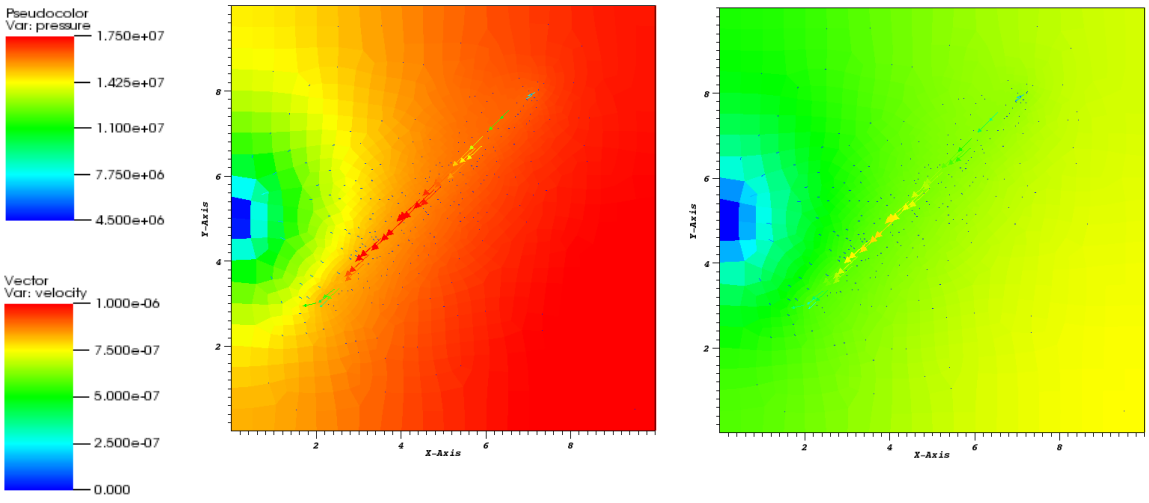

Fig. 5.16—Hard fracture case: pressure and velocity distributions at (a) t = 29 days and (b) t = 70 days in the problem of Fig. 5.15. Note the higher velocities at the earlier time.

Fig. 5.17 compares the water saturation solutions at the same two times as the pressures. The water saturation became higher inside the fracture and near the production area. As mentioned previously (Section 4.3.6), more gas than water moved toward the production area because of its higher mobility. In addition, the rock was deformed by the increase in effective stress, which caused a reduction of the pore space and the consequent compression of the fluids. Gas is more compressible than water so the gas saturation was declined relative to that of water. Water in the fracture is more difficult to remove because of the large permeability difference between the fracture and the intact rock. This indicates that a higher pressure gradient is needed for water to move from the fracture to the low permeability region. As pore pressure decreased, the reservoir began to be compressed by the overburden stress. The magnitude of the compression was at its highest near the upper left corner of the domain, which increased the water saturation in the region. After 70 days, the water saturation near the production area and the fracture was higher than that at day 29. Note that water saturation in the entire domain rose above the initial water saturation. This was because the entire system was compacted by the higher effective stress and the cumulative gas production was considerably larger than the water production, thus leaving more water behind.

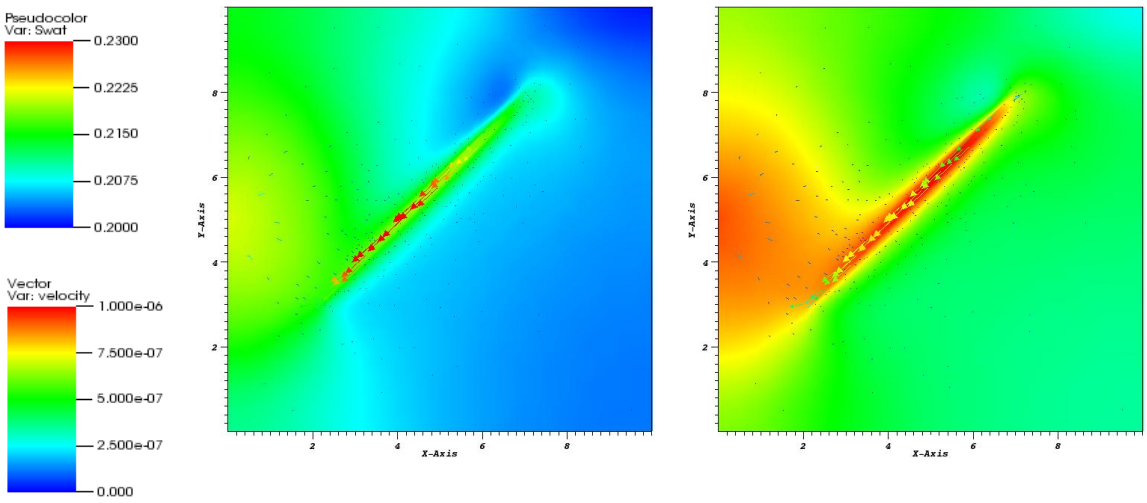

Fig. 5.17—Hard fracture case: water saturation and velocity distributions at (a) t = 29 days and (b) t = 70 days in the problem of Fig. 5.15.

Fig. 5.18 shows the y-direction displacement solutions at = 29 days and t = 70 days of simulation. There is a discontinuity in the displacement solution due to the discrete fracture (a big transition of the displacement field after the discrete fracture). The y-direction displacement is practically uniform along the fracture. This is because the y-direction deformation is largest inside the fracture because of its Young's modulus that is significantly lower than that of the intact rock. The upper left region shows the highest compression because the maximum pressure depletion occurred in the middle of the left boundary (a constant B.H.P boundary).

Fig. 5.19 shows the porosity distribution in the fracture at t = 29 days and t = 70 days. The porosity inside the fracture decreased as the system depressurized. The largest porosity reduction occurs at the mid-point of the fracture. The fracture tips show relatively lower porosity reduction. This is because the fracture tips are surrounded by intact rock with a much larger Young's modulus. The high strength of the intact rock allowed only limited deformation, so it was difficult for the fracture tips to deform under the given stress condition.

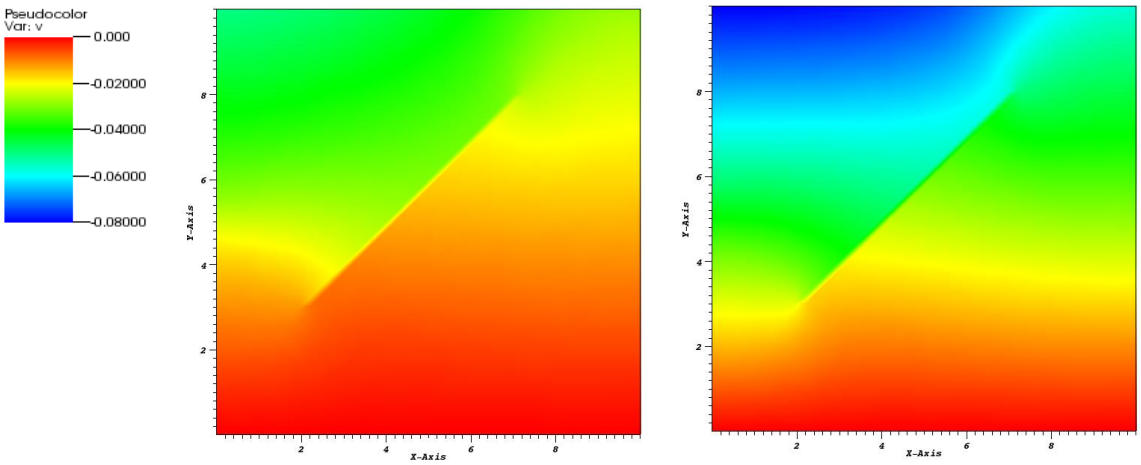

Fig. 5.18—Hard fracture case: Y-direction displacement (m) solutions at (a) t = 29 days and (b) t = 70 days. The discontinuity of the displacement is due to the discrete fracture.

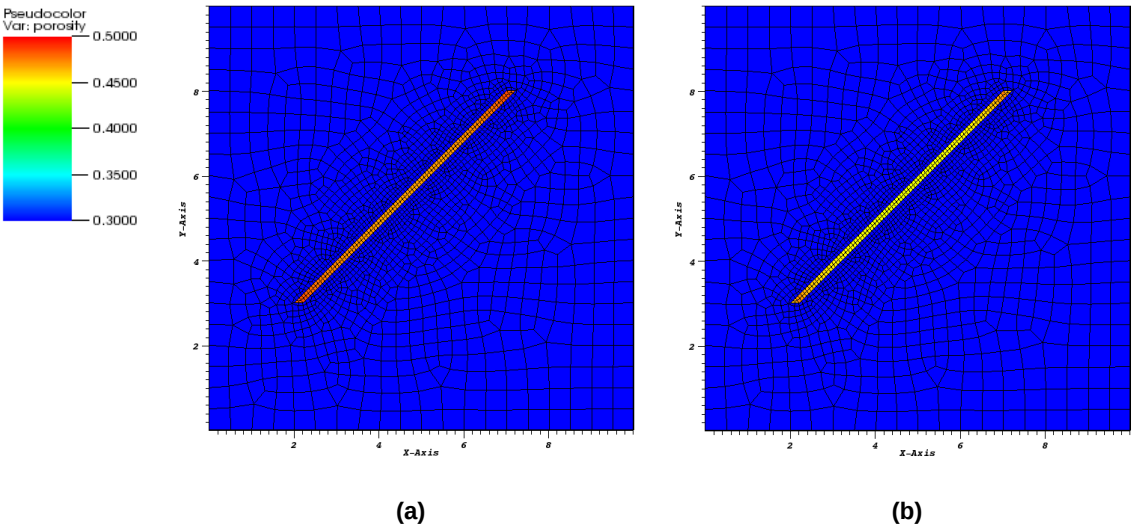

Fig. 5.19—Hard fracture case: porosity distributions in the fracture at (a) t = 29 days and (b) t = 70 days of simulation. For better visualization, the minimum porosity inside the fracture is set to 0.3.

I also investigated the porosity change of the intact rock outside of the fracture. Its initial porosity was 0.1, and it decreased as the system depressurized. **Fig. 5.20** shows the porosity distributions at t= 29 days and t = 70 days. For better visualization, the minimum porosity in the intact rock was set at 0.1. The largest porosity reduction (by 20%) occurred right next to the tips of the fracture at t = 70 days. This was because

the maximum stress occurred near the tips of the fracture. In classical fracture mechanics, the maximum stress in an elliptical hole, which is perpendicular to the applied stress, is defined as

$$\sigma_m = 2\sigma_o\sqrt{\frac{a}{\rho_t}} \quad \text{(5-15)}$$

where σ_o, a, and ρ_t are the applied stress (Pa), the hole half length (m), and the radius of curvature (m), respectively. If the radius of curvature becomes zero, then the maximum stress becomes infinity. The stress concentration factor K_t is the ratio of the maximum stress to the applied stress, and is described as

$$K_t = \frac{\sigma_m}{\sigma_o} = 2\sqrt{\frac{a}{\rho_t}} \quad \text{(5-16)}$$

If the maximum stress at the tip of a fracture becomes higher than the yield strength of the intact rock, then the rock undergoes plastic deformation, which is larger than elastic deformation. Rock failure will follow plastic deformation once a critical stress is reached.

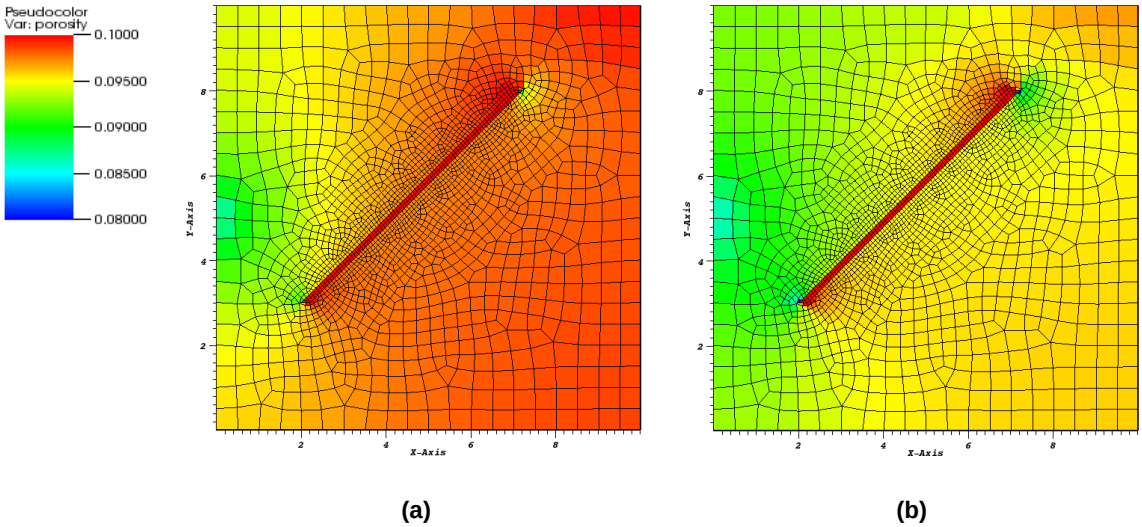

(a) **(b)**

Fig. 5.20—Hard fracture case: porosity distributions in the intact rock at (a) t = 29 days and (b) t = 70 days of simulation in the problem of Fig. 5.15. The largest porosity reduction occurred right next to the tips of the fracture because of the highest stress concentrations there.

I monitored the porosity change with time at three different locations inside the fracture: at the mid-point,, the upper fracture tip, and the lower fracture tip (**Fig. 5.21**). After 70 days, the porosity at the fracture mid-point had been reduced to 89% of its initial value. The porosity at the upper and lower fracture tips had been reduced to 93.3% and 92.6%, respectively, of the initial porosity. The porosity reduction at the lower

tip of the fracture was slightly higher than the one at the upper tip because of the vicinity of the former to the lower part of the domain that was close to the production area (where the pressure was lower). At the beginning of production, compression and dilation occurred simultaneously near the production area due to the large initial pressure drawdown. The area above the production point was compressed, and the area below the production point was dilated. Following depressurization, the system compressed. The lower part of the fracture was close to the production area, so dilation of the intact rock occurred in that area. Note that the porosity in the lower part of the fracture increased slightly at the beginning of production (see **Fig. 5.21 (a)**).

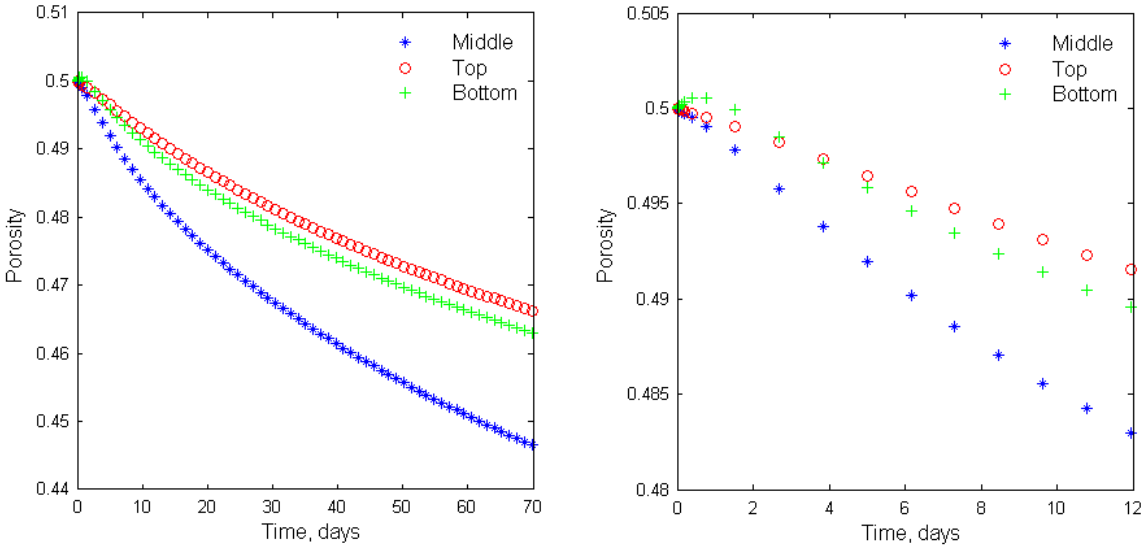

(a) **(b)**

Fig. 5.21—Hard fracture case: (a) evolution of porosity over time at three locations within the fracture: lower tip, mid-point, and upper tip (b) porosity change at the same locations during the earlier part of the simulation.

5.3.2 The Soft Fracture System

I made the geomechanical properties of the fracture softer by using a higher initial porosity (0.6) and exponent (2.5) in Eq. 4-92. The porosity of the intact rock was 0.1. Therefore, Young's moduli of the intact rock and inside the fracture were 2.4 GPa and 3.6 MPa, respectively. The Young's modulus in the fracture was 11 times lower than that in the hard fracture system discussed in Section 5.3.1. The Young's modulus of the intact rock was about twice as large as that in the hard fracture system. The permeability of the fracture and of the intact rock was the same as for the previous hard fracture system. The system was depressurized for 233 days, and the constant B.H.P had been set at 2.0 MPa.

Fig. 5.22 shows the pressure distribution at = 29 and t = 233 days. At t = 233 days, the maximum pressure in the system had fallen below 10 MPa, and the fluid velocities were lower than at t = 29 days.

Fig. 5.23 shows the water saturation and velocity solutions at the same times as in **Fig. 5.22**. The highest water saturation occurred inside the discrete fracture. Comparison to **Fig. 5.17** indicates that, at the same time (t = 29 days) the water saturation in the soft fracture system is higher than in that in the hard fracture system. This is because the pore space inside the soft fracture is more deformable. As a result, the reduction of pore space caused by the imposed stress led to the compression of the gas in the fracture, resulting in higher water saturation inside the fracture. Note that I used a porosity-dependent permeability function in both studies I discussed in Sections 5.3.1 and 5.3.2. A higher reduction of porosity decreased the absolute permeability of the porous media.

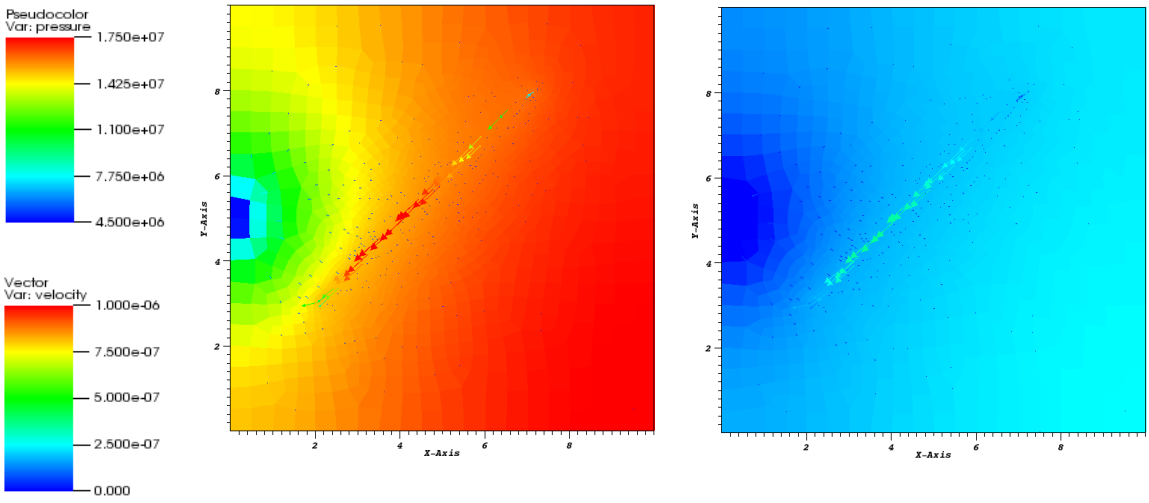

(a) **(b)**

Fig. 5.22—Soft fracture case: pressure (in Pa) and velocity (in m/s) spatial distributions at t = 29 days (a) and t = 233 days (b) of simulation.

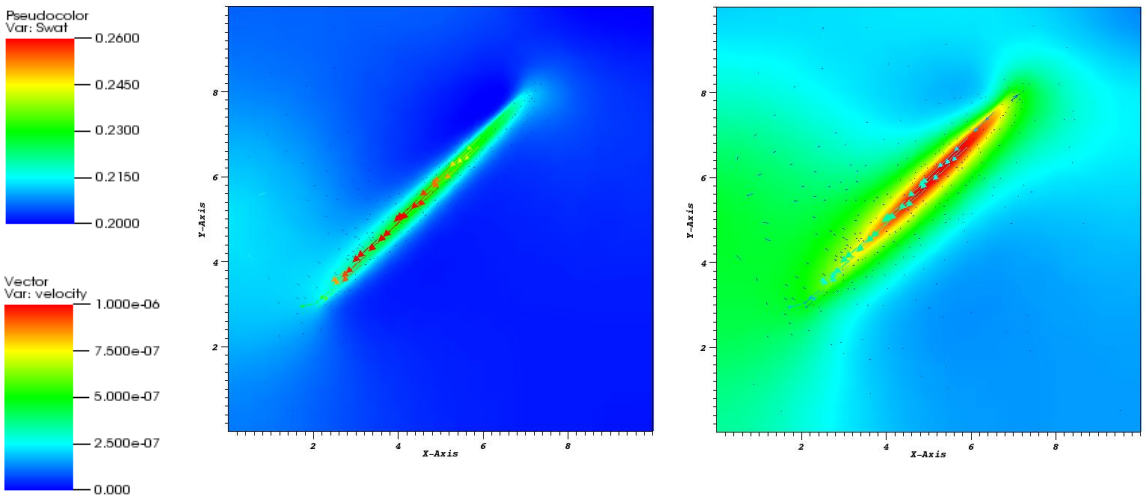

Fig. 5.23—Soft fracture case: water saturation and velocity (in m/s) distributions at t= 29 days (a) and t = 233 days in the problem of Fig. 5.15. The water saturation inside the fracture increased significantly because of the higher mobility of the gas and the porosity reduction

In **Fig. 5.24**, there is the same discontinuity in the displacement solution (caused by the presence of the discrete fracture) that had been observed in the case of the hard rock fracture (**Fig. 5.18**). Note that the y-direction displacement after 233 days is not noticeably larger than in the case of the hard fracture. The area occupied by the discrete fracture was significantly smaller than the area of the intact rock. Therefore, the main contribution to the consolidation after a substantially long period of depressurization came from the pressure depletion and the deformation of the intact rock. Because the discrete fracture had a lower Young's modulus, the porosity reduction in the fracture was expected to be pronounced than the hard fracture case.

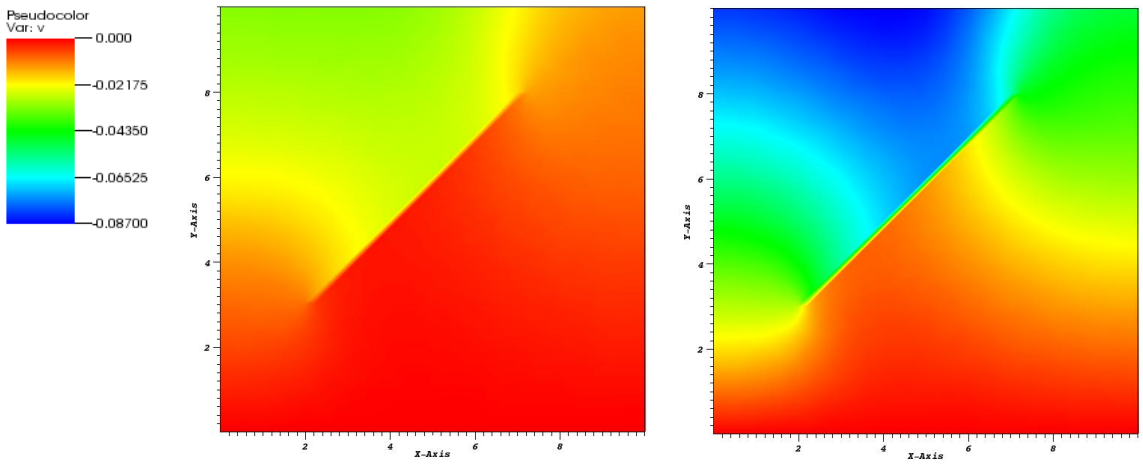

Fig. 5.24—Soft fracture case: Y-direction displacement (in m) distribution at (a) t = 29 days and (b) t = 233 days of simulation. The discontinuity in the displacement was caused by the presence of the discrete fracture.

Fig. 5.25 and **Fig. 5.26** show the porosity distributions inside the fracture and in the intact rock, respectively. As in the hard fracture case, the porosity reduction was the largest at the mid-point of the fracture. Even though the intact rock had a higher Young's modulus than the intact rock in the hard fracture case, the porosity reduction after 233 days was larger because of a larger effective stress in the porous media caused by the depressurization. The stress concentration near the fracture tips was larger than in the hard fracture case.

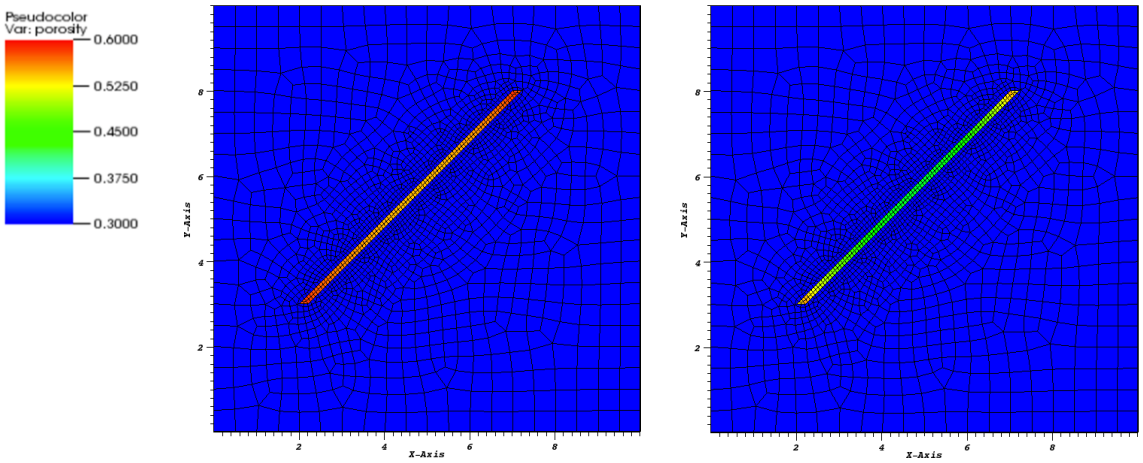

Fig. 5.25—Soft fracture case: Porosity distribution in the fracture at (a) t = 29 days and (b) t = 233 days.

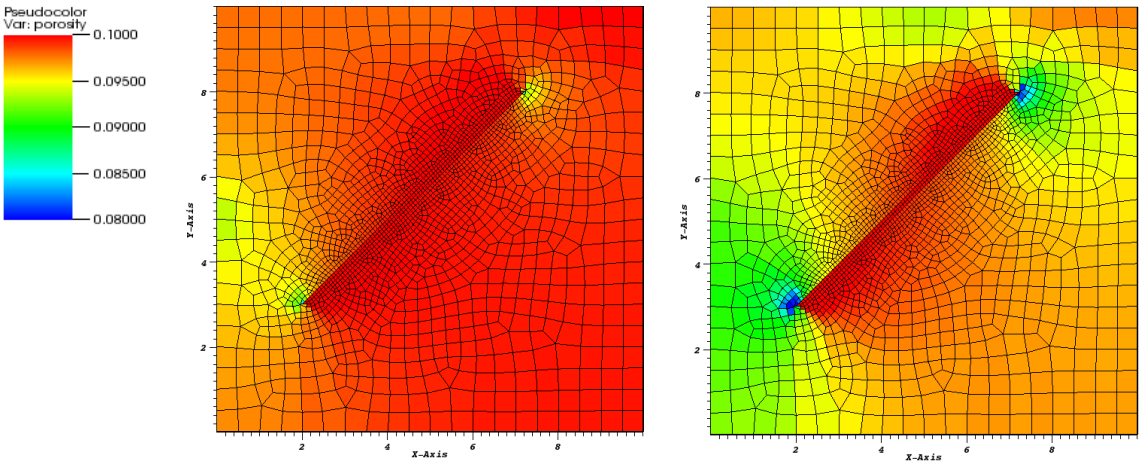

Fig. 5.26—Soft fracture case: Porosity distribution in the intact rock at (a) t = 29 days and (b) t = 233 days. For better visualization of the porosity change, the maximum porosity was set to 0.1. The largest porosity reduction occurred next to the fracture tips because of the highest stress concentration there.

Fig. 5.27 shows the evolution of the porosity over time inside the fracture at the three locations discussed in the hard fracture case: at the mid-point, and the upper and lower tips of the fracture. At t = 233 days, the porosity at the mid-point was 73.4% of the initial porosity, whereas the porosity at the upper and lower fracture tips was 89.3% and 89% of the initial porosity, respectively. The difference in the porosity reduction between the mid-point and the fracture tips was higher than in the hard fracture case because the Young's modulus in the fracture was smaller and the Young's modulus in the intact rock was higher. Thus, the tips of the fracture were surrounded by intact rock of higher strength. At the beginning of the simulation, the increase in porosity of the lower part of the fracture (which had been a distinct feature in the hard fracture case, see Fig. 5.21) did not occur because of the higher Young's modulus of the intact rock, which resulted in a smaller dilation. .

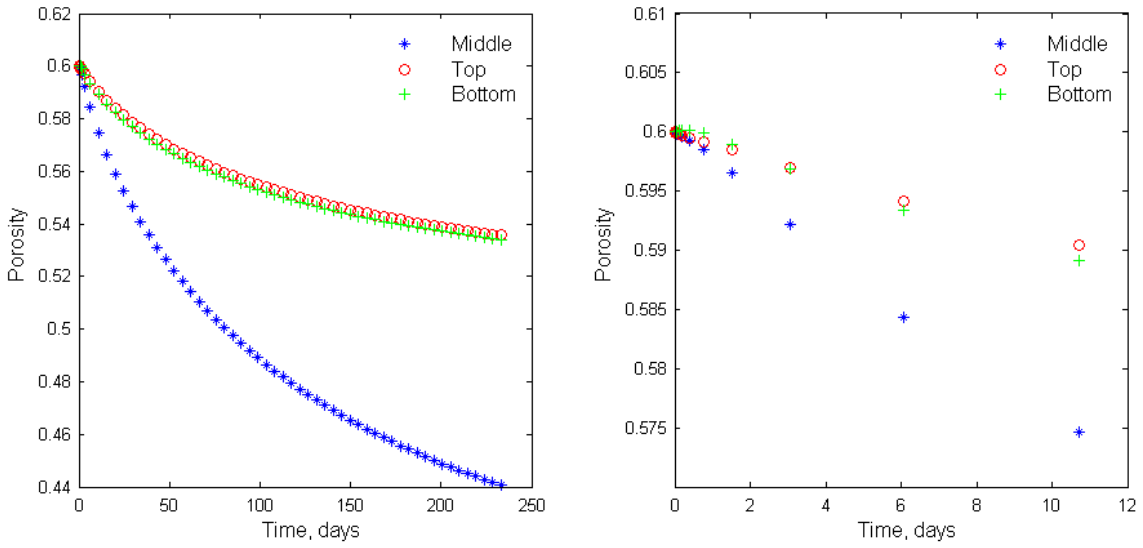

(a) **(b)**

Fig. 5.27—Soft fracture case: (a) evolution of porosity over time at three locations within the fracture: lower tip, mid-point, and upper tip (b) porosity change at the same locations during the earlier part of the simulation.

5.4 Multiple Discrete Fracture Model

In order to add more realism, I modeled a multiple discrete fracture system (**Fig. 5.28**). The domain had four discrete fractures located near its four corners, and a sharp triangularly shaped high-k subdomain extending from the middle of the left boundary to about a third of the domain's length. I assigned a constant B.H.P constraint of 2 MPa to the left end of the high-k subdomain and a no flow boundary condition to the rest of the boundaries. I imposed a sideburden and overburden stress of 20 MPa, with traction vectors imposed at $x = X_{max}$ along the x-direction, and $y = Y_{max}$ along the y-direction. The porosity and permeability were 0.6 and 100 μd in the discrete fractures, and 0.15 and 1 μd in the rock matrix. The high-k subdomain contains three different values of porosity and permeability that are depicted by red, orange, and green (from left to right) colors in **Fig. 5.28,** indicating porosities of 0.7, 0.6, and 0.5, and permeabilities of 150, 100, and 80 μd, respectively. I used Eq. 4-92 to generate the Young's moduli for the fracture and the intact rock; the reference value of the Young's modulus was 40 MPa, and the exponent in Eq.4-92 was 1.5. I ignored capillary and gravitational effects, and used the as initial conditions (pressure and water saturation) and gas and water properties the ones listed in **Table 4.2**.

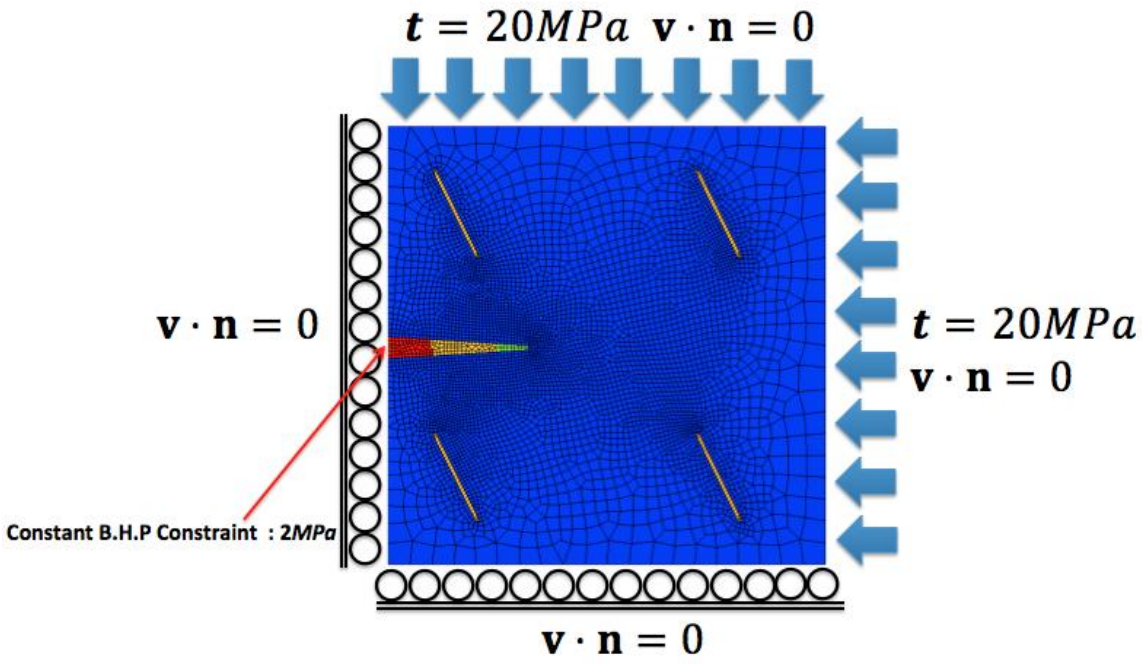

Fig. 5.28—The 2D domain (discretized with an unstructured grid) with a high-permeability subdomain and four discrete fractures used in the multiple discrete fracture problem.

Fig. 5.29 shows the pressure distributions at t = 34 days and t = 168 days. The lowest pressures and the highest velocity vectors occurred inside the high-k subdomain. The pressure propagation started at the x = 0 boundary of the high-k subdomain and the expanding low-pressure region had a triangular shape. At t = 168 days (**Fig. 5.29 (b)**), the maximum pressure in the system had decreased to 9 MPa, and the velocities decreased as well.

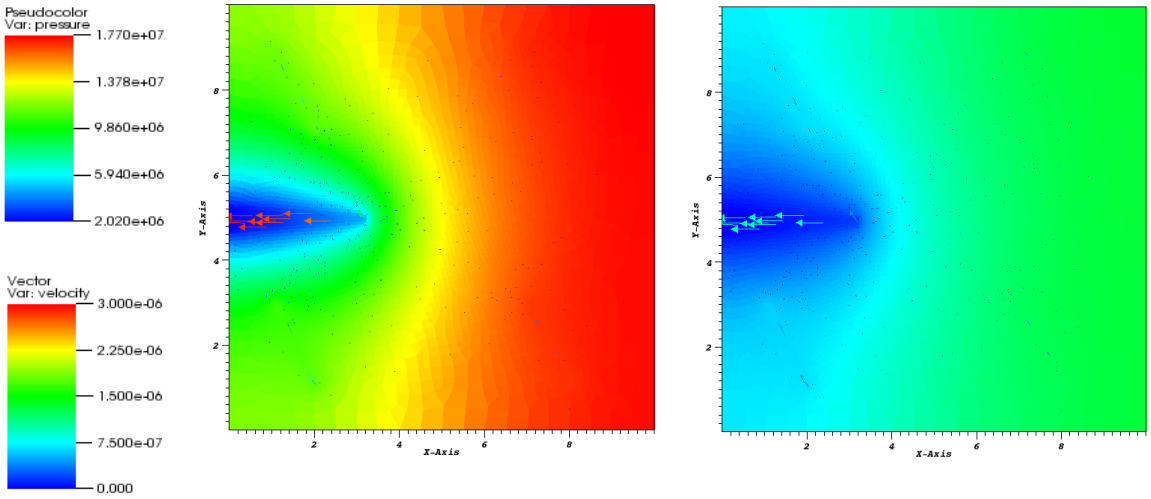

Fig. 5.29—Pressure distributions at (a) t = 34 days and (b) t = 168 days in the problem of Fig. 5.28. The propagation of the low-pressure fronts begins from the high-permeability subdomain.

The highest water saturation occurred inside the high-k subdomain (**Fig. 5.30**). At t = 35 days (**Fig. 5.30 (a)**), the water saturation was higher around the high-k subdomain and the discrete fracture located in the upper left corner because of the pressure gradient caused by the high-k subdomain and the overburden stress. Higher water saturation was observed inside the four discrete fractures because each fracture was compacted by the tractions imposed along the x- and/or the y-direction (**Fig. 5.30 (b)**). After 168 days of depressurization, the water saturation in the entire system increased, and higher velocities were registered in the two discrete fractures located in the upper left and the lower left parts of the domain. Compared to the simulation with a single discrete fracture, the water saturation inside the high-k subdomain was about 1.6 times higher. This was because of the much higher fluid velocities in that subdomain than in the rest of the system, as well as the larger deformations there.

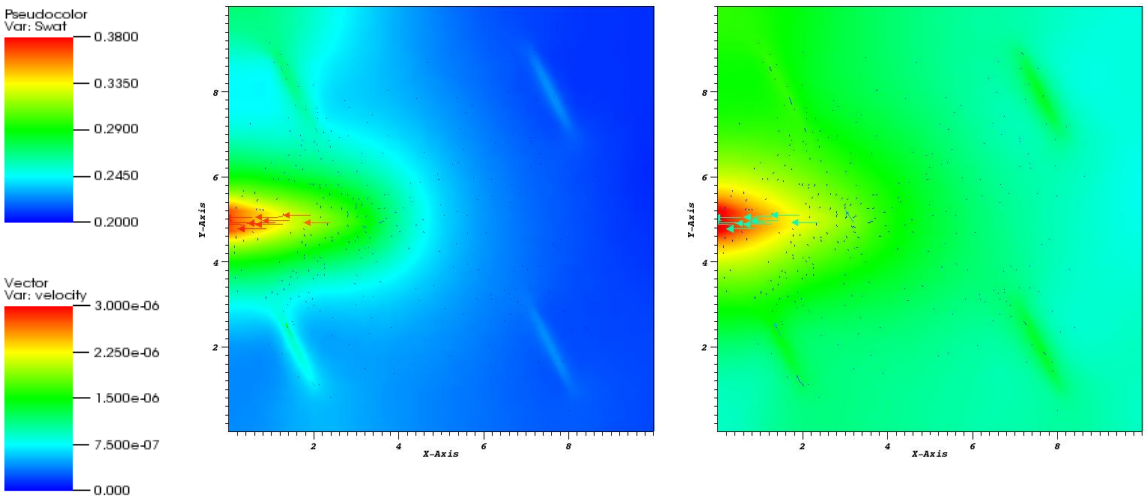

Fig. 5.30—Water saturation and velocity distributions at (a) t = 34 days and (b) t = 168 days in the problem of Fig. 5.28. The water saturation is highest in the high-k subdomain, higher in the fractures and lower in the intact rock.

Deformation occurred along the x-direction (**Fig. 5.31**) because of the traction vector imposed along the x-direction at $x = X_{max}$. There are discontinuities in the x-direction displacement solution mainly caused by the presence of the discrete fractures.

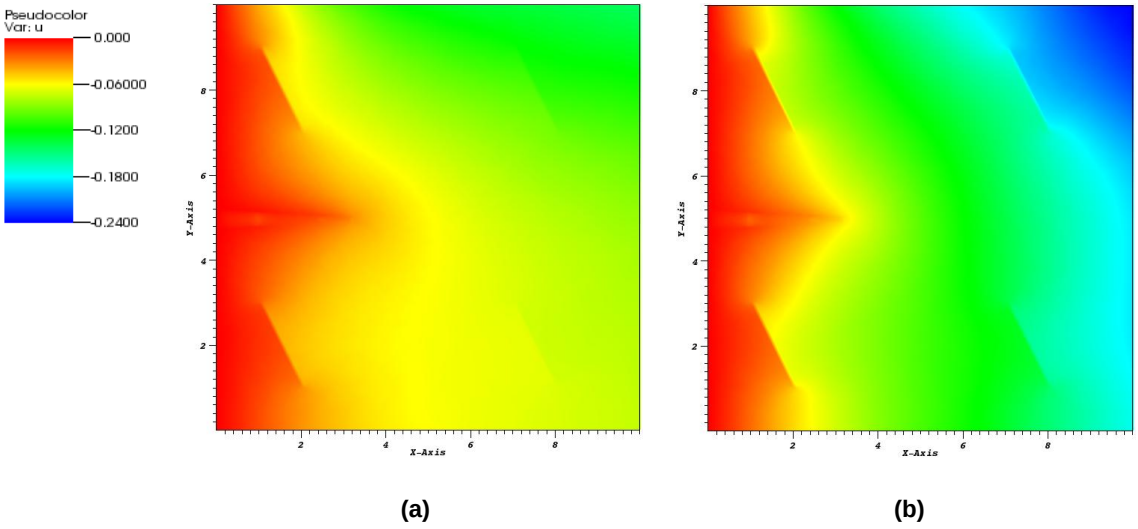

Fig. 5.31— X-direction displacement solutions at (a) t = 34 days and (b) t = 168 days in the problem of Fig. 5.28.

Deformation also occurred along the y-direction due to the y-direction traction vector (**Fig. 5.32**). The y-direction deformation was slightly higher than the x-direction deformation. This was because the largest pressure drop and deformation occurred inside the high-k subdomain: unlike the x-direction displacement, the largest discontinuity of the displacement field occurred because of the presence of this subdomain.

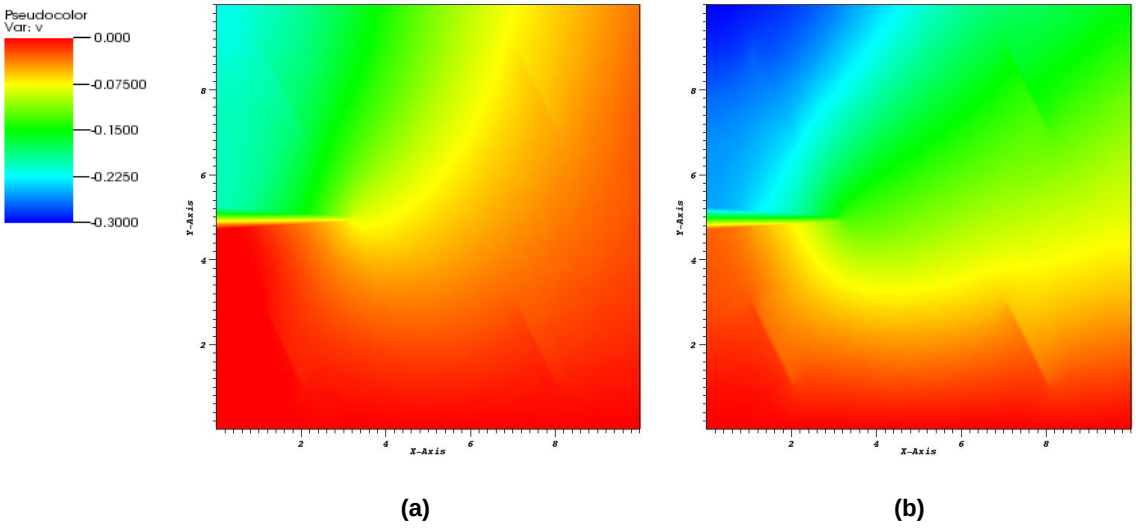

Fig. 5.32—The y-direction displacement distribution at (a) t = 34 days and (b) t = 168 days in the problem of Fig. 5.28 is slightly smaller than the x-direction displacement.

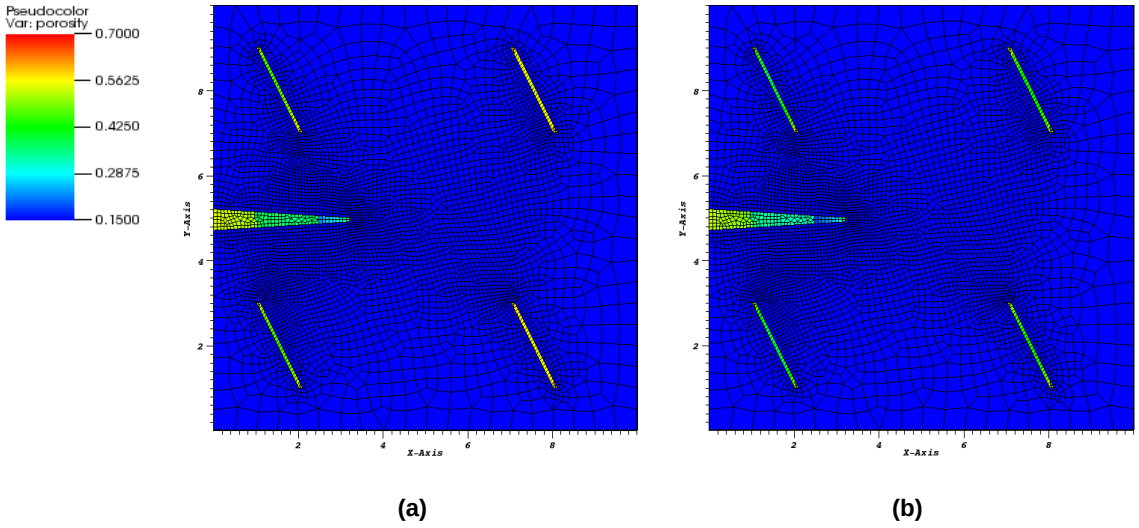

Fig. 5.33— Porosity distributions at (a) t = 34 days and (b) t = 168 days in the problem of Fig. 5.28.

I investigated the porosity change in the fractures (**Fig. 5.33**) and the intact rock (**Fig. 5.34**). As low pressure propagated from the high-k subdomain, the effective stress in the fractures increased, which resulted in a porosity reduction in the high-k subdomain and the discrete fractures. I also observed a porosity reduction in the intact rock. As in the previous simulations, large porosity reduction occurred near the fracture tips (**Fig. 5.34**). The largest porosity reduction in the intact rock occurred near the tip of the high-k subdomain, which indicated that the stress concentration in that region was the highest as well.

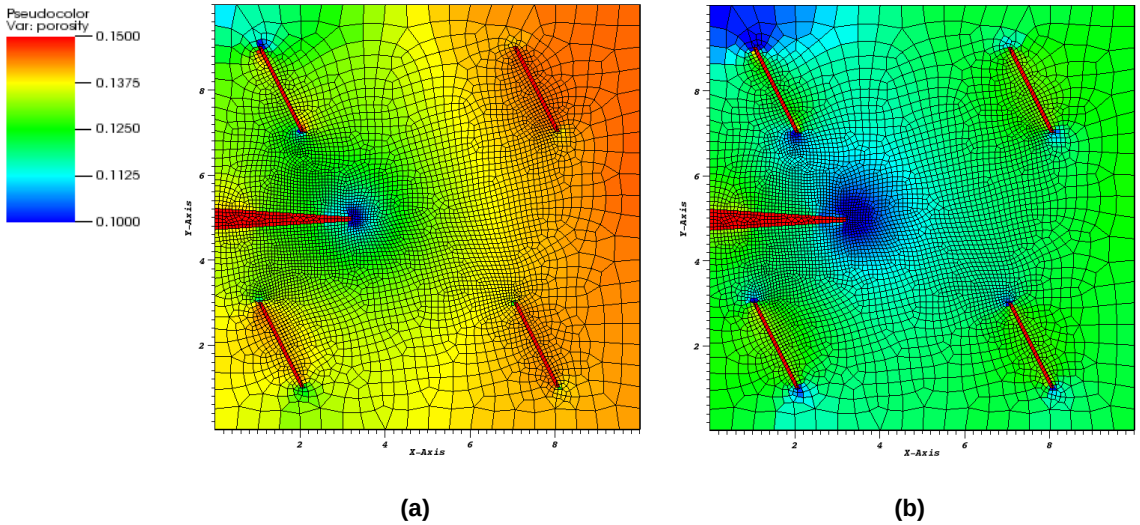

Fig. 5.34—The porosity distributions at (a) t = 34 days and (b) t = 168 days in the problem of Fig. 5.28 show that large porosity reduction in the intact rock occurred near the tips of the fractures and of the high-k subdomain. For better visualization, the maximum porosity was set to 0.15.

Fig. 5.35 shows the evolution of porosity over time in the discrete fractures. U-L, U-R, L-L, and L-R indicate the locations of the discrete fractures, which are in the upper left, upper right, lower left, and lower right region of the domain, respectively. The porosity in the U-L and L-L fractures dropped to 63% and 62% of the initial porosity, and the porosity of U-R and L-R fractures dropped to 70% and 72% of its initial value. The porosity reduction in the discrete fractures located toward the left boundary was more pronounced because of lower pressures in this area. At the beginning of the simulation, porosity in the U-L and L-R fractures rose above the initial porosity because pressure in these fractures increased more than the initial pressure caused by the imposed stress.

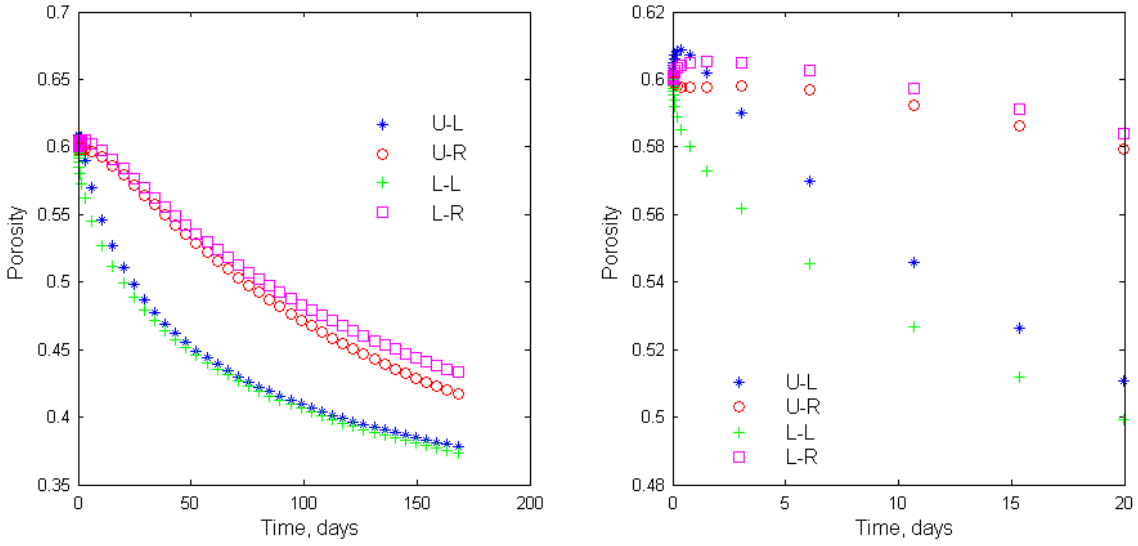

Fig. 5.35—The evolution of porosity over time in the four discrete fractures show that (a) the highest porosity reduction occurred in the two discrete fractures (U-L and L-L) located near the left boundary, and (b) early in the simulation, the porosity in the U-L and L-R fractures rose above the initial porosity because of the pressure increase caused by the imposed stress on the boundary.

I also investigated the porosity change in the triangular high-k subdomain. **Fig. 5.36** shows the porosity change at the left end and the tip of this subdomain. At t = 168 days, the porosity in the subdomain next to the constant-B.H.P. boundary had been reduced to 76% of the initial porosity, and to 73% of the initial porosity at the tip of the subdomain. The porosity reduction inside the triangular high-k subdomain was less than in the discrete fractures (U-L and L-L fractures). The high-k subdomain is parallel to the top boundary and perpendicular to the right boundary. Therefore, the y-direction compression tends to close the fracture, while the x-direction compression tends to open the fracture. From **Fig. 5.36**, it is evident that the largest porosity reduction occurred at the beginning of the production. The sudden pressure drop caused by the specified constant B.H.P on the left end of the triangular high-k subdomain rapidly increased the effective stress, which resulted in a large amount of deformation in this subdomain (acting to close the fracture). In my simulation model, I used a porosity-dependent permeability function so, the porosity reduction caused a reduction in permeability, which in turn lowered the flow rate in the subdomain. In order to avoid the sudden decrease of permeability in the high-k subdomain, it may be necessary to find the optimum B.H.P that minimizes the closure of the fracture and generates an optimum pressure gradient to achieve a suitable flow rate. Then, I can reduce the B.H.P gradually so that the permeability in the fracture will decrease accordingly.

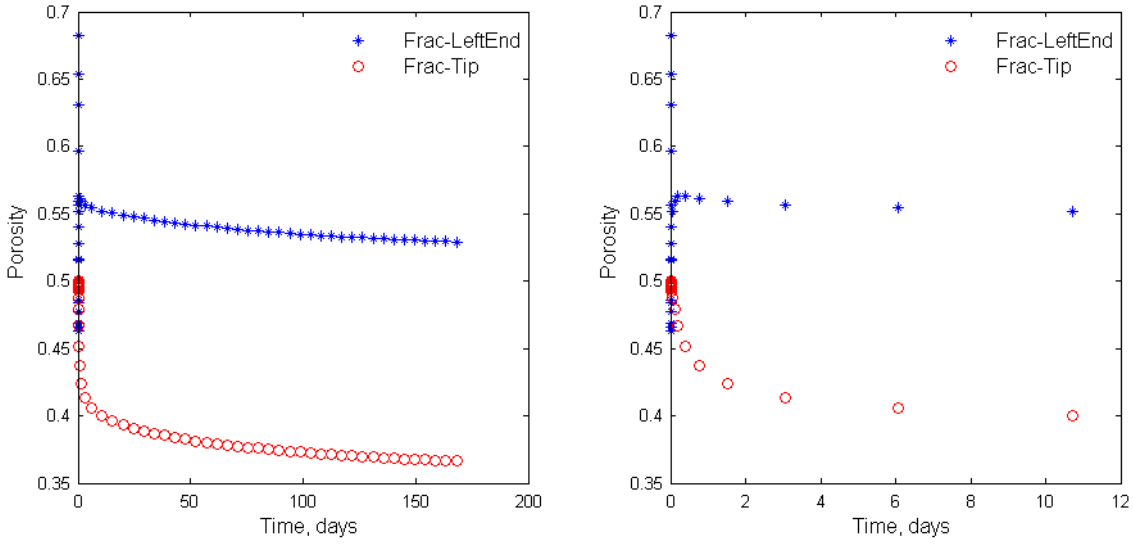

(a) **(b)**

Fig. 5.36—(a) Evolution of porosity over time next to the constant-B.H.P boundary and at the tip of the high-permeability subdomain of Fig. 5.28; (b) the majority of the porosity reduction occurred early.

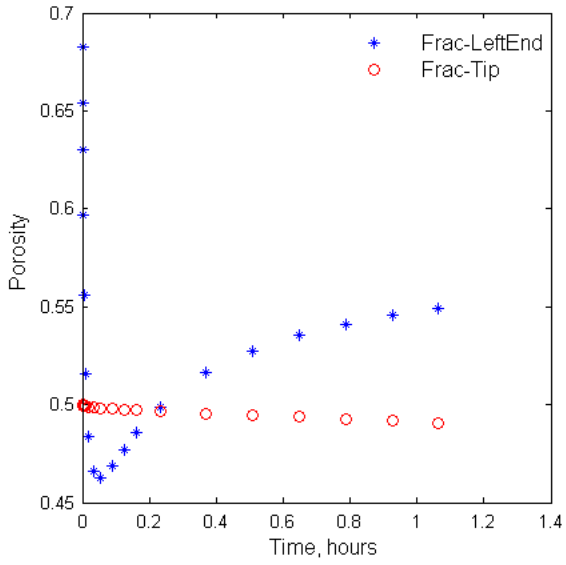

Fig. 5.37—Porosity change in the triangular high-permeability subdomain (at the left end and at its tip) in the early stages of production a rapid porosity reduction occurred near the B.H.P boundary, but porosity recovered partially later as the pressure gradient decreased.

To investigate the very early time behavior of the triangular high-permeability subdomain, I plotted the porosity change in the first 1.2 hours of production (**Fig. 5.37**). The porosity at the left end of this subdomain decreased rapidly to about 0.45, and then recovered as the pressure gradient near the left end became flatter. I observed a similar behavior in the case of the single high-k subdomain model (**Fig. 4.31**).

CHAPTER VI

NUMERICAL UPSCALING OF COUPLED FLOW AND GEOMECHANICS

6.1 Local Upscaling of Permeability and Elastic Stiffness Tensors

6.1.1 Derivation of the Upscaled of Permeability and Elastic Stiffness Tensors

In flow problems in a heterogeneous reservoir, the porosity and permeability are spatially different properties. Similarly, in mechanics problems, elastic stiffness tensors are spatially different properties. Because porosity is a simple volumetric ratio, it is easy to upscale it using volume-weighted averaging. However, since the permeability and elastic stiffness tensors are components of constitutive relations that describe different physical problems, an accurate upscaling of these parameters is very important.

One of the phenomenologically-derived constitutive equations for flow problems is Darcy's law, which, ignoring gravity effects, is expressed as

$$\mathbf{v} = -\frac{\boldsymbol{k}}{\mu}\nabla p \quad \text{(6-1)}$$

where $\mathbf{v}$, $\boldsymbol{k}$, μ, p are a velocity vector (m/s), the second order permeability tensor (md), the viscosity (cp) and pressure (Pa), respectively. The constitutive equation for the mechanics problem is Hooke's law is expressed as

$$\boldsymbol{\sigma} = \boldsymbol{E} : \boldsymbol{\varepsilon} \quad \text{(6-2)}$$

where $\boldsymbol{\sigma}$, $\boldsymbol{E}$, $\boldsymbol{\varepsilon}$ are the second order stress tensor (Pa), the fourth order elastic stiffness tensor (Pa), and the second order strain tensor, respectively. The purpose of upscaling a coupled flow and geomechanics problem is to determine an equivalent $\boldsymbol{k}$ and $\boldsymbol{E}$ that can closely represent the FS physics on the CS grid of the upscaled domain. The flow solver provides the pressure and velocity solutions of the mass balance and of the Darcy's equations. The mass balance equation for incompressible flow and medium is expressed as

$$\nabla \cdot \mathbf{v} = f \quad \text{(6-3)}$$

where $\mathbf{v}$ and f indicate velocity and source and sink, repeatedly.

In order to solve the Eq. 6-1 and Eq. 6-3 I use a mixed finite element formulation. Unlike the control-volume finite element method, the mixed finite element method solves for both the pressure solution and the velocity solution individually, and this provides more accurate approximations of fluid velocities (Durlofsky 1994). I used the lowest order Raviart Thomas space (Raviart and Thomas 1977) for the veloc-

ity solution and a discontinuous Galerkin element for the pressure solution to overcome a possible saddle-point problem (Fortin and Brezzi 1991). In order to make a finite element formulation, I can define spaces of solutions and test functions $p, \mathbf{v}, q$ and $\boldsymbol{w}$ as

$$\boldsymbol{H}(div, \Omega) \equiv \left\{ \boldsymbol{w} \in \left(L^2(\Omega)\right)^d : \nabla \cdot \boldsymbol{w} \in L^2(\Omega) \right\} \quad (6\text{-}4)$$

$$\boldsymbol{S} \equiv \boldsymbol{H}(div, \Omega) \cap \{\boldsymbol{w}: \mathbf{w} \cdot \boldsymbol{n} = 0 \text{ on } \Gamma\} \quad (6\text{-}5)$$

$$W \equiv L^2(\Omega) \quad (6\text{-}6)$$

Then the finite element formulation (weak formulation) is to find $p_h \in W$ and $\mathbf{v_h} \in \boldsymbol{S}$ such that

$$(q, \nabla \cdot \mathbf{v_h})_\Omega = (q, f)_\Omega \, , \forall q \in W \quad (6\text{-}7)$$

$$\left(\boldsymbol{w}, \left(\frac{\boldsymbol{k}}{\mu}\right)^{-1} \mathbf{v_h}\right)_\Omega - (\nabla \cdot \boldsymbol{w}, p_h)_\Omega = -(\boldsymbol{w} \cdot \boldsymbol{n}, p_h)_\Gamma, \forall \boldsymbol{w} \in \boldsymbol{S} \quad (6\text{-}8)$$

where $(a, b)_\Omega = \int_\Omega ab$ and $(a, b)_\Gamma = \int_\Gamma ab$. The velocity and pressure solution are approximated as

$$\mathbf{v_h} = \sum_{e=1}^{\mathrm{n_v}} \boldsymbol{w}_e(x) \mathrm{v}_e \quad (6\text{-}9)$$

$$p_h = \sum_{i=1}^{n_p} q_i(x) p_i \quad (6\text{-}10)$$

where *e* indicates an edge of the element and *i* indicates the center of the element. The resulting linear system is

$$\begin{bmatrix} A & B^T \\ B & 0 \end{bmatrix} \begin{bmatrix} V \\ P \end{bmatrix} = [RHS] \quad (6\text{-}11)$$

The global matrix is indefinite, so the Schur complement (Diaz and Shenoi 1994) is introduced to solve the linear system.

The following example shows the way to determine the upscaled full tensor permeability of heterogeneous media. The upscaled permeability tensor for a 2D domain has four components. Therefore, I need at least four independent equations for a unique solution. When dealing with the mixed finite element formulation, one needs two boundary value problems for the mass balance and the Darcy equations. In this study, a core-flood boundary condition is assumed. For a 2D heterogeneous domain of size *Lx* and *Ly*, the boundary condition is expressed as (x-direction flow)

$$p(0, y) = 1 \quad \text{(6-12)}$$

$$p(L_x, y) = 0 \quad \text{(6-13)}$$

$$\mathbf{v}(x, 0) \cdot \boldsymbol{n} = \mathbf{v}\big(x, L_y\big) \cdot \boldsymbol{n} = 0 \quad \text{(6-14)}$$

where **v** is a velocity vector and $\boldsymbol{n}$ is an outward normal vector on the surface. **Fig. 6.1** shows the size of the domain that I want to upscale and the x-direction core-flood boundary condition.

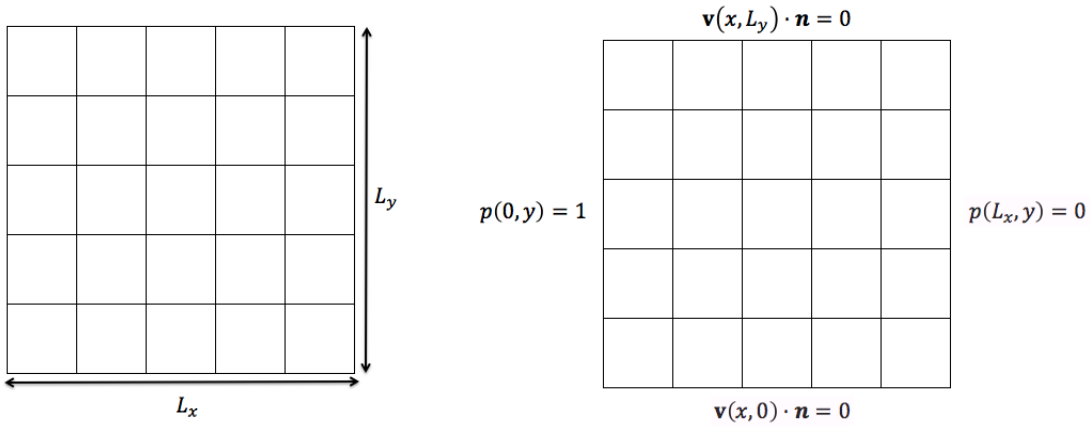

Fig. 6.1—(a) A 2D domain for upscaling and (b) the x-direction core-flood boundary condition on the domain.

Likewise, the core-flood boundary condition of the other direction (y-direction flow) is determined by specifying constant inlet and outlet pressures, and assigning no-flow conditions to the sides parallel to the flow direction. In order to use Darcy's law on the coarse grid blocks, it is necessary to obtain the volume-weighted average of velocities and pressure gradients on the FS domain I want to upscale as

$$\langle \mathbf{v} \rangle^i = \frac{1}{V} \int_V \mathbf{v}^i \, dV \quad \text{(6-15)}$$

$$\langle \nabla p \rangle^i = \frac{1}{V} \int_V (\nabla p)^i \, dV \quad \text{(6-16)}$$

where i = 1, 2 indicate x- and y-direction core-floods respectively. For example, when the index i =1, the x-direction core-flood boundary condition is imposed on the boundary. I can rewrite Darcy's equation as four independent equations as (assuming that the viscosity is one)

$$\langle \mathrm{v} \rangle_x^1 = -\left(k_{xx}^c \langle \frac{\partial p}{\partial x} \rangle^1 + k_{xy}^c \langle \frac{\partial p}{\partial y} \rangle^1 \right) \quad \text{(6-17)}$$

$$\langle \mathrm{v} \rangle_y^1 = -\left(k_{yx}^c \langle \frac{\partial p}{\partial x} \rangle^1 + k_{yy}^c \langle \frac{\partial p}{\partial y} \rangle^1 \right) \quad \text{(6-18)}$$

$$\langle \mathrm{v} \rangle_x^2 = -\left(k_{xx}^c \langle \frac{\partial p}{\partial x} \rangle^2 + k_{xy}^c \langle \frac{\partial p}{\partial y} \rangle^2 \right) \quad \text{(6-19)}$$

$$\langle \mathrm{v} \rangle_y^2 = -\left(k_{yx}^c \langle \frac{\partial p}{\partial x} \rangle^2 + k_{yy}^c \langle \frac{\partial p}{\partial y} \rangle^2 \right) \quad \text{(6-20)}$$

where k_{xx}^c, k_{xy}^c, k_{yx}^c, and k_{yy}^c are the components of the upscaled permeability tensor in a coarse cell. Manipulate the above equations leads to linearly independent equations with respect to the permeability tensors that can be written in matrix form as

$$\begin{bmatrix} \langle \frac{\partial p}{\partial x} \rangle^1 & \langle \frac{\partial p}{\partial y} \rangle^1 & 0 & 0 \\ 0 & 0 & \langle \frac{\partial p}{\partial x} \rangle^1 & \langle \frac{\partial p}{\partial y} \rangle^1 \\ \langle \frac{\partial p}{\partial x} \rangle^2 & \langle \frac{\partial p}{\partial y} \rangle^2 & 0 & 0 \\ 0 & 0 & \langle \frac{\partial p}{\partial x} \rangle^2 & \langle \frac{\partial p}{\partial x} \rangle^2 \\ 0 & 1 & -1 & 0 \end{bmatrix} \begin{bmatrix} k_{xx}^c \\ k_{xy}^c \\ k_{yx}^c \\ k_{yy}^c \end{bmatrix} = \begin{bmatrix} \langle \mathrm{v} \rangle_x^1 \\ \langle \mathrm{v} \rangle_y^1 \\ \langle \mathrm{v} \rangle_x^2 \\ \langle \mathrm{v} \rangle_y^2 \\ 0 \end{bmatrix} \quad \text{(6-21)}$$

The above matrix and vector forms of linearly independent equations have an additional equation that makes the upscaled permeability a symmetric tensor. The added equation satisfies $k_{xy}^c = k_{yx}^c$.

Eq. 6-21 can be solved using the linear least square method as follow. First I define a matrix $\boldsymbol{A}$, a solution vector $\boldsymbol{x}$, and a right hand side vector $\boldsymbol{b}$ as

$$\boldsymbol{A} = \begin{bmatrix} \langle \nabla p \rangle_x^1 & \langle \nabla p \rangle_y^1 & 0 & 0 \\ 0 & 0 & \langle \nabla p \rangle_x^1 & \langle \nabla p \rangle_y^1 \\ \langle \nabla p \rangle_x^2 & \langle \nabla p \rangle_y^2 & 0 & 0 \\ 0 & 0 & \langle \nabla p \rangle_y^2 & \langle \nabla p \rangle_y^2 \\ 0 & 1 & -1 & 0 \end{bmatrix} \quad (6\text{-}22)$$

$$\boldsymbol{x} = \begin{bmatrix} k_{xx}^c \\ k_{xy}^c \\ k_{yx}^c \\ k_{yy}^c \end{bmatrix} \quad (6\text{-}23)$$

$$\boldsymbol{b} = \begin{bmatrix} \langle \mathrm{v} \rangle_x^1 \\ \langle \mathrm{v} \rangle_y^1 \\ \langle \mathrm{v} \rangle_x^2 \\ \langle \mathrm{v} \rangle_y^2 \\ 0 \end{bmatrix} \quad (6\text{-}24)$$

The solution vector $\boldsymbol{x}$ is approximated as

$$\boldsymbol{x} \approx \widehat{\boldsymbol{x}} \quad (6\text{-}25)$$

where $\widehat{\boldsymbol{x}}$ is the solution of a quadratic minimization problem that can be obtained as

$$(\boldsymbol{A}^T\boldsymbol{A})\widehat{\boldsymbol{x}} = \boldsymbol{A}^T\boldsymbol{b} \quad (6\text{-}26)$$

$$\widehat{\boldsymbol{x}} = (\boldsymbol{A}^T\boldsymbol{A})^{-1}\boldsymbol{A}^T\boldsymbol{b} \quad (6\text{-}27)$$

The permeability tensor that is obtained from this computation always satisfies symmetry. However it will not guarantee positive definiteness. The resultant permeability tensors are mostly positive definite. However, if the upscaled permeability tensor is not positive definite, then a boundary value problem is solved on the coarse grid that generates a non-positive definite permeability tensor with different boundary conditions. A periodic boundary condition is a good choice because it always guarantees positive definiteness.

The mechanics solver provides the displacement solution calculated from the geomechanical equilibrium equation as

$$\nabla \cdot \boldsymbol{\sigma} = 0 \quad (6\text{-}28)$$

where $\boldsymbol{\sigma}$ is the total Cauchy stress tensor. Under the assumption of isotropic material, the total Cauchy stress tensor can be expressed as

$$\boldsymbol{\sigma} = \lambda \nabla \cdot \boldsymbol{u}\boldsymbol{I} + 2\mu\boldsymbol{\varepsilon}(\boldsymbol{u}) \quad (6\text{-}29)$$

where λ, μ, b, and $\boldsymbol{I}$ are the first Lamé's constant, shear modulus (the second Lamé's constant), the Biot coefficient, and the second order identity tensor. Note that there is no pressure term in the Cauchy total stress tensor because it only computes the deformation of solid material because of the imposed mechanical boundary conditions.

A space of solution and test function $\boldsymbol{u}$ and $\boldsymbol{v}$ are defined as

$$\boldsymbol{V} \subset (H^1)^d(\Omega) \quad (6\text{-}30)$$

I applied a continuous Galerkin finite element discretization, which can be expressed as

$$(\nabla \cdot \boldsymbol{v}, \lambda \nabla \cdot \boldsymbol{u})_\Omega + 2\big(\varepsilon(\boldsymbol{v}), \mu\varepsilon(\boldsymbol{u})\big)_\Omega = (\boldsymbol{v}, \boldsymbol{t})_\Gamma, \forall\, \boldsymbol{v} \in \boldsymbol{V} \quad (6\text{-}31)$$

The displacement solution is approximated as

$$\boldsymbol{u_h} = \sum_{a=1}^{n_u} v_a(x) u_a \quad (6\text{-}32)$$

where v_a and u_a are a shape function (or test function) and a scalar coefficient at each degree of freedom. In addition $n_u$is the total degrees of freedom of the displacement solution, which is the number of nodes times the dimension $(a \times dim)$. The resulting linear system is

$$[A][U] = [RHS] \quad (6\text{-}33)$$

In order to upscale a heterogeneous elastic medium, I used the Hill condition (Hill 1963) which is the necessary and sufficient condition of equivalence between the mechanically defined elastic material properties and the energetically defined effective properties written as

$$\langle \boldsymbol{\sigma} : \boldsymbol{\varepsilon} \rangle_{\boldsymbol{\Omega}} = \langle \boldsymbol{\sigma} \rangle_{\boldsymbol{\Omega}} : \langle \boldsymbol{\varepsilon} \rangle_{\boldsymbol{\Omega}} \quad (6\text{-}34)$$

where $\langle \boldsymbol{\sigma} \rangle_{\boldsymbol{\Omega}} = \frac{1}{V}\int_V \boldsymbol{\sigma} dV \approx \frac{1}{V}(\boldsymbol{\sigma}_1 V_1 + \boldsymbol{\sigma}_2 V_2 + \boldsymbol{\sigma}_3 V_3 + \boldsymbol{\sigma}_4 V_4 + \boldsymbol{\sigma}_5 V_5)$ and $V = V_1 + V_2 + V_3 + V_4 + V_5$.

If $V_1 = V_2 = V_3 = V_4 = V_5$ which is the case for a uniform grid then $\frac{1}{V}\int_V \boldsymbol{\sigma} dV \approx \frac{1}{5}(\boldsymbol{\sigma}_1 + \boldsymbol{\sigma}_2 + \boldsymbol{\sigma}_3 + \boldsymbol{\sigma}_4 + \boldsymbol{\sigma}_5)$, which is generally expressed as $\frac{1}{V}\int_V \boldsymbol{\sigma} dV \approx \frac{1}{n}\sum_{i=1}^{n} \boldsymbol{\sigma}_i$ and is already implemented in the code.

Eq. 6-34 indicates that the volume-weighted average of the double dot product of stress and strain in a coarse domain is equivalent to the double dot product of the volume-weighted stress and strain in the coarse domain. Strain energy is the elastic energy stored in the material under deformation and defined as

$$U = \frac{\mathbf{1}}{2}\boldsymbol{\varepsilon} : \boldsymbol{E} : \boldsymbol{\varepsilon} \quad \text{(6-35)}$$

where U is the strain energy, which is a scalar value. From Eq. 6-35, a stress tensor is obtained by defining partial derivatives of the elastic energy with respect to a strain tensor as

$$\frac{\partial U}{\partial \boldsymbol{\varepsilon}} = \boldsymbol{E} : \boldsymbol{\varepsilon} = \boldsymbol{\sigma} \quad \text{(6-36)}$$

Eq. 6-36 can be expressed in matrix form as

$$\frac{\partial U}{\partial \boldsymbol{\varepsilon}} = \begin{bmatrix} \sigma_{11} \\ \sigma_{22} \\ \sigma_{33} \\ \sigma_{23} \\ \sigma_{13} \\ \sigma_{12} \\ \sigma_{32} \\ \sigma_{31} \\ \sigma_{21} \end{bmatrix} = \begin{bmatrix} E_{1111} & E_{1111} & E_{1133} & E_{1123} & E_{1113} & E_{1112} & E_{1132} & E_{1131} & E_{1121} \\ E_{2211} & E_{2222} & E_{2233} & E_{2223} & E_{2213} & E_{2212} & E_{2232} & E_{2231} & E_{2221} \\ E_{3311} & E_{3322} & E_{3333} & E_{3323} & E_{3313} & E_{3312} & E_{3332} & E_{3331} & E_{3321} \\ E_{2311} & E_{2322} & E_{2333} & E_{2323} & E_{2313} & E_{2312} & E_{2332} & E_{2331} & E_{2321} \\ E_{1311} & E_{1322} & E_{1333} & E_{1323} & E_{1313} & E_{1312} & E_{1332} & E_{1331} & E_{1321} \\ E_{1211} & E_{1222} & E_{1233} & E_{1223} & E_{1213} & E_{1212} & E_{1232} & E_{1231} & E_{1221} \\ E_{3211} & E_{3222} & E_{3233} & E_{3223} & E_{3213} & E_{3212} & E_{3232} & E_{3231} & E_{3221} \\ E_{3111} & E_{3122} & E_{3133} & E_{3123} & E_{3113} & E_{3112} & E_{3132} & E_{3131} & E_{3121} \\ E_{2111} & E_{2122} & E_{2133} & E_{2123} & E_{2113} & E_{2112} & E_{2132} & E_{2131} & E_{2121} \end{bmatrix} \begin{bmatrix} \varepsilon_{11} \\ \varepsilon_{22} \\ \varepsilon_{33} \\ \varepsilon_{23} \\ \varepsilon_{13} \\ \varepsilon_{12} \\ \varepsilon_{32} \\ \varepsilon_{31} \\ \varepsilon_{21} \end{bmatrix} \quad \text{(6-37)}$$

where all the components in the matrix and vector are expressed in index notation. The integers 1, 2, and 3 indicate the coordinates corresponding to the x, y, and z coordinates. Differentiating Eq. 6-37 with respect to the strain tensor yields (in terms of index notation)

$$\frac{\partial}{\partial \varepsilon_{ij}}\left(\frac{\partial U}{\partial \varepsilon_{ij}}\right) = E_{ijkl} \quad \text{(6-38)}$$

where the indices *i, j, k,* and *l* contain integers from 1 to 3. Note that the second partial derivative in Eq. 6-38 is immaterial so the elastic stiffness tensor is symmetric. For example, if I differentiate the strain energy as

$$\frac{\partial}{\partial \varepsilon_{11}}\left(\frac{\partial U}{\partial \varepsilon_{12}}\right) = \frac{\partial}{\partial \varepsilon_{12}}\left(\frac{\partial U}{\partial \varepsilon_{11}}\right) = E_{1112} = E_{1211} \quad \text{(6-39)}$$

Eq. 6-39 indicates that the elastic stiffness tensor is symmetric. In addition, since stress and strain are symmetric Eq. 6-37 is expressed as

$$\begin{bmatrix}\sigma_{11}\\ \sigma_{22}\\ \sigma_{33}\\ \sigma_{23}\\ \sigma_{13}\\ \sigma_{12}\end{bmatrix}=\begin{bmatrix}E_{1111} & E_{1111} & E_{1133} & E_{1123} & E_{1113} & E_{1112}\\ E_{2211} & E_{2222} & E_{2233} & E_{2223} & E_{2213} & E_{2212}\\ E_{3311} & E_{3322} & E_{3333} & E_{3323} & E_{3313} & E_{3312}\\ E_{2311} & E_{2322} & E_{2333} & E_{2323} & E_{2313} & E_{2312}\\ E_{1311} & E_{1322} & E_{1333} & E_{1323} & E_{1313} & E_{1312}\\ E_{1211} & E_{1222} & E_{1233} & E_{1223} & E_{1213} & E_{1212}\end{bmatrix}\begin{bmatrix}\varepsilon_{11}\\ \varepsilon_{22}\\ \varepsilon_{33}\\ 2\varepsilon_{23}\\ 2\varepsilon_{13}\\ 2\varepsilon_{12}\end{bmatrix} \quad \text{(6-40)}$$

In order to obtain the upscaled elastic stiffness tensor from Eq. 6-35, 21 independent equations needed to be solved. For the 2D domain, 6 independent equations to solve are needed. For the local upscaling problem, the prescribed displacement boundary conditions are imposed as

$$U_{eq}^{1}=\frac{1}{2}[\langle\varepsilon_{11}\rangle_{\Omega} \quad 0 \quad 0]\begin{bmatrix}E_{1111}^{C} & E_{1122}^{C} & E_{1112}^{C}\\ E_{2211}^{C} & E_{2222}^{C} & E_{2212}^{C}\\ E_{1211}^{C} & E_{1222}^{C} & E_{1212}^{C}\end{bmatrix}\begin{bmatrix}\langle\varepsilon_{11}\rangle_{\Omega}\\ 0\\ 0\end{bmatrix} \quad \text{(6-41)}$$

$$U_{eq}^{2}=\frac{1}{2}[0 \quad \langle\varepsilon_{22}\rangle_{\Omega} \quad 0]\begin{bmatrix}E_{1111}^{C} & E_{1122}^{C} & E_{1112}^{C}\\ E_{2211}^{C} & E_{2222}^{C} & E_{2212}^{C}\\ E_{1211}^{C} & E_{1222}^{C} & E_{1212}^{C}\end{bmatrix}\begin{bmatrix}0\\ \langle\varepsilon_{22}\rangle_{\Omega}\\ 0\end{bmatrix} \quad \text{(6-42)}$$

$$U_{eq}^{3}=\frac{1}{2}[0 \quad 0 \quad 2\langle\varepsilon_{12}\rangle_{\Omega}]\begin{bmatrix}E_{1111}^{C} & E_{1122}^{C} & E_{1112}^{C}\\ E_{2211}^{C} & E_{2222}^{C} & E_{2212}^{C}\\ E_{1211}^{C} & E_{1222}^{C} & E_{1212}^{C}\end{bmatrix}\begin{bmatrix}0\\ 0\\ 2\langle\varepsilon_{12}\rangle_{\Omega}\end{bmatrix} \quad \text{(6-43)}$$

where U_{eq}^{1}, U_{eq}^{2}, and U_{eq}^{3} are the equivalent strain energy in each coarse grid block with different boundary conditions. **Fig. 6.2** shows the displacement solution of an isotropic medium under the three different types of boundary conditions.

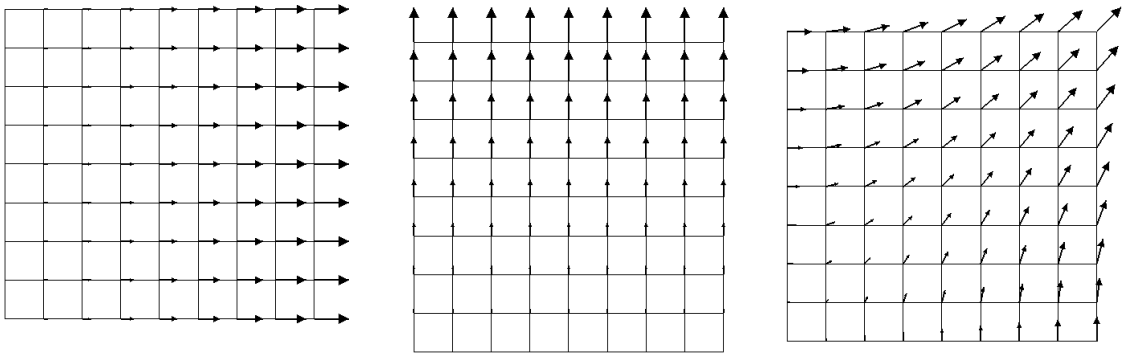

(a) **(b)** **(c)**

Fig. 6.2—Displacement solution of a 2D isotropic medium under (a) x-direction tension, (b) y-direction tension, and (c) pure shear strain.

From Eq. 6-41, Eq. 6-42, and Eq. 6-43, I can obtain E^C_{1111}, E^C_{2222}, and E^C_{1212}. The other three components can be obtained using E^C_{1111}, E^C_{2222}, and E^C_{1212} as

$$U^4_{eq} = [\langle\varepsilon_{11}\rangle_\Omega \quad \langle\varepsilon_{22}\rangle_\Omega \quad 0]\begin{bmatrix} E^C_{1111} & E^C_{1122} & E^C_{1112} \\ E^C_{2211} & E^C_{2222} & E^C_{2212} \\ E^C_{1211} & E^C_{1222} & E^C_{1212} \end{bmatrix}\begin{bmatrix} \langle\varepsilon_{11}\rangle_\Omega \\ \langle\varepsilon_{22}\rangle_\Omega \\ 0 \end{bmatrix} \quad \text{(6-44)}$$

where $E^C_{2211} = E^C_{1122}$. Therefore, E^C_{1122} is calculated from

$$E^C_{1122} = \frac{U^4_{eq} - \left(\langle\varepsilon_{11}\rangle_\Omega\langle\varepsilon_{11}\rangle_\Omega E^C_{1111} + \langle\varepsilon_{22}\rangle_\Omega\langle\varepsilon_{22}\rangle_\Omega E^C_{2222}\right)}{2\langle\varepsilon_{11}\rangle_\Omega\langle\varepsilon_{22}\rangle_\Omega} \quad \text{(6-45)}$$

The equivalent strain energy under a combination of a pure shear strain and x-direction tension is calculated from

$$U^5_{eq} = [\langle\varepsilon_{11}\rangle_\Omega \quad 0 \quad 2\langle\varepsilon_{12}\rangle_\Omega]\begin{bmatrix} E^C_{1111} & E^C_{1122} & E^C_{1112} \\ E^C_{2211} & E^C_{2222} & E^C_{2212} \\ E^C_{1211} & E^C_{1222} & E^C_{1212} \end{bmatrix}\begin{bmatrix} \langle\varepsilon_{11}\rangle_\Omega \\ 0 \\ 2\langle\varepsilon_{12}\rangle_\Omega \end{bmatrix} \quad \text{(6-46)}$$

where $E^C_{1112} = E^C_{1211}$. Therefore, E^C_{1112} is obtained as

$$E^C_{1112} = \frac{U^5_{eq} - \left(\langle\varepsilon_{11}\rangle_\Omega\langle\varepsilon_{11}\rangle_\Omega E^C_{1111} + 4\langle\varepsilon_{12}\rangle_\Omega\langle\varepsilon_{12}\rangle_\Omega E^C_{1212}\right)}{4\langle\varepsilon_{12}\rangle_\Omega\langle\varepsilon_{11}\rangle_\Omega} \quad \text{(6-47)}$$

Likewise, the equivalent strain energy under a combination of a pure shear strain and y-direction tension is calculated from

$$U_{eq}^{6} = [0 \quad \langle\varepsilon_{22}\rangle_{\Omega} \quad 2\langle\varepsilon_{12}\rangle_{\Omega}] \begin{bmatrix} E_{1111}^{C} & E_{1122}^{C} & E_{1112}^{C} \\ E_{2211}^{C} & E_{2222}^{C} & E_{2212}^{C} \\ E_{1211}^{C} & E_{1222}^{C} & E_{1212}^{C} \end{bmatrix} \begin{bmatrix} 0 \\ \langle\varepsilon_{22}\rangle_{\Omega} \\ 2\langle\varepsilon_{12}\rangle_{\Omega} \end{bmatrix} \quad \text{(6-48)}$$

where $E_{2212}^{C} = E_{1222}^{C}$. Therefore, E_{2212}^{C} is obtained as

$$E_{2212}^{C} = \frac{U_{eq}^{6} - (\langle\varepsilon_{22}\rangle_{\Omega}\langle\varepsilon_{22}\rangle_{\Omega}E_{2222}^{C} + 4\langle\varepsilon_{12}\rangle_{\Omega}\langle\varepsilon_{12}\rangle_{\Omega}E_{1212}^{C})}{4\langle\varepsilon_{12}\rangle_{\Omega}\langle\varepsilon_{22}\rangle_{\Omega}} \quad \text{(6-49)}$$

where the displacement field for Eq. 6-44 is obtained by adding the displacement field of Eq. 6-41 and Eq. 6-42. Using the displacement field for Eq. 6-44, U_{eq}^{4} can be obtained from volume weighted averaging of the fine scale strain energy. Likewise, U_{eq}^{5} and U_{eq}^{6} can be obtained by adding the displacement fields of Eq. 6-41 and Eq. 6-43, and Eq. 6-42 and Eq. 6-43, respectively. Note that the volume-weighted average of the strains equals the prescribed strains when I impose the displacement boundary condition ($\langle\varepsilon_{11}\rangle_{\Omega} = \varepsilon_{11}|_{\Gamma}$).

6.2 Numerical Experiments

I conducted four numerical experiments to compare the numerical solutions of the FS and CS models. The FS 2D model had 4096 (64×64) cells, and each cell had a nodal vector solution for the displacement, a pressure solution at the cell center, and a velocity vector at the center of each face. The FS model was upscaled with (4×4) coarse cells, so the resulting CS model had 256 (16×16) cells.

The first numerical experiment had a sink at the corner of the model that depressurized the reservoir. The second experiment was a consolidation problem that had a drainage boundary condition (that is, a constant pressure boundary) at the left and the right side boundaries. The FS flow properties (permeability and porosity) were adapted from the SPE10 problem.

Fig. 6.3 shows the FS porosity (**Fig. 6.3 (a)**) and permeability (**Fig. 6.3 (b)**) fields adapted from the SPE10 problem. This figure shows that the permeability field has a channelized barrier in the middle of the domain which made it difficult for fluid to move between the upper and the lower part of the domain. Since the SPE10 problem specifications do not provide geomechanical data, I used Eq. 4-92 to obtain the FS elastic stiffness tensors, which depend on the initial porosity. I assumed that each fine scale cell had an isotropic elastic stiffness tensor. **Fig. 6.4** shows Lamé's first constant and shear modulus fields when the exponent *n* in Eq. 4-92 is 1.5. Note that the values of the Lamé's first constant and shear modulus vary by up to 1000 times.

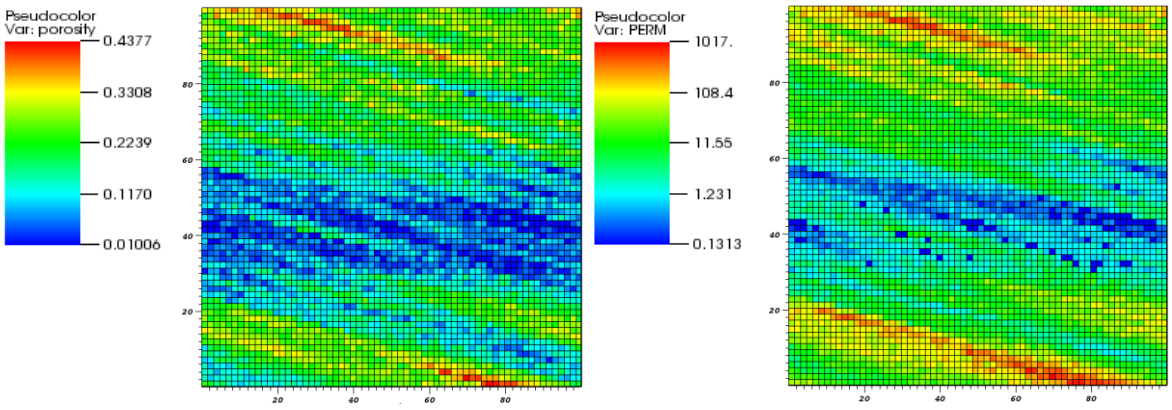

Fig. 6.3—(a) Porosity field and (b) x-direction permeability field used in the problem of upscaling. The y-direction permeability field is assumed to be the same as the x-direction permeability (isotropic). Permeability values vary by up to a factor of 10,000 times. Note that the permeability field follows a logarithmic distribution (permeability in md).

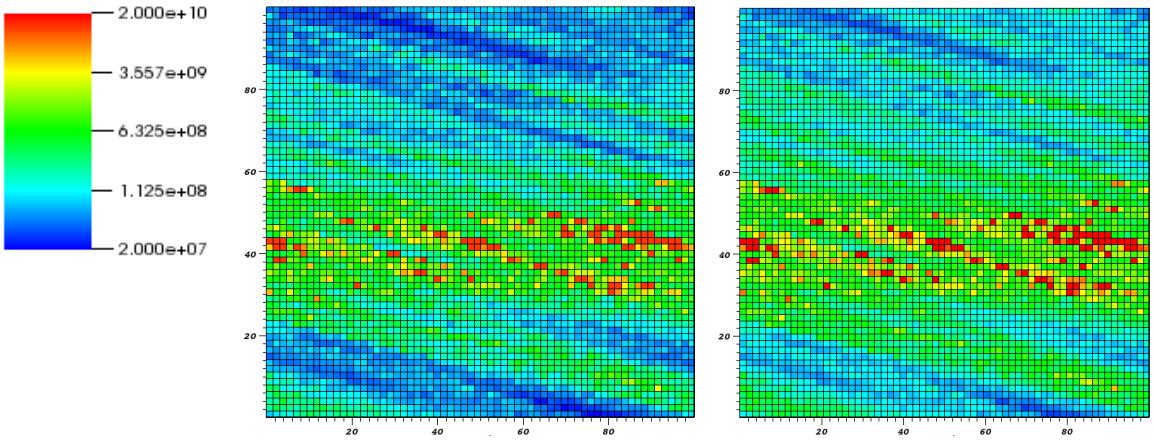

Fig. 6.4—(a) The distribution of Lamé's first constant and (b) the shear modulus field for n = 1.5 in Eq. 4.92. The values in each field vary by up to 1000 times. The units of the Lamé's first constant and of the shear modulus are Pa.

6.2.1 Production from the Sink (Well)

In this problem, a sink (well) with a constant withdrawal rate operated at the lower left corner of the domain (**Fig. 4.5).** For the FS model, I used the permeability and porosity fields shown in **Fig. 6.3**. For the FS mechanical properties, I used the Lamé's first constant and the shear modulus fields shown in **Fig. 6.4**. I obtained upscaled permeability tensors from the pressure solver, and elastic stiffness tensors from the

geomechanical equilibrium equation (mechanics) solver. The fluid viscosity was 1 cp and its compressibility was $1.0 \times 10^{-10}\ pa^{-1}$. An automatic initialization was done before running the production simulation. The sink at the lower left corner of the domain had a production rate of $5 \times 10^{-7} s^{-1}$. The CPU time needed to simulate 60 days of production was 345.59 seconds for the FS model and 19.137 seconds for the CS model. Thus, the computation in the CS model is about 18 times faster than that in the FS model, which indicates a reduction that is a roughly linear function of the number of cells in the system.

Fig. 6.5 shows the pressure solutions of the FS and CS models at the observation point. To compare the pressure solutions of the fine and coarse scale models, the FS pressure values at the observation point were upscaled. This way, it was possible to compare in a consistent manner the pressure solutions of the two representative elements (FS and CS) that have identical dimensions. **Fig. 6.5 (a)** indicates that the FS and CS pressure solutions are in excellent agreement. At the early stage of the simulation (**Fig. 6.5 (b)**), both simulations indicate a pressure rise above the initial pressure.

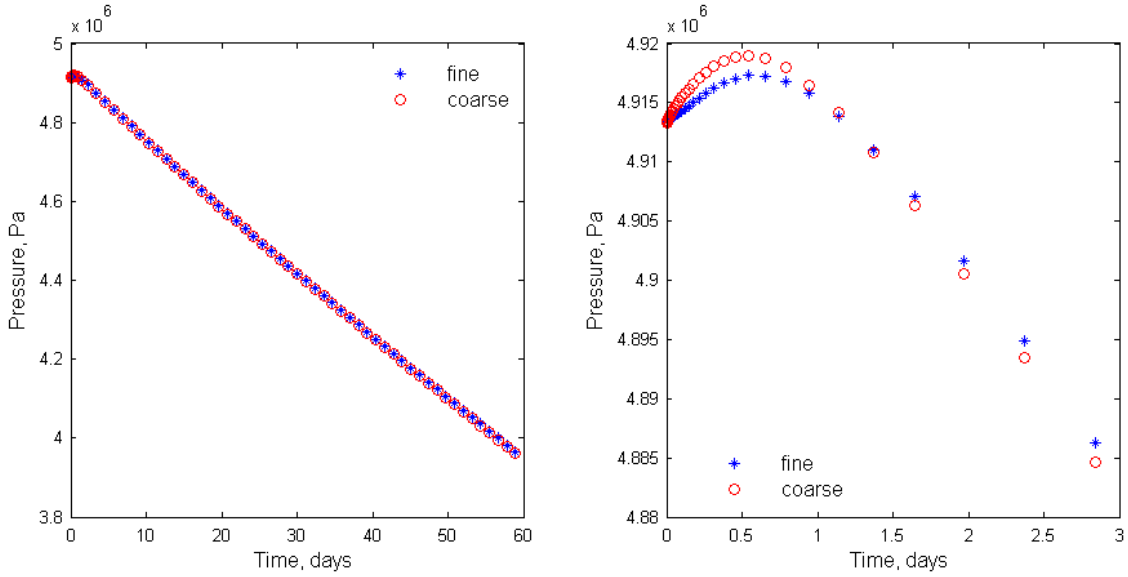

(a) **(b)**

Fig. 6.5—Comparison of the pressure solutions from the FS and CS models at the observation point. (a) There is an excellent agreement of the two solutions during the 60 days of the study. (b) Even at early times in the study, the higher (than the initial) pore pressures from the two models are very close to each other.

Fig. 6.6 shows a good agreement between the local pressure solutions from the FS and CS models at t= 4.75 hrs. Both models capture the pressure rise above its initial level in a large part of the domain (away from the production point), which is caused by mechanical loading.

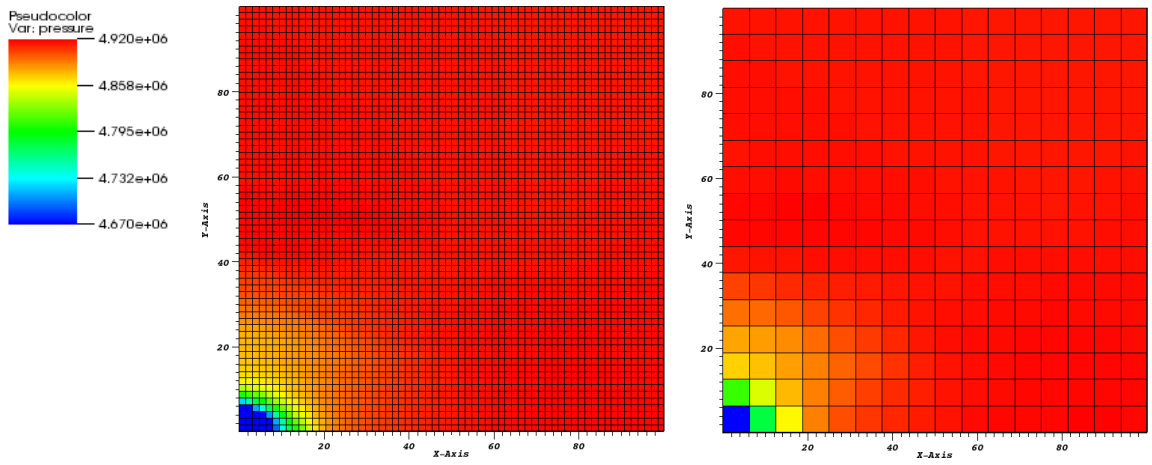

(a) (b)

Fig. 6.6—(a) Pressure (Pa) solutions from the FS model and (b) the CS model at t = 4.6 hrs, showing good agreement and both capturing the pressure rise in large parts of the domain caused by mechanical loading.

Fig. 6.7 and **Fig. 6.8** show the x- and y-direction displacements, respectively, at t = 4.75 hrs. There was a very large displacement at the location of the sink (the result of poroelasticity), where the pressure gradient was at its highest. Negative x- and y-displacements occur near the well, which indicates compression due to the pressure drop near the well.

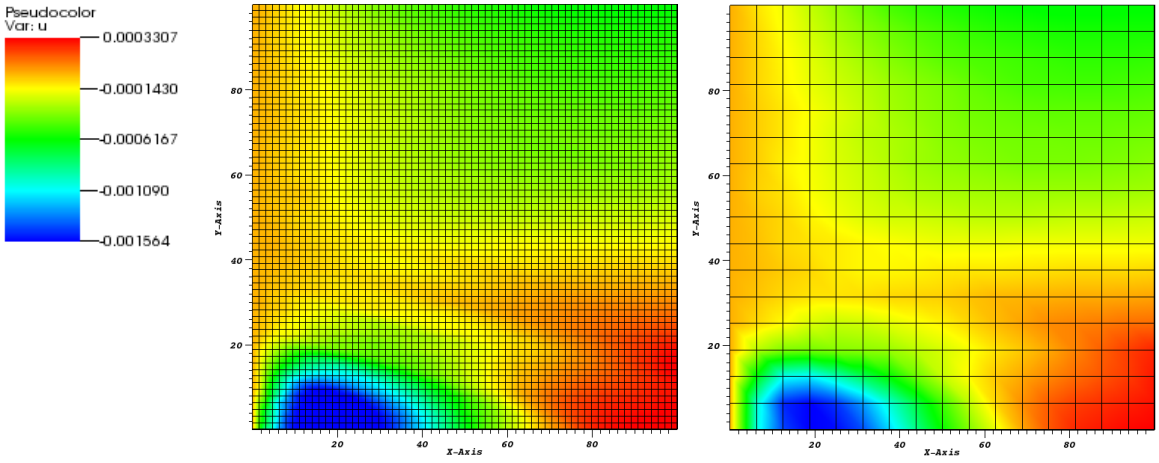

(a) (b)

Fig. 6.7—(a) X-direction displacement (in m) solution from the FS model and (b) the CS model at t = 6.6 hrs. The agreement between the two solutions is good. The x-direction displacement is at its highest near the sink, indicating compression.

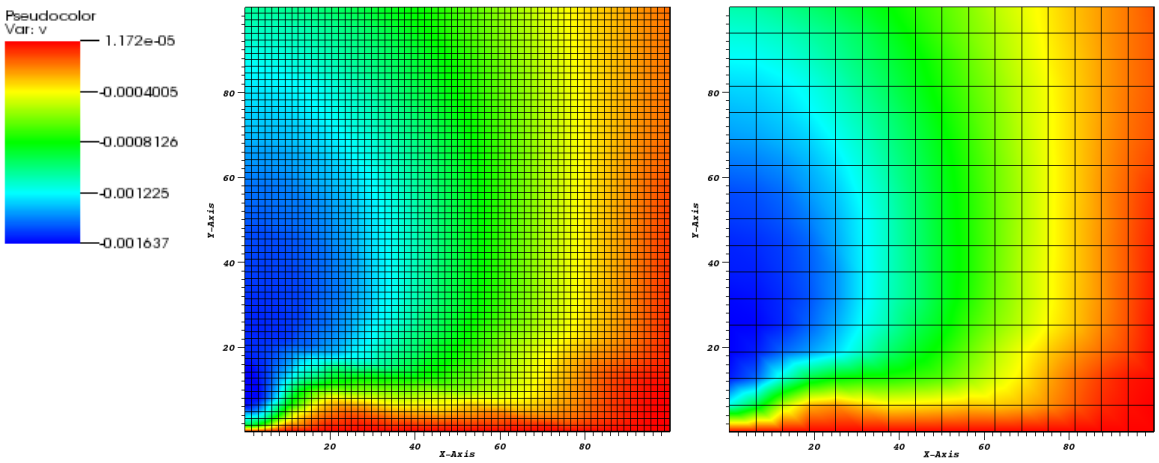

(a) (b)

Fig. 6.8—(a) Y-direction displacement (in m) solution from the FS model and (b) the CS model at t = 6.6 hrs. The agreement between the two solutions is good. As in the case of the x-direction displacement, the y-direction displacement is at its highest near the sink because of compression.

Fig. 6.9 shows the pressure solutions from the two models after 59 days of production. The pressure solution indicates that the fluid in the lower half of the domain had been mainly depleted. This was because of the very low permeability channel in the middle of the reservoir (see **Fig. 6.3(b)**) that inhibited flow from the upper part of the reservoir toward the sink. As a result, the pressure at the upper half of the reservoir remained relatively high compared to that in the lower part. The FS and the CS pressure are in good agreement.

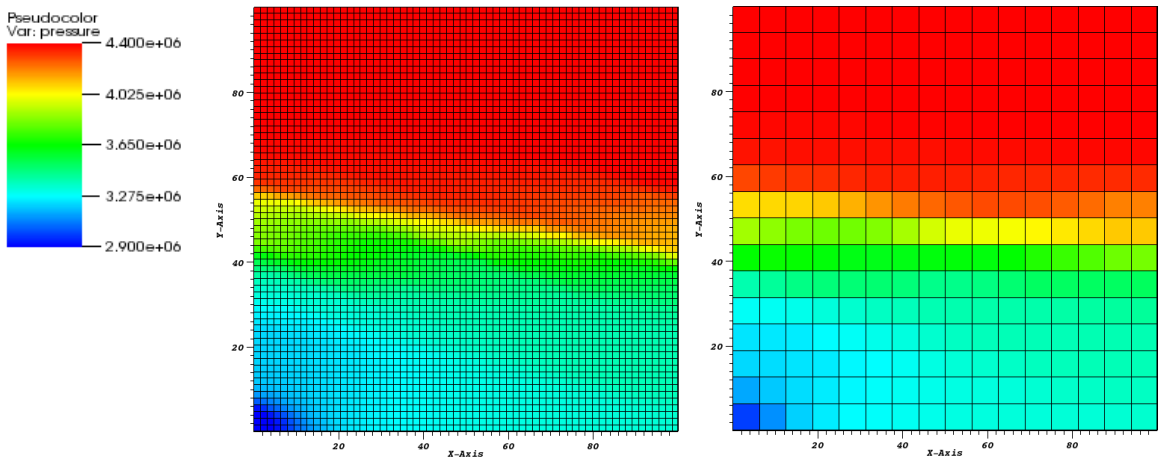

Fig. 6.9—The pressure (Pa) solutions from (a) the FS model and (b) the CS model clearly show the channelized low permeability zone in the middle of the domain that is acting as a barrier, inhibiting fluids from the upper half of the domain to reach to the sink. The two solutions match well.

Fig. 6.10 and **Fig. 6.11** show the x- and y-direction displacements, respectively, after 59 days of production. The displacement solutions clearly show the compaction caused by the mechanical loading. The compaction was at its highest where the mechanical loading was applied. Even though the pressure in the lower region is substantially less than in the upper region, there is no significant difference in the displacements of the two regions. This is because the elastic stiffness tensors of the lower region are higher than those in the upper region. Higher elastic stiffness tensors indicate that a rock is less deformable. The x-displacement map in **Fig. 6.10** shows the regions with higher elastic stiffness tensor are less deformable (shown as green color) than the other regions. The upscaled x- and y-direction displacement solutions match well with the fine scale solutions.

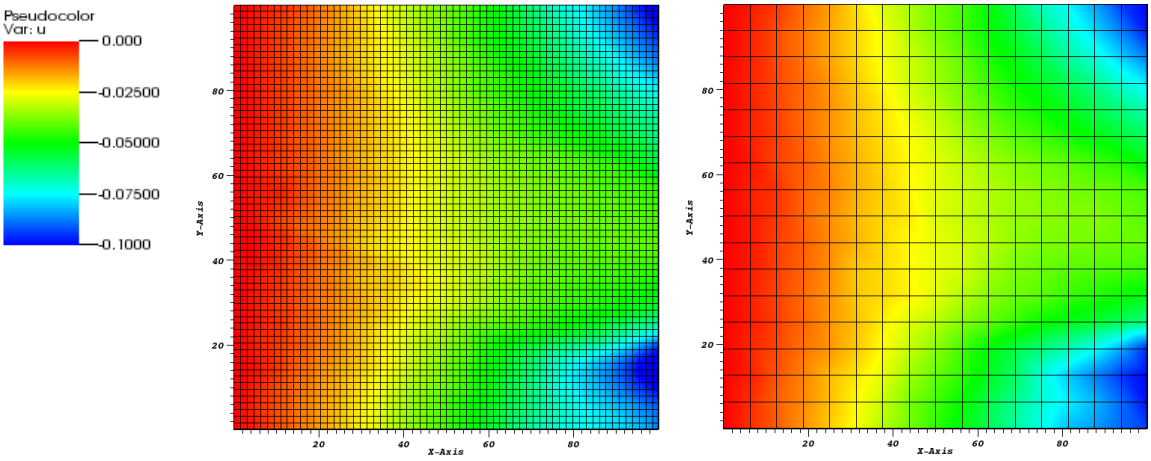

(a) (b)

Fig. 6.10—Comparison of the X-direction displacements (in m) from (a) the FS model and (b) the upscaled CS model. The two solutions agree well.

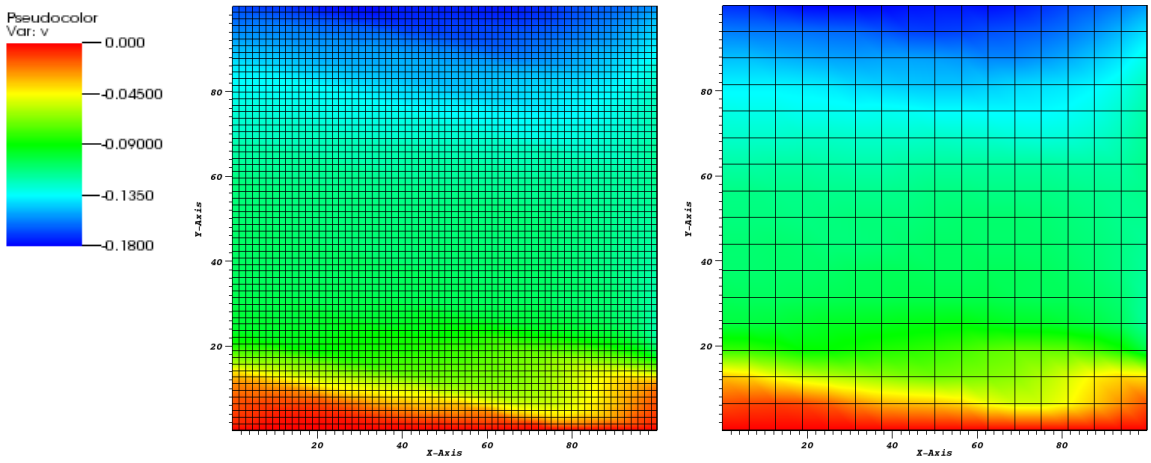

(a) (b)

Fig. 6.11—Comparison of the Y-direction displacements (in m) from (a) the FS model and (b) the upscaled CS model. The two solutions agree well

6.2.2 Consolidation Problem

In this study, I investigated the numerical solution of the consolidation problem shown in **Fig. 6.12**. The size of the reservoir domain is 100 m by 100 m. The domain has a constant pressure boundary on each side (the left and the right ends), and no-flow boundaries at the top and bottom. For the geomechanics problem, it has a roller boundary on the left, right, and bottom boundaries. Traction imposes the overburden stress at the top boundary. Due to the mechanical loading on the top, the system is expected to subside, and the fluid in the reservoir will drain through each constant pressure boundary (left and right). The study does not account for gravitational and capillary effects. The fluid viscosity was 1 cp and the compressibility was $1.0 \times 10^{-10}\ pa^{-1}$. The initial reservoir pressure was 0.1 MPa. The mechanical loading imposed by the traction at the top boundary instantaneously increased the reservoir pressure. Then the pressure decreased continuously because of fluid drainage through left and right boundaries of the domain. The observation point is located near the center of the domain. The CPU time to cover a simulation period of 7.6 days was 198.81 seconds for the FS model and 6.87 seconds for the FS model (i.e., about 29 times faster).

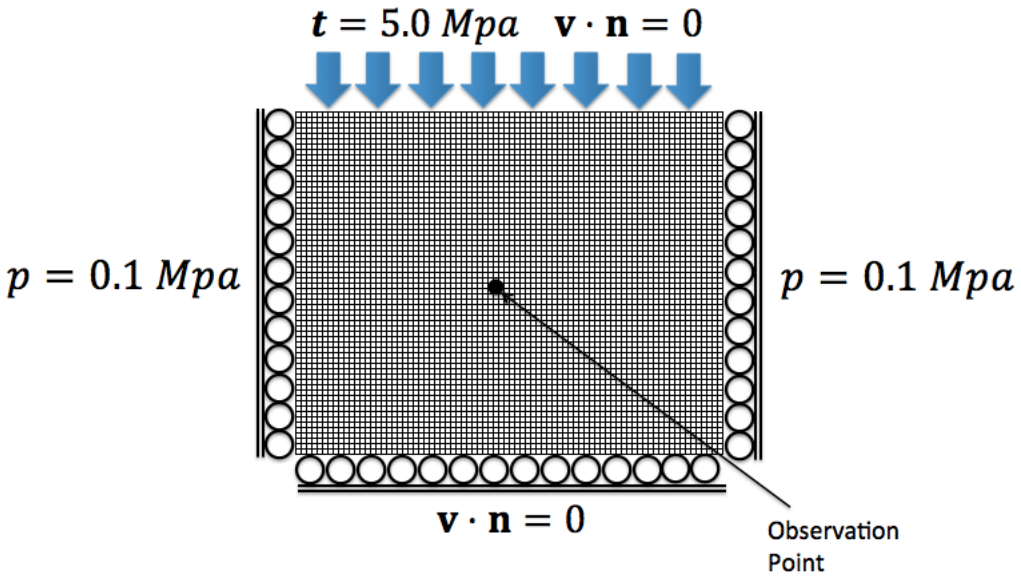

Fig. 6.12—Domain and boundary conditions used in the study of coupled flow and geomechanics in the consolidation problem.

In **Fig. 6.13** I compare the pressure solutions from the FS and CS models at the observation point over the 6.5 days of the simulation period. The agreement is excellent. The pressure decline in **Fig. 6.13(a)** is consistent with the fluid drainage through the boundaries. At the onset of the simulation (**Fig. 6.13(b)**), the pressure rose instantly from 0.1 MPa to 4.5 MPa due to the overburden traction at the top. Then the pore pressure began to decrease, but increased again after several hours before beginning to fall continuously for the rest of the time. This reversal was caused by the increase in the effective stresses near the drainage boundaries, which resulted in higher compression. In addition, the low permeability in the middle of the domain made it difficult for fluid located in that region to flow to the side boundaries, causing an increase in pore pressure (the mechanical response is faster than the pressure propagation). **Fig. 6.14** compares the pressure distributions obtained from the FS and the CS models at t = 6.2 hrs. It clearly shows that the highest pressures occur at the middle of the domain where the permeability is the lowest.

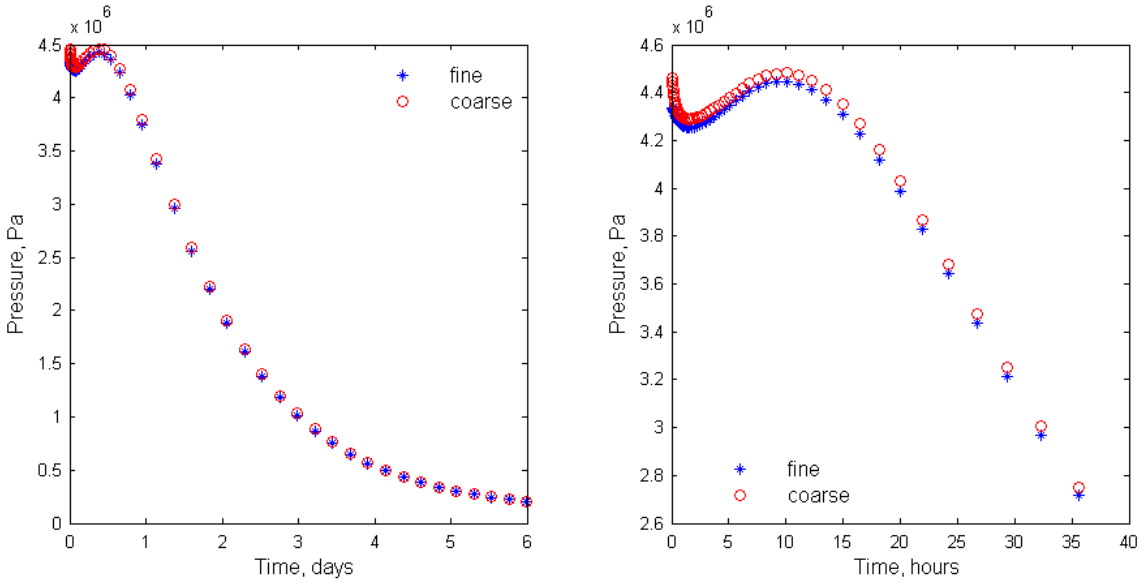

(a) **(b)**

Fig. 6.13—Comparison of the reservoir pressure from (a) the FS and CS models at the observation point during the entire simulation period, and (b) at early times. The agreement of the results of the two models is excellent.

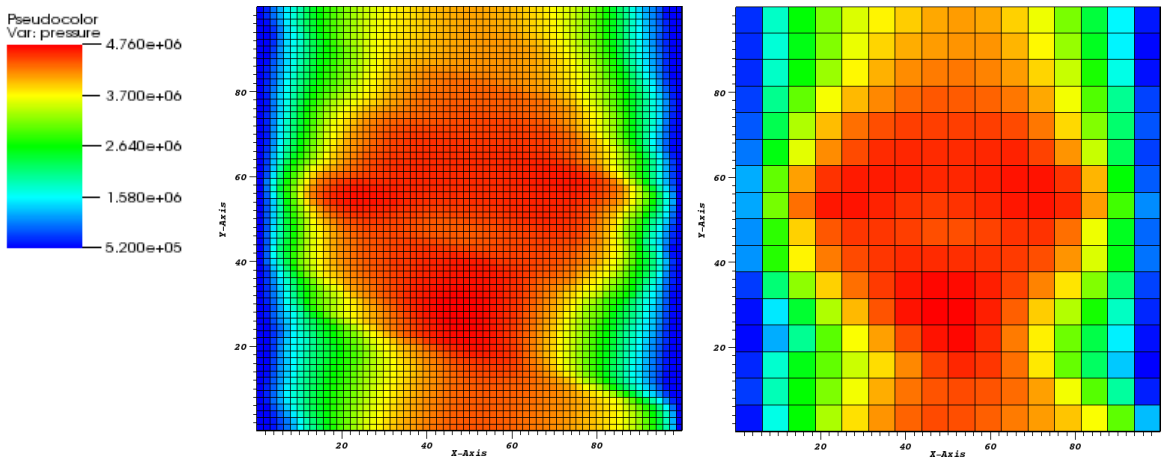

(a) (b)

Fig. 6.14—The pressure (in Pa) distributions from the (a) FS and (b) the CS models at t = 6.2 hrs after the mechanical loading show very good agreement. The highest pore pressure occurs where the permeability is the lowest, thus leading to pore pressure increases due to the mechanical loading.

Fig. 6.15 and **Fig. 6.16** show the x- and y-direction displacement solutions from the FS and CS models, which are in very good agreement. The x-direction displacement is large where the pressure gradient is large (**Fig. 6.15**). As this was a consolidation problem, the largest pressure gradient occurred along the x-direction of the top and bottom regions of the domain (**Fig. 6.14**). This was because these regions have relatively higher permeability and lower values of mechanical properties compared to the middle region. The y-direction displacements in **Fig. 6.15** clearly depict the significant consolidation (compression) caused by the imposed traction.

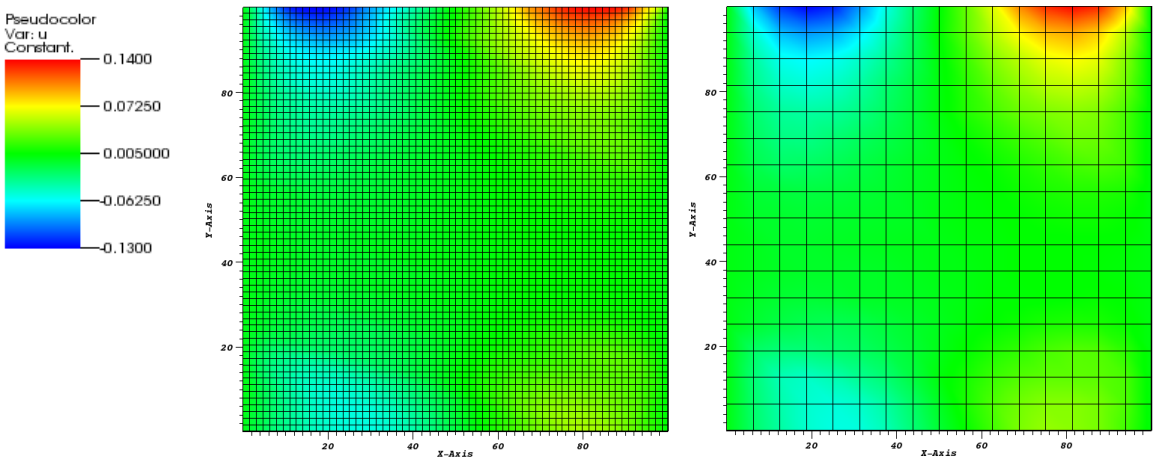

(a) (b)

Fig. 6.15—The X-direction displacement (in m) solutions from (a) the FS and (b) the CS models at t = 6.2 hours after the mechanical loading show a very good agreement. Displacement is large where the pressure gradient is large.

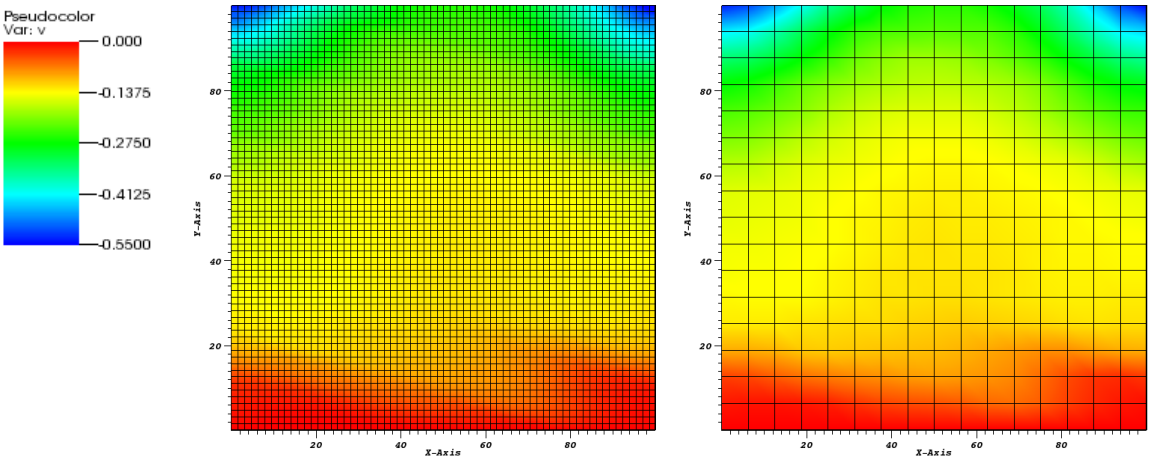

(a) (b)

Fig. 6.16—The Y-direction displacement (in m) solutions from (a) the FS and (b) the CS models at t = 6.2 hours after the mechanical loading show a very good agreement. The consolidation (compression) caused by the imposed traction is evident.

6.2.3 Production from a Tight Gas Reservoir

I applied numerical upscaling of the permeability and of the elastic stress tensors to a problem of production from a tight gas reservoir model. Production from such a reservoir is made possible by induced fractures in the formation, which result in strong heterogeneity. I used the same heterogeneity pattern used in the previous upscaling experiments (see **Fig. 6.3** and **Fig. 6.4**). In order to create permeability and porosity fields typical of a tight gas reservoir, I simply decreased the values used in the earlier upscaling studies. Thus, the porosity was half of that described in **Fig. 6.3 (a),** and permeabilities were smaller than those in **Fig. 6.3 (b)** by a factor of 10^{-3}.

Fig 6.17 shows the resulting porosity and permeability fields. The values of porosity ranged from 0.05 to 0.2 and permeability values ranged from 130 nanodarcy to 1017 μd. As in previous experiments, I used Eq. 4-92 to generate the fine scale mechanical property field. Thus, higher mechanical properties (indicative of high rock strength) corresponded to lower porosity values. I performed a 4×4 upscaling to construct the CS model, used methane as the reservoir gas, and used the Peng-Robinson equation of state (Peng and Robinson 1976) to estimate the gas properties. I imposed a constant flow rate ($2 \times 10^{-7} s^{-1}$) at the lower-left corner of the domain (**Fig. 4.5)**. I assumed isothermal conditions and a reservoir temperature of 30°C. The CPU time to cover 3.2 years of production in the simulation was 1324.4 seconds for the FS model and 91.7 seconds for the CS, i.e., the CS model was over 14 times faster.

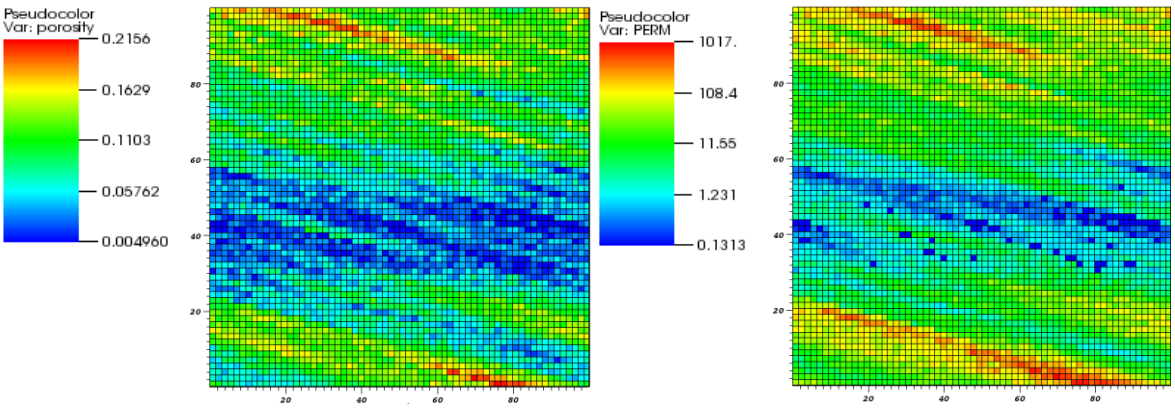

Fig. 6.17—Distributions of (a) porosity and (b) x-direction permeability (in μd) in the tight gas production problem. The x- and y-direction permeability fields are assumed to be the same (isotropic system). The permeability values are up to 10,000 times different.

Fig. 6.18 shows the near-coincidence of the reservoir pressure estimates at the observation point from the FS and CS models. At the beginning of the simulation, both the fine and coarse scale models captured the pressure increase due to mechanical loading (**Fig. 6.18(b)),** and their deviations were practically negligible.

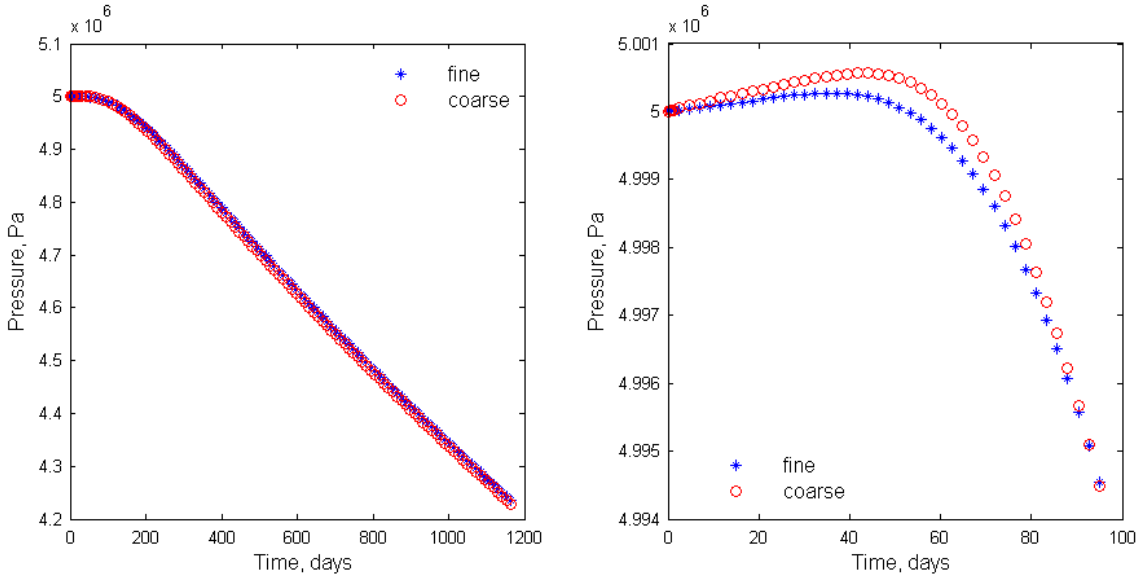

(a) **(b)**

Fig. 6.18—(a) The agreement of the reservoir pressure estimates at the observation point from the FS and CS models is practically perfect, and (b) both models capture the rise in pressure at the beginning of production with negligible deviations.

Fig. 6.19 shows the pressure distributions obtained from the FS and the CS after 146 days of production. Significant pressure drops occurred near the production well and in the high permeability region, but the region with a pressure higher than the initial one is easily discerned. The low permeability zone in the middle of the domain inhibits gas flow toward the production well. The FS and the CS solutions match well.

Fig. 6.20 shows the x-direction displacement solution at t = 146 days. The region near the production well clearly shows the compaction of the rock near the well, which is captured by both the FS and the CS models. The x-direction displacements at the lower left corner of the domain indicate relatively high compaction. This was because the region has relatively high flow properties (permeability and porosity) and low mechanical properties, which made the rock deform easily under the given traction.

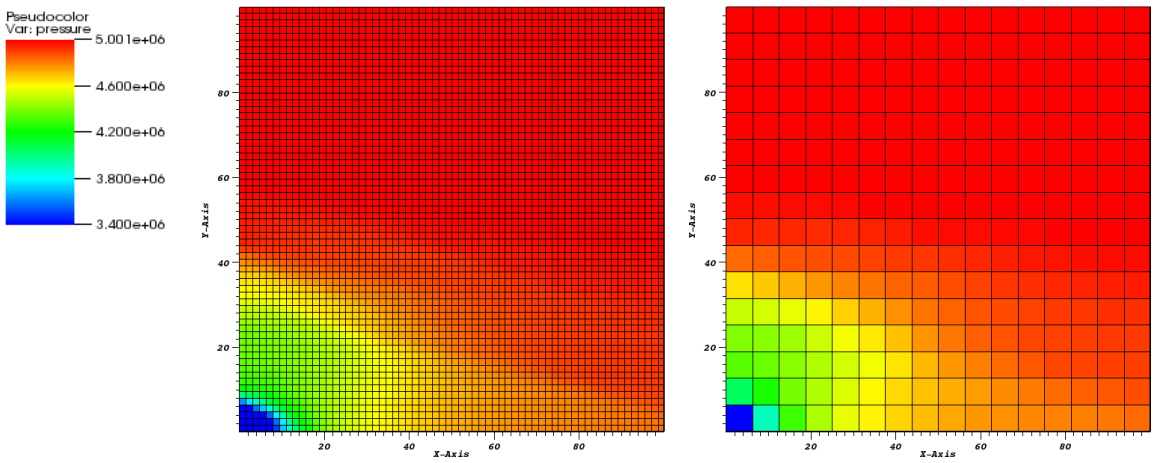

(a) (b)

Fig. 6.19—The pressure (in Pa) distributions from (a) the FS and (b) the CS models after 146 days of production are in good agreement. Note the slight pore pressure increase due to mechanical loading that is captured by both models.

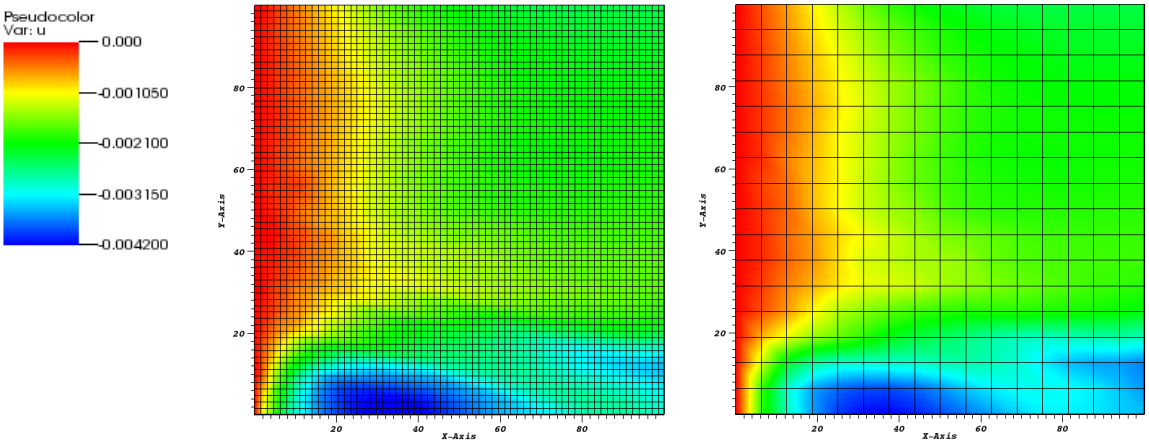

(a) (b)

Fig. 6.20—X-direction displacement (in m) solutions from (a) the FS and (b) the CS models after 146 days of production. The two solutions agree well. The largest x-direction displacement (compaction) occurs near the sink.

Fig. 6.21 shows the y- displacements at t = 146 days. As in the y-direction, there is a good agreement between the FS and the CS solutions. An interesting observation is that compaction along the y-direction is larger than along the x-direction.

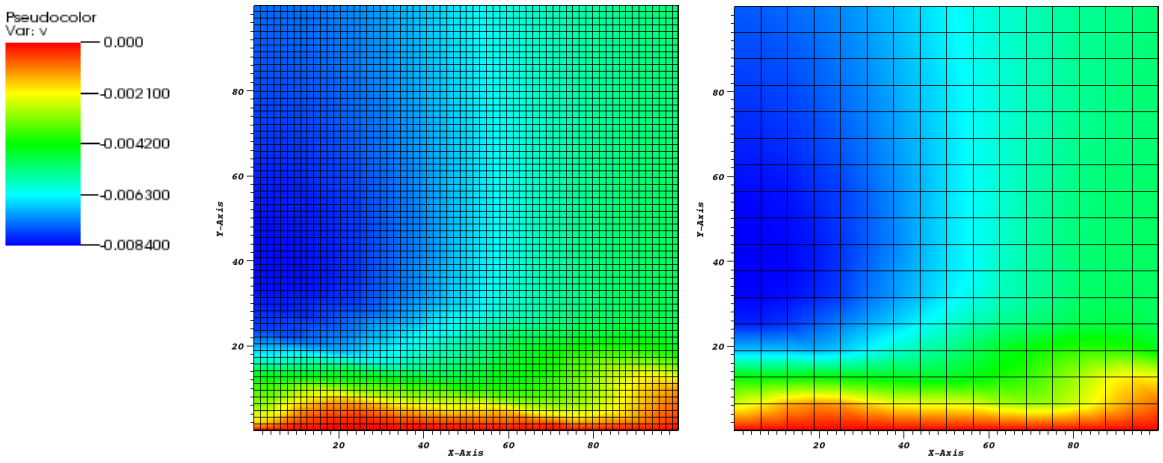

(a) (b)

Fig.6.21—Y-direction displacement (in m) solutions from (a) the FS and (b) the CS model after 146 days of production. The two solutions agree well. As in the x-displacement, the largest y-direction displacement (compaction) occurs near the sink because of the low pressure there.

After 3.2 years of production, I observed that the pressure in the lower half region of the domain notably reduced (**Fig. 6.22**). However, the pressure in the upper half region remained almost same. This is because of the very low permeability of the middle section.

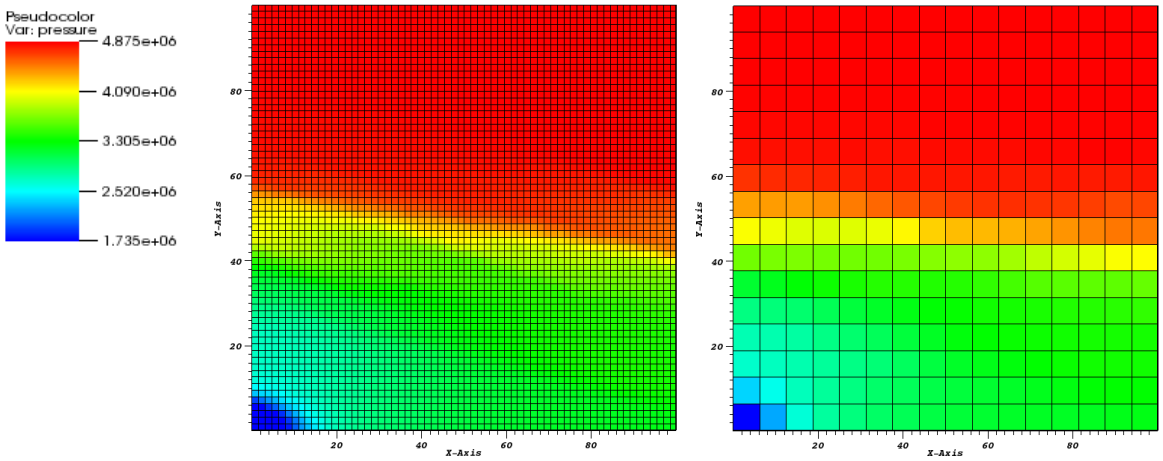

(a) (b)

Fig. 6.22—Pressure (Pa) distributions obtained from (a) the FS and (b) the CS models after 3.2 years of production.

Fig. 6.23 and **Fig. 6.24** show the x- and y-direction displacements solutions, respectively, at t = 3.2 years. The agreement between the two solutions is very good. The x-direction displacements show that compaction was affected by the sideburden; the maximum compaction occurred at the lower right corner of the domain. The y-direction displacements indicate that the domain was consolidated along the y-direction because the pressure in the lower half of the domain decreased considerably and the pressure differentials along the x-direction became very small.

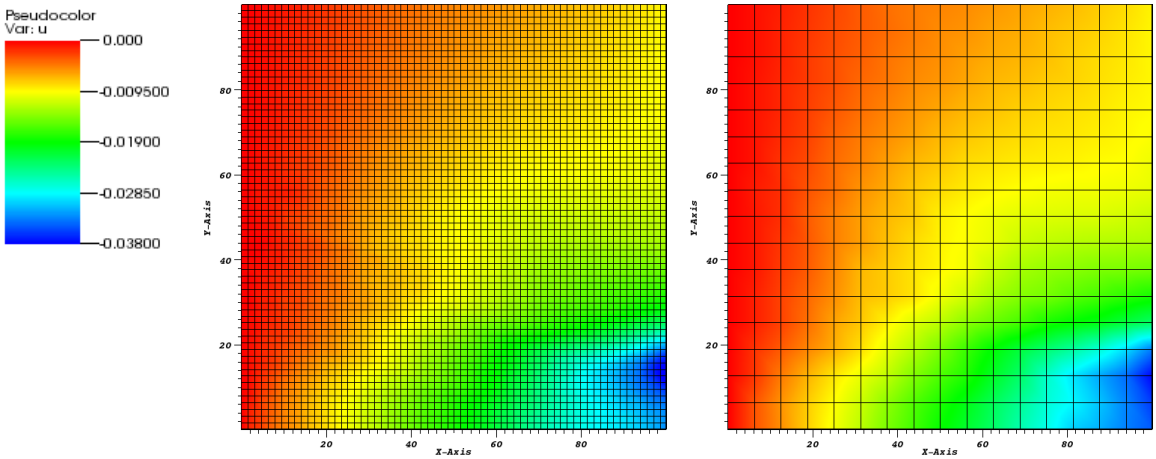

(a) (b)

Fig. 6.23—X-direction displacement (in m) solutions obtained from (a) the FS and (b) the models at t = 3.2 years in the tight gas problem. The very good agreement between the two solutions is obvious.

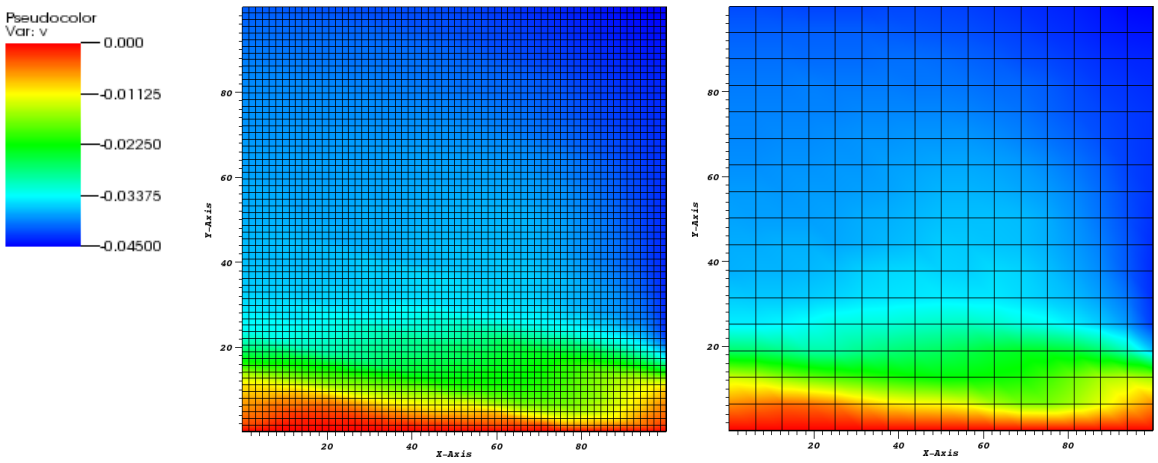

Fig. 6.24—Y-direction displacement (in m) solutions obtained from (a) the FS and (b) the models at t = 3.2 years in the tight gas problem. The two solutions match very well

6.2.4 Waterflooding Simulation

I tested the upscaled multiphysics model in a problem involving waterflooding. I used a *primitive* multiphase flow upscaling, which simply computes the coarse scale saturation in the simulator rather than using pseudo-functions. As previously mentioned, the pseudo-function approach has several drawbacks. First, it is not practical to use for a complex simulation because it needs a large amount of memory to save all the variables. Thus, use of pseudo-functions requires saving all the pseudo-function tables for each coarse gridblock. Furthermore, the pseudo-function tables with limited amounts of data do not adequately represent the pseudo-function curves. Generating a pseudo-function is a time-consuming process because of the need to solve the time-dependent saturation equation for each gridblock until the average saturation becomes nearly one (100% displacement by water). In addition, the pseudo-function approach does not always guarantee a more accurate solution than the primitive models. Under certain conditions, the pseudo-function approach with a standard boundary condition can overestimate the total flow rate in a FS simulation (Chen 2005), and the magnitude of overestimation is even higher than in the primitive upscaling approach.

I used the same FS and CS flow and geomechanical properties (permeability, porosity, and elastic stiffness) I used in the previous experiments (see Sections **6.2.1** and **6.2.2**). The size of the reservoir domain was 100 m by 100 m. The water and oil viscosities were 1 *cp* and 2 *cp* , respectively; their compressibility values were $1.0 \times 10^{-9}\ pa^{-1}$ and $2.0 \times 10^{-9}\ pa^{-1}$, respectively. **Fig. 6.25** shows the 2D reservoir domain (a 2D areal cross section) with boundary conditions. As can be deduced from **Fig. 6.3**, there is a low porosity and permeability zone in the middle of the domain, which makes it difficult for the fluid to flow through. I

located two injection wells at the left corners and two production wells at the right corners. The injected water will easily flow toward the producing wells. The computational time (CPU time) for the CS model was 124 .31 seconds, but that for the FS model was 2483.1 seconds (i.e., about 20 times slower).

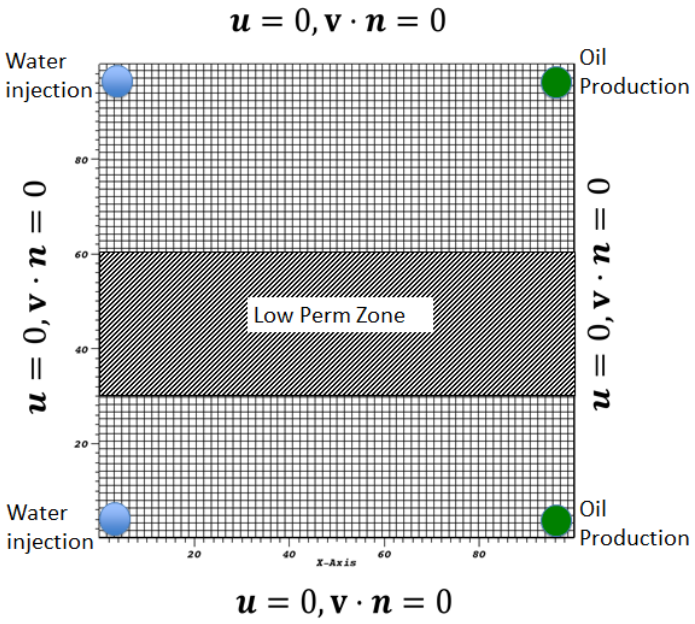

Fig. 6.25—The heterogeneous 2D reservoir domain (a 2D areal cross section) and the boundary conditions used in the upscaling study of the waterflooding problem. The size of the reservoir domain is 100m by 100m. The permeability distribution is described by Fig. 6.3.

Fig. 6.26 shows the saturation and velocity solutions from the FS and CS models at t = 27 days. The CS model captured relatively well the extent of the advancing water saturation front (i.e., the footprint of the invading water front) depicted by the FS model, but could not accurately predict the saturation values. The velocity maps of both the FS and CS models show that the water would not invade the low permeability region, but would flow directly toward the producers located on the other side of the domain through the higher permeability regions.

Fig. 6.27 shows the pressure distributions from the FS and CS models after 27 days of waterflooding, which agree well. These confirm the expectation that the pressure gradient would occur mainly along the x-direction (as controlled by the permeability distributions), thus resulting in velocity vectors with dominant x-direction components. The pressure near the lower left injection well (see **Fig. 6.25**) is higher than that in the vicinity of the upper left injection well because of the lower permeability and porosity at that location.

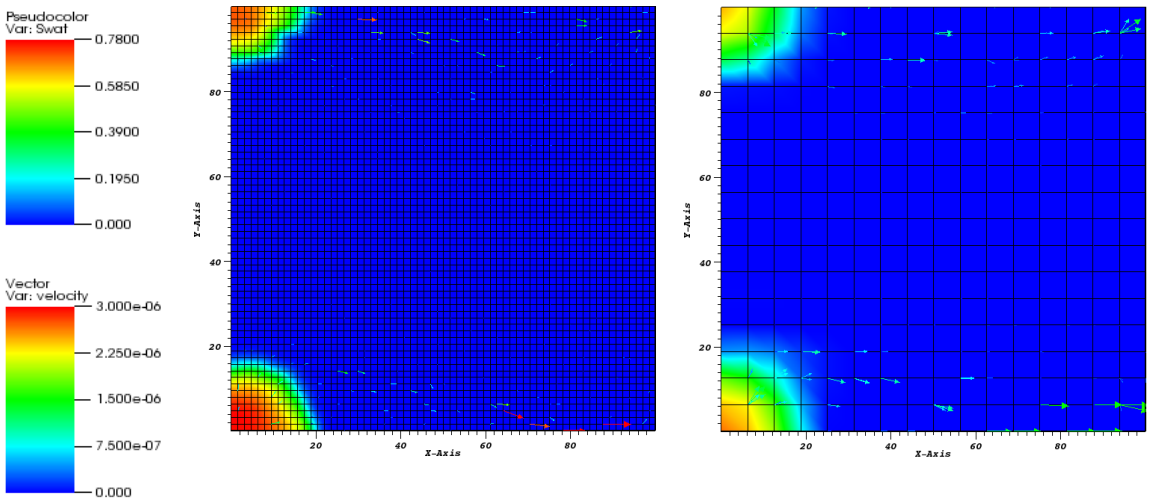

(a) (b)

Fig. 6.26—Waterflooding upscaling problem: saturation and velocity (in m/s) distributions obtained from (a) the FS and (b) the CS models at t = 27 days.

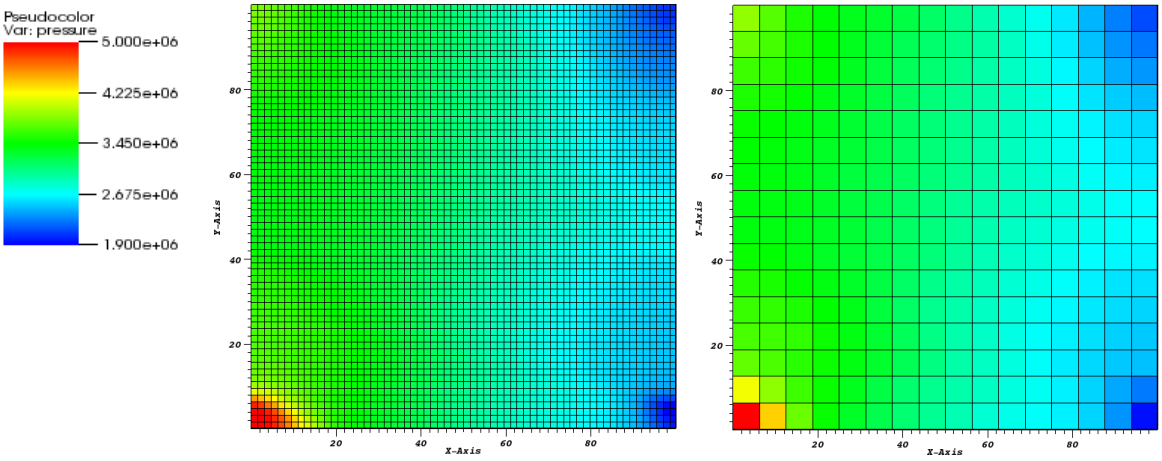

(a) (b)

Fig. 6.27—Waterflooding upscaling problem: the pressure (in Pa) distributions obtained from (a) the FS and (b) the CS models at t = 27 days are in good agreement.

The x-direction displacements indicate their direct dependence on the pressure gradients along the x-direction (**Fig. 6.28**) and show very good agreement between the FS and the CS solutions. The displacements are larger in the upper region of the domain than in the lower region. This is because of the higher porosities in the upper region, and the consequent smaller elastic stiffness tensors there that result in easier and larger rock deformations for a given stress regime.

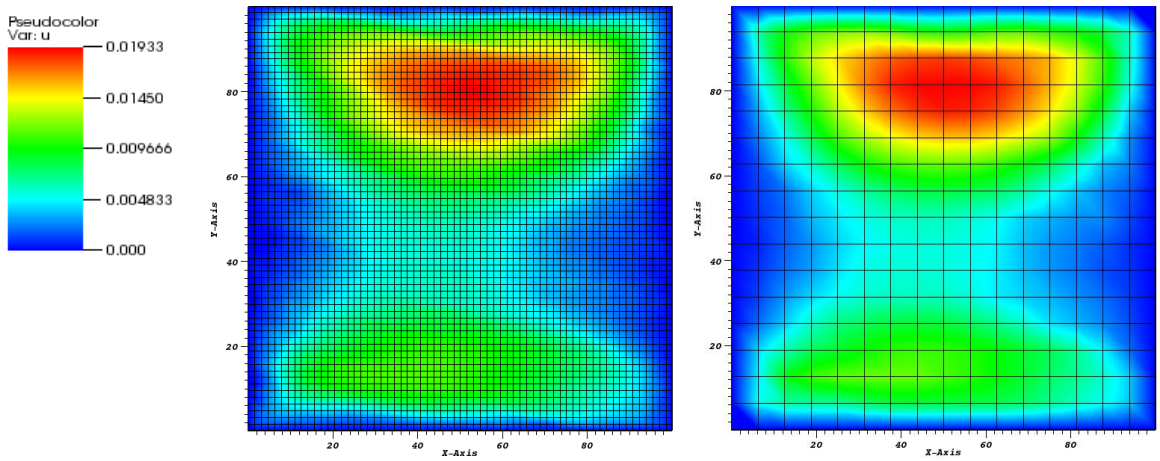

Fig. 6.28—Waterflooding upscaling problem: the x-direction displacement (in m) distributions obtained from (a) the FS and (b) the CS models at t = 27 days are in good agreement.

The y-direction displacements (**Fig. 6.29**) were significantly smaller than the x-displacements because the controlling pressure gradients occurred mainly along the x-direction. Positive displacements occurred near the injection well in the lower region of the domain, and at the production well in the upper region. At the injection well, the increase in pressure due to water injection caused positive deformation along the y-direction. This occurred because of the zero displacement boundary conditions boundaries adjacent to the well, leaving the positive y-displacement (i.e., expansion) as the only possibility. Similarly, the production well in the upper region shows a positive vertical displacement because the pressure drawdown and the zero displacement boundaries in the vicinity allowed rock deformation only in the vertical direction. Similar results were obtained at the remaining two production and injection wells, but these had negative vertical displacements (indicating compression). The CS displacement solution overestimated the negative vertical displacement and underestimated the positive vertical displacement. Overall, **Fig. 6.29** shows that there is a good match between the FS and CS displacement solutions in the x-direction.

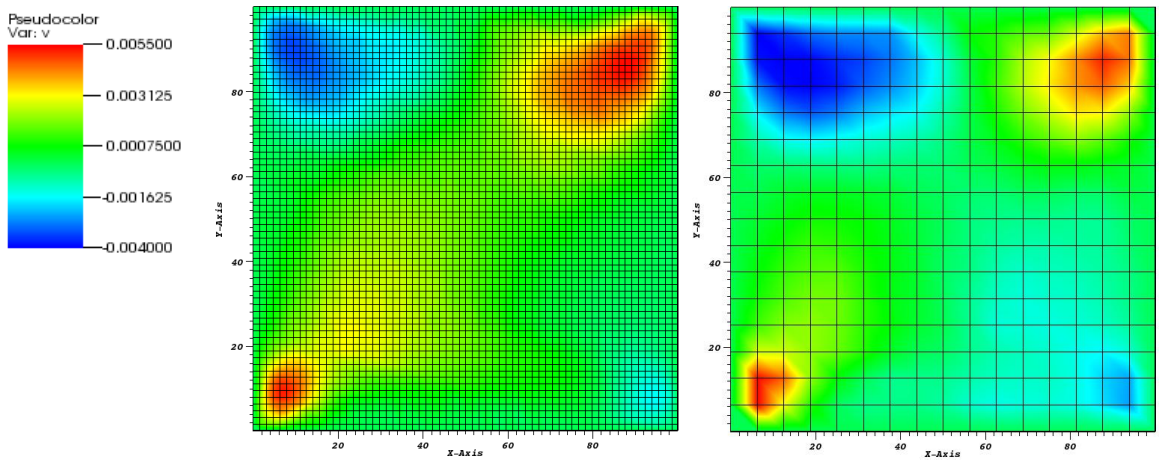

Fig. 6.29—Waterflooding upscaling problem: the Y-direction displacement (in m) distributions obtained from (a) the FS and (b) the CS models at t = 27 days are in good agreement.

At t = 176 days of simulation, the water saturation front had advanced past the middle of the length of the domain. The CS solution captured the important features of the footprint of the invading water saturation front (using the FS solution as the "ground truth"), but predicted a larger area of water invasion. Its performance was less successful in the description of the water saturation levels in the system, which it systematically underpredicted (**Fig. 6.30**). It was difficult to approximate the FS velocity vectors with CS vectors because of the strong heterogeneity of the FS model. Thus, the loss of accuracy in the process of upscaling of the permeability and the elastic stiffness tensors is a major concern. In addition, the use of subgrid modeling led to some loss of the accuracy of the subgrid effect. Despite the loss of some accuracy of the CS saturation solution, it is still a reasonable approximation of the FS solution, over which it maintains a significant advantage.

Figs. 6.31, **Fig. 6.32**, and **Fig. 6.33** show the pressure, the x- and the y-direction displacement solutions, respectively. The results and observations are very similar to those from the previous simulation results corresponding to the state of the system at t = 27 days of waterflooding. In **Figs. 6.31** and **6.32**, there is a good agreement between the FS and the CS solutions; these follow the patterns described in the discussion of **Figs. 6.27** and **6.28,** the conclusions and observations of which they share. The y-direction displacements from both the FS and CS models are consistently smaller than the x-direction displacements, but **Fig. 6.32** clearly shows discrepancies between the solutions from the two models in terms of both extent and magnitude.

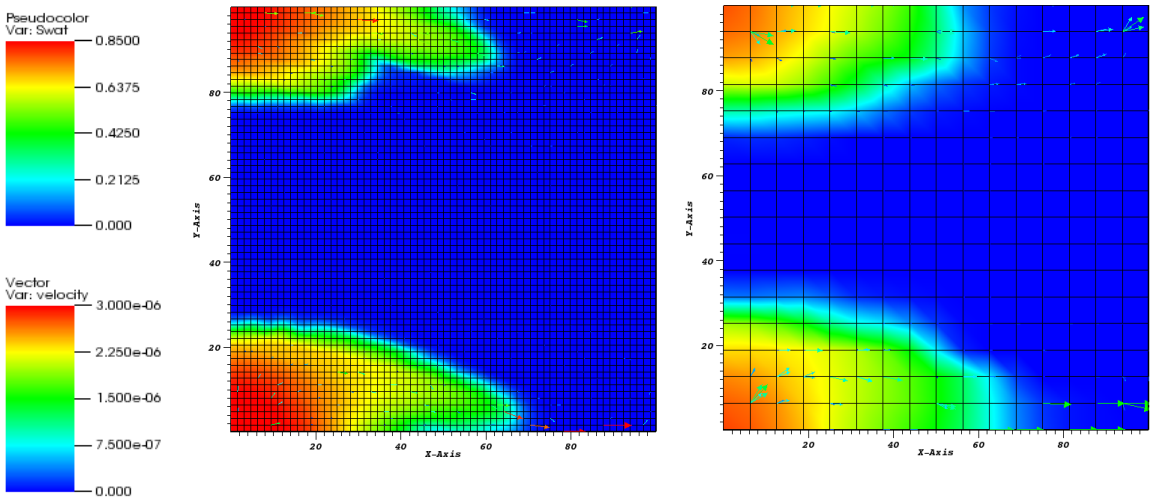

(a) (b)

Fig. 6.30—Waterflooding upscaling problem: saturation and velocity (in m/s) distributions obtained from (a) the FS and (b) the CS models at t = 176 days.

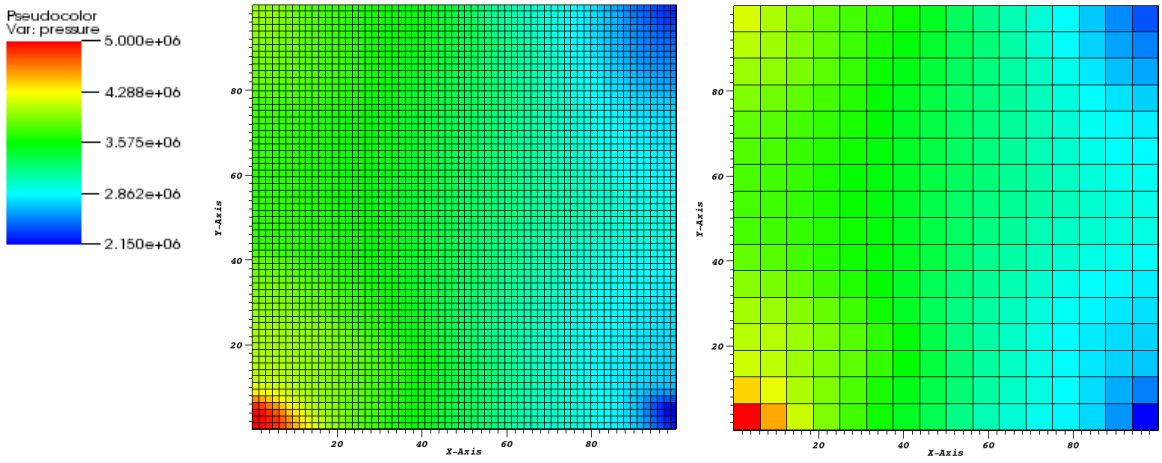

(a) (b)

Fig. 6.31—Waterflooding upscaling problem: the pressure (in Pa) distributions obtained from (a) the FS and (b) the CS models at t = 126 days are in good agreement.

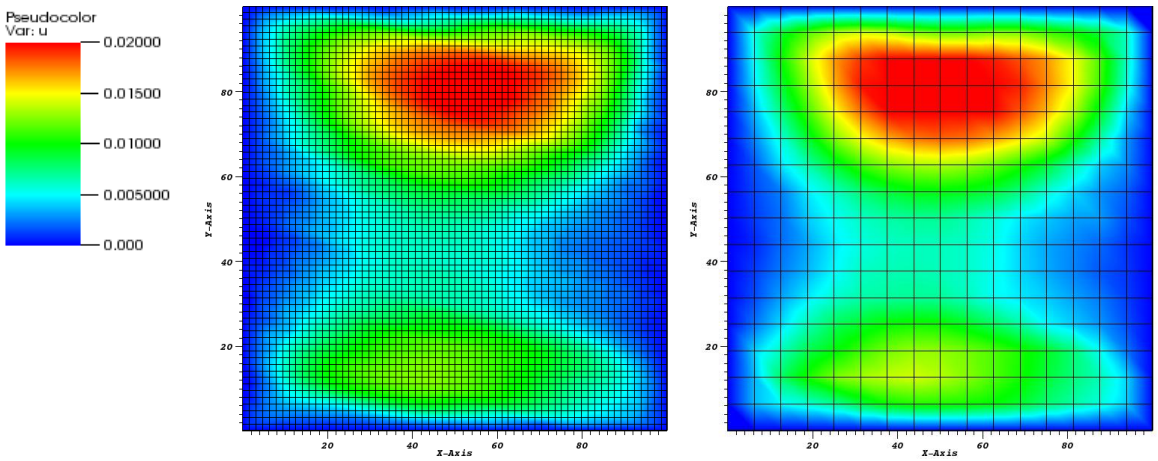

(a) (b)

Fig. 6.32—Waterflooding upscaling problem: the X-direction displacement (in m) distributions obtained from (a) the FS and (b) the CS models at t = 176 days are in good agreement.

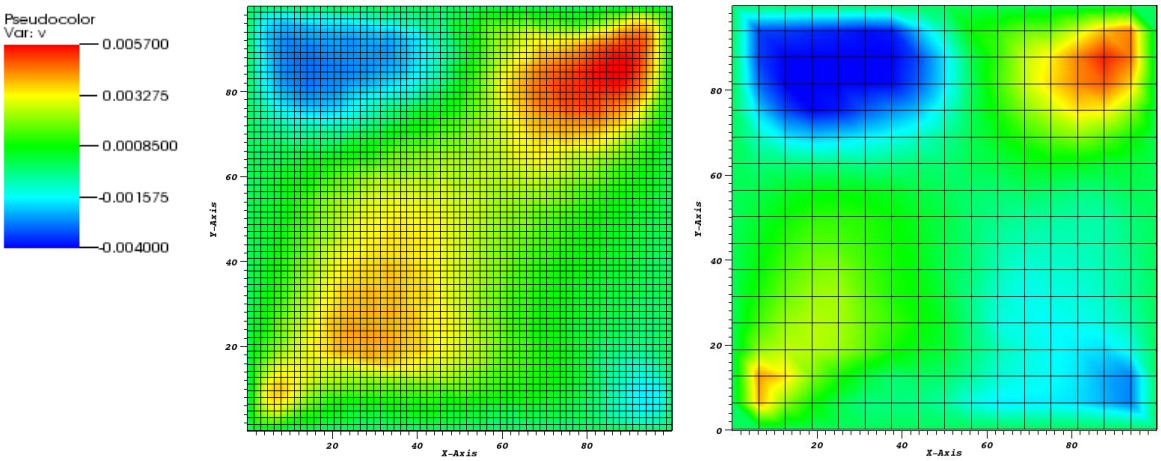

(a) (b)

Fig. 6.33—Waterflooding upscaling problem: the Y-direction displacement (in m) distributions obtained from (a) the FS and (b) the CS models at t = 27 days are in good agreement.

The results of the waterflooding experiment indicate that the CS solution was a good approximation of the FS solution in some of the variables of interest, such as pressure and x-displacements. Its performance is less successful in the prediction of the saturation and the y-displacement distributions, but it still manages to capture all the key features of the distributions can serve as a valuable numerical upscaling process for multiphase flow problems due to its very favorable computation cost.

CHAPTER VII

SUMMARY, CONCLUSIONS AND RECOMMENDATIONS FOR FUTURE WORK

7.1 Summary

In this work I developed a geomechanical reservoir simulator that is fully implicit and uses a fully coupled flow and geomechanics approach to model multiphase flow and rock deformation in a heterogeneous and/or fractured reservoir system. I proposed and implemented a mixed finite element formulation of the pressure and velocity equations in order to obtain more accurate velocity solutions and to satisfy local mass conservation. For the geomechanical equilibrium equations I used a continuous Galerkin finite element formulation which is widely used in the geomechanics community. The advances proposed in this simulator include:

- The ability to model 2D or 3D compressible (gas) and/or slightly compressible (liquid) multiphase flow in heterogeneous and deformable porous media.
- More accurate (and continuous) descriptions of the velocity solutions.
- Better resolution of the saturation solution.
- The ability to realistically model complex geometry of a reservoir using unstructured meshes.
- The incorporation of full tensor permeability and elastic stiffness in the simulation model.

As secondary contributions of this work, I presented a methodology to numerically upscale the permeability and elastic stiffness tensors in order to obtain a coarse-scale description of the given fine-scale multiphysics model. This upscaling approach was implemented it in the simulator. The advantages of this upscaling work are as follows:

- The ability to effectively model both the complex physics and the heterogeneity for coupled flow and geomechanics problems at scales which are more tenable in terms of computation times.
- Improvement of the efficiency of the numerical computation especially for multiphysics, heterogeneous, and large scale problems.

7.2 Conclusions

For this work, I derived a fully coupled system of nonlinear equations to describe multiphase flow in deformable porous media and generated a finite element formulation to simultaneously solve for pressure, saturation, velocity, and displacement. The proposed finite element formulation allows the use unstructured grid meshes for a reservoir with a complex geometry. A fully implicit Newton-Raphson framework was implemented to address highly nonlinear problems such as multiphase flow behavior with compressible fluids, as well as changes in porosity and permeability with respect to primary variables (*i.e.,* pressure, saturation and displacement).

I verified the code using analytical solutions where possible — in this case, the 1D solution was used and good agreement between the numerical and analytical solutions was observed. I also compared this code with a decoupled simulation code for a synthetic reservoir system, which showed the major differences and the importance of coupled flow and geomechanics. I also tested the simulator with full tensor permeability and elastic stiffness by making orthogonal rotations of the permeability and elastic stiffness tensors. I utilized a single crack and a random permeability field to test the saturation solution and I show that the proposed approach provides better resolution of the saturation solution than the discontinuous Galerkin method.

As a synthetic application of a field case, I used the proposed code to model a tight gas reservoir system saturated with water and gas and having a high permeability subdomain. For this particular case I observed significant rock deformation during the production period. In addition, I found that the water saturation increases when the pore space in the rock is reduced due to deformation (which is intuitive given that water is the wetting fluid).

Using unstructured meshes, I can locally refine the area in which I want to obtain a higher degree of accuracy for the numerical solution (*i.e.*, near well and/or fractures). I next applied the code and unstructured meshes to model a tight gas reservoir system with both a single discrete fracture and multiple discrete fractures. By generating the high-resolution discrete fracture models with unstructured meshes, I found that I could identify more detailed flow features than using a structured mesh. As would be expected, I observed much higher flow velocities inside the discrete fracture(s) than for the native reservoir rock. I specifically observed changes in the displacement field caused by fractures and the porosity reduction caused by depressurization. Intuitively, the large pressure gradients inside the fracture permit closure of the fracture(s), which substantially lowers the flow rate inside the fracture over time — these features were observed directly in the simulation cases generated for this part of the work.

As a validation study, I generate a numerical upscaling of the coupled flow and geomechanics problem for a highly heterogeneous system. I used a flow solver with a mixed finite element discretization to solve for both pressure and velocity fields in order to conduct the flow-based upscaling. I used a mechanics solver that has a continuous Galerkin discretization to solve for the displacement. I conducted a 4×4 upscaling that reduced 4096 cells to 256 cells. The upscaled permeability and elastic stiffness tensors were used for fully coupled flow and geomechanics simulations.

I conducted four numerical experiments to test the fine-scale and coarse-scale solutions. The numerical experiments clearly showed that the numerical simulation at the coarse-scale model captured the salient multiphysics features of the fine scale model. These numerical experiments also show why heterogeneity is a critical factor that affects the numerical solutions for both flow and geomechanics.

Comparison of the upscaled solution with the fine-scale solution indicates that the upscaled solution matches well with the fine-scale solution with very favorable computational efficiency. Although an observation that may be specific to the cases tested, the results obtained suggest that numerical upscaling can be applied to a very heterogeneous reservoir system when a coupled flow and geomechanics solution is desired.

7.3 Recommendations for Future Work

In this work I limited my investigations to a linear elasticity to model the deformation of rock. However, nonlinear plastic deformation or damage propagation should also be modeled to obtain a more realistic behavior for a given fracture(s) in the reservoir. I identified that stress concentrations near the tips of the fracture could result in plastic deformation followed by generation of a secondary fracture. Using the fully implicit Newton-Raphson framework, nonlinear plasticity and damage models should be relatively straight-forward to implement.

Adaptive grid refinement would be an interesting feature to add to model fracture propagation. One could begin with a coarse mesh that is locally refined in each time step using an error estimator. In modeling fracture propagation, the saturation front and the region where the fracture begins to propagate would then be adaptively refined. This is not a trivial undertaking due to the re-gridding that would be required (conceivably from time-step to time-step), but adaptive grid refinement would significantly enhance the resolution of both small-scale and medium-scale flow and geomechanical features.

Parallel computing is a required component for constructing numerical solutions for large-scale multiphysics problems. An object-oriented programming framework in the C++ finite element library allows us to implement parallel computing packages (*i.e.*, PETSc and Trilinos) as a module. Implementation of the proposed solution in a parallel computing domain should be a near-term priority (as a recommendation).

In this study, only synthetic reservoir models were used to establish and evaluate the capabilities of the TAM-CFGM simulator. Extensive numerical experiments should be performed to better evaluate the flow and geomechanical physics — as an example, I used the same magnitude of traction vectors for the vertical and horizontal stress fields. It is recommended that different values of these traction vectors should be used because these traction vectors can induce different stress states in the system, and in reality, most (if not all) subsurface formations have different values of in-situ stresses.

It is strongly recommended that numerical experiments be performed with capillary pressure capabilities included in the model — in particular, for the case of fractured reservoir systems. We would note that capillary pressure will affect both fracture flow and flow in the native-state reservoir rock system. Lastly, gravity effects should also be included in these types of models; although the effects are assumed to be small, there is no guarantee that the effect will be negligible, especially for gas-water flow systems.

NOMENCLATURE

TAM-CFGM	=	Texas A&M Coupled Flow and Geomechanics Simulator
CS	=	Coarse-scale
FS	=	Fine-scale
M^k	=	Accumulation of a component k, kg/m^3
$\boldsymbol{F}^k$	=	Flux vector of a component k, kg/m^2s
q^k	=	Source and sink of component k, kg/m^3s
$\boldsymbol{n}$	=	Normal vector, dimensionless
TPFA	=	Two point flux approximation
MPFA	=	Multi point flux approximation
IC	=	Iteratively-coupled
ρ_f	=	Fluid density, kg/m^3
$\tilde{\mathbf{v}}$	=	Interstitial fluid velocity, m/s
$\mathbf{v}_s$	=	Solid phase velocity, m/s
$\tilde{\mathbf{v}}_{\boldsymbol{fs}}$	=	Relative interstitial velocity of the fluid with respect to the solid phase, m/s
$\boldsymbol{k}$	=	Second order permeability tensor, *md* or m^2
c_f	=	Compressibility of fluid, 1/Pa
$\boldsymbol{u}$	=	Displacement vector, *m*
b	=	Biot's coefficient, dimensionless
K_s	=	solid grain stiffness, Pa
ε_v	=	Volumetric strain, dimensionless
M_g	=	Molar mass of the gas, g/mol or kg/kmol
Z_g	=	Compressibility of the gas, dimensionless
R	=	Gas constant, J/mol-Kelvin or J/kmol-Kelvin
T	=	Absolute temperature, Kelvin
$\boldsymbol{\sigma}$	=	Total Cauchy stress tensor, Pa
$\boldsymbol{\sigma}'$	=	Effective stress tensor, Pa
$\boldsymbol{\sigma_0}$	=	Initial total stress tensor, Pa
$\boldsymbol{I}$	=	Second order identity tensor, dimensionless
ρ_b	=	Bulk density, kg/m^3
λ	=	First Lamé's constant, Pa
μ	=	Second Lamé's constant (shear modulus), Pa
$\boldsymbol{k}_{ref}$	=	Reference permeability tensor, *md* or m^2

ϕ_{ref}	=	Reference porosity, dimensionless
γ	=	Experimentally determined constant, dimensionless
$\tilde{\mathbf{v}}_{\boldsymbol{g}}$	=	Interstitial velocity of gas phase, m/s
$\tilde{\mathbf{v}}_{\boldsymbol{w}}$	=	Interstitial velocity of water phase, m/s
ρ_g	=	Gas phase density, kg/m^3
ρ_w	=	Water phase density, kg/m^3
p_t	=	Total pressure, Pa
p_{cg}	=	Capillary pressure between gas and water, Pa
$\mathbf{v}_t$	=	Total velocity, m/s
k_{rw}	=	Relative permeability of water phase, dimensionless
k_{rg}	=	Relative permeability of gas phase, dimensionless
λ_w	=	Mobility of water phase, 1/cp
λ_g	=	Mobility of gas phase, 1/cp
λ_t	=	Total mobility, 1/cp
F_w	=	Fractional flow of water phase, dimensionless
Ω	=	Domain
Γ	=	Boundary
DG	=	Discontinuous Galerkin
$\boldsymbol{E}$	=	Fourth order elastic stiffness tensor, Pa
$[RHS]$	=	Right hand side vector
U	=	Strain energy per unit volume, J/m^3

REFERENCES

Aavatsmark, I. 2002. An introduction to multipoint flux approximations for quadrilateral grids. *Computational Geociences* **6** (3-4): 405–453.

Aavatsmark, I., Barkve, T., and Mannseth, T., 1996. Discretization on Non-Orthogonal, Quadrilateral Grids for Inhomogeneous, Anisotropic Media. J*ournal of Computational Physics* **127** (1): 2–14. http://dx.doi.org/10.1006/jcph.1996.0154.

Allen, D.R. 1972. Environmental Aspects of Oil Producing Operations-Long Beach, California. *Journal* of *Petroleum Technology* **24** (2): 125–131. 3450-PA. http://dx.doi.org/10.2118/3450-PA.

Aziz, K. and Settari, A. 1979. Petroleum Reservoir Simulation. Applied Science Publishers Ltd., London.

Bagheri, M. and Settari, A. 2006. Effects of fractures on reservoir deformation and flow modeling. *Can. Geotech. J.* **43** (6): 574–586. http://dx.doi.org/10.1139/t06-024.

Bagheri, M. and Settari, A. 2008a. Modeling of Geomechanics in Naturally Fractured Reservoirs. *SPE Reservoir Evaluation & Engineering* **11** (1): 108–118. SPE-93083-PA. http://dx.doi.org/10.2118/93083-PA.

Bagheri, M. and Settari, A. 2008b. Modeling Fluid Flow in Deformable Fractured Reservoirs using Full Tensor permeability. Paper SPE 113319 presented at the 2009 SPE Europec/EAGE Annual Conference and Exhibition, Rome, Italy, 9-12 June http://dx.doi.org/10.2118/113319-MS.

Bai, M., Elsworth, D., and Roegiers, J.-C. 1993a. Modeling of naturally fractured reservoirs using deformation dependent flow mechanism. *Int. J. Rock Mech. Min. Sci. & Geomech. Abstr.* **30** (7): 1185–1191. http://dx.doi.org/10.1016/0148-9062(93)90092-R.

Bai, M., Elsworth, D., and Roegiers, J.-C. 1993b. Multiporosity/multipermeability approach to the simulation of naturally fractured reservoirs. *Water Resources Research* **29** (6): 1621–1633. http://dx.doi.org/10.1029/92WR02746.

Bai, M., Meng, F., Roegier, J.C., and Abousleiman, Y. 1998. Modeling Two-Phase Fluid Flow and Rock Deformation in Fractured Porous Media. *Poromechanics*, Balkema, Rotterdam.

Bandis, S.C., Lumsden, A.C. 1983. Fundamentals of rock fracture deformation. *Int. J. Rock Mech. Min. Sci. Geomech. Abstr.,* **20** (6): 255–279.

Bangerth, W. 2006. The deal.II tutorial: step-20. http://dealii.org/developer/doxygen/deal.II/step_20.html/

Bangerth, W., Hartmann, R., and Kanschat, G. 2007. deal.II—a general purpose object oriented finite element library. *ACM Transactions on Mathematical Software* **33** (4): 24–27.

Barker, J.W. and Fayers, F.J. 1994. Transport Coefficients for Compositional Simulation with Coarse Grids in heterogeneous Media. *SPE Advanced Technology Series* **2** (2): 103–112. SPE-22591-PA. http://dx.doi.org/10.2118/22591-PA.

Barker, J.W. and Thibeau, S. 1997. A Critical Review of the Use of Pseudo Relative Permeabilities for Upscaling. *SPERE* **12** (2): 138–143. SPE-35491-PA. http://dx.doi.org/10.2118/35491-PA.

Begg, S.H, Carter, R.R., and Dranfield, P. 1989. Assigning Effective Values to Simulator Gridblock Parameters for Heterogeneous Reservoirs. *SPE Journal* **4** (4): 455–463. SPE-16754-PA. http://dx.doi.org/10.2118/16754-PA.

Boe, O. 1994. Analysis of an upscaling method on conservation of dissipation. *Transport in Porous Media* **17** (1): 77–86. http://dx.doi.org/10.1007/BF00624051.

Biot, M.A. 1941. General Theory of Three-Dimensional Consolidation. *J. Appl. Phys.* **12** (155): 154–164. http://dx.doi.org/10.1063/1.1712886.

Buckley, S.E and Leverett, M.C. 1942. Mechanism of Fluid Displacement in Sands. *AIME* **146** (1): 107–116. 942107-G. http://dx.doi.org/10.2118/942107-G.

Chalon, F., Mainguy, M., Longuemare, P., and Lemonnier, P. 2004. Upscaling of elastic properties for large scale geomechanical simulations. *Int. J. Numer. Anal. Meth. Geomech* **28** (11): 1105–1119. http://dx.doi.org/10.1002/nag.379.

Chavent, G. and Roverts, J.-E. 1991. A unified physical presentation of mixed, mixed-hybrid finite element method and standard finite difference approximations for the determination of velocities in water flow problems. *Advances in Water Resources* **14** (6): 329–347. http://dx.doi.org/10.1016/0339-1708(91)90020-O.

Chen, Y. 2005. Upscaling and Subgrid Modeling of Flow and Transport in Heterogeneous Reservoirs. PhD dissertation, Stanford University, Stanford, California.

Chen, Y. and Durlofsky, L.J. 2006. Efficient incorporation of global effects in upscaled models of two-phase flow and transport in heterogeneous formations. *Multiscale Model. Simul.* **5** (2): 445–475. http://dx.doi.org/10.1137/060650404.

Chen, Y. and Durlofsky, L.J. 2008. Ensemble-Level Upscaling for Efficient Estimation of Fine Scale Production Statistics. *SPE Journal* **13** (4): 400–411. SPE-106086-PA. http://dx.doi.org/10.2118/106086-PA.

Chen, Y., Durlofsky, L.J., Gerritsen, M., and Wen, X.H. 2003. A coupled local-global upscaling approach for simulating flow in highly heterogeneous formations. *Advances in Water Resources* **26** (10): 1041–1060. http://dx.doi.org/10/1016/S0309-1708(03)00101-5.

Christie, M.A. 1996. Upscaling for Reservoir Simulation. *JPT* **48** (11): 1004–1010. SPE-37324-MS. http://dx.doi.org/10.2118/37324-MS.

Christie, M.A. 2001.Flow in Porous Media–Scale Up of Multiphase Flow. *Current Opinion in Colloid and Interface Science* **6** (3): 236–241. http://dx.doi.org/10.1016/S1359-0294(01)00087-5.

Christie, M.A. and Blunt, M.J. 2001. Tenth SPE Comparative Solution Project: A Comparison of Upscaling Techniques. *SPEREE* **4** (4): 308–317. SPE-72469-PA. http://dx.doi.org/10.2118/72469-PA.

Christie, M.A., Mansfield, M., and King, P.R. 1995. A Renormalization-based upscaling technique for WAG Floods in Heterogeneous Reservoirs. Paper SPE 29127 presented at the SPE Reservoir Simulation Symposium, San Antonio, Texas, 12–15 February. http://dx.doi.org/10.2118/29127-MS.

Chueh, C.C., Secanell, M., Bangerth, W., and Djilali, N. 2010. Multi-level adaptive simulation of transient two-phase flow in heterogeneous porous media. *Computers & Fluids* **39** (9): 1585–1596. http://dx.doi.org/10.1016/j.compfluid.2010.05.011.

Cryer, C.W. 1963. A comparison of the three-dimensional consolidation theories of Biot and Terzaghi. *Q. J. Mech. Appl. Math.* **16** (4): 401–412. http://dx.doi.org/10.1093/qjmam/16.4.401.

Dalow, B.L., Ewing, R.E., and Wheeler, M.F. 1984. Mixed Finite Element Method for Miscible Displacement Problems in Porous Media. *SPE Journal* **24** (4): 391–398. SPE-10501-PA. http://dx.doi.org/10.2118/10501-PA.

Darman, N.H., Pickup, G.E., and Sorbie, K.S. 2002. A comparison of two-phase dynamic upscaling methods based on fluid potentials. *Computational Geosciences* **6** (1): 5–27. http://dx.doi.org/10.1023/A:1016572911992.

Dean, R.H., Gai, X., Stone, C.M., and Minkoff, S.E. 2006. A Comparison of Techniques for Coupling Porous Flow and Geomechanics. *SPE Journal* **11** (1): 132–140. SPE-79709-PA. http://dx.doi.org/10.2118/79709-PA.

Du, J. and Wong, R.C.K. 2009. Coupled Geomechanics Reservoir Simulation of UTF Phase A Project Using a Full Permeability Tensor. *Journal of Canadian Petroleum Technology* **48** (7): 66–73. http://dx.doi.org/10.2118/09-07-66.

Durlofsky, L.J. 1991. Numerical calculation of equivalent grid block permeability tensors for heterogeneous porous media. *Water Resources Research* **27**: 699–708. http://dx.doi.org/10.1029/91WR00107.

Durlofsky, L.J. 1994. The accuracy of mixed and control volume finite element approximations to Darcy velocity and related quantities. *Water Resources Research*, **30** (4): 965–973. http://dx.doi.org/10.1029/94WR00061.

Durlofsky, L.J. and Chien, M.C.H. 1993. Development of a Mixed Finite-Element-Based Compositional Reservoir Simulator. Paper SPE 25253 presented at the SPE Reservoir Simulation Symposium, New Orleans, Louisiana, 28 February-3 March. http://dx.doi.org/10.2118/25253-MS.

Edwards, M.G. and Rogers, C.F. 1998. Finite volume discretization with imposed flux continuity for the general tensor pressure equation. *Computational Geosciences* **2** (4): 259–290. http://dx.doi.org/10.1023/A:101151050406.

Ewing, R.E. and Heinemann, R.F. 1983. Incorporation of Mixed Finite Element Methods in Compositional Simulation for Reduction of Numerical Dispersion. Paper SPE 12267 presented at the SPE Reservoir Simulation Symposium, San Francisco, California, 15-18 November. http://dx.doi.org/10.2118/12267-MS.

Ferronato, M., Castelletto, N., and Gamboati, G. 2010. A fully coupled 3-D mixed finite element model of Biot consolidation. *Journal* of *Computational Physics* **229** (20): 4813–4830. http://dx.doi.org/10.1016/j.jcp.2010.03.018.

Fortin, M. and Brezzi, F. 1991. Mixed and Hybrid Finite Element Methods. Springer Ser. Comput. Math. **15**, Springer-Verlag, New York.

Gai, X. 2004. A Coupled Geomechanics and Reservoir Flow Model on Parallel Computers. PhD dissertation, University of Texas at Austin, Austin, Texas.

Geertsma, J. 1957. The Effect of Fluid Pressure Decline on Volumetric Changes of Porous Rocks. *Trans AIME* **210**: 331–340.

Geuzaine, C. and Remacle, J-.F. 2009. Gmsh: a three-dimensional finite element mesh generator with built-in pre- and post-processing facilities. *Int. J. Numer. Method Eng.* **79** (11): 1309–1331.

Ghosh, S., Lee, K., and Moorthy, S. 1995. Multiple scale analysis of heterogeneous elastic structures using homogenization theory and voronoi cell finite element method. *Int. J. Solids Structures*, **32** (1): 27–62. http://dx.doi.org/10.1016/0020-7683(94)00097-G.

Gomez-Hernandez, J.J. and Journel, A.G. 1994. Stochastic Characterization of Grid Block Permeabilities. *SPE Formation Evaluation* **9** (2): 93–99. http://dx.doi.org/10.2118/22187-PA.

Grechka, V. and Kachanov, M. 2006a. Effective elasticity of fractured rocks. *The Leading Edge* **25** (2): 152–155. http://dx.doi.org/10.1190/1.2172305.

Grechka, V. and Kachanov, M. 2006b. Effective elasticity of fractured rocks with closely spaced and intersecting cracks. *Geophysics* **71** (3): D85–D91. http://dx.doi.org/10.1190/1.2197489.

Grechka, V. and Kachanov, M. 2006c. Effective elasticity of fractured rocks: A snapshot of the work in progress. *Geophysics* **71** (6): W45–W58. http://dx.doi.org/10.1190/1.2360212.

Guedes, J.M. and Kikuchi, N. 1990. Preprocessing and postprocessing for materials based on the homogenization method with adaptive finite element methods. *Comput. Methods Appl. Mech. Eng*. **83** (2): 143–198. http://dx.doi.org/10.1016/0045-7825(90)90148-F.

Guermond, J.-L. and Pasquetti, R. 2008.Entropy-based nonlinear viscosity for Fourier approximations of conservation laws. *Computes Rendus Mathematique* **346** (13-14): 801–806. http://dx.doi.org/10.1016/j.crma.2008.05.013.

Gutierrez, M., Lewis, R.W. and, Masters, I. 2001. Petroleum Reservoir Simulation Coupling Fluid Flow and Geomechanics. *SPE Reservoir Evaluation and Engineering* **4** (3): 164–172. http://dx.doi.org/10.2118/72095-PA.

Hill, R.1963. Elastic properties of reinforced solids: some theoretical principles. *J. Mech. Phys. Solids* **11** (5): 357–372. http://dx.doi.org/10.1016/0022-5096(63)90036-X.

Hoteit, H. and Firoozabadi, A. 2006a. Compositional Modeling by the Combined Discontinuous Galerkin and Mixed Methods. *SPE Journal* **11** (1): 19–34. SPE-90276-PA. http://dx.doi.org/10.2118/90276-PA.

Hoteit, H. and Firoozabadi, A. 2006b. Compositional Modeling of Discrete-Fractured Media without Transfer Functions by the Discontinuous Galerkin and Mixed Methods. *SPE Journal* **11** (3): 341–354. SPE-90277-PA. http://dx.doi.org/10.2118/90277-PA.

Huang, H., Wattenbarger, R.C., Gai, X., William, P.B., Hehmeyer, O.J., Wang, J., and Long, T.A. 2013. Using a fully coupled flow and geomechanical simulator to model injection into heavy oil reservoirs. *Int. J. Numer. Meth. Fluids* **71** (6): 671–686. http://dx.doi.org/10.1002/fld.3679.

Huet, C. 1990. Application of variational concepts to size effects in elastic heterogeneous bodies. *J Mech Phys Solids* **38** (6): 813–841. http://dx.doi.org/10.1016/0022-5096(90)90041-2.

Jha, B. and Juans, R. 2007. A locally conservative finite element framework for the simulation of coupled flow and reservoir geomechanics. *Acta Geotech.* **2** (3): 139–153. http://dx.doi.org/10.1007/s11440-007-0033-0.

Khajeh, M.M., Chalaturnyk, R.J., and Boisvert, J.B. 2012. A Numerical Local Upscaling Approach For Elastic Rock Mechanical Properties: Dealing With Heterogeneity. Paper ARMA 12-654 presented at the 46th U.S. Rock Mechanics/Geomechanics Symposium, Chicago, Illinois, 24-27 June.

Khaled, M.Y., Beskos, D.E., and Aifantis, E.C. 1984. On the theory of consolidation with double porosity-III A finite element formulation. *Int. J. Numer. Anal. Methods Geomech.* **8**: 101–123.

Khalid-Naghadeh, N. and Valliappan, S. 1991. Flow through fissured porous media with deformable matrix: Implicit formulation. *Water Resources Research* **27** (7): 1703–1709. http://dx.doi.org/10.1029/91WR0161.

Kim, J., Moridis, G.J., Yang, D., and Rutqvist, J. 2012. Numerical Studies on Two-Way Coupled Fluid Flow and Geomechanics in Hydrate Deposits. *SPE Journal* **17** (2): 485-501. SPE-141304-PA. http://dx.doi.org/10.2118/141304-PA.

King, M.J. and Mansfield, M. 1999. Flow simulation of geologic models. *SPE Journal* **2** (4): 351–367. SPE-57469-PA. http:/dx.doi.org/10.2118/57469-PA.

King, M.J., King, P.R., McGill, C.A., and Williams, J.K. 1995. Effective properties for flow calculations. *Transport in Porous Media* **20** (1-2): 169–196. http://dx.doi.org/10.1007/BF00616929.

Klausen, R.A. and Winther, R. 2006. Convergence of multipoint flux approximations on quadrilateral grids. *Numerical Methods for Partial Differential Equations* **22** (6): 1438–1454. http://dx.doi.org/10.1002/num.20158.

Kouznetsova, V., Brekelmans, W.A.M., and Baaijens, F.P.T. 2001. An approach to micro-macro modeling of heterogeneous materials. *Computational Mechanics*. **27** (1): 37–48.

Kyte, J.R. and Berry, D.W. 1975. New Pseudo Functions to Control Numerical Dispersion. *SPE Journal* **15** (4): 269–276. SPE-5105-PA. http://dx.doi.org/10.2118/5105-PA.

Larsson, F., Runesson, K., and Su, F. 2010. Computational homogenization of uncoupled consolidation in micro-heterogeneous porous media. *Int. J. Numer. Anal. Meth. Geomech.* **34** (14): 1431–1458. DOI: http://dx.doi.org/10.1002/nag.862.

Lee, S.H., Durlofsky, L.J., Lough, M.F., and Chen, W.H. 1998. Finite Difference Simulation of Geologically Complex Reservoirs With Tensor Permeabilities. *SPE Reservoir Evaluation and Engineering* **1** (6): 567–574. SPE-52637-PA. http://dx.doi.org/10.2118/52637-PA.

Lewis, R.W. and Ghafouri, H.R. 1997. A novel finite element double porosity model for multiphase flow through deformable fractured porous media. *Int. J. Numer. Anal. Meth. Geom*. **21** (11) 789–816.

Lewis, R.W. and Pao, W.K.S. 2002. Numerical Simulation of Three-Phase Flow in Deforming Fractured Reservoirs. *Oil & Gas Science and Technology* **57** (5): 499–514. http://dx.doi.org/10.2516/ogst:2002033.

Lewis, R.W. and Schrefler, B.A. 1998. The Finite Element Method in the Static and Dynamic Deformation and consolidation of Porous Media. Second Edition, John Wiley & Sons, New York.

Lohne, A., Virnovsky, G., and Durlofsky, L.J. 2006. Two-Stage Upscaling of Two-Phase Flow: From Core to simulation Scale. *SPE Journal* **11** (3): 269–276. SPE-89422-PA. http://dx.doi.org/10.2118/89422-PA.

Mainguy, M. and Longuemare, P. 2002. Coupling fluid flow and rock mechanics: formulations of the partial coupling between reservoir and geomechanics simulators. *Oil Gas Sci Tech* **57** (4): 355–367.

Matringe, S.F., Juanes, R., and Tchelepi, H.A. 2008. Tracing Streamlines on the Unstructured Grids from Finite Volume Discretizations. *SPE Journal* **13** (4): 423–431. http://dx.doi.org/10.2118/103295-PA.

Miehe, C., and Koch, A. 2002. Computational micro-to-macro transition of discretized microstructures undergoing small strain. *Arch. Appl. Mech*. **72** (4-5): 300–317. http://dx.doi.org/10.1007/s00419-002-0212-2.

Mlacnik, M.J. and Durlofsky, L.J. 2006. Unstructured grid optimization for improved monotonicity of discrete solutions of elliptic equations with highly anisotropic coefficients. *Journal of Computational Physics* **216** (1): 337–361. http://dx.doi.org/10.1016/j.jcp.2005.12.007.

Moinfar, A., Sepehrnoori, K., Johns, R.T, and Varavei, A. 2013. Coupled Geomechanics and Flow Simulation for an Embeded Discrete Fracture Model. Paper SPE 163666 presented at the 2013 SPE Reservoir Simulation Symposium, The Woodlands, Texas, 18-20 February. http://dx.doi.org/10.2118/163666-MS.

Monteagudo, J.E.P. and Firrozabadi, A. 2004. Control-Volume method for numerical simulation of two-phase immiscible flow in two-and three-dimensional discrete-fractured media. *Water Resources Research* **40** (7): 1–20. http://dx.doi.org/10.1029/2003WR002996.

Monteagudo, J.E.P., Rodriguez, A.A., and Florez, H. 2011. Simulation of Flow in Deformable Fractured Porous Media. Paper SPE 141267 presented at the 2011 SPE Reservoir Simulation Symposium, The Woodlands, Texas, 21-23 February. http://dx.doi.org/10.2118/141267-MS.

Moridis, G.J., Kowalsky, M., and Pruess, K. 2008. TOUGH+HYDRATE v1.0 User's Manual: A Code for. the Simulation of System Behavior in Hydrate-Bearing Geologic Media. Report LBNL-00149E, Lawrence Berkeley National Laboratory, Berkeley, California.

Pahr, D.H. and Zysset, P.K. 2008. Influence of boundary conditions on computed apparent elastic properties of cancellous bone. *Biomech Model Mechnobiol* **7** (6):463–476. http://dx.doi.org/10.1007/s10237-007-0109-7.

Pao, W.K.S. and Lewis, R.W. 2002. Three-Dimensional Finite Element Simulation of Three-Phase Flow in a Deformable Fissured Reservoir. *Comput. Methods Appl. Mech. Engrg*. **191** (6):463–476. http://dx.doi.org/10.1006/S0045-7825(01)00420-0.

Peng, D. Y., and Robinson, D. B. 1976. A New Two-Constant Equation of State. *Industrial and Engineering Chemistry: Fundamentals* **15**: 59–64. http://dx.doi.org/10.1021/i160057a011.

Pickup, G.E., Ringrose, P.S., Jensen, J.L., and Sorbie, K.S. 1994. Permeability tensors for sedimentary structures. *Mathematical Geology* **26** (2): 227–250. http://dx.doi.org/10.1007/BF02082765.

Potsepaev, R., Farmer, C.L., and Fitzpatrick, A.J. 2009. Multipoint Flux Approximations vis Upscaling. Paper SPE 118979 presented at the SPE Reservoir Simulation Syposium, The Woodlands, Texas, 2–4 February. http://dx.doi.org/10.2118/118979-MS.

Raviart, P.A. and Thomas, J.M. 1977. A mixed finite element method for second order elliptic problems. *Mathematical Aspects of Finite Element Methods* Lecture Notes in Mathematical Series **606**: 292–315. http://dx.doi.org/10.1007/BFb0064451.

Rutqvist, J. and Moridis, G.J. 2009. Numerical Studies on the Geomechanical Stability of Hydrate-Bearing Sediments. *SPE Journal* **14** (2): 267–282. SPE-126129-PA. http://dx.doi.org/10.2118/126129-PA.

Rutqvist, J. and Tsang, C.-F. 2002. A study of caprock hydromechanical changes associated with CO_2-injection into a brine formation. *Environmental Geology* **42** (2-3): 296–306.

Saad, N., Cullick, A.S., and Honarpour, M.M. 1995. Effective Relative Permeability in Scale-Up and Simulation. paper SPE 29592 presented at the SPE Low Permeability Reservoirs Symposum, Denver, Colorado, 19–22 March. http://dx.doi.org/10.2118/29592-MS.

Salama, A., Sun, S., and Amin, M.F.E. 2013. A Multipoint Flux Approximation on the Steady-State Heat Conduction Equation in Anisotropic Media. *Journal of Heat Transfer* **135** (4): 1–6. http://dx.doi.org/10.1115/1.4023228.

Settari, A. and Mourits, F.M. 1994. Coupling of geomechanics and reservoir simulation models. Paper presented at the Eighth International Conference on Computer Methods and Advances in Geomechanics, West Virginia, USA, 22-28 May.

Settari, A. and Mourits, F.M. 1998. A Coupled Reservoir and Geomechanical Simulation System. *SPE Journal* **3** (3): 219–226. SPE-50939-PA. http://dx.doi.org/10.2118/50939-PA.

Settari, A. and Walters, D.A. 2001. Advances in Coupled Geomechanical and Reservoir Modeling with Applications to Reservoir Compaction. *SPE Journal* **6** (3): 334–342. SPE-74142-PA. http://dx.doi.org/10.2118/74142-PA.

Settari, A., Al-Ruwaili, K., and Sen, V. 2013. Upscaling of Geomechanics in Heterogeneous Compacting Reservoirs. Paper SPE 163641 presented at the SPE Reservoir Simulation Symposium, The Woodlands, Texas, 18–20 February. http://dx.doi.org/10.2118/163641-MS.

Smit, R.J.M., Brekelmans, W.A.A., and Meijer, H.E.M. 1998. Prediction of the mechanical behavior of nonlinear heterogeneous systems by multi-level finite element modeling. *Comput. Methods Appl. Mech. Eng*. **155** (1-2): 181–192. http://dx.doi.org/10.1016/S0045-7825(97)00139-4.

Soave, G. Equilibrium Constants from a Modified Redlich–Kwong Equation of State. 1972. C*hem. Eng. Sci.* **27** (6): 1197–1203. http://dx.doi.org/10.1016/0009-2509(72)80096-4.

Stone, H.L. 1991. Rigorous Black Oil Pseudo Functions. Paper SPE 21207 presented at the SPE Symposium on Reservoir Simulation, Anaheim, California, 17–20 February. http://dx.doi.org/10.2118/21207-MS.

Su, F., Larsson, F., and Runesson, K. 2011. Computational homogenization of coupled consolidation problems in micro-heterogeneous porous media. *Int. J. Numer. Method Eng.* **88** (11): 1198–1218. http//dx.doi.org/10.1002/nme.3221.

Suzuki, S. 2011. Pattern-Based Approach to Multiphase Flow Upscaling Using Distance-Based Clustering. Paper SPE 146639 presented at the SPE Annual Technical Conference and Exhibition, Denver, Colorado, 30 October–2 November. http://dx.doi.org/10.2118/146639-MS.

Terzaghi, K. 1923. Theoretical Soil Mechanics. *John Wiley*, New York.

Tran, D., Settari, A., and Nghiem, L. 2004. New Iterative Coupling Between a Reservoir Simulator and a Geomechanics Module. *SPE Journal* **9** (3): 362–369. SPE-88989-PA. http://dx.doi.org/10.2118/88989-PA.

Valliappan, S. and Khalili-Naghadeh, N. 1990. Flow through fissured porous media with deformable matrix. *Int. J. Numer. Method Eng.* **29** (5): 1079–1094.

Verruijt, A. 1995. Computational Geomechanics. Kluwer Academic Publishers, London.

Wan, J. 2002. Stabilized finite element methods for coupled geomechanics and multiphase flow. PhD dissertation, Stanford University, Stanford, California.

Wang, C.Y. 2006. Scale and boundary condition effects on elastic moduli of trabecular bone. MS thesis, Concordia University, Montreal, Quebec, Canada.

Warren, J.E. and Price, H.S. 2004. Flow in Heterogeneous Porous Media. *SPE Journal* **1** (3): 153–169. 1579-G. http://dx.doi.org/10.2118/1579-G.

Warren, J.E. and Root, P.J. 1963. The behavior of naturally fractured reservoirs. *SPE Journal* **3**: 245–255.

Wen, X.H., Chen, Y., and Durlofsky, L.J. 2006. Efficient 3D implementation of local-global upscaling for reservoir simulation. *SPE Journal* **11** (4): 443–453. SPE-92965-PA. http://dx.doi.org/10.2118/92965-PA.

Wen, X.H., Durlofsky, L.J., Edwards, M.G. 2003. Use of border regions for improved permeability upscaling. *Mathematical Geology* **35** (5):521–47. http://dx.doi.org/10.1023/A:1026230617943.

Wheeler, M.F. and Gai, X. 2007. Iteratively Coupled Mixed and Galerkin Finite Element Methods for Poro-Elasticity. *Numerical Methods for Partial Differential Equations* **23** (4): 785–797. http://dx.doi.org/10.1002/num.20258.

Wheeler, M.F. and Perszynska, M. 2002. Computaional engineering and science methodologies for modeling and simulation of subsurface applications. *Advances in Water Resources* **25** (8-12): 1147–1173. http://dx.doi.org/10.1016/S0309-1708(02)00105-7.

Wheeler, M.F. and Yotov, I. 2006. A multipoint flux mixed finite element method. *SIAM. J. Numer. Anal*. **44** (5): 2082–2106.

Wheeler, M.F., Xue, G., and Yotov, I. 2012. A multipoint flux mixed finite element method on distroted quadrilaterals and hexahedra. *Numerische Mathematik* **121** (1): 165–204. http://dx.doi.org/10.1007/s00211-011-0427-7.

White, J.A. 2009. Stabilized finite element methods for coupled flow and geomechanics. PhD dissertation, Stanford University, Stanford, California.

Wilson, R.K. and Aifantis, E.C. 1982. On the theory of consolidation with double porosity-II. *Int. J. Eng. Sci*. **20**: 1009–1035.

Wu, X.H., Efendiev, Y.R., and Hou, T.Y. 2002. Analysis of upscaling absolute permeability. *Discrete and Continuous Dynamical Systems–Serues B* **2** (2):185–204.

Younes, A., Ackerer, P., and Chavent, G. 2004. From mixed finite elements to finite volumes for elliptic PDEs in two and three dimensions. *Int. J. Numer. Meth. Engng*. **59** (3): 365–388. http://dx.doi.org/10.1002/nme.874.

Zhang, H.W. and Fu, Z.D. 2010. Coupling upscaling finite element method for consolidation analysis of heterogeneous saturated porous media. *Advances in W*ater *Resources*. **33** (1): 34–47. http://dx.doi.org/10.1016/j.advwatres.2009.10.1005.

Zhang, H.W, Fu, Z.D, and Wu J.K. 2009 Coupling multiscale finite element method for consolidation analysis of heterogeneous saturated porous media. *Advances in W*ater *Resources.* **32** (2): 268–79. http:dx.doi.org/10.1016/j.advwatres.2008.11.002.

Zhang, P., Pickup, G., Christie, M. 2008. A New Practical Method for Upscaling in Highly Heterogeneous Reservoir Models. *SPE Journal* **13** (1): 68–76. SPE-103760-PA. http://dx.doi.org/10.2118/103760-PA.

Zijl, W. and Trykozko, A. 2002. Numerical homogenization of two-phase flow in porous media. *Comput. Geosci*. **6** (1): 49–71. http:dx.doi.org/10.1023/A:1016577012900.

Zysset, P.K. 2003. A review of morphology-elasticity relationships in human trabecular bone: theories and experiments. *J. Biomech.* **36** (10) 1469–1485. http://dx.doi.org/10.1016/S0021-9290(03)00128-3.

APPENDIX A

STRESS AND STRAIN RELATION

I derive the stress and strain relation for a homogeneous rock. The stress and strain relation is defined by Hooke's law

$$\boldsymbol{\sigma} = \boldsymbol{E} : \boldsymbol{\varepsilon} \quad \text{(A-1)}$$

where $\boldsymbol{\sigma}$ is the second order stress tensor; $\boldsymbol{E}$ is the fourth order elastic stiffness tensor; $\boldsymbol{\varepsilon}$ is the second order strain tensor. Assuming a homogeneous rock the stress and strain relation can be expressed as (matrix and vector notation)

$$\begin{bmatrix} \sigma_{11} \\ \sigma_{22} \\ \sigma_{33} \\ \sigma_{23} \\ \sigma_{31} \\ \sigma_{12} \end{bmatrix} = \begin{bmatrix} 2\mu+\lambda & \lambda & \lambda & 0 & 0 & 0 \\ \lambda & 2\mu+\lambda & \lambda & 0 & 0 & 0 \\ \lambda & \lambda & 2\mu+\lambda & 0 & 0 & 0 \\ 0 & 0 & 0 & \mu & 0 & 0 \\ 0 & 0 & 0 & 0 & \mu & 0 \\ 0 & 0 & 0 & 0 & 0 & \mu \end{bmatrix} \begin{bmatrix} \varepsilon_{11} \\ \varepsilon_{22} \\ \varepsilon_{33} \\ 2\varepsilon_{23} \\ 2\varepsilon_{31} \\ 2\varepsilon_{12} \end{bmatrix} \quad \text{(A-2)}$$

where λ is first Lamé's constant and μ is the second Lamé's constant (shear modulus). By matrix and vector multiplication each stress component is obtained as

$$\sigma_{11} = (2\mu+\lambda)\varepsilon_{11} + \varepsilon_{22}\lambda + \varepsilon_{33}\lambda = 2\mu\varepsilon_{11} + \lambda(\varepsilon_{11}+\varepsilon_{22}+\varepsilon_{33}) = 2\mu\varepsilon_{11} + \lambda\nabla\cdot\boldsymbol{u} \quad \text{(A-3)}$$

$$\sigma_{22} = \lambda\varepsilon_{11} + (2\mu+\lambda)\varepsilon_{22} + \varepsilon_{33}\lambda = 2\mu\varepsilon_{22} + \lambda(\varepsilon_{11}+\varepsilon_{22}+\varepsilon_{33}) = 2\mu\varepsilon_{22} + \lambda\nabla\cdot\boldsymbol{u} \quad \text{(A-4)}$$

$$\sigma_{33} = \lambda\varepsilon_{11} + \lambda\varepsilon_{22} + (2\mu+\lambda)\varepsilon_{33} = 2\mu\varepsilon_{33} + \lambda(\varepsilon_{11}+\varepsilon_{22}+\varepsilon_{33}) = 2\mu\varepsilon_{33} + \lambda\nabla\cdot\boldsymbol{u} \quad \text{(A-5)}$$

$$\sigma_{23} = 2\mu\varepsilon_{23} \quad \text{(A-6)}$$

$$\sigma_{31} = 2\mu\varepsilon_{31} \quad \text{(A-7)}$$

$$\sigma_{12} = 2\mu\varepsilon_{12} \quad \text{(A-8)}$$

In general form, the stress in a homogeneous rock is written as

$$\boldsymbol{\sigma} = \lambda\nabla\cdot\boldsymbol{u}\boldsymbol{I} + 2\mu\boldsymbol{\varepsilon} \quad \text{(A-9)}$$

Now, I want to express starain energy as

$$\boldsymbol{\varepsilon}(\boldsymbol{v}) : \boldsymbol{\sigma}(\boldsymbol{u}) = [\varepsilon_{11} \quad \varepsilon_{22} \quad \varepsilon_{33} \quad 2\varepsilon_{23} \quad 2\varepsilon_{31} \quad 2\varepsilon_{12}] \begin{bmatrix} \sigma_{11} \\ \sigma_{22} \\ \sigma_{33} \\ \sigma_{23} \\ \sigma_{31} \\ \sigma_{12} \end{bmatrix} \quad \text{.....(A-10)}$$

where $\boldsymbol{\varepsilon}(\boldsymbol{v})$ is the second order strain tensor. Note that $\boldsymbol{v}$ is the displacement vector, which is the same as $\boldsymbol{u}$. The inner product of the two vectors in Eq. A-10 is written as

$$\boldsymbol{\varepsilon}(\boldsymbol{v}) : \boldsymbol{\sigma}(\boldsymbol{u}) = \varepsilon_{11}\sigma_{11} + \varepsilon_{22}\sigma_{22} + \varepsilon_{33}\sigma_{33} + 2\varepsilon_{23}\sigma_{23} + 2\varepsilon_{31}\sigma_{31} + 2\varepsilon_{12}\sigma_{12} = 2\mu\varepsilon_{11}(\boldsymbol{v})\varepsilon_{11}(\boldsymbol{u}) + \lambda\nabla \cdot \boldsymbol{u}\varepsilon_{11}(\boldsymbol{v}) + 2\mu\varepsilon_{22}(\boldsymbol{v})\varepsilon_{22}(\boldsymbol{u}) + \lambda\nabla \cdot \boldsymbol{u}\varepsilon_{22}(\boldsymbol{v}) + 2\mu\varepsilon_{33}(\boldsymbol{v})\varepsilon_{33}(\boldsymbol{u}) + \lambda\nabla \cdot \boldsymbol{u}\varepsilon_{33}(\boldsymbol{v}) + 4\mu\varepsilon_{23}(\boldsymbol{v})\varepsilon_{23}(\boldsymbol{u}) + 4\mu\varepsilon_{31}(\boldsymbol{v})\varepsilon_{31}(\boldsymbol{u}) + 4\mu\varepsilon_{12}(\boldsymbol{v})\varepsilon_{12}(\boldsymbol{u}) \quad \text{.....(A-11)}$$

Eq. A-11 can be reduced to

$$\boldsymbol{\varepsilon}(\boldsymbol{v}) : \boldsymbol{\sigma}(\boldsymbol{u}) = \boldsymbol{\varepsilon}(\boldsymbol{v}) : \mu\boldsymbol{\varepsilon}(\boldsymbol{u}) + \lambda(\nabla \cdot \boldsymbol{u})(\nabla \cdot \boldsymbol{v}) \quad \text{.....(A-12)}$$

Eq. A-12 is the same as the weak form of the displacement equation without the pressure and gravity. In a bilinear form this can be written as

$$\big(\boldsymbol{\varepsilon}(\boldsymbol{v}), \boldsymbol{\sigma}(\boldsymbol{u})\big)_{\Omega} = 2\big(\boldsymbol{\varepsilon}(\boldsymbol{v}), \mu\boldsymbol{\varepsilon}(\boldsymbol{u})\big)_{\Omega} + \big(\lambda(\nabla \cdot \boldsymbol{v}), (\nabla \cdot \boldsymbol{u})\big)_{\Omega} \quad \text{.....(A-13)}$$

The tensor product of the strain operator and the pore pressure is expressed as

$$\boldsymbol{\varepsilon}(\boldsymbol{v}) : bp\boldsymbol{I} = [\varepsilon_{11} \quad \varepsilon_{22} \quad \varepsilon_{33} \quad 2\varepsilon_{23} \quad 2\varepsilon_{31} \quad 2\varepsilon_{12}] \begin{bmatrix} bp \\ bp \\ bp \\ 0 \\ 0 \\ 0 \end{bmatrix} = (\nabla \cdot \boldsymbol{v})bp \quad \text{.....(A-14)}$$

In terms of a bilinear form,

$$(\boldsymbol{\varepsilon}(\boldsymbol{v}), bp\boldsymbol{I})_{\boldsymbol{\Omega}} = (\nabla \cdot \boldsymbol{v}, bp)_{\boldsymbol{\Omega}} \quad \text{.....(A-15)}$$

APPENDIX B

UNSTRUCTURED MESH GENERATION USING GMSH

I used Gmsh to generate unstractured meshes. Gmsh has the capability to generate unstructured meshes with triangular or quadrilateral elements. I can simply download Gmsh from the website (http://geuz.org/gmsh/). Gmsh has a user-friendly feature, which I can generate a mesh using a graphical user interface or C++ like input file called "geo file". I will show a step-by-step example to generate mesh with Gmsh. One thing we have to remember is that most of the finite element codes enumerate the nodes of an element in counter clock-wise direction. Therefore, we need to make sure that we follow a consistent direction of enumeration when generating a mesh with Gmsh. Otherwise, Gmsh could generate a mesh file that contains both counter clock-wise and clock-wise numbering, which many FEM codes may not handle. When a code which only handles counter clock-wise numbering sees the clock-wise numbering of nodes in an element it may assume that the area or volume of the element is negative and would show errors or provide unrealistic simulation results.

As a demonstration, I will generate a single fracture mesh shown in **Fig. B.1**.

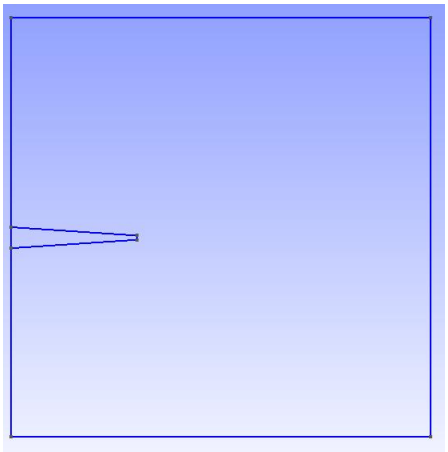

Fig. B.1—A sketch of a single fracture in a square box domain.

First, I create a geo file then assigns points that I connect to make lines (straint line, spline, B-spline, circle arc, and ellipse arc). I can do this with the graphical user interface in Gmsh or directly using the geo file. If I use the graphical user interface to create a sketch Gmsh automatically creates a geo file and writes all the commands in the geo file. Following are the command lines that create the points

```
Mesh.RecombineAll=1;
Mesh.RecombinationAlgorithm=1;
Mesh.Algorithm=8;
Mesh.MshFileVersion=1;
lc=0.5;
lc1=0.1;
Point(1) ={0, 0, 0, lc};
Point(2) = {10.0, 0, 0, lc};
Point(3) = {0, 10.0, 0, lc};
Point(4) = {10.0, 10.0, 0, lc};
Point(5) = {0, 5.0,0,lc1};
Point(6) = {0, 4.5,0,lc1};
Point(7) = {3.0, 4.7,0,lc1};
Point(8) = {3.0, 4.8,0,lc1};
```

The first three lines indicate the options that I use. In this case, it is a quadrilateral mesh generation algorithm. The fourth line indicates an option that generates an output as the legacy version (first version of Gmsh). Lc1 indicates the element characteristic parameter that determines the element size of the mesh. If I want to make a finer mesh in a certain region I can make this characteristic length parameter smaller so that Gmsh generates a locally refined mesh. In this problem I want to refine the area where the fracture exists. Once I make points, it will be visualized in the Gmsh program shown in **Fig. B.2**.

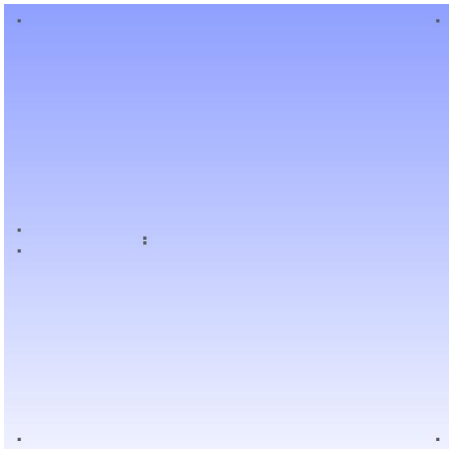

Fig. B.2—Points generated by the geo file. By connecting the points we can generate a sketch that describes a fracture in a 2D square box domain.

I need to connect the points to make lines. Keep in mind that whenever we make a modification of our geo file we need to reload our geo file in the Gmsh program. Therefore, Gmsh can update new information from the modified geo file. After connecting the points, I can obtain a sketch of a single fracture that would look like **Fig. B.1**.

After generating a sketch, I can make a plane surface by selecting lines. When I select lines to construct the surface I need to follow the counter clock-wise convention so that Gmsh will generate a mesh based on the counter clock wise convention. The following geo file commands generate surfaces for the fracture and the outside of the fracture (intact rock).

```
Mesh.RecombineAll=1;
Mesh.RecombinationAlgorithm=1;
Mesh.Algorithm=8;
Mesh.MshFileVersion=1;
lc=0.5;
lc1=0.1;
Point(1) ={0, 0, 0, lc};
Point(2) = {10.0, 0, 0, lc};
Point(3) = {0, 10.0, 0, lc};
Point(4) = {10.0, 10.0, 0, lc};
Point(5) = {0, 5.0,0,lc1};
Point(6) = {0, 4.5,0,lc1};
Point(7) = {3.0, 4.7,0,lc1};
Point(8) = {3.0, 4.8,0,lc1};

Line(1) = {3, 5};
Line(2) = {5, 6};
Line(3) = {6, 7};
Line(4) = {7, 8};
Line(5) = {8, 5};
Line(6) = {6, 1};
Line(7) = {1, 2};
Line(8) = {2, 4};
Line(9) = {4, 3};

Line Loop(10) = {5, 2, 3, 4};
Plane Surface(11) = {10};
Line Loop(12) = {1, -5, -4, -3, 6, 7, 8, 9};
Plane Surface(13) = {12};
```

Note that the negative convention of the Line Loop(12) was to make sure the construction of the surface follows the counter clock wise direction. After generating the surfaces I can generate a mesh by selecting the 2D meshing option in the graphical user interface. **Fig. B.3** shows the unstructured mesh that was created with Gmsh. The area inside and near the fracture was locally refined.

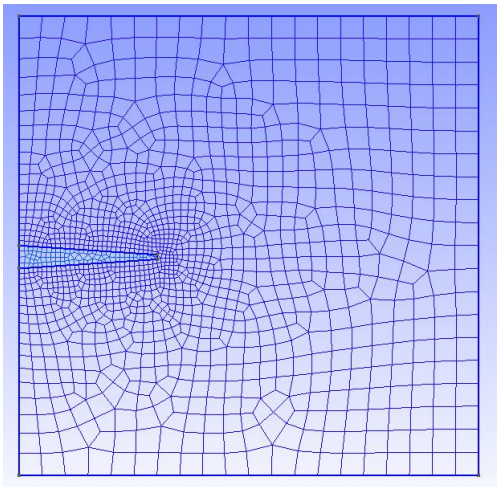

Fig. B.3—2D quadrilateral mesh of a single fracture. The fracture was locally refined by using different value of the element characteristic parameter.

After creating a mesh file I need to do some post processing of the mesh file so our FEM code can read the mesh file.